River Rapids

Conference Proceedings of the Society for Experimental Mechanics Series

Topics in Modal Analysis & Parameter Identification in Structural Dynamics, Volume 8

Timothy Marinone
Jon Furlich
Sheyda Davaria



Proceedings of the 44th IMAC, A Conference and Exposition on Structural Dynamics 2026

River Publishers

Conference Proceedings of the Society for Experimental Mechanics Series

Series Editor

Kristin B. Zimmerman
Society for Experimental Mechanics, Inc.,
Bethel, USA

The Conference Proceedings of the Society for Experimental Mechanics Series presents early findings and case studies from a wide range of fundamental and applied work across the broad range of fields that comprise Experimental Mechanics. Series volumes follow the principle tracks or focus topics featured in each of the Society's two annual conferences: IMAC, A Conference and Exposition on Structural Dynamics, and the Society's Annual Conference & Exposition and will address critical areas of interest to researchers and design engineers working in all areas of Structural Dynamics, Solid Mechanics and Materials Research.

Timothy Marinone · Jon Furlich · Sheyda Davaria
Editors

Topics in Modal Analysis & Parameter Identification in Structural Dynamics, 2026, Vol. 8

Proceedings of the 44th IMAC, A Conference and Exposition on Structural Dynamics 2026



River Publishers

Published, sold and distributed by:

River Publishers
Broagervej 10
9260 Gistrup
Denmark

www.riverpublishers.com

ISBN 97887-438-1447-4 (Hardback)

ISBN 97887-438-1419-1 (eBook)

https://doi.org/10.13052/rp-9788743814191

Conference Proceedings of the Society for Experimental Mechanics

An imprint of River Publishers

© The Society for Experimental Mechanics, Inc. 2026

This work is subject to copyright. All rights are solely and exclusively licensed by the Publisher, whether the whole or part of the material is concerned, specifically the rights of translation, reprinting, reuse of illustrations, recitation, broadcasting, or reproduction in any other physical way, and transmission or information storage and retrieval, electronic adaptation, computer software, or by similar or dissimilar methodology now known or hereafter developed.

The use of general descriptive names, registered names, trademarks, service marks, etc. in this publication does not imply, even in the absence of a specific statement, that such names are exempt from the relevant protective laws and regulations and therefore free for general use. The publisher, the authors, and the editors are safe to assume that the advice and information in this book are believed to be true and accurate at the date of publication. Neither the publisher nor the authors or the editors give a warranty, expressed or implied, with respect to the material contained herein or for any errors or omissions that may have been made. The publisher remains neutral with regard to jurisdictional claims in published maps and institutional affiliations.

Preface

Topics in Modal Analysis & Parameter Identification in Structural Dynamics represents one of ten volumes of technical papers presented at the 44th IMAC, A Conference and Exposition on Structural Dynamics, organized by the Society for Experimental Mechanics, and held January 19-22, 2026. The full proceedings also include volumes on Nonlinear Structures & Systems; Dynamics of Civil Structures; Model Validation and Uncertainty Quantification; Dynamic Substructuring & Transfer Path Analysis; Special Topics & Experimental Techniques in Structural Dynamics; Computer Vision & SLDV for Structural Dynamics; Dynamic Environments and Durability Testing; Topics in Modal Analysis & Parameter Identification in Structural Dynamics; Data Science in Engineering; and Structural Health Monitoring, Metamaterials, Metastructures & Additive Manufacturing and Dynamics of Biomedical & Bioinspired Systems.

Each collection presents early findings from experimental and computational investigations on an important area within Structural Dynamics. Topics in Modal Analysis and Parameter Identification in Structural Dynamics represents papers on enabling technologies for dynamic systems and applications of Modal Analysis in specific application areas.

The organizers would like to thank the authors, presenters, session organizers, and session chairs for their participation in this track.

Editors:

Timothy Marinone – ATA Engineering, Inc., San Diego, CA, USA;
Jon Furlich – ATA Engineering, Inc., San Diego, CA, USA;
Sheyda Davaria – Northrop Grumman, Reston, VA, USA

Contents

1 **Modal Survey Testing Using Combined Acoustic and Conventional Excitation Techniques** 1
Kevin Napolitano, Dr. Michael Yang, Dale Schick, and David Kimpton

2 **A Spectral Matrix Estimation Scheme for Pseudorandom Excitation with Concurrent Phase Combinations** 9
Kevin Napolitano and William Fladung

3 **Vibration-Based System Identification of Structural Dynamics using a Stochastic Gradient SINDy** 19
Celso T. do Cabo, Raymond Joshua, and Zhu Mao

4 **A Comparison of Uncertainty Quantification Methods for Damping Ratio Estimates from Tall, Modular Buildings** 27
Patrick Brewick and John Hickey

5 **3D Printing Approaches for Reproducible Measurement of Vibroacoustically Excited Triboelectric Nanogenerators** 35
Nakul S. Deshpande, Eric C. Bryant, Thomas Z. Box, Thomas S. Cox, Audrey L. Evans, Natalie White, Kent X. Eng, Stephen J. Kao, Darrel T. Beckman, Christopher A. Mizzi, Luke B. Beardslee, and Amanda E. King

6 **Ice Detection on Plate Structures Using Modal Curvature and Piezoelectric Sensor Networks** 43
Lorenzo Stagi, Nicola Roveri, Salvatore Ameduri, Antonio Concilio, and Jean-François Deü

7 **High-precision Modal Parameter Identification Algorithm Based on QR Decomposition** 53
J. M. Liu and F. Liu

8 **Expanding the Versatility of Resonant Ultrasound Spectroscopy** 65
Andres Garcia (A&M), Kayleigh Hanlon (UIUC), Matthew Luci (RHIT), Mentors: Paul Geimer (MST-8), Mathew Hayne (MST-16), and Georgios Koutsakis (UNM)

9 **Extraction of Boundary Impedance via Traveling Wave Analysis** 79
William C. Rogers, Mohammad I. Albakri, and Pablo A. Tarazaga

10 **Operational Modal Analysis of the Bear Mountain Bridge and Comparisons with Finite Element Model** 87
CDT Gautam Namjoshi, CDT Ethan Espinosa, CDT Philip Williams, Courtney Clark, Dr. Qian Chen, and Dr. Thomas J. Matarazzo

11 **Experimental System Identification and Tower-Top Dynamic Response of Monopile-Supported Offshore Wind Turbines During Installation** 95
Saravanan Bhaskaran, Max Kruse, Andrew Goupee and Amrit Verma

12 **Verification and Convergence of Multi-Harmonic Balance Algorithms for Future Application in Sierra/SD Finite Element Code** 103
Oliver Khan, Dalton L. Stein, Nathan Schill, Robert J. Kuether, and David M. Day

13 **Quantification of Vibrational Power Dissipation in a Coupled Panel System Using Experimental Modal Analysis** 109
Karsten Hilgarth, Yeongeun Ki, Daniel Litowitz, Eric Williamson, Karthik Boddapati, Hongcheng Tao, Charlotte Moss, Greg Shaver, John T. Evans, Andres F. Arrieta, and James M. Gibert

14 Guided Analysis Tools for Highly Efficient Impact Testing and Modal Parameter Estimation 123
Bart Peeters, Simone Manzato, and Mattia Dal Borgo

15 Tips, Tricks, and Obscure Features for Operational Modal Analysis with Cross Spectra 131
William Fladung and Kevin Napolitano

16 Time-Reversed Vibration-Induced Particle Motion on an Elastic Plate 139
Abigail Smith, Sanchita Das, Samikhshak Gupta, and Vijaya V. N. Sriram Malladi

17 Damping Identification Using FBG Sensors in Controlled Thermal and Pressure Conditions 145
Lorenzo Sclafani, Antonello Binni, Silvia Milana, Antonio Culla, and Antonio Carcaterra

18 Experimental-Based Investigation of Standing and Traveling Waves in a Petri Dish using Piezoelectric Actuation 151
Rachel Cole, Samikhshak Gupta, Vijaya V. N. Sriram Malladi, Smitha Rao Hatti, and Adrienne Minerick

Chapter 1
Modal Survey Testing Using Combined Acoustic and Conventional Excitation Techniques

Kevin Napolitano, Dr. Michael Yang, Dale Schick, and David Kimpton

Abstract There is increasing interest in the aerospace community to reduce testing cost, risk, and schedule impacts by combining as many structure-related tests as practicable into a single test setup. This paper presents a method to perform modal survey testing in a direct field acoustic (DFA) test setup by using DFA inputs to excite acoustically sensitive structural modes and base inputs to excite high effective mass modes. While both input methods are able to excite many of the same modes of a test article, the combination of excitation methods allows for excitation of all modes that will be excited during launch. Furthermore, test data from both excitation methods can be combined with fixed base correction techniques to remove the effects of uncertain boundary conditions that are typically present when performing DFA testing.

Keywords Signal processing · Modal testing · Environmental testing · Direct field acoustic testing · Fixed base correction

Introduction

There is an increasing desire within the aerospace community to develop and deploy vehicles at an increasing pace, and one potential way of reducing development time is to perform as many different tests in as few testing configurations as possible [1], [2]. One way to do this is to perform a high-quality modal survey test to validate an analysis model while the test article is configured for an acoustic qualification test. The main challenge with this approach is not the use of acoustics as a source of excitation, but rather that the test article is usually mounted to a transportation cart that is oftentimes poorly modeled and dynamically active over the typical frequency range of a modal survey test.

This paper presents a method to perform modal survey testing in a direct field acoustic (DFA) test setup by using acoustic sources to excite acoustically sensitive structural modes and base inputs using conventional excitation techniques, such as shakers or impact devices, to excite modes sensitive to base excitation. While both input methods are able to excite many of the same modes of a test article, the combination of excitation methods allows for excitation of all modes that will be excited during launch. Furthermore, test data from both excitation methods can be combined with a fixed base correction (FBC) technique to remove the effects of uncertain boundary conditions that are typically present when performing DFA testing.

Kevin Napolitano · Dr. Michael Yang
ATA Engineering, Inc., San Diego, CA 92128
e-mail: kevin.napolitano@ata-e.com; myang@ata-e.com

Dale Schick
Acoustic Research Systems, Shepherdstown, WV 25443
e-mail: d.schick@acousticrs.com

David Kimpton
Northrop Grumman Space Systems, Sterling, VA 20166
e-mail: David.Kimpton@ngc.com

© The Author(s), under exclusive license to River Publishers 2026

Kristin B. Zimmerman, PhD (eds.), *Topics in Modal Analysis & Parameter Identification in Structural Dynamics, 2026, Vol. 8*,
Conference Proceedings of the Society for Experimental Mechanics Series, https://doi.org/10.13052/rp-9788743814191

Review of Modal Survey Tests Using Acoustic Excitation

Programs can save cost and schedule by performing DFA testing at a customer's facility in lieu of performing traditional acoustic testing at remote facilities. Fig. 1 presents a typical DFA test setup using Acoustic Research Systems' (ARS) Neutron^{TM} acoustic exciters. The test article is surrounded by a large number of independent acoustic sources while it is mounted on a either a transportation cart or another boundary condition—perhaps mounted directly to a seismic mass suitable for modal survey tests. Each acoustic exciter is similar to a typical electrodynamic modal shaker in that they are both driven by magnetic voice coil actuators. The difference is how the force is transmitted to a test article. The force generated by a modal shaker is transmitted directly to a test article through a stinger rod and is directly measured with a load cell, whereas the pressure from an acoustic exciter is transmitted to the test article through air and cannot be directly measured. Further savings can be realized if modal survey tests can be performed while a test article is configured for a DFA test.

Acoustic excitation is beneficial in exciting acoustically sensitive modes; and some acoustic devices like the Neutron^{TM} exciters are capable of a wider bandwidth, especially in the lower frequencies, than is typical. Two major factors that contribute to this capability are:

1. High initial efficiency through acoustic impedance matching (horn loading) and drivers with very high field strength to coil resistance ratios, and
2. Low mechanical losses through extremely robust construction – any flexure in the structure of the loudspeaker will be somewhat parasitic to the output unless the construction is very rigid.

The second point provides the added benefit of allowing their use for low-frequency modal testing above 2 Hz.

As such, recent research has been performed to explore how modal parameters (shape, frequency, damping) can be extracted from either test-measured or frequency response function (FRF)-synthesized cross-spectrum matrices that were created using acoustic excitation [3]–[6].

The main challenge with in situ acoustic modal testing is that the boundary condition, which is typically a transportation cart, is oftentimes dynamically active and not well modeled. A secondary challenge is that not all target modes may be excited well by acoustic excitation alone, which may lead to poorly extracted modes. The inability of a given exciter to not excite all modes is typical of any modal excitation technique and is oftentimes overcome by performing additional tests with exciters at different locations on the test article.



Fig. 1 Typical acoustic qualification test setup

Review of Fixed Base Correction

One way to address the boundary condition challenge is to mount the test article on a well-modeled support that can be inserted into the analysis model and incorporated in the model updating effort. Another way to address both the uncertain boundary condition and the excitation of all the target modes in a modal survey test is to supplement the acoustic test with conventional excitation sources, such as modal shakers and impact testing, and use the FBC technique [7] to measure FRFs associated with the boundary fixed.

FBC exploits the fact that when using drive point accelerations as references, mode shapes associated with the resulting FRFs are associated with those same acceleration degrees of freedom (DOF) fixed. The method has been used to measure fixed base modes on a variety of dynamically active boundary conditions including six-DOF base shake systems [8], shaker tables [7], and static testing fixtures [9].

In order to implement the method on a transportation cart, the number of shaker or impact locations used to excite the cart must be equal to or greater than the number of dynamically active shapes of the transportation cart over the frequency range of interest. The exciters must also be able to activate the dynamically active shapes.

Combining Acoustic Excitation and Fixed Base Correction

The straightforward way to implement FBC with acoustic excitation is to run all the exciters simultaneously including both the numerous acoustic excitation sources and the modal shakers mounted to the base, and then use both the acoustic sources and the base acceleration sources as references when calculating FRFs. The resulting FRFs, including the acoustic excitation sources, will be associated with those acceleration reference DOFs fixed.

There, however, may be future scenarios where a very large number of independent acoustic references, on the order of 80 or more, may be employed that could make calculating FRFs difficult and time-consuming. As such, this section presents an alternative approach that estimates modes from the fixed base corrected output cross-spectral matrix using FRFs from a separate test where only the accelerations of the boundary are used as references to remove motion from the base. The approach follows a Master's thesis by L.M. Elias [10] that separated responses due to disturbance sources from disturbances due to dynamically active boundaries.

The FRF equation using acoustic sources and boundary accelerations as references can be written as

$$\{A\} = \begin{bmatrix} H_{Ap} & H_{AB} \end{bmatrix} \begin{Bmatrix} P \\ A_B \end{Bmatrix} \tag{1}$$

where $\{A\}$ are measured responses such as accelerations, $\{A_B\}$ are the boundary accelerations and can be generalized coordinates such as constraint shapes, $\{P\}$ are the acoustic sources, $[H_{Ap}]$ is the FRF matrix associated with the acoustic sources {P} activated while holding the base accelerations $\{A_B\}$ equal to zero, and $[H_{AB}]$ is the test-measured FRF matrix due to exciting the boundary directly while holding the acoustic sources equal to zero. In practice, it is straightforward to generate the matrix $[H_{AB}]$ directly by exciting the base directly with conventional exciters while not turning on the acoustic sources. The matrix $[H_{Ap}]$, however, cannot be measured if the base is not excited directly because it is not possible to hold the base accelerations equal to zero while the acoustic sources are activated. Instead, the matrix must be generated from test data where all of the conventional base exciters and each acoustic source are activated.

To remove the requirement of calculating the matrix $[H_{Ap}]$ directly, a first test that measures the matrix $[H_{AB}]$ directly is performed by exciting the boundary directly while the acoustic sources are turned off; i.e., {P}={0}. Thus,

$$\{A\} = [H_{AB}]\{A_B\} \tag{2}$$

Equation (1) is expanded to $\{A\} = [H_{Ap}]\{P\} + [H_{AB}]\{A_B\}$, where $[H_{Ap}]\{P\}$ and $[H_{AB}]\{A_B\}$ are the response of the system due to the acoustic sources assuming the base accelerations are equal to zero and the response due to the base accelerations assuming the acoustic sources are equal to zero, respectively. This equation can be rewritten to solve for $[H_{Ap}]\{P\}$ as

$$\left\{\overline{A}\right\} = [H_{Ap}]\{P\} = \{A\} - [H_{AB}]\{A_B\} \tag{3}$$

where $\left\{\overline{A}\right\}$ is the response of the acoustic inputs holding the base accelerations fixed. Since $\{A\}$ and $\{A_B\}$ are measured and $[H_{AB}]$ is known, the product $\left\{\overline{A}\right\}$ can be calculated for each frame of data to calculate the output cross-spectrum $[S_{\overline{AA}}]$ as

$$[S_{\overline{AA}}] = \left\{\overline{A}\right\}\left\{\overline{A}\right\}^H \tag{4}$$

The frames are then averaged together to calculate the total response cross-spectrum due to acoustic inputs holding the base motion equal to zero. The resulting cross-spectrum matrix is then used to estimate modal parameters using operational modal analysis techniques.

Experimental Example

A previous presentation [5] documents the results of combining FRFs associated with acoustic sources with FRFs using conventional shaker excitation.

In this example, response cross-spectrum data from the same test article is calculated for two sets of tests: acoustic random input, and base impact test data. The impact test data is then used to calculate FRFs associated with the base accelerations as references. Then, Equation (4) is used to generate response cross-spectrum due to acoustic sources while holding the base accelerations fixed.

The test article in Fig. 2, a satellite mass model provided by Northrop Grumman Corporation, is mounted to its transportation cart, which is a typical testing configuration for acoustic qualification testing. For this test, however, the transportation cart was supported on isolators used to regularize and isolate the transfer of loading from the cart to the ground. A total of 24 Neutron^{TM} acoustic sources were used in an eight-stack configuration with three sources per stack. Control microphones placed in front of each source were used to set voltage levels for its corresponding source. ATA Engineering (ATA)-owned modal shakers were used to excite the base of the test article as well, but this paper presents the results using impact testing on the base to generate the base FRFs.

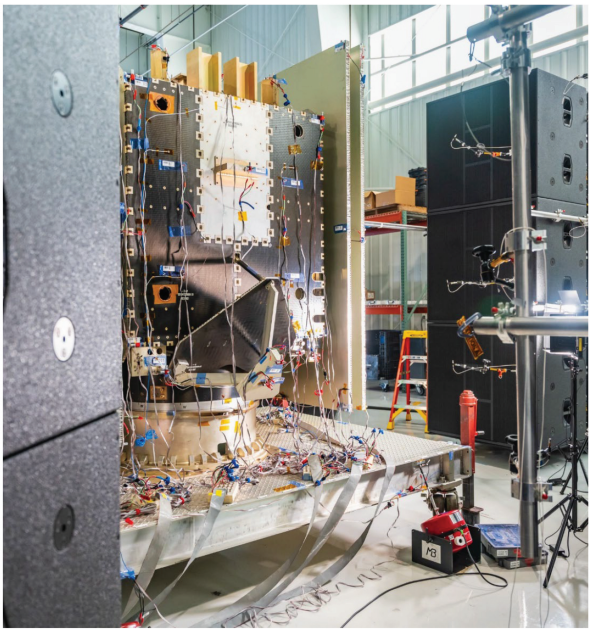

Fig. 2 Test article

A test display model is presented in Fig. 3. A total of 151 response accelerometers were mounted to the test article including twelve seismic accelerometers, which were mounted to observe the six rigid body modes of the transportation cart, the primary twist mode of the cart, and the three out-of-plane deformations (two roll and one vertical) of the center connection.

Impacts were performed using an uninstrumented mallet with a soft eraser bonded to the impact face to shape the frequency content of the impact to lower frequencies. Approximately five to eight impacts were performed near each of the twelve seismic accelerometers mounted on the transportation cart. The impacts were spaced greater than 8 seconds apart so that 8-second frames could be used to calculate FRFs. Ten transportation acceleration constraint shapes were used as references when calculating FRFs. The six rigid body modes of the transportation cart were supplemented with outer perimeter twist. Three additional constraint shapes were added: the of overall inner square rigid body RX, and RY, and Z motion out of phase with outer perimeter rigid body RX, RY, and RZ motion, respectively.

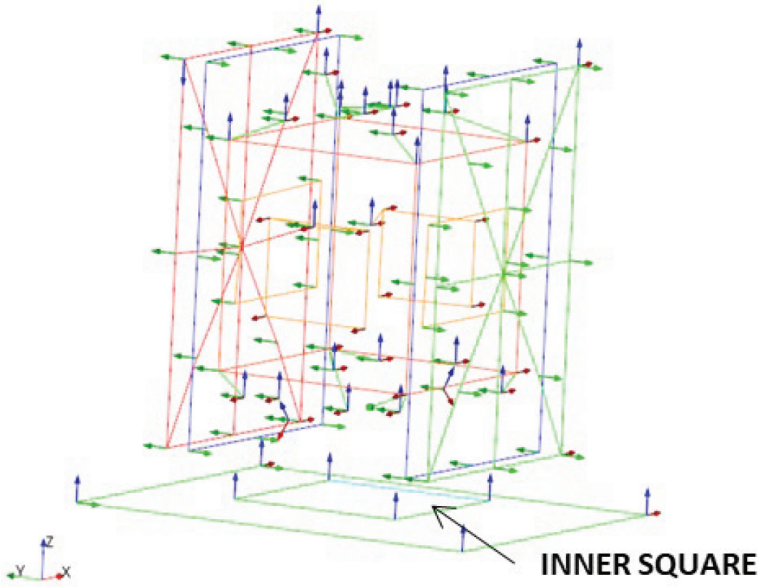

Fig. 3 Test article and accelerometer locations

For ten minutes, independent random signals from 0–200 Hz were input into each of the 24 acoustic sources. Overlap processing with a Hanning window was performed on 8-second frames of data to ensure that the frequency spacing for the acoustic sources was the same as for the impact tests.

Fig. 4 presents the first three singular values of the full 151-by-151 acceleration cross-spectrum matrix due to acoustic and impact inputs. Note that while many of the modal frequencies are the same, the acoustic exciters emphasize acoustically sensitive modes while the base impacts excite modes sensitive to base input. This is consistent with any source of excitation for modal tests, and maximizing the quality of the mode-shape fit is most often based on how distinct its peak is in the test data.

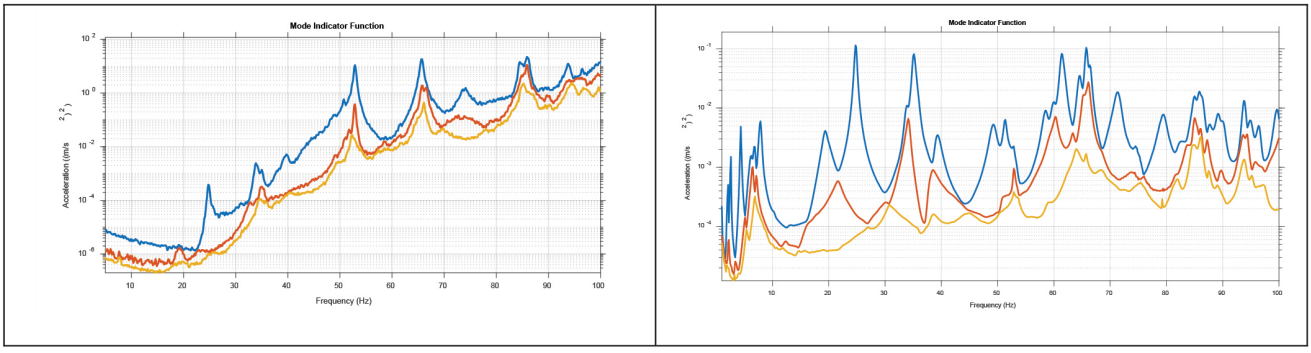

Fig. 4 First three singular values of natural acoustic (left) and impact test (right) cross-spectrum matrices

Note that the response cross-spectrum from the impact hammer can be used because the input spectrum was smooth; i.e., no frames of data with double hits were processed. Also note that the previous presentation [5] presents a case not examined in this paper where the acoustic sources were injected with a Multi-Sine excitation at low frequency to excite five of the six low-frequency rigid body modes of the test article.

Examples of three modes extracted from the acoustic test data are presented in Fig. 5.

The cross-spectrum matrix of the acoustic sources while holding the base fixed is calculated using Equation (4). The first three singular values of both cross-spectrum matrices are presented in Fig. 6, along with the first three singular values of the FRF matrix associated with base accelerations as references. Note that the peaks in the fixed base corrected cross-spectrum matrix match those of the fixed base corrected FRFs for many frequencies, including the two primary modes. However, not all peaks are present in both sets because the FRFs associated with the base accelerations emphasize high effective mass modes while the cross-spectrum matrix from the acoustic sources emphasize acoustically sensitive modes.



Fig. 5 Example of test-measured natural modes from the acoustic source cross-spectrum matrix

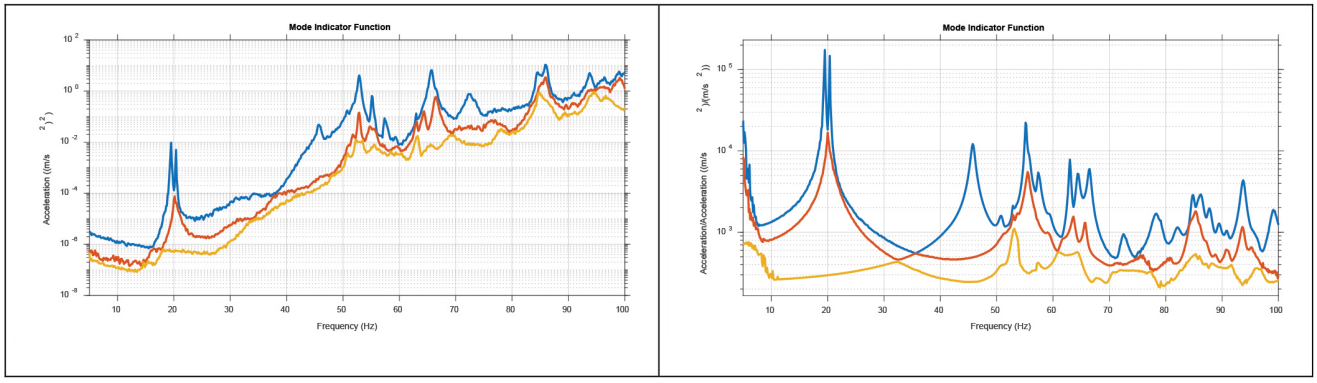

Fig. 6 First three singular values of acoustic corrected cross-spectrum matrix (left), and base acceleration FRF matrix (right)

In order to verify fixity, mode shapes were extracted from the fixed base corrected cross-spectrum matrix using the OPOLY parameter estimation tool in ATA's MATLAB-based IMAT^{TM} software [11]. Three of these modes are presented in Fig. 7, and the transportation cart does not move.

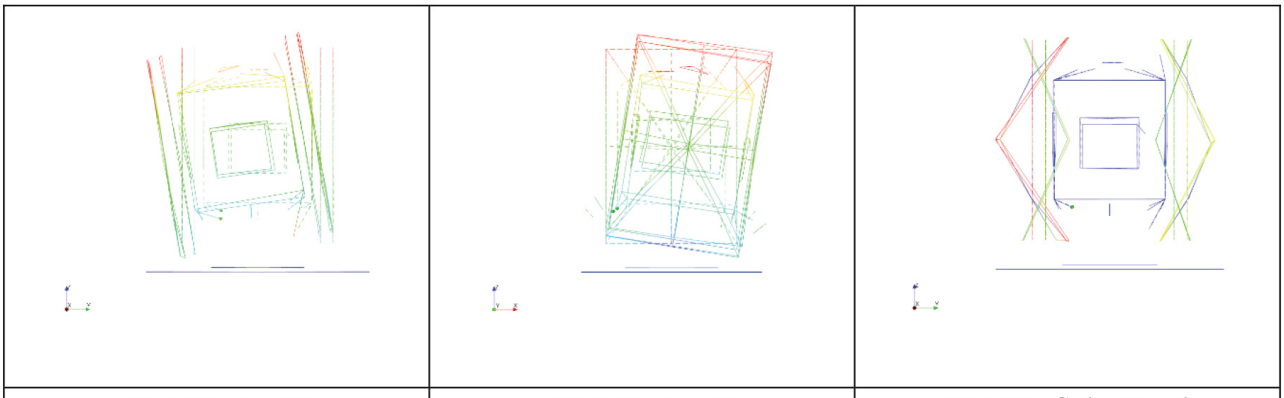

Fig. 7 Example of test-measured fixed base modes

As with almost every modal survey test that is conducted, some modes of interest may not be well excited because the location and orientation of the excitation source is not positioned properly. In these cases, it is oftentimes beneficial to excite the test article in a way that will emphasize a mode in question with whatever means is most expedient. For example, if the primary torsion mode of the test article were not well excited, perhaps the acoustic sources could be rotated so that they could provide both radial and rotational inputs instead of providing a purely radial input.

Summary and Observations

This paper verifies that data from acoustic sources can be combined with conventional sources for modal survey tests, and also presents a method to process acoustic test data when the number of independent sources becomes very large.

Acoustic excitation is beneficial in exciting acoustically sensitive modes. Acoustic sources are also ideal for cases where the modal test is performed in an acoustic qualification test configuration if only for the fact that they are already assembled and available.

If the boundary such as a transportation cart is well modeled, then the test results from the acoustic sources, either from calculated FRFs or from response cross-spectra, and the FRFs associated with conventional excitation techniques can be used directly to update an analysis model. In addition, FBC works with acoustic sources, which is important for cases when performing a modal survey test in a DFA test configuration is desirable and when well-modeled boundary conditions are not available. The additional benefit of combining FBC with acoustic excitation is that all high effective mass modes and acoustically sensitive modes are well excited and can be extracted.

References

1. Cross, K., Melendez, G., Arnold, F., Brenner, K., Throneberry, G., and Soine, D., "Combining Pyroshock with MIMO Vibration," *Proceedings of the 34th Aerospace Testing Seminar*, Los Angeles, CA, April 2025.
2. Throneberry, G., Melendez, G., and Cross, K., "Developments on Combined Thermal-Vibration MIMO Testing," *Proceedings of the 34th Aerospace Testing Seminar*, Los Angeles, CA, April 2025.
3. Schick, D., Hayes, D., Napolitano, K., Kerrian, P., Yang, M., Fogt, V., and Goit, M., "Modal Testing of the NASA VIPER Spacecraft Using Acoustic Excitation," *Proceedings of the 34th Aerospace Testing Seminar*, Los Angeles, CA, April 2025.
4. Napolitano, K., Yang, M., Friedlander, E., and Schick, D., "Mode Shape Extraction Using Direct Field Acoustic Noise Test Data," *Proceedings of the 43rd International Modal Analysis Conference*, Orlando, FL, February 2025.
5. Napolitano, K., Yang, M., Schick, D., Hayes, D., and Kimpton, D., "Experimental Modal Analysis Using Acoustic Excitation," *Proceedings of the Spacecraft and Launch Vehicles Dynamic Environments Workshop*, El Segundo, CA, June 2025.
6. Peeters, B., Alvarez Blanco, M., Musella, U., Waimer, S., Di Lorenzo, E., and Carrella, A., "Identifying the Structural Behaviour of a Specimen During Spacecraft Acoustic Testing by Operational Modal Analysis," *Proceedings of the 7th International Operational Modal Analysis Conference*, Ingolstadt, Germany, May 2017.
7. Napolitano, K., "Fixed Base Modal Testing of the SWFO Sensor Platform on an Environmental Shaker," *Proceedings of the Spacecraft and Launch Vehicle Dynamic Environments Workshop*, El Segundo, CA, June 2023.
8. Napolitano, K., Staab, L., Winkel, J., Akers, J., and Suarez, V., "Fixed Base Modal Survey of the Orion European Service Module Structural Test Article (E STA)," *Proceedings of the Spacecraft and Launch Vehicle Dynamic Environments Workshop*, El Segundo, CA, June 2017.
9. Spivey, N., Saltzman, R., Wieseman, C., Napolitano, K., and Smith, B., "Passive Aeroelastic Tailored Wing Modal Test Using the Fixed Base Correction Method," *Proceedings of the 38th International Modal Analysis Conference*, Houston, TX, February 2020.
10. Elias, L.M., "A Structurally Coupled Disturbance Analysis Method Using Dynamic Mass Measurement Techniques, with Application to Spacecraft-Reaction Wheel Systems," Masters of Science in Aeronautics and Astronautics Thesis, Massachusetts Institute of Technology, 2001.
11. Hensley, D., Antoun, G., Fladung, B., and Napolitano, K., "Using the IMAT Toolbox in the Modal Test Process," *Sound and Vibration* 47(6), pp. 6–12, June 2013.

Chapter 2
A Spectral Matrix Estimation Scheme for Pseudorandom Excitation with Concurrent Phase Combinations

Kevin Napolitano and William Fladung

Abstract Pseudorandom is an excitation technique that allows the user to precisely define source signal auto-spectral density values by assigning a sinusoidal magnitude and phase at the center of each frequency bin. It is used in single-degree-of-freedom environmental testing and modal testing. In order to extend the method to multiple sources for modal testing, sequential sets of varying phase combinations must be applied. This paper shows how combining Daniell spectral estimation with optimal phasing assignment at each specified frequency can result in a precisely defined source cross-spectral density matrix that can help extend pseudorandom to multiple-degree-of-freedom environmental testing and also has the potential to be used for operational modal analysis that uses cross-spectrum directly to estimate modes.

Keywords Spectral estimation · Modal testing · Environmental testing · Daniell · Pseudorandom

Introduction

Pseudorandom is an excitation technique that allows the user to precisely define source signal auto-spectral density values by assigning the magnitude and phase of a sinusoidal input at the center of each frequency bin [1]. Typically, a pseudorandom source signal is generated from a spectrum with the associated frequency spacing and is repeated for several frames. After transients decay, the steady-state response satisfies the assumption of the discrete Fourier transform (DFT) that the signals are periodic. In order to extend pseudorandom excitation to multiple-reference modal tests, sequential tests must be performed with each test having a different phase combination between the sources at every frequency.

The main advantages of pseudorandom excitation are that it is a leakage-free technique that requires no windows and allows the user to specify a precise level at each frequency. Single-axis shaker controllers can exploit this feature to precisely define input auto-spectrum at all required frequencies. The main disadvantage of pseudorandom excitation for modal testing is that, once data is collected, there is no way to increase the frequency resolution by altering signal processing parameters. Also, time is taken between each source phase change as the structure settles into a steady-state response.

While this method can result in very clean frequency response functions (FRFs), it is not useful for multiple-reference random shaker control because the control signal would need to change in the middle of a test with each phasing combination.

This paper presents a method to generalize the pseudorandom excitation method for multiple sources by exploiting the Daniell spectral estimation method [2] to apply the different source phasing combinations concurrently. Doing so can help provide a uniform excitation over the course of a test and can minimize data collection times. Combined with optimal phasing assignment [3], off-diagonals of a source signal cross-spectrum matrix can be precisely defined, and therefore the response auto-spectrum matrix can also be precisely defined, which allows for the precision of pseudorandom excitation to be extended to environmental testing as well as allows for modal analysis of tests with very large numbers of references, such as those associated with acoustic excitation [4], [5], where the calculation of FRFs can be burdensome.

Kevin Napolitano · William Fladung
ATA Engineering, Inc., San Diego, CA 92128
e-mail: kevin.napolitano@ata-e.com; bfladung@ata-e.com

© The Author(s), under exclusive license to River Publishers 2026

Kristin B. Zimmerman, PhD (eds.), *Topics in Modal Analysis & Parameter Identification in Structural Dynamics, 2026, Vol. 8*,
Conference Proceedings of the Society for Experimental Mechanics Series, https://doi.org/10.13052/rp-9788743814191

Concurrent Phase Combinations Using Daniell Spectral Estimation

Bartlett spectral estimation [6] involves performing a DFT on a several frames of time-history data and then taking the average of their respective cross-spectral matrices, such that

$$[S_{WZ}(\omega_i)] = (1/N)\sum_{k=1}^{N}\{w_k(\omega_i)\}\{z_k(\omega_i)\}^H \tag{1}$$

where $\{w_k(\omega_i)\}$ and $\{z_k(\omega_i)\}$ are the DFT of the "kth" frame of data for two sets of channels at a given frequency (ω_i), and *N* is the total number of frames of data. At its fundamental level, Daniell spectral estimation involves calculating a DFT of the entire time history and summing the spectral lines near the frequency of interest, such that

$$[S_{WZ}(\omega_i)] = \left(\frac{1}{2m+1}\right)\sum_{k=i-m}^{i+m}\{w(\omega_k)\}\{z(\omega_k)\}^H \tag{2}$$

where $\{w(\omega_k)\}$ and $\{z(\omega_k)\}$ are the DFT of the kth frequency bin for two sets of channels, and *m* is the number of frequency bins to the left and right of the frequency of interest.

As with traditional pseudorandom excitation, a sine wave is generated at the center of each frequency bin, and therefore a window is not needed to reduce leakage since the assumption of periodicity associated with the DFT is satisfied once the system reaches steady state.

If the number of averaged spectral lines is greater than or equal to the number of references, and if the phase between the source signals is chosen such that the columns of the reference cross-spectrum matrix, $[X(\omega_i)]$, are independent, then the reference cross-spectra matrix is invertible and FRFs can be calculated.

If the phase between spectral lines is chosen in an optimal manner, then the off-diagonal elements of the reference cross-spectra matrix can be numerically zero for the Daniell spectral estimation method. An example using optimal phase is presented in Equation (3). The optimal phase angles, $[\theta]$, for three frames are defined, and their complex value on a unit circle, $[X]$, is shown where x=w=z, and m=1 in Equation (2). The average of the cross-spectrum of the three frames is then calculated and is equal to the identity matrix.

$$[\theta] = \begin{bmatrix} \begin{Bmatrix} 0 \\ 0 \\ 0 \end{Bmatrix} & \begin{Bmatrix} 0 \\ 120 \\ -120 \end{Bmatrix} & \begin{Bmatrix} 0 \\ -120 \\ 120 \end{Bmatrix} \end{bmatrix}, [X] = \begin{bmatrix} \begin{Bmatrix} 1 \\ 1 \\ 1 \end{Bmatrix} & \begin{Bmatrix} 1 \\ -1/2 - i\sqrt{3/4} \\ -1/2 + i\sqrt{3/4} \end{Bmatrix} & \begin{Bmatrix} 1 \\ -1/2 + i\sqrt{3/4} \\ -1/2 - i\sqrt{3/4} \end{Bmatrix} \end{bmatrix}$$

$$[S_{XX}] = 1/3\left(\begin{bmatrix} 1 & 1 & 1 \\ 1 & 1 & 1 \\ 1 & 1 & 1 \end{bmatrix} + \begin{bmatrix} 1 & -1/2 + i\sqrt{3/4} & -1/2 - i\sqrt{3/4} \\ -1/2 - i\sqrt{3/4} & 1 & 1/2 + i\sqrt{3/4} \\ -1/2 + i\sqrt{3/4} & -1/2 - i\sqrt{3/4} & 1 \end{bmatrix} + \begin{bmatrix} 1 & -1/2 - i\sqrt{3/4} & -1/2 + i\sqrt{3/4} \\ -1/2 + i\sqrt{3/4} & 1 & -1/2 - i\sqrt{3/4} \\ -1/2 - i\sqrt{3/4} & -1/2 + i\sqrt{3/4} & 1 \end{bmatrix}\right) = \begin{bmatrix} 1 & 0 & 0 \\ 0 & 1 & 0 \\ 0 & 0 & 1 \end{bmatrix} \tag{3}$$

Example of three-frame, three-source example of optimal phase assignment leading to zero off-diagonals. Phase angles are specified in degrees, and the matrix [X] are its complex values with a magnitude of 1.

In the case of Daniell spectral estimation, the three frames are applied concurrently and are associated with the three frequency bins of the DFT closest to the frequency range of interest. In the case of Bartlett spectral estimation, the three frames are applied sequentially and their average is calculated. An example using two phase combinations is presented in Fig. 1.

If a realizable reference cross-spectrum matrix with non-zero off-diagonals is required for multiple-input environmental testing, it can be generated by pre- and post-multiplying the diagonal matrix by a complex vector and its Hermitian, respectively. This vector is oftentimes the singular vectors of a desired reference cross-spectrum matrix scaled by their associated singular values.

Since the reference cross-spectra with concurrent phasing have been defined, an inverse DFT can be applied to generate a time-history signal that is a summation of all the sine waves with their associated phases at the center of each frequency bin. This time history can be replicated any number of times to generate multi-reference pseudorandom time-history signals of arbitrary length. In this way, multiple frames can be averaged together to reduce variance error due to measurement noise.

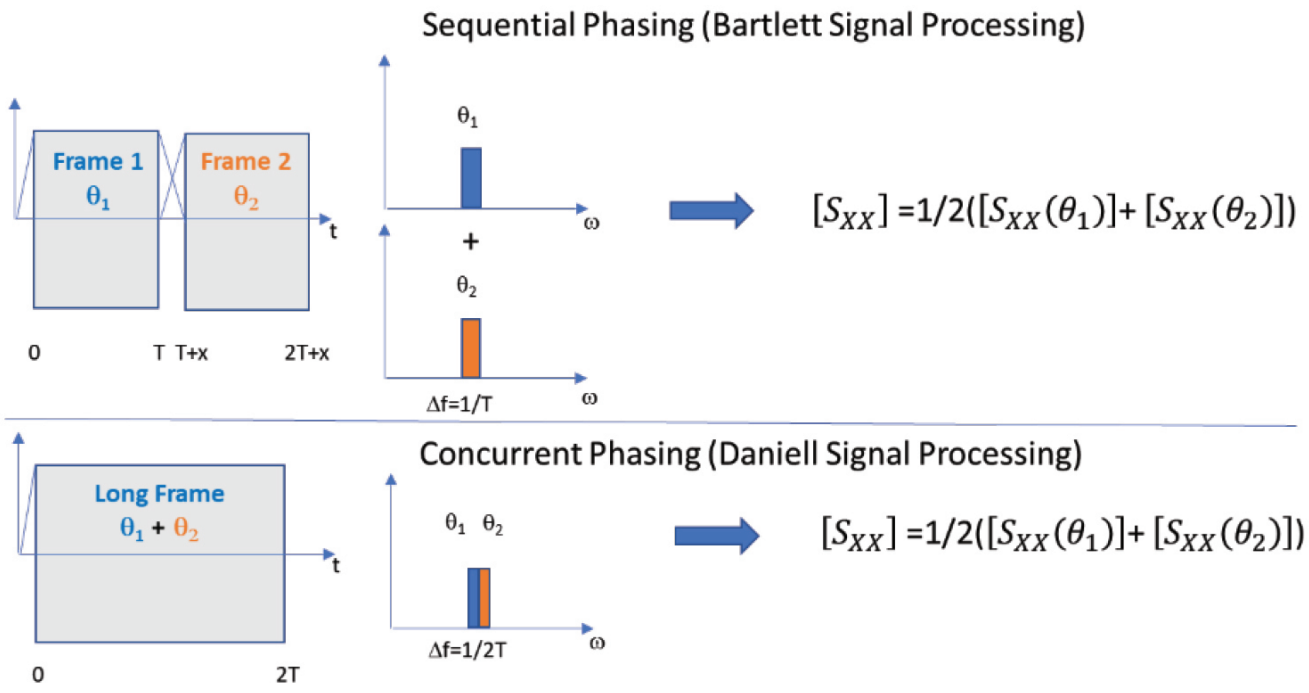

Fig. 1 Example of sequential versus concurrent phase combinations

Furthermore, overlap processing can be used to update the spectral matrices at a faster rate than waiting for a full frame of data to be completed, allowing for the calculation of multiple reference FRFs in the same amount of time as those that are conventionally calculated.

Numerical Examples

This section presents some numerical examples on a lumped parameter model with no noise to demonstrate that the proposed signal definition and signal processing technique can lead to clean reference and response cross-spectral density matrices.

Analysis Model

A seven-degree-of-freedom (DOF) lumped parameter model (Fig. 2) is used to demonstrate the proposed signal generation and signal processing technique. Each mass has a value of 1, each spring has a value of 10,000, and damping was assigned as 1% viscous after modes were solved. Forces are applied at DOFs 1X+, 3X+, and 5X+, and acceleration responses are measured at all seven DOFs. The modal parameters are shown in Table 1.

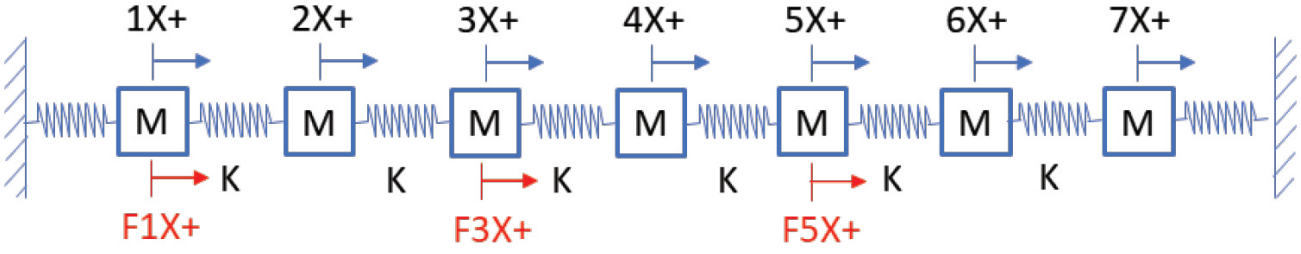

Fig. 2 Seven-DOF lumped parameter model

Table 1 Lumped parameter modal properties

Mode No.	Frequency(Hz)	Damping(% critical)
1	6.21	1
2	12.18	1
3	17.68	1
4	22.51	1
5	26.47	1
6	29.41	1
7	31.21	1

Time-History Signal Generation

The pseudorandom input signals are generated by first calculating the frequency-domain inputs. The frequency-domain inputs $X(\omega)$. The FRF matrix, $H(\omega)$ is used to calculate the outputs in the frequency domain, $Y(\omega)$. Once calculated, both the inputs and outputs are converted to the time domain, $x(t)$ and $y(t)$ and are then replicated as many times as required to obtain the desired time-history length.

The true random input was generated in the time domain and zero-padded at the beginning and end to satisfy the assumptions of the DFT, which was applied to generate the frequency-domain input. The FRF matrix was then used to generate the output frequency-domain results, which were then transformed to the frequency time domain. The original input time-history and output time-history functions were then used for signal processing.

Signal processing techniques are then used to calculate frequency domain functions (Fig. 3) such as cross-spectra, reference cross-spectra, response cross-spectra, and FRFs.

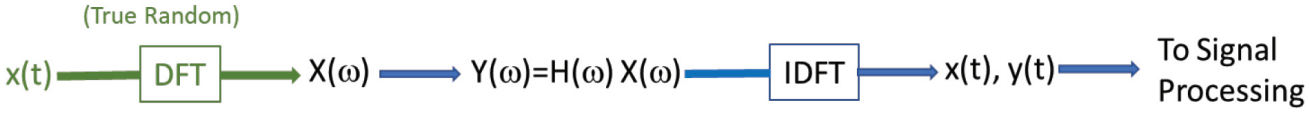

Fig. 3 Response time-history calculation

Case 1: True Random

The first case presented uses a true random excitation as the input. Frequency-domain results using the Welch spectral estimation method [7] are shown in Fig. 4. Ten minutes of simulated test data were processed using a Hanning window and 90% overlap processing to calculate FRF and spectral matrices. The Daniell method (Fig. 5) is applied by zero padding before and after the excitation is activated and turned off to satisfy the assumptions of the DFT that the signal is completely observed. As expected with a true random excitation, the FRF results are clean and there is good separation between the off-diagonal terms of the reference cross-spectra matrix and the diagonal terms. The noise in the reference auto-spectrum and its off-diagonal terms results in a cross-spectrum matrix and response auto-spectrum terms with noise.

Case 2: Multi-Reference Pseudorandom with Random Phase Assignment

The second case presented uses a pseudorandom excitation with a random phase assignment for the input signals at each frequency. For this case, the desired frequency resolution for the processed signals is 0.05 Hz, and the number of frequency bins per analyzed frequency was selected to be 5, which helped minimize the risk of generating reference cross-spectrum matrices with high condition numbers. Therefore, the frequency bin width to generate the signal was 0.01 Hz (0.05 Hz/5 frames), which corresponds to a 100-second frame of simulated test data. The 100-second frame of data was replicated six times to extend the total active time to ten minutes. Frequency-domain results using the Welch spectral estimation method are shown in Fig. 6. Ten minutes of data were processed using a Hanning window and 90% overlap processing to calculate FRF and spectral matrices. Since the input time history repeats every 100 seconds, the Daniell method (Fig. 7) is applied by selecting any 100-second set of data after the transient effects at startup have settled. After settling, the periodic signals satisfy the assumption of the DFT. Overlap processing of 100-second frames is also performed at a 90% overlap rate using the steady-state data up until the excitation source is turned off. It should be noted that because the simulated data in this paper is noise-free, results using one 100-second frame are the same as using many frames. As expected, the FRFs are still

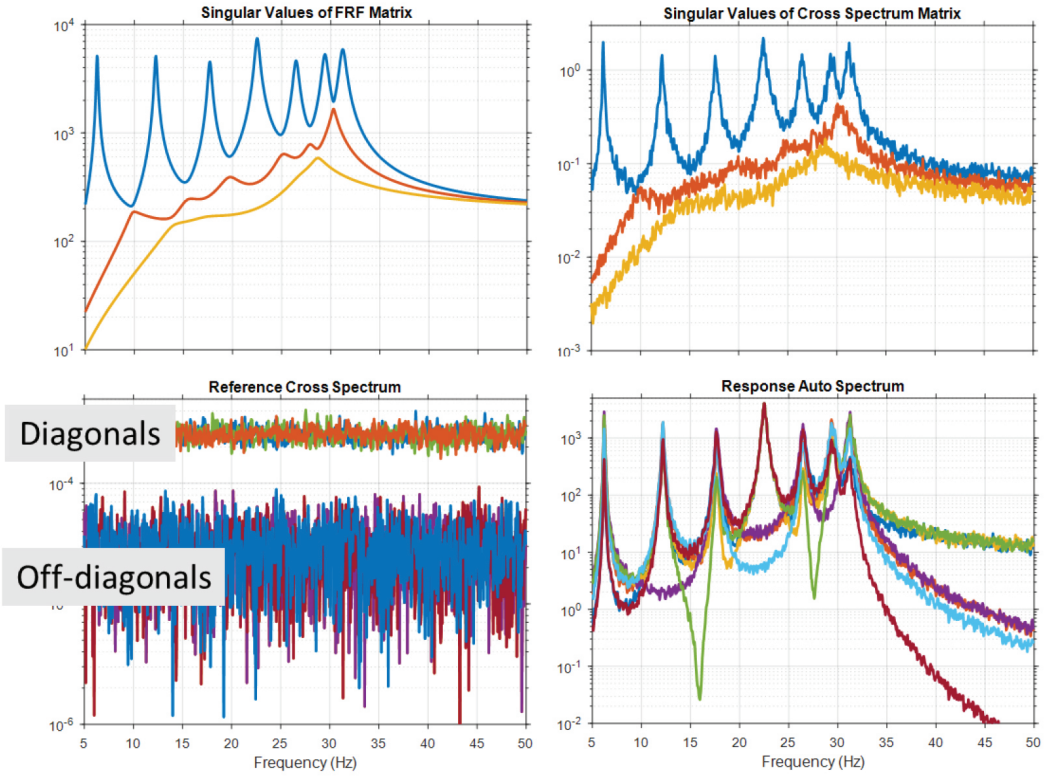

Fig. 4 True random, Welch

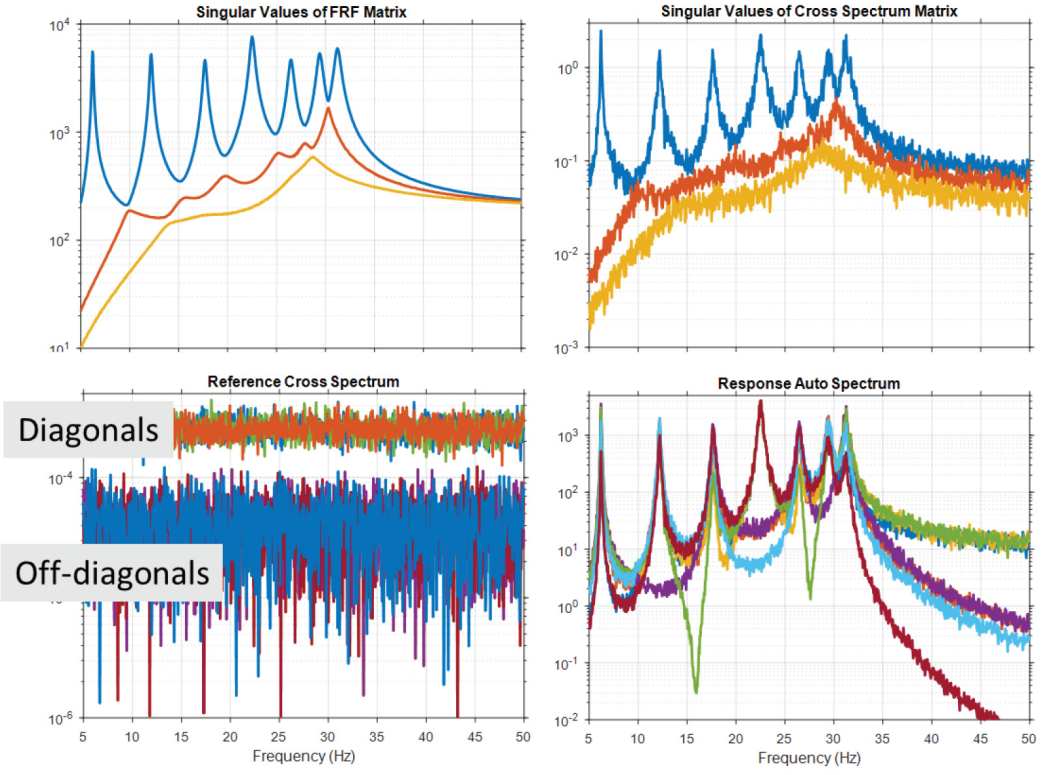

Fig. 5 True random, Daniell

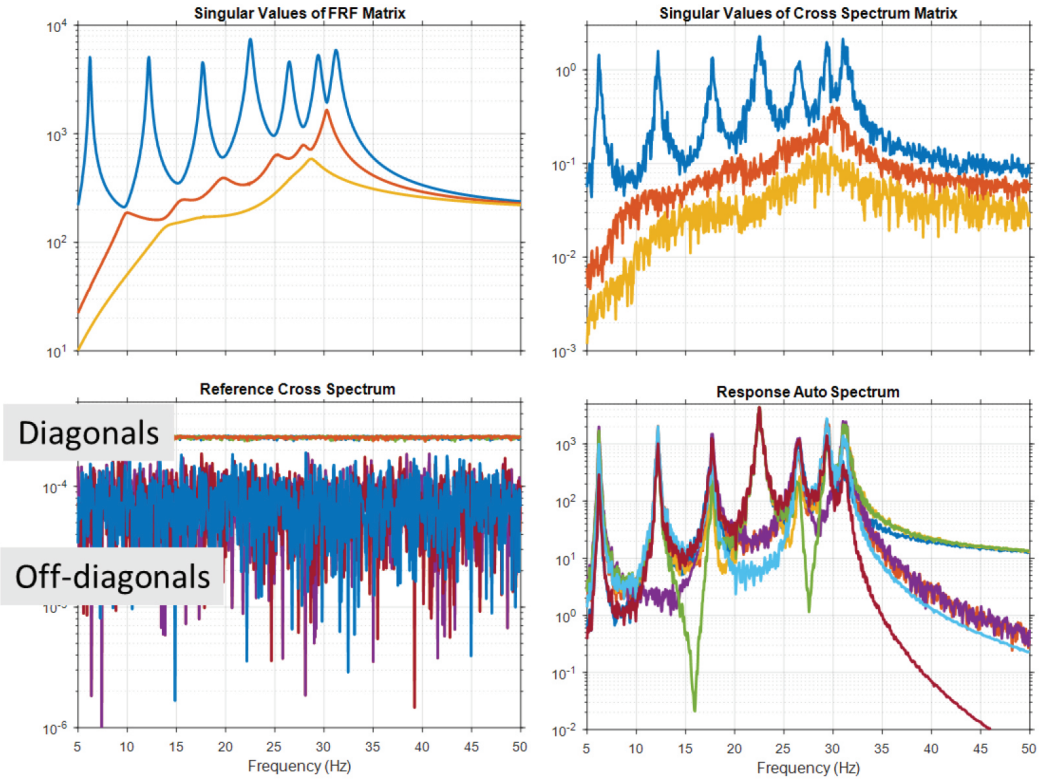

Fig. 6 Multi-reference pseudorandom with random phasing, Welch

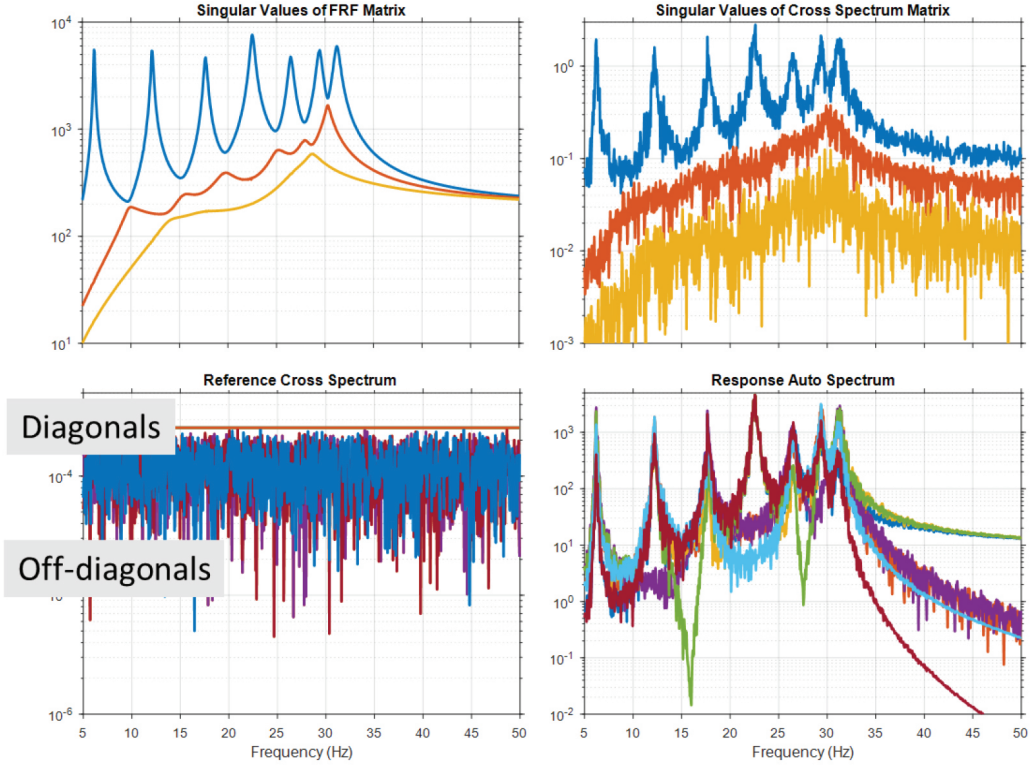

Fig. 7 Multi-reference pseudorandom with random phasing, Daniell

clean, and the diagonals of the reference cross-spectrum matrix are mostly flat; in fact, the diagonals are constant for Daniell spectral estimation. The off-diagonal terms of the reference cross-spectrum matrix for both signal processing cases are higher than the previous case. The "noise" in the off-diagonal terms results in noisy response cross-spectra and auto-spectra data.

Case 3: Multi-Reference Pseudorandom with Optimal Phasing

The third case presented uses a pseudorandom excitation with optimal phase assignment for the input signals at each frequency. For this case, the desired frequency resolution for the processed signals is 0.05 Hz, and the number of frequency bins per analyzed frequency was selected to be 5. Therefore, the frequency bin width to generate the signal was 0.01 Hz (0.05 Hz/5 frames), which corresponds to a 100-second frame of simulated test data. The phase was assigned to each set of five 0.01 Hz frequency bins used to calculate the cross-spectrum of the resultant 0.05 Hz frequency spacing such that the off-diagonal terms of the reference cross-spectrum matrix were minimized. The 100-second frame of data was replicated six times to extend the total active time to ten minutes. Frequency-domain results using the Welch spectral estimation method are shown in Fig. 8. Ten minutes of data were processed using a Hanning window and 90% overlap processing to calculate FRF and spectral matrices. Since the input time history repeats every 100 seconds, the Daniell method (Fig. 9) is applied by selecting any 100-second set of data after the transient effects at startup have settled. After settling, the periodic signals satisfy the assumption of the DFT. Overlap processing of 100-second frames was also performed at a 90% overlap rate using the steady-state data up until the excitation source is turned off. As expected, the FRFs are still clean, the diagonals of the reference cross-spectrum matrix contain less noise, and the off-diagonal terms are lower than Cases 1 and 2. However, for Daniell spectral estimation, the off-diagonal terms are mathematically equal to zero. While both signal processing tech-

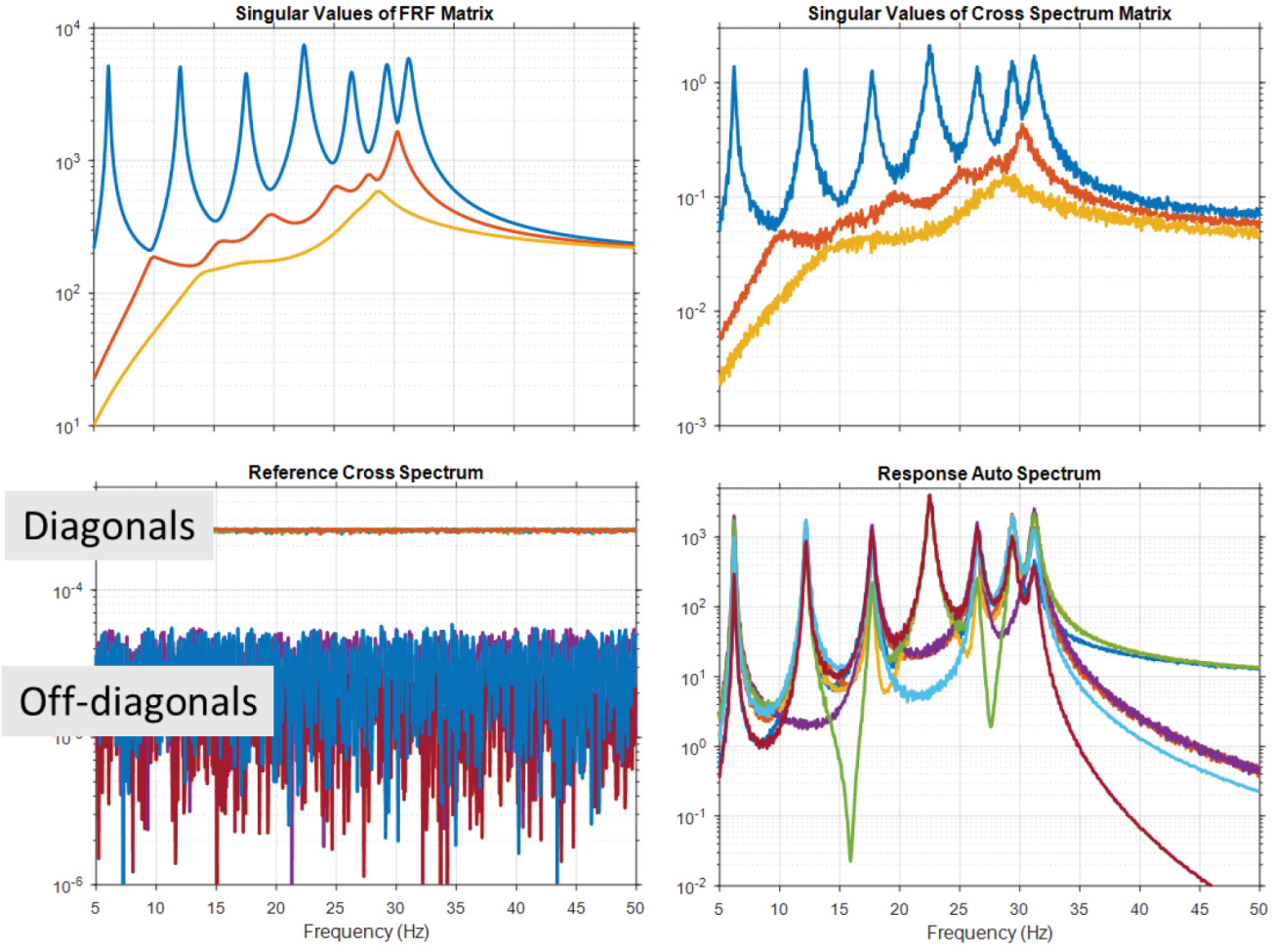

Fig. 8 Multi-reference pseudorandom with optimal phasing, Welch

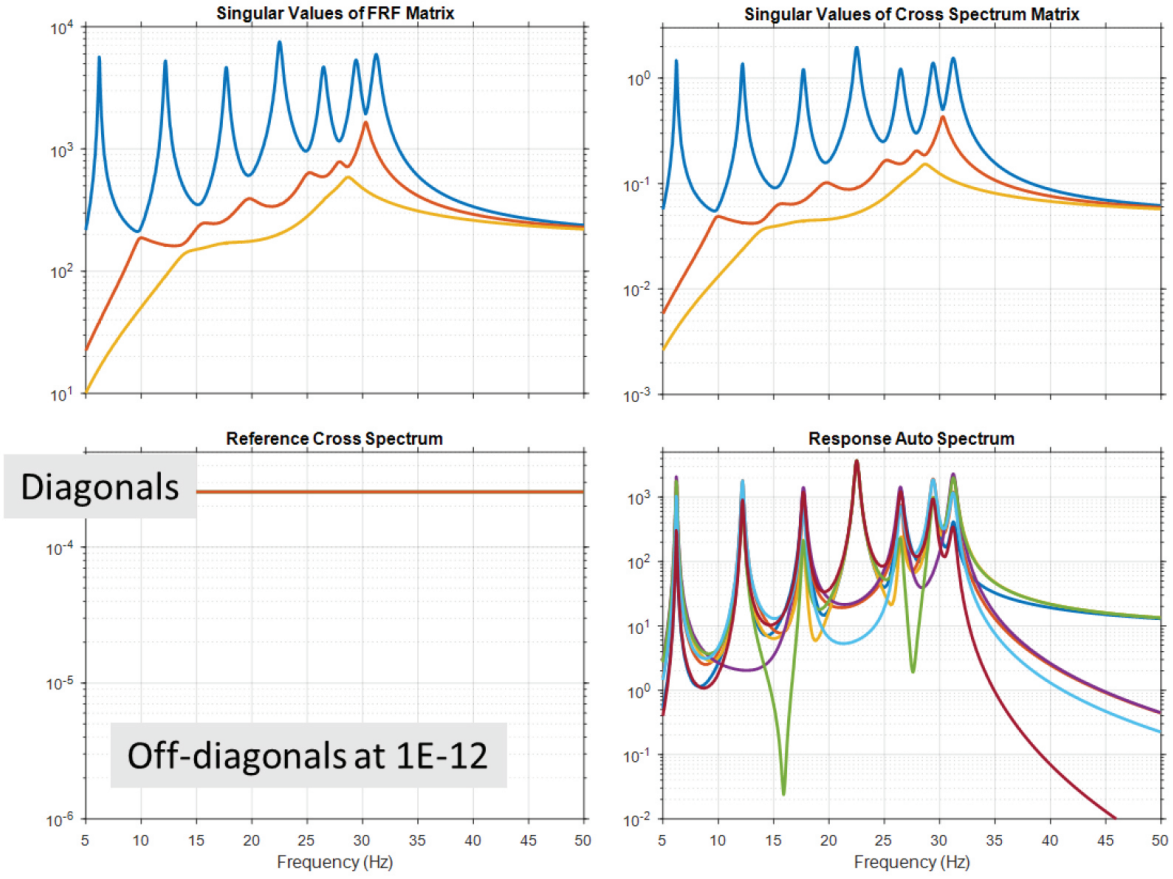

Fig. 9 Multi-reference pseudorandom with optimal phasing, Daniell

niques result in cleaner cross-spectrum and response cross-spectrum functions than Case 1 and 2, the results are noise-free with Daniell spectral estimation.

Summary

This paper has presented a method to define an optimally phased, multi-reference pseudorandom source signal that can be used to generate cleaner spectral matrices. Pseudorandom with concurrent optimal phasing addresses the disadvantages of traditional consecutively phased pseudorandom excitation including fewer skipped transient frames and having the ability to apply a consistent signal over an entire test. The matrices can be further cleaned by using Daniell spectral estimation that matches the optimally phased source signal definition. The ability to generate clean spectral matrices could be useful for more precise definition of multi-input/multi-output environmental control algorithms, or it could be used for operational modal survey test applications where cross-spectral density matrices are used directly to estimate modes, such as acoustic modal applications.

References

1. Peeters, B., Carrella, A., Lau, J., Gatto, M., and Coppotelli, G., "Advanced shaker excitation signals for aerospace testing," I*n: Proulx, T. (eds) Advanced Aerospace Applications, Volume 1*, Conference Proceedings of the Society for Experimental Mechanics Series, Springer, New York, NY, pp, 229–241, 2011.
2. Daniell, P.J., "Discussion on the paper by M. S. Bartlett 'On the theoretical specification and sampling properties of autocorrelated time-series,'" *Suppl. J. R. Stat. Soc.* 8(1), pp. 88–90, 1946.

3. Napolitano, K.L., and Yoder, N.C., "Optimal Phasing Combinations for Multiple Input Source Excitation," *Proceedings of the 32nd International Modal Analysis Conference*, February 2014.
4. Napolitano, K., Yang, M., Friedlander, E., and Schick, D., "Mode Shape Extraction Using Direct Field Acoustic Noise Test Data," *Proceedings of the 43rd International Modal Analysis Conference*, February 2025.
5. Peeters, B., Alvarez Blanco, M., Musella, U., Waimer, S., Di Lorenzo, E., and Carrella, A., "Identifying the Structural Behaviour of a Specimen During Spacecraft Acoustic Testing by Operational Modal Analysis," *Proceedings of the 7th International Operational Modal Analysis Conference*, May 2017.
6. Bartlett M.S., "Periodogram Analysis and Continuous Spectra," *Biometrika* 37(1–2), pp. 1–16, 1950.
7. Welch, P.D., "The use of fast Fourier transform for the estimation of power spectra: A method based on time averaging over short, modified periodograms," *IEEE Transactions on Audio and Electroacoustics* 15(2), pp. 70–73, 1967.

Chapter 3
Vibration-Based System Identification of Structural Dynamics using a Stochastic Gradient SINDy

Celso T. do Cabo, Raymond Joshua, and Zhu Mao

Abstract System identification is a challenging field of research. Oftentimes, it is possible to obtain certain information from a system based on measurements and models. In vibrational systems, for instance, natural frequencies and mode shapes can be obtained based on measurements. However, estimating the partial differential equations (PDEs) of a system is a complex challenge. Many approaches to model the system's behavior rely on physical information, such as in FEA models. When the physics information of the system is missing, data-driven approaches are a feasible solution to create a digital twin of the real system. Among the techniques for system identification available, the sparse identification of nonlinear dynamics (SINDy) is a library-based model that performs a linear regression using the measurement and its derivatives to estimate possible parameters existing in the system. However, structural vibrations consist of second-order PDEs with mass and stiffness dependences between the degrees of freedom. It is proposed that a modification of the current SINDy is employed by developing a gradient descent with penalty terms to keep the physical meaning of the PDEs. Results show that the model can predict the matrices of the system, with high signal reconstruction and mode shape estimation. The values obtained are compared with FEA models to verify their accuracy.

Keywords Machine learning · System identification · Sparse identification · Nonlinear dynamics · Structural dynamics

Introduction

Monitoring the dynamic behavior of structures is of great importance in evaluating the system's integrity. In many applications, it is possible to identify damage or to predict the remaining useful life of a system based on its vibration [1]. However, the system's dynamic often has complex behavior, and it is difficult to model. In many cases, a baseline is adopted as the initial system or nondamaged condition of the structure, and future changes are assumed to be damaged. In other cases, where some knowledge is available of the structure, it is possible to generate a mathematical or simulation model of the system, and deviations from the simulation are classified as damage.

In cases where physical knowledge is not available, data-driven techniques can be employed either to understand the complex behavior of the measurement collected or to simplify the system's behavior [2]. However, such approaches require large amounts of data collected and sometimes are not feasible to perform. In the case of nonlinear dynamics, it is even more difficult to obtain the governing equations without previous knowledge of the system [3]. Another approach is to identify some information about the system, based on the measurements obtained. Among such techniques, fuzzy logic, or

Celso T. do Cabo · Zhu Mao
Department of Mechanical and Materials Engineering, Worcester Polytechnic Institute, Worcester, MA 01609
e-mail: ctdocabo@wpi.edu; zmao2@wpi.edu

Raymond Joshua
Honeywell Federal Manufacturing & Technologies, LLC operates the Kansas City, National Security Campus for the United States Department of Energy / National Nuclear, Security Administration under Contract Number DE-NA0002839
e-mail: rjoshua@kcnsc.doe.gov

*Footnote for Authorization for:
NSC-614-5856
DE-NA0002893

© The Author(s), under exclusive license to River Publishers 2026

Kristin B. Zimmerman, PhD (eds.), *Topics in Modal Analysis & Parameter Identification in Structural Dynamics, 2026, Vol. 8*,
Conference Proceedings of the Society for Experimental Mechanics Series, https://doi.org/10.13052/rp-9788743814191

physics-informed neural networks (PINNs) can be employed [4–6]. Some techniques rely on linear regression, such as the sparse identification of nonlinear dynamics (SINDy) [7]. This technique proposes performing measurements of a dynamical system, then calculating its derivatives or integral to create a library of parameters to estimate the governing equations. It proved to be successful in diverse applications, such as single degree of freedom systems (SDOF) or rotating machines [8–10]. SINDy was also employed in nonlinear problems for system identification and implicit equations [11, 12]. Previously, different modifications in its structure were proposed, including optimization methods to obtain the governing equation using SINDy, including PDEs estimation [13–15]. This work proposes the usage of the SINDy model to identify the PDEs of a continuous system's vibration. For that, SINDy is modified to employ a stochastic gradient descent with penalty terms to obtain the most realistic governing equations possible. The schematics of the proposed approach are presented in Figure 1.

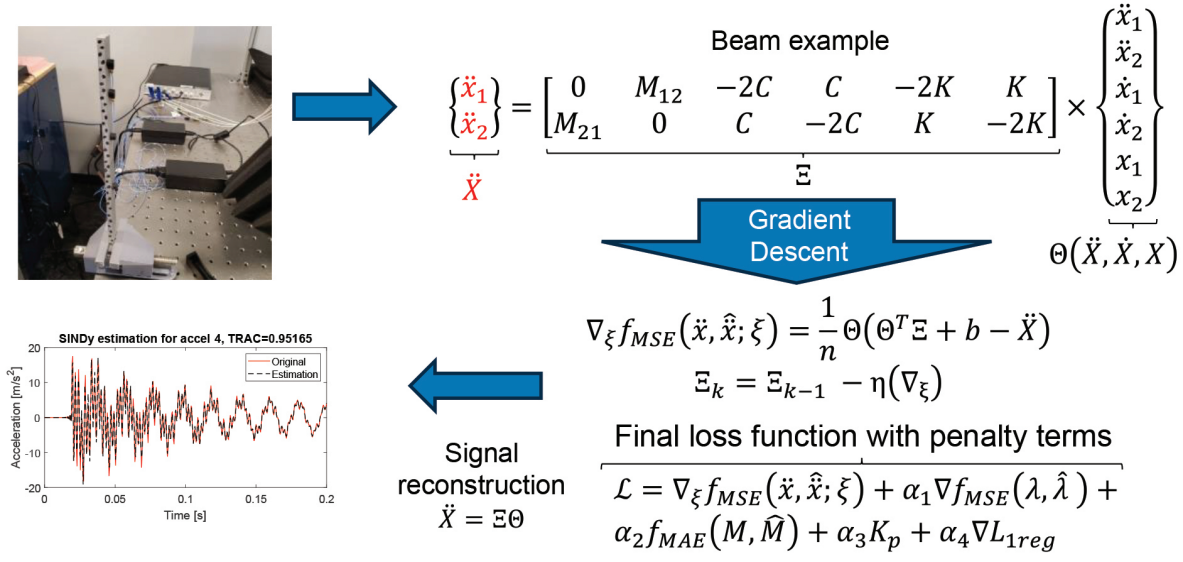

Fig. 1 Flowchart of proposed SGD SINDy model

Theory background

The Sparse Identification of Nonlinear Dynamics (SINDy) model was initially introduced by Brunton et al. [7] and consists of a linear regression method to estimate the parameters of a governing equation. For the case of vibrational systems, where the governing equation of the system consists of a second-order PDE. The measurement is given by a matrix with different measurements of acceleration $\left[\ddot{X}\right]$. This signal will be reconstructed based on a combination of parameters using the derivatives or integrals of the signal. For instance, if the acceleration is the measurement for this case, the library of parameters $\Theta\left(\dot{X}, X\right)$ will consist of velocities and displacements obtained from integrating the measurements. In addition, in case of nonlinear systems, other terms can be included, such as a cubic nonlinear spring. Finally, the parameters Ξ are estimated according to Equation (1).

$$\Xi = \left(\Theta^T\Theta\right)^{-1}\Theta^T\ddot{X} \tag{1}$$

The linear regression model has a high performance when estimating the parameters, obtaining the ideal solution with the smallest error. Although the model works well for second-order PDEs, continuous systems have dependency between the degrees of freedom (DOFs) in both mass and stiffness components. Thus, even the solution with the smallest error will have a low accuracy. A new model based on stochastic gradient descent (SGD) is proposed to counter such issues. For that, the gradient of the mean squared error (MSE) is calculated as shown in Equation (2).

$$\nabla_\xi f_{MSE}\left(\ddot{x}, \hat{\ddot{x}}, \xi\right) = \frac{1}{n}\Theta\left(\Theta^T\Xi + b - \ddot{X}\right) \tag{2}$$

After calculating the gradient of the MSE, the parameters are updated based on Equation (3).

$$\Xi_k = \Xi_{k-1} - \eta\left(\nabla_\xi\right) \tag{3}$$

Where η is the learning rate and hyperparameter of the model. In addition, when modifying the approach to an SGD, restrictions of the algorithm can be performed. For instance, the library of parameters can also include the mass terms on it, changing the existing one to a $\Theta\left(\ddot{X}, \dot{X}, X\right)$. Then, to avoid a case where $\ddot{X}_{ii} = \ddot{X}_{ii}$ the diagonal of the parameters is forced to be always zero. This will lead to a new solution where the masses are also dependent on different DOFs. However, inverse problems often are ill-posed problems, with different possible combinations of parameters to obtain the same signal reconstruction. Therefore, different penalty terms were included in the SINDy model, such that, with limited information of the system, it is possible to obtain a more realistic estimation of the governing equations. Some of those terms were previously introduced by the authors and are described in the following equations.

$$\hat{M} = \sum_{i=1}^{n} M_{ii} \tag{4}$$

In Equation (4), $\hat{M}$ is the total mass of the system, which can be estimated or measured depending on the application. To bound the system's mass matrix to a similar value to the total mass of the system, it is assumed that the sum of the diagonal terms of the mass matrix will be the same as the total mass of the system. The mass of the first DOF will be estimated based on the optimization of the main absolute error (MAE) as shown in Equation (5).

$$M_{11}^{k+1} = M_{11}^{k} + \eta_m \left| \hat{M} - \sum_{i=1}^{n} M_{ii} \right| \tag{5}$$

Then, the other terms of the diagonal can be calculated based on the following equation:

$$M_{ii} = \frac{\xi_{i-1,i}}{\xi_{i,i-1}} \times M_{i-1,i-1} \tag{6}$$

Where $\xi_{i,j}$ is one of the terms in the matrix Ξ. Another penalty term previously implemented was a term to encourage symmetry in the matrices obtained by the model. This is obtained by following Equation (7) below.

$$A_p = \frac{\left[A - A^T\right]}{\|A\|} \tag{7}$$

Here, the A matrix can be any of the matrices of the governing equations, such as the mass, stiffness, or damping matrices. The model, including the previously mentioned penalty terms, can estimate the governing equations of the system, with a time response assurance criterion (TRAC) of above 90%. However, the eigenvalues of the obtained matrices are not the same as the values measured in the experiment. In addition, in case of nonlinear systems, where multiple terms need to be implemented in the library, the model will predict all of the terms to achieve a higher accuracy, even if those terms are not present in the original system. Previously, an eigenvalue estimator was implemented in the framework using the derivatives of the eigenvalues. But this model only predicted correctly one of the natural frequencies. To improve the accuracy of the eigenvalue estimation, another approach was implemented using a perturbation analysis for eigenvalue estimation [16]. Starting with the generalized eigenvalue problem, described in Equation (8).

$$KU = \Lambda MU \tag{8}$$

where, K is the stiffness matrix of the system, M its mass matrix, U the unitary matrix with the mode shape vectors of the system and Λ the diagonal matrix with the eigenvalues of the system. It is possible to add a perturbation term in the equation, modifying it from Equation (8) to (9).

$$\left(K_0 + \delta K\right)\left(u_0 + \delta u\right) = \left(\lambda_0 + \delta\lambda\right)\left(M_0 + \delta M\right)\left(u_0 + \delta u\right) \tag{9}$$

The perturbation terms are represented with the δ, while the initial estimation for each of the terms is represented with the subscription 0. In addition, the desired eigenvalue can be estimated by approximating the eigenvalue as presented in Equation (10).

$$\lambda \approx \lambda_0 + \epsilon\delta\lambda \tag{10}$$

where, ϵ is the perturbation term. This term was included to add complexity to the solution. By simplifying Equation (9) and isolating the perturbation term for the eigenvalue $\delta\lambda$, the estimation of the eigenvalue will then be given by:

$$\lambda \approx \lambda_0 + \epsilon u^T \left(\delta K - \lambda_0 \delta M\right) u \tag{11}$$

This estimation of the eigenvalue can be included in the MSE between the natural frequencies measured from the experiment and the estimation from Equation (11). By deriving the MSE of the eigenvalue, the new term can be included in the optimization together with the gradient descent. The derivation of the MSE of the eigenvalue with respect to the stiffness and mass matrices are given by Equations (12) and (13), respectively.

$$\frac{\partial f_{MSE}\left(\lambda,\widehat{\lambda}\right)}{\partial K} = -2\epsilon u^T\left(\widehat{\lambda}-\lambda_0-\epsilon u^T\left(\delta K-\lambda_0\delta M\right)u\right)u \tag{12}$$

$$\frac{\partial f_{MSE}\left(\lambda,\widehat{\lambda}\right)}{\partial M} = -2\epsilon\lambda_0 u^T\left(\widehat{\lambda}-\lambda_0-\epsilon u^T\left(\delta K-\lambda_0\delta M\right)u\right)u \tag{13}$$

Here, $\widehat{\lambda}$ represents the measured eigenvalue from the experiment, which is given by the natural frequency square. In addition, a regularization term was included in the model to encourage sparsity in the model obtained. In the case of nonlinear systems, it is difficult to estimate what type of nonlinearity is occurring. Therefore, when generating the matrix with possible parameters, multiple different types of nonlinearities can be included. In addition, in cases where it is unknown if the test has nonlinearities (e.g., boundary conditions are not ideal) it is encouraged to include such terms in the model. However, the model will predict the solution with the least error available, even if it has to estimate nonlinearities that are nonexistent in the system. Therefore, the L_1 norm or least absolute shrinkage and selection operator (LASSO) regression was implemented. This technique is known for encouraging sparsity in the model, increasing zero values for some of the parameters [17]. The model was implemented in the loss function as shown in Equation (14).

$$L_1 = |\xi| \tag{14}$$

Then, the gradient of the L_1 norm is calculated as presented in Equation (15).

$$\nabla L_1 = \begin{cases} 1 \text{ if } \xi \geq 0 \\ -1 \text{ if } \xi < 0 \end{cases} \tag{15}$$

The final loss function for the stochastic gradient SINDy model is presented in Equation (16).

$$\mathcal{L} = \nabla_\xi f_{MSE}\left(\ddot{x},\widehat{\ddot{x}},\xi\right) + \alpha_1 \nabla f_{MSE}\left(\lambda,\widehat{\lambda}\right) + \alpha_2 f_{MAE}\left(M,\hat{M}\right) + \alpha_3 A_p + \alpha_4 \nabla L_1 \tag{16}$$

The terms α_i in Equation (16) account for the weights for each of the penalty terms presented in the loss function. Normally, those weights are hyperparameters of the machine learning model and need to be manually specified. However, such tasks can be time-consuming and greatly impact the performance of the algorithm. Therefore, in addition to the penalty terms, a learning rate annealing technique, commonly employed in physics-informed neural networks (PINNs) was also implemented [18]. This technique automatically calculates the weights based on the maximum gradient of the reconstruction part, versus the average of the loss obtained by each of the specific terms as shown in Equation (17).

$$\widehat{\alpha}_i = \frac{\max_\xi\left\{\left|\nabla_\xi \mathcal{L}_\xi\left(\xi_n\right)\right|\right\}}{\left|\overline{\nabla_\xi \mathcal{L}_i\left(\xi_n\right)}\right|} \tag{17}$$

Equation (17) will estimate the term $\widehat{\alpha}_i$ for each epoch while training the model. Then, to increase the stability of the calculations, this term is averaged with previous iterations, leading to the final weight as described in Equation (18).

$$\alpha_i = (1-\beta)\,\alpha_i + \beta\widehat{\alpha}_i \tag{18}$$

Where β is the stabilization coefficient and select how aggressive the change in the weights is. Typically, $\beta = 0.1$. With this, the algorithm will learn each of the weights automatically and does not require extra hyperparameter tuning from the user.

Experimental Setup and Data Processing

The testing setup for the stochastic gradient descent SINDy, uses a simple cantilever beam with accelerometers attached to it. Since the cantilever beam has a simple behavior, its analytical solution can be obtained for its natural frequencies and mode

shapes. From Rao [19], the first two natural frequencies of the cantilever beam are at 82.9Hz and 519.9Hz. Since the model requires the integration of the measurement to obtain the velocity and displacement at each accelerometer, the sampling frequency (f_s) was set at 12.8kHz.

To detect nonlinearities in the system, a different setup was performed, with the same cantilever beam, however, with a soft boundary condition. In this case, another natural frequency appeared between the two mode shapes, and when evaluating the mode shapes via video-based sensing, it can be seen that the mode shape resonates with the boundary.

To process the acquired acceleration, initially, an integration method is performed. Currently, the integration technique employed is the trapezoid integration, that can be approximated following Equation (19) below.

$$\int_a^b f(t)\,dt \approx \sum_{n=1}^{N} \frac{(f(t_n) + f(t_{n+1}))}{2} \Delta t \tag{19}$$

The error of this numerical integration technique was compared with other techniques, such as using the Fourier properties to integrate in the frequency domain or using the Simpson's rule. All the techniques had a similar performance. Thus, the trapezoid rule showed better computational efficiency and was selected for integration. In addition, when performing numerical integration, any offset component in the signal can lead to a drift in the integrated result. Then, a high-pass filter was employed to remove such drift. Different filters were tested to verify which has the best performance for this case. Starting with a fifth-order Butterworth filter was employed. To verify if the error obtained by this filter was the smallest possible error, a comparison study was conducted. A cantilever plate was excited with a sine sweep from 10Hz to 1kHz and a sampling frequency of 12.5kHz. For this experiment, both accelerometers and LDV were employed at the same time, such that the acceleration measurement could be integrated and compared with the velocity measured by the LDV. It was observed that without any filtering, the TRAC of the measurements would be 78%, while employing the Butterworth filter ended up around 98%. When estimating the governing equations of the system, a fast transition is desired. Therefore, an elliptic filter was employed instead. The performance of the elliptic filter for the validation test was similar to that of the Butterworth. However, when applying to the real test, an increase in the accuracy of the results was observed. Currently, all tests use an elliptic filter with 0.1 peak-to-peak passband ripple in dB and 30 stopband attenuation in dB scale.

System Identification Results and Discussion

In order to compare the results of the SGD SINDy model, the traditional technique was employed, where the linear regression described in Equation (1) is used to obtain the parameters. The results when using the linear regression approach are presented in Figure 2.

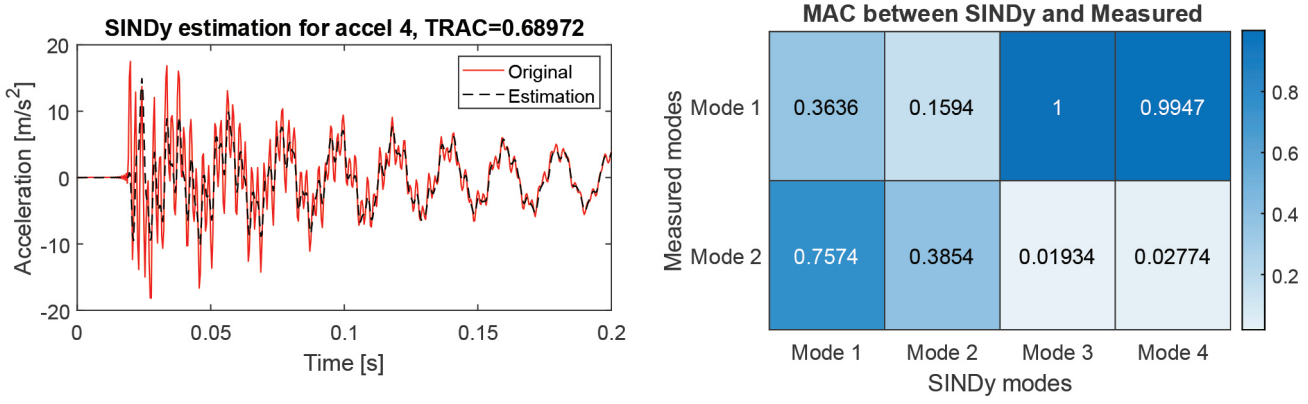

Fig. 2 Results from conventional SINDy; (a) Signal reconstruction of accelerometer 4 and (b) MAC between measurement and eigenvectors from SINDy

When employing the conventional linear regression model for SINDy, the assumption of independence between the terms in the mass matrix leads to low accuracy when reconstructing the measurements from the obtained model. As presented in Figure 2(a), the accelerometer closest to the base of the cantilever beam, which has most of the high-frequency content, will

have a TRAC of only around 68%. In addition, when comparing the mode shapes measured in the experiment with the ones obtained by the eigen decomposition of the mass and stiffness matrices, it can be seen in Figure 2(b) that although the first mode shape has a MAC of 100%, the second mode shape achieves only 75% of MAC. After implementing the SGD process with the penalty terms to obtain the PDEs of the system, the following hyperparameters were used for training:

Table 1 Hyperparameters for SGD SINDy training

Hyperparameter	# of Epochs	Batch Size	Learning Rate	Mass LR	$\alpha_{initial}$	ϵ
Value	10,000	128	1.5×10^{-4}	1.5×10^{-4}	0.1	0.01

When performing the SGD SINDy with the stiff boundary condition, it is possible to see that even the accelerometer with high-frequency content will have a high TRAC, with more than 90% reconstruction, as presented in Figure 3(a). In addition, the MAC for the mode shapes extracted in the experiment and the ones obtained by the eigen solution of the mass and stiffness matrices are above 90% for the first two mode shapes as presented in Figure 3(b).

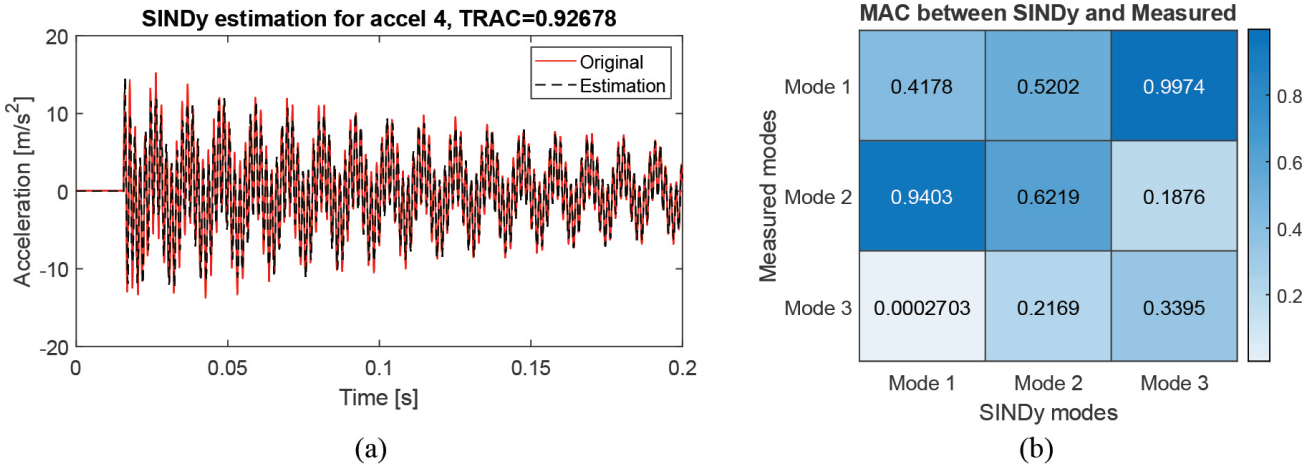

Fig. 3 Results from SGD SINDy; (a) Signal reconstruction of accelerometer 4 and (b) MAC between measurement and eigenvectors from SINDy

In addition, this approach had the gradient annealing implemented in the code, which led to the best selection of each of the weights of the penalty terms. The change in weight versus the number of epochs is given in Figure 4.

In Figure 4, the weights for the three penalty terms are presented. In the top left corner, the weight for the regularization factor is presented as $\nabla_\theta L_1$ is shown. The initial estimation for the weight is 1, which then will change based on each epoch until it converges to a value close to 0.1. On the top right, the values for the symmetry term are presented as $\nabla_\theta Symmetry$. This term has a different behavior than expected, while previously a small value was set as the symmetry penalty, when using learning rate annealing, the weight converges to a much higher value, on the 10,000 orders. Finally, the bottom part of the figure presents the weight value for the perturbation model. Since the symmetry term had a high value for the weights, the resulting matrices all had symmetric values, as shown in Equation (20).

$$M_{SINDy} = \begin{bmatrix} 0.038 & -0.0376 & 0.0182 \\ -0.0376 & 0.0388 & -0.0223 \\ 0.0182 & -0.0223 & 0.0232 \end{bmatrix} \text{ and } K_{SINDy} = \begin{bmatrix} 6.745 & 0 & -0.992 \\ 0 & -1.036 & -0.337 \\ -0.992 & -0.337 & 4.055 \end{bmatrix} 10^3 \tag{20}$$

In addition, the perturbation method used estimates the eigenvalue of the system, allows a good estimation of the natural frequencies, based on the eigen solution of the mass and stiffness matrices obtained in Equation (20). The comparison between the natural frequencies obtained via SINDy and the measured natural frequencies are presented in Table 2.

As presented in the table, the first natural frequency has an almost perfect estimation with errors in the decimals. While the second natural frequency, which has a much smaller amplitude and is more difficult to obtain, has an error smaller than 5%. Finally, the SINDy model was compared between linear and nonlinear problems. As presented previously, the SINDy model was employed in the linear example, which led to the results presented. In addition, a second experiment was generated, where the boundary condition is soft and has a new mode shape between the two mode shapes obtained. When generating the library of parameters, a cubic spring was implemented for both cases, while one of them has a linear behavior

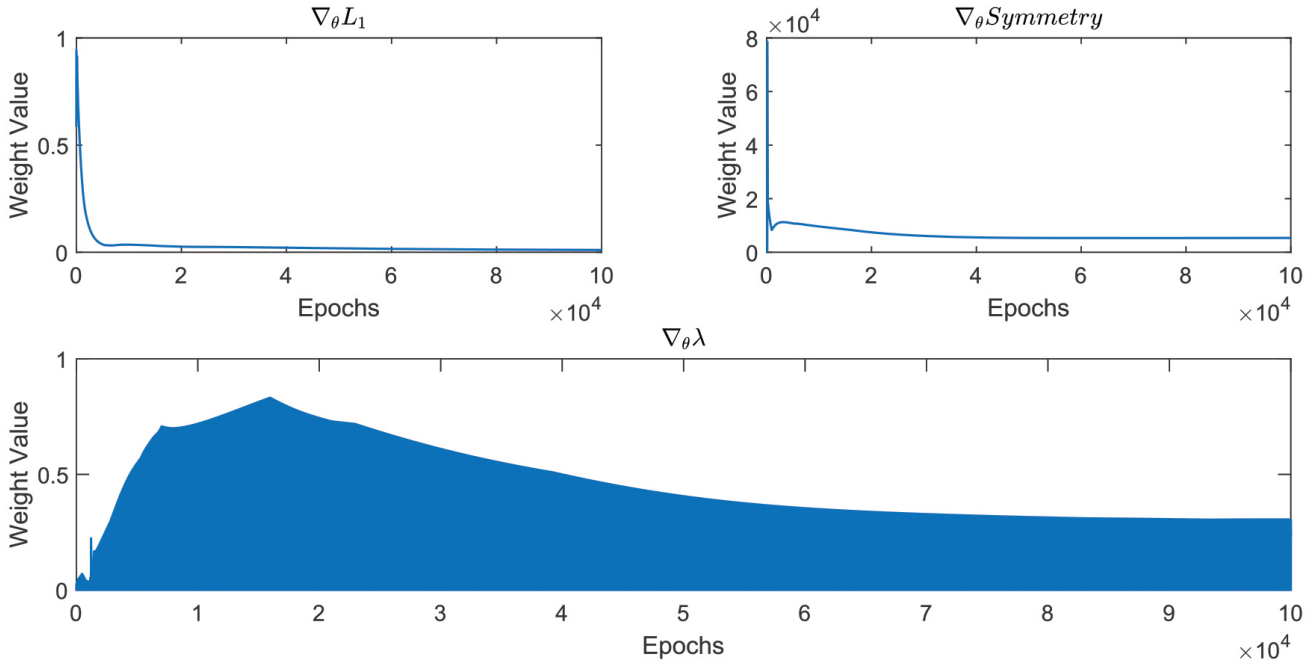

Fig. 4 Weights of learning rate annealing versus epochs while training SGD SINDy

Table 2 Natural frequency estimation using SGD SINDy

Measured Frequency [Hz]	SINDy Estimation [Hz]	% Error
89.6	89.7	0.1
576.3	591.2	2.6

and is expected to have zero values for the cubic spring. The second application has nonlinearities from the boundary conditions and is expected to have more terms to describe the behavior of the system accurately. In Equation (21) the comparison between the cubic spring matrices is given.

$$[K_3]_{linear} = \begin{bmatrix} 0 & 0 & 0 \\ 0 & 0 & 0 \\ 0 & 0 & 3.12 \end{bmatrix} \times 10^{10} \text{ and } [K_3]_{nonlinear} = \begin{bmatrix} 1.93 & 0.07 & -0.15 \\ 0 & -0.49 & -0.07 \\ -0.16 & -0.08 & 0.07 \end{bmatrix} \times 10^{12} \tag{21}$$

The nonlinear condition has terms in almost every position of the stiffness matrix. Which is needed to maintain a good accuracy of the model. However, when the same nonlinear spring is implemented in the linear case, most of its values become zero, with the exception of one of the terms. However, when observing the amplitude of this value, it is two orders of magnitude smaller than the ones obtained by the nonlinear case. Thus, the value of the linear would be smaller than the smallest value obtained by the nonlinear case.

Conclusion

The proposed approach to modify the SINDy algorithm developed by Brunton et al. [7], is focused on obtaining second-order PDEs, more specifically, in continuous vibration, where there exists a dependence between the degrees of freedom in both mass and stiffness matrices. The modification of the algorithm to a stochastic gradient descent allowed the implementation of different penalty terms, such that the resulting PDE has a similar behavior to the one expected for a continuous vibration system. The reconstruction of the signal and the mode shapes estimated by the model have above 90% accuracy, and the eigenvalues estimated are also close to the natural frequencies measured. In addition, the model is capable of predicting nonlinear terms as long as they are included in the library of parameters.

The future work of the project can be focused on further improving the technique for different types of forced vibration tests. The current model works for impact tests, which are similar to a free vibration test. In addition, the number of sensors and natural frequencies measured must be similar. Investigation into implementing SINDy with modal reduction techniques can be a solution for better estimating the system dynamics.

Acknowledgments This work is supported by the Department of Energy Kansas City National Security Campus Managed by Honeywell under contract # N000510678.

References

1. C. Zhang, A. A. Mousavi, S. F. Masri, G. Gholipour, K. Yan, and X. Li, "Vibration feature extraction using signal processing techniques for structural health monitoring: A review," Mechanical Systems and Signal Processing, vol. 177, p. 109175, 2022.
2. Y.-J. Cha, R. Ali, J. Lewis, and O. Büyük?ztürk, "Deep learning-based structural health monitoring," Automation in Construction, vol. 161, p. 105328, 2024.
3. O. Nelles and O. Nelles, Nonlinear dynamic system identification. Springer, 2020.
4. F. Abdullah and P. D. Christofides, "Data-based modeling and control of nonlinear process systems using sparse identification: An overview of recent results," Computers & Chemical Engineering, vol. 174, p. 108247, 2023.
5. T. Liu and H. Meidani, "Physics-informed neural networks for system identification of structural systems with a multiphysics damping model," Journal of Engineering Mechanics, vol. 149, no. 10, p. 04023079, 2023.
6. M. Raissi, P. Perdikaris, and G. E. Karniadakis, "Physics-informed neural networks: A deep learning framework for solving forward and inverse problems involving nonlinear partial differential equations," Journal of Computational physics, vol. 378, pp. 686-707, 2019.
7. S. L. Brunton, J. L. Proctor, and J. N. Kutz, "Discovering governing equations from data by sparse identification of nonlinear dynamical systems," Proceedings of the national academy of sciences, vol. 113, no. 15, pp. 3932-3937, 2016.
8. C. Lathourakis and A. Cicirello, "Physics-enhanced sparse identification of nonlinear oscillator with coulomb friction," in International Conference on Nonlinear Dynamics and Applications, 2023: Springer, pp. 507-517.
9. C. Lathourakis and A. Cicirello, "Physics enhanced sparse identification of dynamical systems with discontinuous nonlinearities," Nonlinear Dynamics, pp. 1-28, 2024.
10. S. Piramoon, M. Ayoubi, and S. Bashash, "Modeling and Vibration Suppression of Rotating Machines Using the Sparse Identification of Nonlinear Dynamics and Terminal Sliding Mode Control," IEEE Access, 2024.
11. S.-C. Huang, H.-W. Chen, and M.-H. Tien, "Predicting Nonlinear Modal Properties by Measuring Free Vibration Responses," Journal of Computational and Nonlinear Dynamics, vol. 18, no. 4, p. 041005, 2023.
12. K. Kaheman, J. N. Kutz, and S. L. Brunton, "SINDy-PI: a robust algorithm for parallel implicit sparse identification of nonlinear dynamics," Proceedings of the Royal Society A, vol. 476, no. 2242, p. 20200279, 2020.
13. P. Goyal and P. Benner, "Discovery of nonlinear dynamical systems using a Runge–Kutta inspired dictionary-based sparse regression approach," Proceedings of the Royal Society A, vol. 478, no. 2262, p. 20210883, 2022.
14. Y. Liu, S. Shi, Y. Fang, and A. Fu, "Robust data-driven wave excitation force estimation for wave energy converters with nonlinear probabilistic modelling," Ocean Engineering, vol. 310, p. 118726, 2024.
15. K. Champion, B. Lusch, J. N. Kutz, and S. L. Brunton, "Data-driven discovery of coordinates and governing equations," Proceedings of the National Academy of Sciences, vol. 116, no. 45, pp. 22445-22451, 2019.
16. A. Greenbaum, R.-c. Li, and M. L. Overton, "First-order perturbation theory for eigenvalues and eigenvectors," SIAM review, vol. 62, no. 2, pp. 463-482, 2020.
17. I. Goodfellow, Y. Bengio, and A. Courville, Deep Learning. MIT Press, 2016.
18. S. Wang, Y. Teng, and P. Perdikaris, "Understanding and mitigating gradient flow pathologies in physics-informed neural networks," SIAM Journal on Scientific Computing, vol. 43, no. 5, pp. A3055-A3081, 2021.
19. S. S. Rao, Vibration of continuous systems. John Wiley & Sons, 2019.

Chapter 4
A Comparison of Uncertainty Quantification Methods for Damping Ratio Estimates from Tall, Modular Buildings

Patrick Brewick and John Hickey

Abstract The accurate quantification of energy dissipation is essential if the light damping ratios of tall, slender structures are to be properly leveraged during design and deployment. For instance, residential buildings, including modular construction, must adhere to rather stringent vibration criteria, often severely limiting acceptable acceleration responses. Most conventional tall buildings achieve these criteria by controlling aerodynamic loading via changes in shape over the building height, or through the addition of extra lateral stiffness via outrigger elements. However, both of these approaches are challenging to implement in modular construction. Thus, modular construction for residential projects are subject to strict vibration criteria, but lack the traditional means for vibration control. Further complicating matters, damping ratios are notoriously difficult to estimate with precision, yet design decisions are often based on the assumed or identified damping value.

This study presents a comprehensive comparison of uncertainty quantification methods for damping ratio estimation. Using acceleration data recorded in a tall, modular building, damping ratios are identified using an analytical modal decomposition within the random decrement technique. However, in order to quantify the uncertainty associated with the identified damping ratios, both bootstrapping techniques as well as a hierarchical Bayesian approach are applied. Comparative results, including statistics and confidence intervals, are provided for the first few fundamental modes along with a discussion of the capabilities of both methods.

Keywords Damping · Random decrement · Hierarchical bayesian · Bootstrapping · Analytical modal decomposition

Introduction

The response of tall buildings to environmental loads is controlled by modal properties such as the natural frequencies, mode shapes and damping ratios [1, 2]. Natural frequencies and mode shapes can be generally estimated with relative confidence; however, modal damping ratios are significantly more challenging to predict with certainty since they cannot be calculated analytically [3]. However, given their central role in structural dynamic behavior, accurate estimates of damping are crucial for predicting structural responses to dynamic loads. As a result, the improved precision of damping estimation has become an important objective within the field of system identification [4], especially when data is available from full-scale, finished structures [5, 6, 7].

Operational modal analysis (OMA) is an output-only methodology for system identification that utilizes the dynamic response of a structure without any knowledge of the exciting forces [8]. A vast range of OMA techniques have been proposed in literature, including the random decrement technique [9], stochastic subspace identification (SSI) [10], frequency domain decomposition [11], various Bayesian approaches [12, 13], and a series of enhancements and combinations of these techniques (e.g. [14, 15, 16, 17, 18]). With the notable exception of Bayesian approaches, most OMA techniques were initially

Patrick Brewick
Department of Civil and Environmental Engineering & Earth Sciences, University of Notre Dame, Notre Dame, Indiana, USA
e-mail: pbrewick@nd.edu

John Hickey
Department of Civil, Structural and Environmental Engineering, Trinity College Dublin, Dublin, Ireland
e-mail: John.Hickey@tcd.ie

© The Author(s), under exclusive license to River Publishers 2026

Kristin B. Zimmerman, PhD (eds.), *Topics in Modal Analysis & Parameter Identification in Structural Dynamics, 2026, Vol. 8*,
Conference Proceedings of the Society for Experimental Mechanics Series, https://doi.org/10.13052/rp-9788743814191

developed to return deterministic values for modal parameters of interest. However, various schemes for uncertainty quantification (UQ) have been employed or developed to augment some common deterministic OMA techniques. For instance, the perturbation-based SSI method for estimating the covariance of modal parameters [19] has been further generalized and evolved by a series of others [20, 21]. Kijewski and Kareem [22] also investigated how uncertainty in damping ratios could be quantified through bootstrapping, applying bootstrap estimates to random decrement signatures.

Conventional Bayesian frameworks, and uncertainty estimation frameworks that augment deterministic OMA techniques, typically quantify the epistemic estimation uncertainties of modal parameters [23]. However they are not designed to represent the variability in a single modal parameter estimate inferred from multiple data-sets or under varying environmental conditions. This can result in under-estimation of total parameter uncertainty [24]. This limitation has motivated the adoption of hierarchical Bayesian approaches for model calibration and model updating [24, 23, 25, 26]. Hierarchical probabilistic models introduce additional flexibility that accounts for variability in the inferred parameters while maintaining many of the strengths of the traditional Bayesian approach [27, 28]. In a structural dynamics context hierarchical models allow uncertainty in the modal parameters and hyper-parameters that define the distributions of modal parameters to be considered concurrently.

This study analyzes the fusion of bootstrapping and hierarchical Bayesian methods within OMA to more thoroughly consider the uncertainty in modal damping ratio estimates. Both approaches utilize the classical random decrement modal identification technique [9] to derive the damping ratio estimates, with an analytical modal decomposition [29] employed to isolate modal responses of interest. This study uses data from an in-situ monitoring campaign undertaken to monitor the dynamic behavior of a tall modular building, *10 Degrees*, in London, UK. While typical damping ratios have been established for conventional structures through multilateral monitoring campaigns, this is not the case for modular construction; thus, determining appropriate indicative values for use in design remains a challenge. Using the data from *10 Degrees*, this study attempts to quantify the uncertainty in the identified damping ratios of the first three fundamental modes. Moreover, the approaches developed within this study incorporate data from multiple events and channels in order to find a single, unified distribution for the modal damping ratios.

Background

The random decrement technique (RDT) [9] is a time domain-based approach for damping estimation that assumes the response of a single degree-of-freedom (SDOF) system can be decomposed into homogeneous and particular responses that are dependent on the initial conditions and forcing, respectively [30]. When response measurements, such as acceleration time histories, are available for a given structure, the RDT operates on segments of these responses. The segments are created by taking time windows of a set length wherein the first point in the window satisfies a given threshold condition that typically specifies both an amplitude x_0 and slope (or velocity) $\dot{x}_0$ criteria [22]. By setting the triggering condition to an appropriate level, multiple segments can be obtained from a given acceleration time history. It can be shown that averaging over a large number of segments with identical triggering conditions leads the ensemble averages of the initial velocity and forced response components to tend to zero, leaving only the response due to the initial displacement [9, 31]. The result is that the remaining signal represents the free decay response of the SDOF system. Given the finite duration of observed acceleration time histories in practice, the random decrement signature (RDS) can be written as

$$D_{x_0}(\tau) = \frac{1}{N_{\text{segs}}} \sum_{n=1}^{N_{\text{segs}}} \left(x_n(\tau) \middle| x_n(0) = x_0 \text{ and } \dot{x}(0) = \dot{x}_0 \right) \tag{1}$$

where $D_{x_0}(\tau)$ is the RDS, $x_n(\tau)$ represents the nth discrete segment of a given time history conditionally triggered by $x_n(0) = x_0$ and $\dot{x}(0) = \dot{x}_0$, and N_{segs} is the total number of segments.

The RDT can also be applied to multi-degree of freedom (MDOF) systems if the modes are well-separated by isolating the modal responses and treating them as SDOF systems [32]. However, a beating phenomenon can be observed in the RDS for closely spaced modes, which means the RDT cannot be directly used for evaluating the damping ratio. To overcome this issue, the RDT is commonly combined with signal decomposition methods, such as analytical modal decomposition (AMD)[29]. The AMD approach separates the frequency contents of a time series exactly; hence, it has been applied in conjunction with the RDT for damping identification in a number of studies [33, 16, 34].

The time history segments of response data that satisfy the specified trigger condition can be treated as random samples, where the set of N_{segs} segments constitutes the sample population. A bootstrap sample is formed from this population by drawing N_{segs} samples with replacement, *i.e.*, the number of samples drawn is equivalent to the number of identified segments. This operation is performed N_B times to create a set of N_B replicates. The dynamic properties, *e.g.*, damping

ratios or natural frequencies, can subsequently be estimated for each replicate. The standard error se from the replicate estimates is then obtained according to [35]

$$se = \left\{ \sum_{b=1}^{N_B} \left[\hat{\theta}^*(b) - \overline{\hat{\theta}^*} \right]^2 / (N_B - 1) \right\}^{1/2} \tag{2}$$

where $\hat{\theta}^*(b)$ represents the estimate of the dynamic property of interest based on the bth bootstrap replicate sample and $\overline{\hat{\theta}^*}$ represents the bootstrap mean, which is given by

$$\overline{\hat{\theta}^*} = \sum_{b=1}^{N_B} \hat{\theta}^*(b)/N_B \,. \tag{3}$$

Note that the standard error operates similarly to a measure of the standard deviation of the estimates. It is also essential for the sample population to be representative of the typical behavior of the actual process in order for the bootstrapping approach to work properly [22].

Estimates of the damping ratio from the RDS can also be considered from a Bayesian perspective. This study modifies the hierarchical Bayesian methodology from [25] for damping estimation via sets of modal RDS. Only a brief synopsis of the hierarchical Bayesian approach is presented herein; full details can be found in [25]. Collecting the RDS for the pth mode for every data set produces $\mathcal{D}_p = \{D_{i,p},\, i = 1, 2, \ldots, N_\mathcal{D}\}$, where $i = 1, 2, \ldots, N_\mathcal{D}$ and where $N_\mathcal{D}$ is the number of data sets. It can be assumed that an exponential decay function can predict the behavior of a given modal RDS. The ensuing prediction error, *i.e.*, the discrepancy between an estimated RDS and the model-predicted decay function $\hat{f}_{i,p}(k\Delta t; \boldsymbol{\theta}_p)$, at a given sample time $k\Delta t$ can then be defined as

$$e_{i,p}(k\Delta t; \boldsymbol{\theta}_p) = D_{i,p}(k\Delta t) - \hat{f}_{i,p}(k\Delta t; \boldsymbol{\theta}_p) \tag{4}$$

where $D_{i,p}(k\Delta t)$ represents the pth modal RDS created from the ith data set and $\boldsymbol{\theta}_p$ is a vector containing the relevant model parameters for the pth mode. Uncertainty in the prediction errors, which arises from both modeling errors and measurement noise, can be described by a zero-mean multivariate Gaussian distribution with covariance matrix $\boldsymbol{\Sigma}_p$ for each mode. The variability across data sets allows the parameter vector $\boldsymbol{\theta}_{i,p}$ to correspond to $D_{i,p}$. The covariance $\boldsymbol{\Sigma}_p$ can also be further defined as $\boldsymbol{\Sigma}_p = \{\boldsymbol{\Sigma}_{i,p}, i = 1, \ldots, N_\mathcal{D}\}$.

Adopting a hierarchical approach expands the uncertainty in $\boldsymbol{\theta}_p$ by parameterizing it as a Gaussian distribution $N(\boldsymbol{\theta}_p \,|\, \boldsymbol{\mu}_{\boldsymbol{\theta}_p}, \boldsymbol{\Sigma}_{\boldsymbol{\theta}_p})$ with mean $\boldsymbol{\mu}_{\boldsymbol{\theta}_p}$ and covariance $\boldsymbol{\Sigma}_{\boldsymbol{\theta}_p}$. Using this hierarchical framework leads to two classes of parameters: one set of data-specific parameters (in $\boldsymbol{\theta}_p$) for a given mode and another set of hyper-parameters, $\boldsymbol{\mu}_{\boldsymbol{\theta}_p}$ and $\boldsymbol{\Sigma}_{\boldsymbol{\theta}_p}$, to describe the distribution of $\boldsymbol{\theta}_p$. Based on this, the outputs from $\hat{f}_{i,p}(k\Delta t; \boldsymbol{\theta}_p)$ are conditional on $\boldsymbol{\theta}_{i,p}$, while parameter vector $\boldsymbol{\theta}_{i,p}$ is conditioned on hyper-parameters $\boldsymbol{\mu}_{\boldsymbol{\theta}_p}$ and $\boldsymbol{\Sigma}_{\boldsymbol{\theta}_p}$.

Assuming the RDS generated by the different data sets are statistically independent and that $D_{i,p}$ only depends on $\boldsymbol{\theta}_{i,p}$ and $\boldsymbol{\Sigma}_{i,p}$ allows a likelihood function to be defined as

$$\mathcal{L}(\mathcal{D}_p) = \prod_{i=1}^{N_\mathcal{D}} p(D_{i,p} | \boldsymbol{\theta}_{i,p}, \boldsymbol{\Sigma}_{i,p}) \,. \tag{5}$$

Further assuming that prediction errors $e_{i,p}(k\Delta t; \boldsymbol{\theta}_{i,p})$ from Equation 4 are independently and identically distributed (i.i.d.) according to a zero-mean Gaussian distribution with variance $\left(\sigma_e^{(i,p)}\right)^2$ allows the likelihood function for a particular RDS $D_{i,p}$ to be written as

$$\mathcal{L}(D_{i,p}) = p(D_{i,p} | \boldsymbol{\theta}_{i,p}, \boldsymbol{\Sigma}_{i,p}) = \prod_{k=1}^{n_{t_i}} \left(\sqrt{2\pi}\sigma_e^{(i,p)}\right)^{-1} \exp\left[-\frac{\left(e_{i,p}(k\Delta t; \boldsymbol{\theta}_{i,p})\right)^2}{2\left(\sigma_e^{(i,p)}\right)^2} \right] . \tag{6}$$

The prior distribution for $\boldsymbol{\theta}_{i,p}$ is defined as $N(\boldsymbol{\theta}_{i,p} | \boldsymbol{\mu}_{\boldsymbol{\theta}_p}, \boldsymbol{\Sigma}_{\boldsymbol{\theta}_p})$ while the prior distribution of the hyper-parameters can be expressed as $p(\boldsymbol{\mu}_{\boldsymbol{\theta}_p}, \boldsymbol{\Sigma}_{\boldsymbol{\theta}_p})$. Additionally, the prior distribution of $\boldsymbol{\Sigma}_{i,p}$ is not dependent on the hyper-parameters, rather it is determined by the prediction error variance. Choosing a non-informative prior for the prediction error variance and then marginalizing the joint posterior over $\boldsymbol{\Sigma}_{i,p}$ leads to [25]

$$p(\{\boldsymbol{\theta}_{i,p}\}_{i=1}^{N_\mathcal{D}}, \boldsymbol{\mu}_{\boldsymbol{\theta}_p}, \boldsymbol{\Sigma}_{\boldsymbol{\theta}_p} | \mathcal{D}_p) \propto p(\boldsymbol{\mu}_{\boldsymbol{\theta}_p}, \boldsymbol{\Sigma}_{\boldsymbol{\theta}_p}) \prod_{i=1}^{N_\mathcal{D}} \left[N(\boldsymbol{\theta}_{i,p} | \boldsymbol{\mu}_{\boldsymbol{\theta}_p}, \boldsymbol{\Sigma}_{\boldsymbol{\theta}_p}) \exp(-L_1(\boldsymbol{\theta}_{i,p})) \right] \tag{7}$$

where $L_1(\boldsymbol{\theta}_{i,p})$ is the function described by

$$L_1(\boldsymbol{\theta}_{i,p}) = -\ln\left\{\left[\sum_{k=1}^{n_{t_i}} e_{i,p}(k\Delta t, \boldsymbol{\theta}_{i,p})^2\right]^{-n_{t_i}/2}\right\}. \tag{8}$$

For large data sets the expression $\exp(-L_1(\boldsymbol{\theta}_{i,p}))$ can be asymptotically approximated by a Gaussian distribution such that $\exp(-L_1(\boldsymbol{\theta}_{i,p})) \propto N(\boldsymbol{\theta}_{i,p}\,|\,\boldsymbol{\theta}^*_{i,p}, \boldsymbol{\Sigma}^*_{\boldsymbol{\theta}_{i,p}\boldsymbol{\theta}_{i,p}})$. The mean value $\boldsymbol{\theta}^*_{i,p}$ of this distribution approximation is found through minimizing $L_1(\boldsymbol{\theta}_{i,p})$ through optimization. The covariance matrix $\boldsymbol{\Sigma}^*_{\boldsymbol{\theta}_{i,p}\boldsymbol{\theta}_{i,p}}$ for the approximation is defined as the inverse of the Hessian matrix of $L_1(\boldsymbol{\theta}_{i,p})$ evaluated at $\boldsymbol{\theta}^*_{i,p}$, *i.e.*, $[\nabla\nabla^{\mathrm{T}} L_1(\boldsymbol{\theta}_{i,p})]^{-1}_{\boldsymbol{\theta}_{i,p}=\boldsymbol{\theta}^*_{i,p}}$, where $\nabla(\cdot)$ denotes the gradient operator and ^{T} is the transpose.

Assuming that the solution $\boldsymbol{\theta}^*_{i,p}$ to Equation 8 is globally identifiable and further marginalizing over $\boldsymbol{\theta}_{i,p}$ yields a final expression for the posterior distribution of the hyper-parameters

$$p(\boldsymbol{\mu}_{\boldsymbol{\theta}_p}, \boldsymbol{\Sigma}_{\boldsymbol{\theta}_p}|\mathcal{D}_p) \propto p(\boldsymbol{\mu}_{\boldsymbol{\theta}_p}, \boldsymbol{\Sigma}_{\boldsymbol{\theta}_p}) \prod_{i=1}^{N_{\mathcal{D}}} N(\boldsymbol{\mu}_{\boldsymbol{\theta}_p}|\boldsymbol{\theta}^*_{i,p}, \boldsymbol{\Sigma}_{\boldsymbol{\theta}_p} + \boldsymbol{\Sigma}^*_{\boldsymbol{\theta}_{i,p}\boldsymbol{\theta}_{i,p}}). \tag{9}$$

The posterior distribution of the model parameters can then be found through an application of the total probability theorem and integration over the domain over the hyper-parameters such that

$$p(\boldsymbol{\theta}_p|\mathcal{D}_p) \approx \frac{1}{N_{\mathrm{s}}} \sum_{m=1}^{N_{\mathrm{s}}} N(\boldsymbol{\theta}_p|\boldsymbol{\mu}^{(m)}_{\boldsymbol{\theta}_p}, \boldsymbol{\Sigma}^{(m)}_{\boldsymbol{\theta}_p}) \tag{10}$$

where $\boldsymbol{\mu}^{(m)}_{\boldsymbol{\theta}_p}$ and $\boldsymbol{\Sigma}^{(m)}_{\boldsymbol{\theta}_p}$ are the mth out of N_{s} total samples drawn from $p(\boldsymbol{\mu}_{\boldsymbol{\theta}_p}, \boldsymbol{\Sigma}_{\boldsymbol{\theta}_p}|\mathcal{D}_p)$.

Analysis

The data used in this study comes from acceleration recordings collected during a monitoring campaign at the *10 Degrees* development in Croydon, South London [34]. The monitoring campaign collected data from two tri-axial accelerometers installed at different locations just below roof level. The accelerometers had sampling rates of 20 Hz. While the accelerometers measured both lateral and vertical directions, this study only considers the recordings from the lateral directions, *i.e.*, each accelerometer is treated as having measurements in the x and y directions. This study analyzes data from three events during that campaign, which includes 12 total raw acceleration recordings. However, after preliminary review of the raw acceleration data, only 10 acceleration data sets were deemed fit for further analysis; two acceleration data sets from the first event had been corrupted by construction noise. The selected acceleration data is also passed through a low-pass filter to remove frequency content above 1 Hz.

Previous analyses of the building suggested that the first three primary modes are located around 0.31 Hz, 0.36 Hz and 0.44 Hz [34]. Therefore, the AMD method is formulated to decompose the acceleration data into three modal responses. The RDT technique is applied to each AMD signal, creating a collection of ten RDS for each mode. While it has been shown that damping ratio estimates are independent of trigger level, the creation of the RDS is still based on the specified triggering condition. Therefore, different trigger levels are evaluated by varying the threshold according to the standard deviation of each underlying AMD signal. The triggering levels vary from one to three standard deviations for a total of three trigger levels.

For the bootstrap analysis, a total of $N_B = 500$ bootstrap replicates, each composed of N_{segs} sample segments, are created for each modal RDS at a given trigger level. Note that the number of segments N_{segs} differs between modal RDS and trigger level. The damping ratio is estimated by fitting a decaying function to each of the N_B modal RDS.

For the Bayesian analysis, this study employs bounded uniform distributions for the prior probability density functions (pdfs) such that $\boldsymbol{\mu}_{\boldsymbol{\theta}_p} \sim U(0,1)$ for both damping ratios and natural frequencies. The covariance matrix $\boldsymbol{\Sigma}_{\boldsymbol{\theta}_p}$ is assumed to be diagonal with uniform distributions for each entry described by $\sigma_{\theta_p} \sim U(0,2)$. A direct search global optimization is utilized for minimizing Equation 8 and subsequently determining parameter vector $\boldsymbol{\theta}^*_{i,p}$. Covariance matrix $\boldsymbol{\Sigma}^*_{\boldsymbol{\theta}_{i,p}\boldsymbol{\theta}_{i,p}}$ is computed using direct differentiation to find and evaluate the Hessian at $\boldsymbol{\theta}^*_{i,p}$. When needed, a transitional Markov Chain Monte Carlo (TMCMC) method [36] is used for generating samples, where N_{s} is set at $10,000$.

Using the estimates from the RDS with 20 periods, the asymptotic uncertainty estimates derived from the minimization of Equation 8 and its accompanying inverse Hessian are directly compared to the distributions of damping ratio estimates

derived from the bootstrapping approach for each of the first three modes in Figure 1. The mean value from the asymptotic estimates mostly coincide with the mean values from the bootstrap distributions, indicated by the white circles. There are some instances wherein the mean values are slightly different. This occurs because the damping ratio estimates are found by fitting Equation 4 for the bootstrapping approach but by minimizing Equation 8 for the asymptotic approximations within the hierarchical Bayesian method. It should also be noted that the $3\sigma^*$ bounds from the asymptotic approximations are not nearly as wide as the bootstrapping distributions. The bootstrapping results reflect estimates created from $N_B = 500$ different realizations of the modal RDS, while the asymptotic approximations are created from evaluating a single RDS. Thus, a greater degree of variation from bootstrapping is expected.

The use of $N_B = 500$ realizations also speaks to the additional computational effort required for the bootstrapping method. A benefit of the hierarchical approach is that it requires only a single evaluation of each RDS to produce uncertainty estimates. It also provides an organized framework for incorporating data from multiple events and channels. In contrast, bootstrapping requires many more RDS evaluations and does not offer a pathway for unifying uncertainty estimates outside of approaches such as ensemble averaging.

Since the bootstrap distributions are highly congruous to the uncertainty approximations made via the L_1 function in Equation 8, this study explores replacing the asymptotic approximations with the bootstrapping distributions within the hierarchical Bayesian approach. To complete this substitution, the full bootstrapping distribution cannot be directly used as the hierarchical Bayesian operates based on the mean $\boldsymbol{\theta}^*_{i,p}$ and variance $\boldsymbol{\Sigma}^*_{\boldsymbol{\theta}_{i,p}\boldsymbol{\theta}_{i,p}}$ of parameters $\boldsymbol{\theta}_{i,p}$. Thus, the mean and variance associated with each distribution is extracted for each unique combination of event, channel, and trigger threshold, just as for the original hierarchical Bayesian implementation.

Figure 2 presents a comparison of the marginal distributions for the modal damping ratios generated using both hierarchical Bayesian approaches, *i.e.*, the standard approach with individual estimates produced using L_1 and the bootstrapping substitution approach, for all three modes. The marginals generated for ζ_3 are essentially identical between cases; however, the distributions for the damping ratios of Modes 1 and 2 have some differences. For instance, the pdfs created with bootstrapping are narrower than their original counterparts. This behavior might seem unexpected considering that the boot-

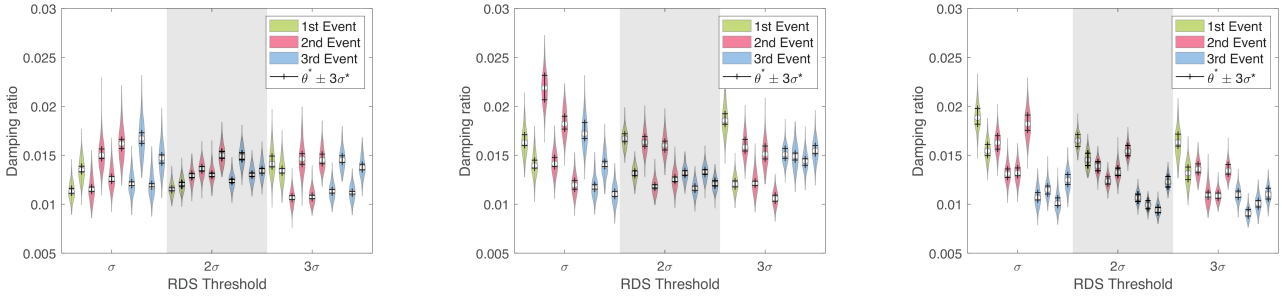

(a) Mode 1 (b) Mode 2 (c) Mode 3

Fig. 1 Comparison of uncertainty in damping ratio estimates derived from bootstrapping (colored distributions) and the asymptotic approximations using Equation 8 (black lines)

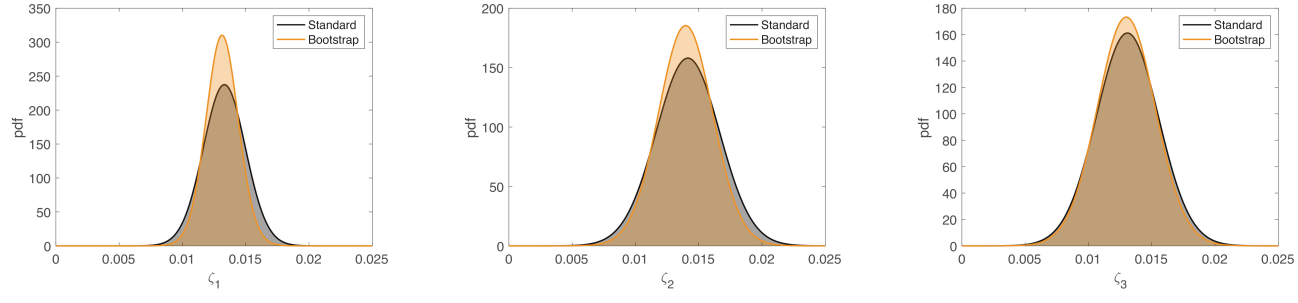

(a) Mode 1 (b) Mode 2 (c) Mode 3

Fig. 2 Comparison of marginal distributions of modal damping ratios generated using the standard hierarchical Bayesian approach and bootstrapping substitution

strapping results generally return similar mean values but higher individual variances for each data set than the asymptotic approximations with Equation 8, as illustrated by Figure 1. However, the narrower distributions for the asymptotic assumptions lead to greater uncertainty in the mean value, creating a lower maximum likelihood region with a broader distribution. This effect is most pronounced for Mode 1 but can also be observed to some extent in the damping ratio distributions for Modes 2 and 3.

Conclusion

This study presents a comparative analysis of different methods for quantifying uncertainty in damping ratio estimates using data from a tall, modular building. The modular building, *10 Degrees* in London, UK, was instrumented with accelerometers whose responses are converted into RDS and subsequently utilized for damping identification via fitting of exponential decay functions. To ensure separation into modal RDS, the AMD technique is applied, which yields RDS for three fundamental modes. The uncertainty in the damping ratios is quantified through both bootstrapping and a hierarchical Bayesian approach.

The results revealed that the bootstrapping method and hierarchical Bayesian approach yield similar individual mean damping ratios while the associated variance tends to be significantly larger with bootstrapping. This was due in part to the hierarchical Bayesian method's reliance on an asymptotic assumption of uncertainty, which involved an evaluation of a single RDS, while the bootstrapping variance came from evaluations of 500 different RDS.

This study also analyzed the impact of replacing the asymptotic approximations for the individual RDS with bootstrapping statistics and found that the final distributions did not significantly change. The main notable difference was that the similar means with wider variance values from the bootstrapping results led to a more concentrated likelihood around the overall mean value and, thus, a slightly narrower distribution than that produced using asymptotic assumptions. However, the overall effect is still a similar distribution of uncertainty for a given damping ratio.

Acknowledgments The authors wish to express their thanks to the Naughton Fellowships Faculty Research Accelerator Program, which funded this research. The authors also wish to thank Tide Construction, who facilitated data gathering and supplied information about the *10 Degrees* project, as well as Shane Linehan and Vincent Barrett at Barrett Mahony Consulting Engineers for their support with this work.

References

1. Kijewski-Correa, T. and Pirnia, J.D. "Dynamic behavior of tall buildings under wind: insights from full-scale monitoring". *The structural design of tall and special buildings*, 16(4):471–486 (2007)ifnextchar.gobble.
2. Bajrić, A., Høgsberg, J., and Rüdinger, F. "Evaluation of damping estimates by automated operational modal analysis for offshore wind turbine tower vibrations". *Renewable Energy*, 116:153–163 (2018)ifnextchar.gobble.
3. Spence, S.M. and Kareem, A. "Tall buildings and damping: a concept-based data-driven model". *Journal of Structural Engineering*, 140(5):04014005 (2014)ifnextchar.gobble.
4. Brewick, P. and Smyth, A. "An investigation of the effects of traffic induced local dynamics on global damping estimates using operational modal analysis". *Mechanical Systems and Signal Processing*, 41(1-2):433–453 (2013)ifnextchar.gobble.
5. Smith, R., Merello, R., and Willford, M. "Intrinsic and supplementary damping in tall buildings". *Proceedings of the Institution of Civil Engineers - Structures and Buildings*, 163(2):111–118 (2010)ifnextchar.gobble.
6. Li, Q., Zhou, K., and Li, X. "Damping estimation of high-rise buildings considering structural modal directions". *Earthquake Engineering and Structural Dynamics*, 49(6):543–566 (2020)ifnextchar.gobble.
7. Kareem, A. and Gurley, K. "Damping in structures: its evaluation and treatment of uncertainty". *Journal of wind engineering and industrial aerodynamics*, 59(2-3):131–157 (1996)ifnextchar.gobble.
8. Rainieri, C. and Fabbrocino, G. "Operational modal analysis: overview and applications". *Strategies for reduction of the seismic risk*, pages 29–44 (2008)ifnextchar.gobble.
9. Cole, H. "On-line failure detection and damping measurement of aerospace structures by random decrement signatures". Technical Report CR-2205, NASA (1973)ifnextchar.gobble.
10. Peeters, B. and De Roeck, G. "Reference-based stochastic subspace identification for output-only modal analysis". *Mechanical systems and signal processing*, 13(6):855–878 (1999)ifnextchar.gobble.
11. Brincker, R., Zhang, L., and Andersen, P. "Modal identification of output-only systems using frequency domaindecomposition". *Smart materials and structures*, 10(3):441 (2001)ifnextchar.gobble.
12. Yuen, K.V. and Katafygiotis, L.S. "Bayesian fast Fourier transform approach for modal updating using ambient data". *Advances in Structural Engineering*, 6(2):81–95 (2003)ifnextchar.gobble.
13. Au, S.K., Zhang, F.L., and Ni, Y.C. "Bayesian operational modal analysis: theory, computation, practice". *Computers & Structures*, 126:3–14 (2013)ifnextchar.gobble.

14. Brincker, R., Ventura, C.E., and Andersen, P. "Damping estimation by frequency domain decomposition". In *Proceedings of IMAC 19: A conference on structural dynamics: Februar 5-8, 2001, Hyatt Orlando, Kissimmee, Florida, 2001*, pages 698–703. Society for Experimental Mechanics (2001)ifnextchar.gobble.
15. Hong, A.L., Ubertini, F., and Betti, R. "New stochastic subspace approach for system identification and its application to long-span bridges". *Journal of Engineering Mechanics*, 139(6):724–736 (2013)ifnextchar.gobble.
16. Wen, Q., Hua, X., Chen, Z., Niu, H., and Wang, X. "AMD-based random decrement technique for modal identification of structures with close modes". *Journal of Aerospace Engineering*, 31(5):04018057 (2018)ifnextchar.gobble.
17. Xiong, C., Wang, M., and Chen, W. "Data-driven structural dynamic characteristics investigation by combining RDT and IVMD method". *Structures*, 55:2295–2306 (2023)ifnextchar.gobble.
18. Ni, P., Yin, Z., Han, Q., and Du, X. "Output-only structural identification with random decrement technique". *Structures*, 51:55–66 (2023)ifnextchar.gobble.
19. Reynders, E., Pintelon, R., and De Roeck, G. "Uncertainty bounds on modal parameters obtained from stochastic subspace identification". *Mechanical systems and signal processing*, 22(4):948–969 (2008)ifnextchar.gobble.
20. Döhler, M. and Mevel, L. "Efficient multi-order uncertainty computation for stochastic subspace identification". *Mechanical Systems and Signal Processing*, 38(2):346–366 (2013)ifnextchar.gobble.
21. Mellinger, P., Döhler, M., and Mevel, L. "Variance estimation of modal parameters from output-only and input/output subspace-based system identification". *Journal of Sound and Vibration*, 379:1–27 (2016)ifnextchar.gobble.
22. Kijewski, T. and Kareem, A. "On the reliability of a class of system identification techniques: insights from bootstrap theory". *Structural Safety*, 24(2):261–280 (2002)ifnextchar.gobble.
23. Behmanesh, I. and Moaveni, B. "Accounting for environmental variability, modeling errors, and parameter estimation uncertainties in structural identification". *Journal of Sound and Vibration*, 374:92–110 (2016)ifnextchar.gobble.
24. Behmanesh, I., Moaveni, B., Lombaert, G., and Papadimitriou, C. "Hierarchical Bayesian model updating for structural identification". *Mechanical Systems and Signal Processing*, 64-65:360–376 (2015)ifnextchar.gobble.
25. Sedehi, O., Papadimitriou, C., and Katafygiotis, L.S. "Probabilistic hierarchical Bayesian framework for time-domain model updating and robust predictions". *Mechanical Systems and Signal Processing*, 123:648–673 (2019)ifnextchar.gobble.
26. Jia, X., Sedehi, O., Papadimitriou, C., Katafygiotis, L.S., and Moaveni, B. "Hierarchical Bayesian modeling framework for model updating and robust predictions in structural dynamics using modal features". *Mechanical Systems and Signal Processing*, 170:108784 (2022)ifnextchar.gobble.
27. Nagel, J.B. and Sudret, B. "A unified framework for multilevel uncertainty quantification in Bayesian inverse problems". *Probabilistic Engineering Mechanics*, 43:68–84 (2016)ifnextchar.gobble.
28. Brewick, P.T. "Hierarchical Bayesian calibration of deck deflection models using distributed fiber optic strain data". *Engineering Structures*, 298:117077 (2024)ifnextchar.gobble.
29. Chen, G. and Wang, Z. "A signal decomposition theorem with hilbert transform and its application to narrowband time series with closely spaced frequency components". *Mechanical systems and signal processing*, 28:258–279 (2012)ifnextchar.gobble.
30. Chopra, A.K. *Dynamics of Structures: Theory and Applications to Earthquake Engineering*. Pearson, Hoboken, NJ, 6th edition (2023)ifnextchar.gobble.
31. Vandiver, J.K., Dunwoody, A.B., Campbell, R.B., and Cook, M.F. "A mathematical basis for the random decrement vibration signature analysis technique". *Journal of Mechanical Design*, 104(2):307–313 (1982)ifnextchar.gobble.
32. Tamura, Y. and Suganuma, S.y. "Evaluation of amplitude-dependent damping and natural frequency of buildings during strong winds". *Journal of Wind Engineering and Industrial Aerodynamics*, 59(2):115–130 (1996)ifnextchar.gobble.
33. Wang, Z. and Chen, G. "Analytical mode decomposition with Hilbert transform for modal parameter identification of buildings under ambient vibration". *Engineering Structures*, 59:173–184 (2014)ifnextchar.gobble.
34. Hickey, J., Moore, H., Broderick, B., and Fitzgerald, B. "Structural damping estimation from live monitoring of a tall modular building". *The Structural Design of Tall and Special Buildings*, 33(1):e2067 (2024)ifnextchar.gobble.
35. Efron, B. and Tibshirani, R. *An introduction to the bootstrap*. Chapman and Hall, New York (1993)ifnextchar.gobble.
36. Ching, J. and Chen, Y.C. "Transitional Markov chain Monte Carlo method for Bayesian model updating, model class selection, and model averaging". *Journal of Engineering Mechanics*, 133(7):816–832 (2007)ifnextchar.gobble.

Chapter 5
3D Printing Approaches for Reproducible Measurement of Vibroacoustically Excited Triboelectric Nanogenerators

Nakul S. Deshpande*, Eric C. Bryant*, Thomas Z. Box, Thomas S. Cox, Audrey L. Evans, Natalie White, Kent X. Eng, Stephen J. Kao, Darrel T. Beckman, Christopher A. Mizzi, Luke B. Beardslee, and Amanda E. King

Abstract Triboelectric nanogenerators (TENGs) are a rapidly growing technology with applications ranging from energy harvesting to vibrational sensing. In this work, we present a method to quantify the voltage output of TENGs upon vibroacoustic excitation via the use of rigid, 3D-printed fixtures. Our goal in utilizing such fixtures was to mitigate or eliminate the deleterious effect of buckling deformations on the performance of our TENGs. The developed fixture features a beveled ring that presses into the clamped membrane and allows us to qualitatively tension the films. Vibrational modes from films in this fixture become highly reproducible. We complement our experiments with a continuum formulation to quantify the influence of the printed fixtures on the membrane tension within the TENG. Tensioning thin films to modify voltage generation within frequency ranges opens future possibilities for tuning TENG performance via device design.

Introduction

Triboelectric nanogenerators are an emerging vibrational energy harvesting technology. At their most basic level, TENGs are easily constructed by affixing two dielectric films that have been coated on one side with an electrode material (Fig. 1). Any motion that causes friction within the interstitial space creates a tribo-generated charge that can subsequently be used in either energy harvesting or vibrational sensing techniques. Numerous research groups have collectively demonstrated that TENGs can be made from a wide variety of dielectric materials. Since their initial disclosure, TENGs have found a wide suite of applications [1] ranging from devices used to measure humidity and airflow [2] and to harvest energy from the environment (in the form of waves and wind) [3], in wearable and soft robotics [4], and in mobile electronics and biomechanical applications [5]. This wide plethora of applications rely on mechanical inputs to the TENG that result in one of two modes of activation: clapping (i.e., separation-contact) and lateral sliding.

Nakul S. Deshpande · Eric C. Bryant · Thomas Z. Box · Thomas S. Cox · Audrey L. Evans · Darrel T. Beckman · Christopher A. Mizzi · Amanda E. King(✉)
Los Alamos National Laboratory
e-mail: ndeshpande@lanl.gov; ecbryant@lanl.gov; tbox@lanl.gov; tscox@lanl.gov; audreyevans@lanl.gov; dbeckman@lanl.gov; mizzi@lanl.gov; aeking@lanl.gov

Natalie White
Brigham Young University
e-mail: njwhite219@gmail.com

Kent X. Eng
Princeton University
e-mail: ke9722@princeton.edu

Stephen J. Kao
University of New Mexico
e-mail: tundra@unm.edu

Luke B. Beardslee
Silixa LLC
e-mail: luke.b.beardslee@gmail.com

© The Author(s), under exclusive license to River Publishers 2026

Kristin B. Zimmerman, PhD (eds.), *Topics in Modal Analysis & Parameter Identification in Structural Dynamics, 2026, Vol. 8*, Conference Proceedings of the Society for Experimental Mechanics Series, https://doi.org/10.13052/rp-9788743814191

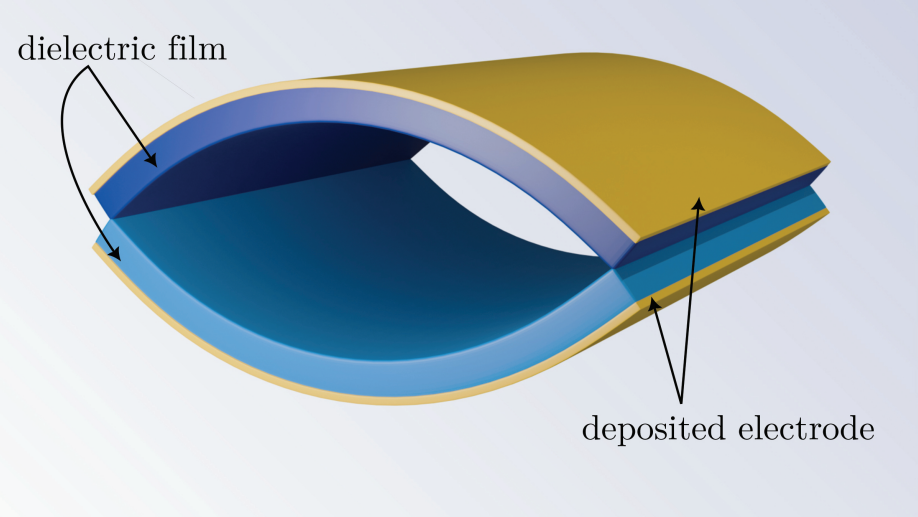

Fig. 1 TENG schematic. TENGs consist of two dielectric films, coated with an electrode, and brought into frictional contact

While TENGs have been extensively researched and new form factors are disclosed regularly, the TENG community has not, to date, established standardized testing metrics and figures of merit (FOM) that allow quantitative comparisons across the wide catalog of current and future TENG packages [6]. Assessing TENG performance has generally relied on measurements of the output voltage alone [7] without considering neither the effect of the type and strength of the mechanical energy input [8] nor how the TENG was affixed to a test surface. In this study, we develop and test 3D-printed testing fixtures that enable the reproducible testing of TENGs and propose coherence analysis as an approach to ultimately permit the quantitative comparison of TENGs of differing form factors.

Methods

Experimental Methods

3D-printing of fixtures. Fixtures were designed in SolidWorks, and printed using a Formlabs Fuse 1+ 3D printer, using Nylon 12.

Construction of TENGs. TENGs were constructed by placing electrode-coated films in the 3D-printed fixtures such that the uncoated sides were in contact. Selected dielectric films are shown in Table 1, and were purchased from McMaster Carr. The films were cut into predetermined shapes using a Cricut Maker 3 prior to being coated with ∼70 nm of gold via physical vapor deposition techniques.

Testing. All testing efforts, regardless of films tested, involved vibroacoustic excitation using a linear acoustic chirp (0.001 Hz to 4000 Hz in 0.2 s) provided by a speaker. The deformation resulting from vibroacoustic excitation was measured with a PolytecTM laser Doppler vibrometer (LDV) to quantify the magnitude and phase of the velocity at the surface of the tested films at discrete points (N $\sim$ 800). Velocity is measured in the frequency domain within a span of 0.001 Hz to 4000 Hz, with a Fast Fourier Transform (FFT) bin resolution of 5 Hz. Single films, as well as double film combinations (i.e., two films that were lacking a gold electrode), were measured in this manner after emplacing them in a fixture. In addition to being interrogated by LDV measurements, TENGs were subjected to voltage measurements upon vibroacoustic excitation. Leads were connected to a NI DAQ Sound and Vibration Device, NI USB-4432). A calibrated microphone placed approximately 10 cm away from the face of the TENG provided a means of calculating the vibroacoustic coherence of the TENGs according to the following equations:

$$C_{xy} = \frac{P_{xy}^2}{P_{xx} * P_{yy}}, \quad P(\nu) = \frac{1}{K}\sum_{k=1}^{K} P_k(\nu) \tag{1}$$

where P_{xx} and P_{yy} are power spectral density estimates of time-series data x and y, and P_{xy} is the cross spectral density estimate of inputs x and y [9]. Note that the power-spectral-density operator, $P(\nu)$, maps $\nu = \frac{i}{M}$ for $-(\frac{M}{2} - 1) \leq i \leq \frac{M}{2}$,

where the windowing parameter M is the number of data points in each segment of the power spectral density estimate. Microphone and TENG output voltage data were collected for 10 s, resulting in the collection of data from 50 chirps.

Table 1 Tested polymer films. All films are sourced from McMaster-Carr, and are cut to the dimensions of the fixtures

Polymer	**Thickness** (μm)
Kapton	25, 76
Polyethylene (PE)	101, 254
Polyethylene terephthalate (PET)	76
Polytetrafluoroethylene (PTFE)	76
Polyvinyl chloride (PVC) : Unplasticized	127
Polyvinyl chloride (PVC) : Plasticized	406
Polyvinylidene fluoride (PVDF)	76, 254

Numerical Methods

We performed frequency domain structural dynamics simulations in COMSOL [10], generally following canonical formulations [11]. To model the response and behavior of single films, double film combinations, and TENGs, these simulations require (1) the elastic material properties and (2) the initial state. Material properties are selected from those reported by McMaster-Carr of the polymer films, while the initial strain field is first applied, then adjusted such that that simulation solution matches the experimentally measured peaks of the FFT.

Results and Discussion

Our work was motivated by the current lack of both standardized testing methods and FOM approaches in the TENG literature. The postulation that enclosing the TENG would lead to reproducible measurements was tested by encasing the TENG within a rigid 3D-printed fixture and subsequently exciting the TENG with a vibroacoustic chirp. Vibroacoustic measurements present several advantages: they are nondestructive, easily reproducible, and can be quickly executed. To disentangle the contributions due to potential interactions between the two films of our TENGs, we measured the vibroacoustic response of single films and verified our experimental results using a numerical model. In total, we measured the vibroacoustic response of ten polymer thin films (Table 1) and the voltage response of fourteen thin film combinations. Multiplicative combinations of thin films restrict the volume of data we can show, and thus we focus below on salient results to avoid redundancy.

Vibroacousitcs of single films in square and circular fixtures

Our initial efforts focused on employing square fixtures. A representative vibroacoustic response of a square film (127 μm thick PVC) is shown in (Fig. 2). Numerous sharp peaks are evident between 0 and 50 Hz; due to their lower spectral power, these peaks are interpreted as noise. We observe similar peaks in the same frequency range for all tested films when employing the square fixtures. In PVC, the first vibrational mode appears as a single prominent peak at 670 Hz. The spatial map of the first vibrational mode reveals a single amplitude peak located within the center of the film. The second and third vibrational modes appear at 1560 Hz and 1620 Hz, respectively; the spatial map reveals three amplitude peaks in both the second and third vibrational modes, with the features rotated 90 degrees from each other. The fourth mode occurs at 1915 Hz and visually has four amplitude peaks placed in a square formation around a central feature. The fifth mode occurs at 2440 Hz, and the spatial map reveals five amplitude peaks arranged along the diagonal of the square (Fig. 2).

Thin films enclosed in circular fixtures exhibit the first five vibrational modes at frequencies less than 500 Hz. Peaks of these modes are sharp and closely spaced. A representative vibroacoustic response of a circular film (254 μm thick PE) is shown in (Fig. 2). The first vibrational mode occurs at 140 Hz and has as an off-center amplitude peak. The second and third vibrational modes occur at 205 and 250 Hz, respectively, and have two amplitude peaks rotated 90 degrees from each other. The fourth vibrational mode occurs at 325 Hz and exhibits a quadrupolar symmetry. The fifth vibrational mode occurs at 465 Hz and appears to have six amplitude peaks surrounding a seventh peak.

Classical structural dynamics relationships [11] reproduce the experimental phenomenology observed above, albeit with important differences between the square and circular fixtures. Simulations conducted in the square geometry reproduce the

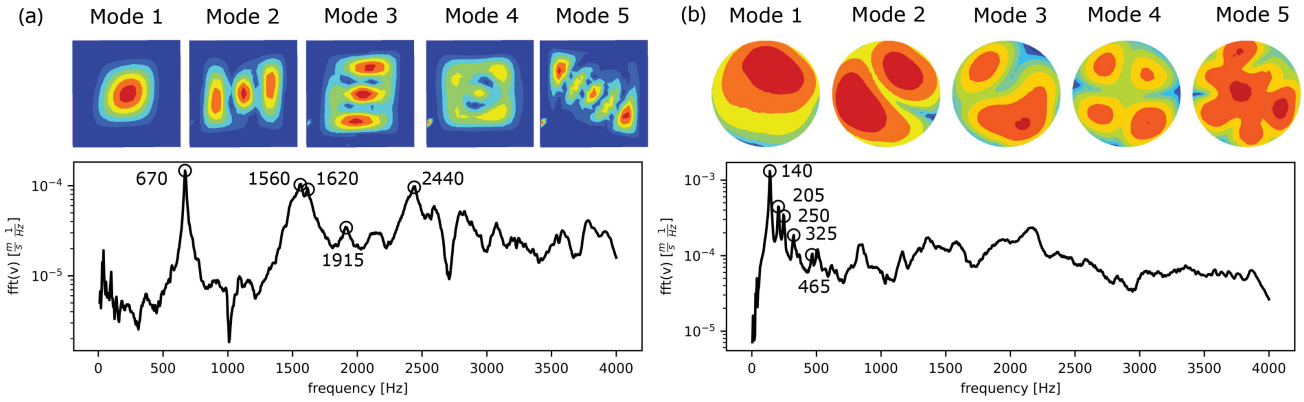

Fig. 2 Experimental vibroacoustic phenomenology: Spatial maps of the first five vibrational modes (top row), identified from peaks in the FFT (bottom row), for (a) PVC 127μm in a square fixture and (b) PE 254 μm in a circular fixture. Open circles in the FFT indicate peaks. Both experimental results come from measurements on clamped, un-tensioned single films

observed modal shapes: a single amplitude peak in the first vibrational mode, two amplitude peaks rotated from each other in the second and third vibrational modes, and four-fold symmetric distribution of amplitude peaks in the fourth vibrational mode. The calculated frequencies at which the modes occur do not match the experimentally measured values. We attribute this mismatch to both the inherent anisotropy of the material and the potential inconsistencies when initially tensioning the film. However, we could more accurately predict the frequency of the vibrational modes when the peaks were fitted independently of each other.

The inability to accurately predict the vibrational frequencies of the observed modal shapes of films in square fixtures prompted us to move towards circular test fixtures, which could be more accurately predicted (Fig. 3, Table 2). These efforts demonstrate that the initial choice of a coordinate system, dictated by the initial selection of fixture design, prescribes the ability to match experiment with modeling. Other key parameters that influence modeling efforts include material properties, initial strain within the fixture, and boundary tension. Because material properties do not significantly change during loading

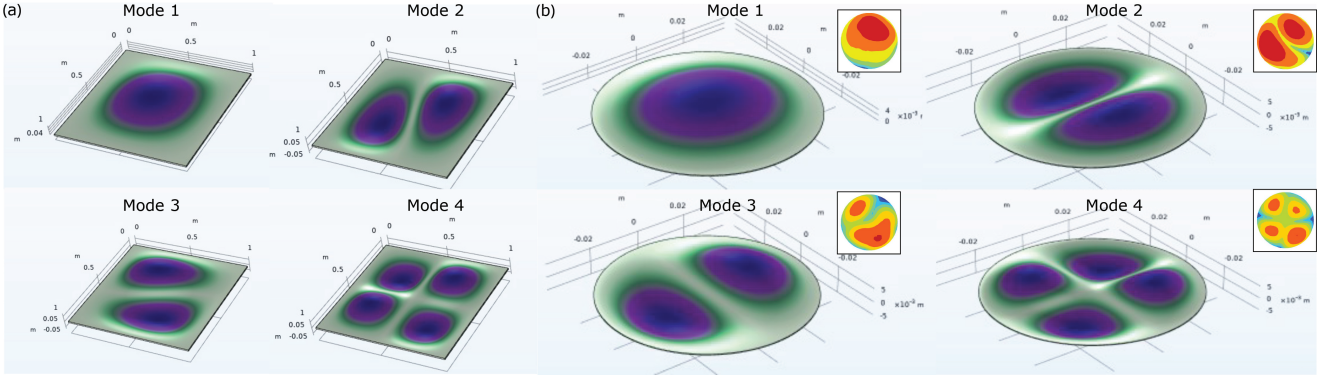

Fig. 3 Simulated vibroacoustic responses. Experimental vs. simulated vibrational modes for (a) PVC 406 μm in a square fixture and (b) PVDF 254 μm in a circular fixture. Insets of simulation results indicate experimental results at the same modes

Table 2 Experimental vs. simulated modal frequencies for PVC 406 μm in a square fixture and PVDF 254 μm in a circular fixture

	Square				**Circle**			
Mode	1	2	3	4	1	2	3	4
Vibrometer frequency (Hz)	518	787	853	1096	229	297	353	459
FEA frequency (Hz)	503	793	835	1051	206	307	377	445

within the fixture or during vibroacoustic testing, the discrepancies between experiment and simulation likely originate in stresses imposed by emplacing the film within the fixture. Rectifying these discrepancies will rely on accurate measurement of the initial film strain within the fixture and proper treatment of the boundary conditions. To ultimately apply these insights to TENGs, we envision extending our employed simulation methods [11] to multi-film systems. Such approaches could include numerical methods for Lagrangian overlap coupling [12], as such overlap coupling is currently unavailable in commercial finite element analysis packages such as COMSOL. We are currently developing such capabilities in our laboratories.

Vibroacoustics of dual film systems in circular fixtures

After establishing the general behavior of vibrating single films and calibrating a corresponding numerical model, we moved to dual film assemblies. The experimental study of dual film assemblies presents a key question: do both films, when in contact with each other, exhibit comparable vibroacoustic responses with respect to mode shapes and resonant frequencies? If comparable vibroacoustic responses are observed, the implication is that an interaction between both films is occurring and thus needs to be incorporated into any numerical modeling approach. The experimental challenge became the design of a fixture that could independently clamp, tension, and connect the films (Fig. 4).

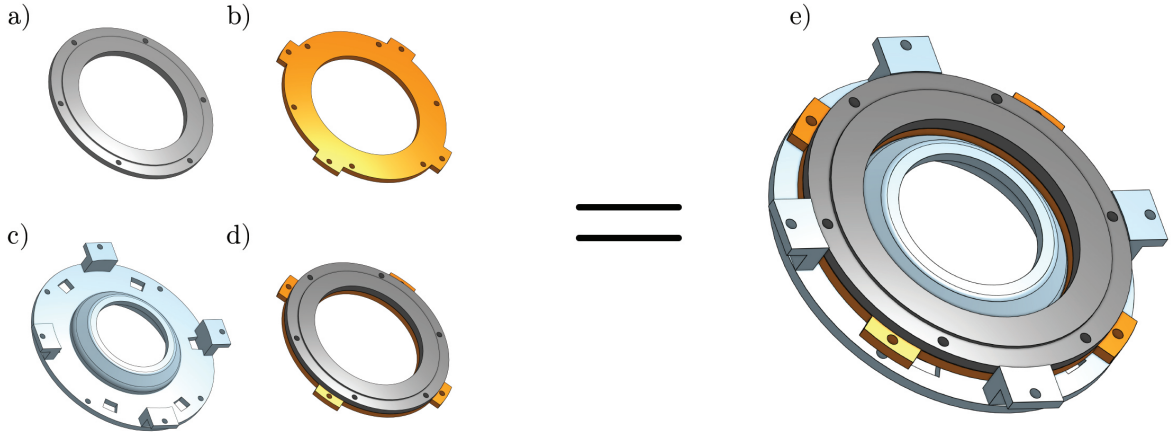

Fig. 4 3D printed fixture components. (a) Base plate. (b) Top ring. (c) Base for tension (d) Clamped configuration. (e) Clamped and tensioned configuration. Tension is administered to the film by the indentation of component c) which presses the film

When clamped, untensioned films are brought into contact, their vibroacoustic responses have some weak overlap at low frequencies and little similarity at high frequencies (Fig. 5). However, when tension is applied by pressing component c) into the film (Fig. 4), the vibroacoustic response of both films are brought into agreement, with a high degree of overlap across the entire frequency range (Fig. 5).

Quantifying the response of TENGs using coherence as a FOM

There currently exists a lack of standardized metrics and FOMs for characterizing the performance of TENGs. In a vast majority of literature reports on these devices, TENGs are not measured relative to standard instruments such as accelerometers or microphones; this knowledge gap has arguably prevented TENGs from being more widely adopted in vibrational energy harvesting and vibrational sensing applications. In this initial effort, we focused on characterizing the voltage response of TENGs as a function of frequency and evaluating our results against a calibrated microphone. Such efforts could have implications in designing TENGs well-matched to vibrational energy harvesting from systems that exhibit persistent, characteristic vibrational frequencies (e.g., the swaying motion of a bridge or energy harvesting systems in hybrid vehicles).

Use of a calibrated microphone allowed us to utilize coherence to quantitatively compare TENGs emplaced in circular fixtures (Fig. 6). Coherence is a statistical measurement that quantifies the linear correlation between two signals in the frequency domain; a value of 1 indicates perfect linear correlation, while a value of 0 indicates no correlation at all at a specific frequency. For most of our tested TENG combinations, coherence increases as the input vibrational frequency increases. Coherence is highly sensitive to the choice of parameter M (the length of the time-series segment over which the

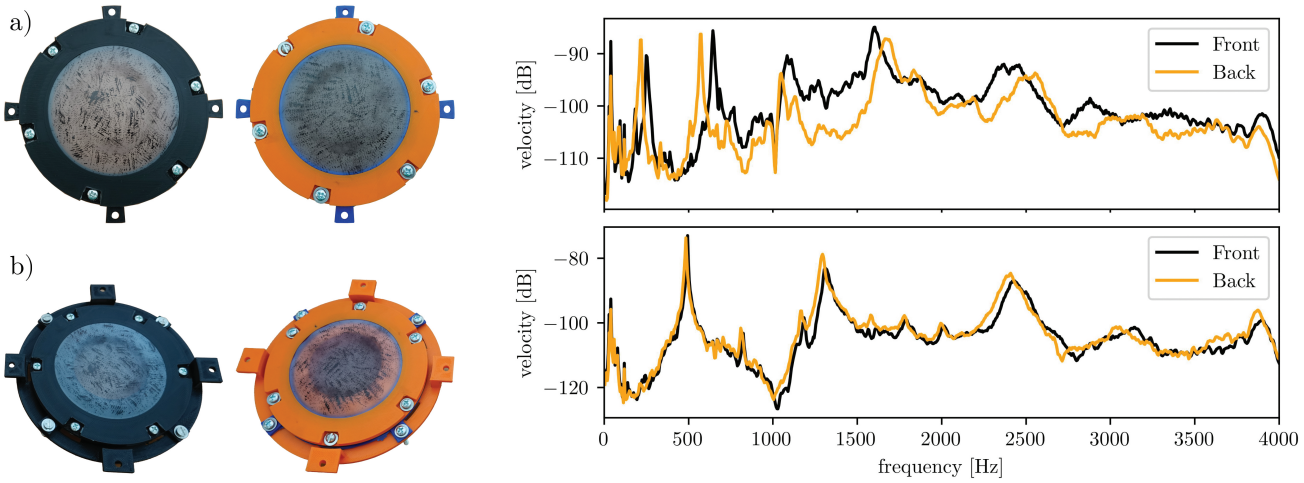

Fig. 5 Behavior of clamped and tensioned films. (a) Top row indicates clamped configuration and vibroacoustic response (b) Bottom row indicates clamped and tensioned configuration. Note that tensioned samples show consistent, repeatable FFT responses both in double-flim geometries and across experimental realizations

power spectral density is computed). We observe an increase in coherence as the parameter M (the length of the time-series segment over which the power spectral density is computed) is increased. Averaging the coherence values across the input frequency range yields the data shown in Fig. 7. This plot suggests that the pairings of Kapton and PE in a TENG is the most promising TENG for applications involving vibrational frequencies between 0 and 4000 Hz, while pairings of 254 μm thick PVDF with Kapton would be poor harvesters and sensors in similar applications.

Our work indicates that vibroacoustic coherence is a potential FOM to systematically characterize and benchmark the performance of TENG devices. This method can be used to identify optimal TENG design parameters and aid in identifying those parameters that dictate the mechanisms governing TENG performance. The latter is crucial because TENG applica-

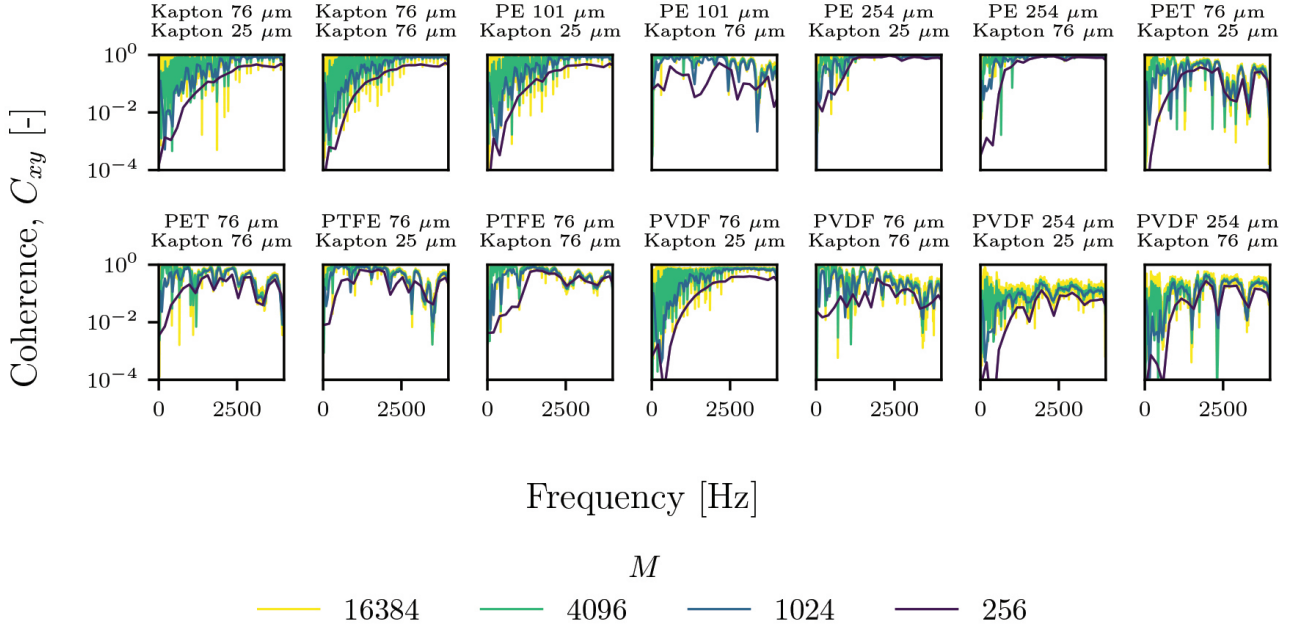

Fig. 6 Summary TENG coherence. Each panel indicates a unique TENG configuration and the corresponding coherence measure. Coherence is computed between a microphone recording of the chirp signal and the voltage output of the indicated TENG combination. Colors indicate varying values of the parameter M

tions continue to grow, but the mechanisms underpinning their operation remain elusive [13]. For example, the triboelectric effect — the phenomenon by which rubbing two materials together causes charge to transfer between them [14] — is central to TENGs, but is still not fully understood despite having been known for at least 2500 years [15]. In part, this is because triboelectricity is a complex process [16] likely involving multiple charged species [17] whose transfer is driven by some combination of electromechanical [18] and/or thermal [19] factors. We anticipate that vibroacoustic coherence characterization of TENGs, paired with more local measurements, can be applied to gain insights into these basic research questions.

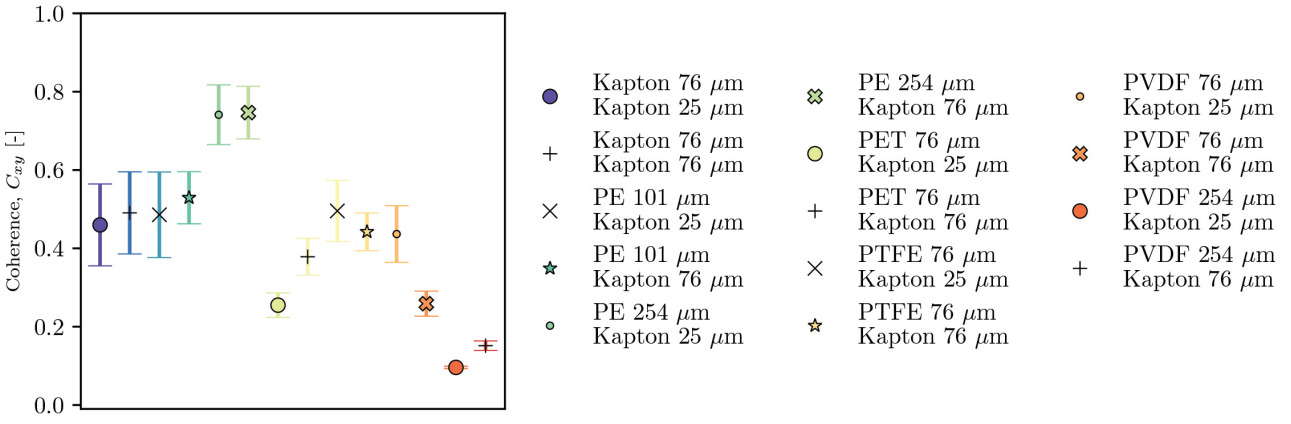

Fig. 7 Frequency averaged vibroacoustic coherence of tested TENG devices. Mean and variance of coherence for all tested films. Each marker indicates a unique TENG combination, errorbars indicate the variance of C_{xy} computed across the frequency domain of 0-4000 Hz

Conclusions

Our goals in this work were to demonstrate a robust experimental workflow in fabricating TENG devices, to demonstrate the basic validity of linearized elastic structural dynamics, and to propose vibroacoustic coherence as a FOM to quantify the output performance of TENG devices. We found that combinations of Kapton and PE provide the highest degree of coherence, and that the choice of experimental geometries strongly influences the details of the numerical simulations. Simply moving from a square to a circular geometry allowed for the prediction and match of the peak resonant frequencies as well as the spatial maps of the vibrational modes. Finally, we found that the benefit of vibroacoustic coherence is its simplicity. It is experimentally tractable, via an accessible acoustics-based workflow. With the plethora of driving mechanisms that exist in TENG response, a single metric agnostic to the nature of the excitation source that can relate input to output is extremely useful in comparing TENGs across many applications.

Previous research has called into question the ability of TENGs to behave reproducibly both as a function of time and between TENGs made of identical materials. Explanations for observed deviations in performance include temperature and humidity. During execution of our work, we have found that controlling tension within the fixtures leads to more consistent experimental results, and we postulate that this parameter has been a neglected consideration in the evaluation of TENG performance in previously published studies. Additionally, there are several caveats to TENG performance indicated in the comparison in (Fig. 7). For instance, the manufacturing process of thin polymeric materials likely alters their linearized electro-elastodynamic parameters. While the material parameters reported by manufacturers are accurate to a degree, the variability resulting from differences in manufacturing processes is significant enough to be considered in how the simulations match the experiments. In future work, stronger control over the fabrication of the polymers themselves would be beneficial and could provide independent measurements of the materials.

In future simulations, our reformulation is now amenable to additional energetic contributions that enforce damped cross-domain interactions for multi-film and film-fixture contact – as characterized either by a displacement jump or an overlap coupling method [20, 12]. An FEA-prescribed initial stress-based initialization [21] has been preliminary vetted (as, thus far, intrinsically necessary for thin-film calibration): initial stress may perform differently than in prior COMSOL modeling. Stepping towards fully-resolved multiphysics numerical simulations relies upon a robust experimental workflow and numerical simulations that are physically justified. However, we note that charge generation and transport is not a

phenomenon unique to TENGs. Each mode of deformation has been linked or inferred to activate a different physical source of voltage generation [22]. This knowledge should be coupled with growing recognition of and capabilities for simulating the electrodynamics [23] for a complete picture of TENG deformation and charge generation.

References

1. Prabhakar Yadav et al. “Applications of Multifunctional Triboelectric Nanogenerator (TENG) Devices: Materials and Prospects”. Sustainable Energy & Fuels 7.16 (2023), pp. 3796–3831. DOI: 10.1039/D3SE00714F.
2. Vu Nguyen and Rusen Yang. “Effect of Humidity and Pressure on the Triboelectric Nanogenerator”. Nano Energy 2.5 (Sept. 2013), pp. 604–608. DOI: 10.1016/j.nanoen.2013.07.012.
3. Xiaonan Wen et al. “Harvesting Broadband Kinetic Impact Energy from Mechanical Triggering/Vibration and Water Waves”. ACS Nano 8.7 (July 2014), pp. 7405–7412. DOI: 10.1021/nn502618f.
4. Min Pan et al. “Triboelectric and Piezoelectric Nanogenerators for Future Soft Robots and Machines”. iScience 23.11 (Nov. 2020), p. 101682. DOI: 10.1016/j.isci.2020.101682.
5. Xiaole Cao et al. “Multidiscipline Applications of Triboelectric Nanogenerators for the Intelligent Era of Internet of Things”. Nano-Micro Letters 15.1 (Dec. 2022), p. 14. DOI: 10.1007/s40820-022-00981-8.
6. Daniel M. Mulvihill et al. “How to Test Triboelectric Nanogenerators: Key Factors for Standardized Performance Evaluation”. Advanced Energy Materials (Aug. 2025), e02920. DOI: 10.1002/aenm.202502920.
7. Sihong Wang, Long Lin, and Zhong Lin Wang. “Nanoscale Triboelectric-Effect-Enabled Energy Conversion for Sustainably Powering Portable Electronics”. Nano Letters 12.12 (Dec. 2012), pp. 6339–6346. DOI: 10.1021/nl303573d.
8. Simiao Niu et al. “Theoretical Investigation and Structural Optimization of Single-Electrode Triboelectric Nanogenerators”. Advanced Functional Materials 24.22 (June 2014), pp. 3332–3340. DOI: 10.1002/adfm.201303799.
9. P. Welch. “The Use of Fast Fourier Transform for the Estimation of Power Spectra: A Method Based on Time Averaging over Short, Modified Periodograms”. IEEE Transactions on Audio and Electroacoustics 15.2 (June 1967), pp. 70–73. DOI: 10.1109/TAU.1967.1161901.
10. COMSOL Multiphysics®. COMSOL AB, Stockholm, Sweden.
11. Subrata Mukherjee. “Variational Principles in Dynamic Thermoviscoelasticity”. International Journal of Solids and Structures 9.10 (Oct. 1973), pp. 1301–1316. DOI: 10.1016/0020-7683(73)90116-9.
12. S. P. Xiao and T. Belytschko. “A Bridging Domain Method for Coupling Continua with Molecular Dynamics”. Computer Methods in Applied Mechanics and Engineering 193.17 (May 2004), pp. 1645–1669. DOI: 10.1016/j.cma.2003.12.053.
13. Zhong Lin Wang. “From Contact Electrification to Triboelectric Nanogenerators”. Reports on Progress in Physics 84.9 (Sept. 2021), p. 096502. DOI: 10.1088/1361-6633/ac0a50.
14. Daniel J. Lacks and R. Mohan Sankaran. “Contact Electrification of Insulating Materials”. Journal of Physics D: Applied Physics 44.45 (Oct. 2011), p. 453001. DOI: 10.1088/0022-3727/44/45/453001.
15. Paul Iversen and Daniel J. Lacks. “A Life of Its Own: The Tenuous Connection between Thales of Miletus and the Study of Electrostatic Charging”. Journal of Electrostatics 70.3 (June 2012), pp. 309–311. DOI: 10.1016/j.elstat.2012.03.002.
16. L. D. Marks and K. P. Olson. “Flexoelectricity, Triboelectricity, and Free Interfacial Charges”. Small, p. 2310546. DOI: 10.1002/smll.202310546.
17. Giulio Fatti et al. “Uncertainty and Irreproducibility of Triboelectricity Based on Interface Mechanochemistry”. Physical Review Letters 131.16 (Oct. 2023), p. 166201. DOI: 10.1103/PhysRevLett.131.166201.
18. C. A. Mizzi, A. Y. W. Lin, and L. D. Marks. “Does Flexoelectricity Drive Triboelectricity?” Physical Review Letters 123.11 (Sept. 2019), p. 116103. DOI: 10.1103/PhysRevLett.123.116103.
19. Eui-Cheol Shin et al. “Derivation of a Governing Rule in Triboelectric Charging and Series from Thermoelectricity”. Physical Review Research 4.2 (May 2022), p. 023131. DOI: 10.1103/PhysRevResearch.4.023131.
20. Alexander Lindsay et al. “Automatic Differentiation in MetaPhysicL and Its Applications in MOOSE”. Nuclear Technology 207.7 (July 2021), pp. 905–922. DOI: 10.1080/00295450.2020.1838877.
21. Guancong Ma et al. “Acoustic Metasurface with Hybrid Resonances”. Nature Materials 13.9 (Sept. 2014), pp. 873–878. DOI: 10.1038/nmat3994.
22. Daniel Moreno-Garcia, Kaitlin M Howell, and Luis Guillermo Villanueva. “Flexoelectricity in Amorphous Hafnium Oxide (HfO2)”.
23. Shengquan Li et al. “Numerical Simulations of Piezoelectricity and Triboelectricity: From Materials, Structures to Devices”. Applied Materials Today 37 (Apr. 2024), p. 102092. DOI: 10.1016/j.apmt.2024.102092.

Chapter 6
Ice Detection on Plate Structures Using Modal Curvature and Piezoelectric Sensor Networks

Lorenzo Stagi, Nicola Roveri, Salvatore Ameduri, Antonio Concilio, and Jean-François Deü

Abstract Ice accretion on engineering structures such as aircraft and wind turbines can severely compromise safety and efficiency, highlighting the need for reliable detection and localization strategies. In this work, a modal-based methodology is proposed to identify ice on plate-like structures exploiting deviations in curvature mode shapes, reconstructed using a network of piezoelectric transducers, between a reference ice-free state and the iced configuration. Both numerical and experimental investigations were carried out on the same aluminum plate instrumented with 42 piezoelectric patches, enabling direct comparison between simulation and measurements.

Numerical simulations were first performed to assess the method's sensitivity to different ice geometries and thicknesses. The analysis considered both curvature mode shapes and their spatial derivatives, showing that the use of second derivatives significantly improves localization accuracy, particularly in the presence of irregular or distributed ice patterns. The same plate was then tested experimentally, with paraffin patches employed as ice surrogates. Operational Modal Analysis techniques were used to extract mode shapes from frequency response functions, and the proposed localization algorithm was applied.

Results consistently confirmed the numerical findings, with the second derivative of curvature providing the most explicit and robust localization of the iced regions. The study highlights the potential of modal curvature analysis, combined with a dense piezoelectric array, as an effective and lightweight strategy for spatially resolved ice detection. Moreover, the same transducer network could be subsequently exploited for active ice removal, paving the way toward fully integrated sensing–actuation systems for autonomous de-icing.

Keywords Piezoelectric · Ice detection · Curvature mode shapes · Curvature derivatives · Structural health monitoring

Introduction

Ice formation poses a significant challenge in both wind energy and aviation sectors, where it compromises safety, reduces operational efficiency, and accelerates structural degradation. On wind turbine blades, even moderate ice buildup alters the aerodynamic profile, leading to power losses of up to 50% annually, while simultaneously increasing fatigue loads and inducing structural imbalance, thereby shortening service life [1]. In aviation, icing affects boundary-layer behavior, reducing lift, increasing drag and stall speed, and may ultimately lead to hazardous loss-of-control incidents [2].

Current ice detection methods are mostly indirect [3], relying on performance degradation metrics combined with environmental data such as temperature and humidity. However, these approaches lack responsiveness and do not provide precise

Lorenzo Stagi · Nicola Roveri
Department of Mechanical and Aerospace Engineering, Sapienza University of Rome, Rome, Italy
e-mail: lorenzo.stagi@uniroma1.it; nicola.roveri@uniroma1.it

Salvatore Ameduri · Antonio Concilio
Italian Aerospace Research Centre (CIRA), Capua, Italy
e-mail: S.Ameduri@cira.it; A.Concilio@cira.it

Jean-François Deü
Structural Mechanics Laboratory, Conservatoire National des Arts et Métiers, Paris, France
e-mail: jean-francois.deu@lecnam.net

© The Author(s), under exclusive license to River Publishers 2026

Kristin B. Zimmerman, PhD (eds.), *Topics in Modal Analysis & Parameter Identification in Structural Dynamics, 2026, Vol. 8*,
Conference Proceedings of the Society for Experimental Mechanics Series, https://doi.org/10.13052/rp-9788743814191

information about the ice's location or quantity. A reliable, real-time, and spatially resolved detection system would not only improve flight safety but also enhance the efficiency of de-icing systems by enabling targeted intervention.

Piezoelectric sensor networks represent a promising solution [4]: when bonded or embedded into a structure, they can cover large surface areas with minimal added weight and aerodynamic penalty, while also providing quantitative information on the extent and morphology of ice deposits. Among the various sensing strategies, electromechanical impedance (EMI) methods have gained considerable attention; these methods are based on monitoring variations in the electrical impedance of the piezoelectric transducers, which reflect changes in the mechanical properties of the host structure. For example, Zhang et al. [5] demonstrated the feasibility of using EMI indicators combined with neural network classifiers for reliable ice detection on cables. Building on this work, Maio et al. [6] showed that applying principal component analysis enhances sensitivity in composite plates. More recently, Wiedemann et al. [7] proposed an integrated approach for helicopter rotor blades, where impedance variations are used for ice detection and low-frequency excitations actively remove ice accumulations.

Although electromechanical-impedance features remain an active research direction, the most widely adopted approach for icing detection is based on ultrasonic guided-wave interrogation [8]. In this method, piezoelectric transducers bonded to the structure generate and receive propagating Lamb waves. Well established in Structural Health Monitoring (SHM) and non-destructive testing of thin plates, this technique exploits the high sensitivity of Lamb-wave attenuation, velocity, and mode conversion to structural inhomogeneities; by tracking these parameters, information about defect size and location can be inferred [9, 10, 11]. The same principle extends to icing: an accreted ice layer perturbs the Lamb-wave field through scattering, additional damping, and phase-velocity shifts. Several researchers have demonstrated this effect. Zhang et al. [12] developed a delay-based algorithm that identifies ice by measuring the additional travel time of a wave packet relative to a baseline; their approach was validated experimentally on a plate with two piezoelectric elements and an intervening ice patch. Similarly, Pohl [13] designed a local sensor that detects ice through concurrent variations in amplitude and velocity. For spatial mapping, Zhao et al. [14] introduced a probability-based reconstruction method capable of accurately identifying the geometry of ice deposits.

Ice can also be detected by exploiting changes in modal parameters, such as natural frequencies and mode shapes, caused by ice accretion. Gantasala et al. [15] showed that such changes could be used to detect and quantify ice. Later, the same author introduced a neural network-based method that, using natural frequencies as input, could estimate both the quantity and location of ice with a weighted average percentage error of 17.53%. In a related effort, Tsiapoki et al. [16] applied a similar frequency-based neural network model to a full-scale wind turbine blade, further validating this approach.

In the present study, a modal strategy is adopted to perform ice localization by analyzing changes in the curvature mode shapes of the structure. The use of modal curvature is a well-established approach in SHM [17, 18], where it has been widely employed for damage detection and localization due to its high sensitivity to local stiffness variations. By extending this concept to icing scenarios, the present work investigates whether curvature-based indicators can also provide robust and spatially resolved information on ice accretion. Deviations between measured and reference curvature mode shapes are exploited to detect and localize ice accretion, with the most affected regions exhibiting the largest discrepancies. Furthermore, a specific focus of this work is to investigate whether operating on the derivatives of the curvature mode shapes can enhance detection performance.

The proposed algorithm was first validated numerically and subsequently tested experimentally. A simplified setup was implemented using a $420 \times 360\, mm$ aluminum plate instrumented with 42 piezoelectric transducers. An additional feature of this setup is its potential integration with an active de-icing strategy, whereby the same network could be used not only for detection but also for ice removal once accretion is identified. In this context, Song et al. [19] developed a de-icing approach on a plate-like structure similar to the one investigated in this work, combining piezoelectric actuation with a genetic algorithm, enabling the system to maximize the stresses required to break the ice precisely where it is present while leaving the rest of the structure unaffected. This result highlights the strong potential of piezoelectric networks to serve as both sensing and actuation platforms, paving the way toward fully integrated solutions for autonomous ice management.

Curvature Derivatives and Local Effects

The study of higher-order derivatives of curvature mode shapes has already been carried out for beam-like structures in [20]. Here, the key steps of that formulation are recalled. Moreover, for exposition clarity, the one dimensional formulation is considered; the two dimensional generalization follows by replacing $\phi'' = \kappa_{i,j}$ and $\phi^{iv} = \Delta^4\phi$. Consider an Euler–Bernoulli beam with spatially varying elastic and inertial properties. The modal equation of motion is

$$(EI(x)\,\phi''(x))'' + \rho(x)A(x)\,\omega^2\phi(x) = 0, \tag{1}$$

where $\phi(x)$ is the mode shape, $EI(x)$ the flexural rigidity, and $\rho(x)A(x)$ the mass per unit length. Defining the modal curvature as $\kappa(x) = \phi''(x)$, the equation can be rewritten as

$$EI(x)\,\kappa''(x) + 2(EI)'(x)\,\kappa'(x) + (EI)''(x)\,\kappa(x) + \rho(x)A(x)\,\omega^2\phi(x) = 0. \tag{2}$$

Dividing by $\phi(x)$ yields the local relation

$$\frac{\kappa''(x)}{\phi(x)} = -\frac{\rho(x)A(x)}{EI(x)}\,\omega^2 - 2\,\frac{(EI)'(x)}{EI(x)}\,\frac{\kappa'(x)}{\phi(x)} - \frac{(EI)''(x)}{EI(x)}\,\frac{\kappa(x)}{\phi(x)}. \tag{3}$$

This expression shows how higher-order derivatives of curvature reflect local variations in structural properties. In homogeneous systems, with constant EI and ρA, the derivative terms vanish and the ratio κ''/ϕ reduces to the constant value $-(\rho A/EI)\,\omega^2$, with no spatial variation. When stiffness varies, however, the terms involving $(EI)'/EI$ and $(EI)''/EI$ introduce localized peaks in κ'/ϕ and κ/ϕ, making them sensitive to cracks, stiff patches, or mechanical inhomogeneities. Conversely, mass variations mainly affect the baseline of κ''/ϕ through the term $-(\rho A/EI)\,\omega^2$, without necessarily producing localized discontinuities.

From this derivation, it follows that higher-order derivatives amplify local changes: while curvature κ already reflects stiffness through its proportionality to bending moment, κ' and κ'' emphasize gradients and discontinuities, offering a more discriminating diagnostic tool. The drawback is their sensitivity to noise, which makes regularization or filtering strategies necessary in experiments.

In the context of icing, a deposited patch increases local stiffness and produces mass addition, influencing all the terms κ'/ϕ and κ/ϕ and shifting the baseline of κ''/ϕ. This distinction allows deviations observed in experimental data to be directly associated with the structural modifications induced by ice accretion. Based on these considerations, the proposed methodology evaluates not only the reconstructed modal curvature from the piezoelectric network but also its first and second derivatives in order to investigate whether the enhanced sensitivity can improve the localization of iced regions.

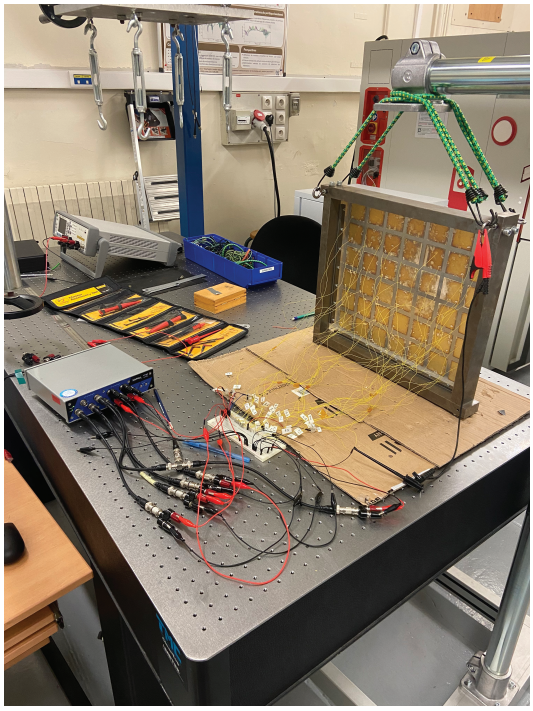

Fig. 1 Picture of the plate from which it is possible to notice the yellow patches (the piezoelectric transducer) and the steel frame

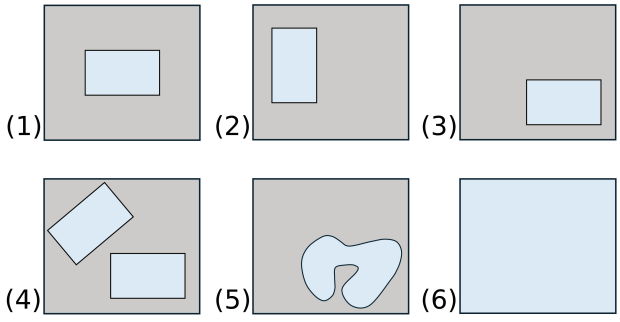

Fig. 2 Position of the patch of ice for the six analyzed configurations. In case 6 the patch covers all the plate

Table 1 Geometrical configurations and thickness for different analyzed configurations

Condition	Dimension [mm]	Thickness [mm]
1	200×120	2
2	200×120	2
3	200×120	2
4	2 patches of 200×120	2
5	*irregular shape*	2
6	420×360	5

Model description

The study focuses on a simply supported aluminum rectangular plate with dimensions $l_x = 420\ mm$, $l_y = 360\ mm$, and thickness $h_s = 3\ mm$. The plate is instrumented with 42 square piezoelectric transducers (side length $l_p = 50\ mm$, thickness $h_p = 0.5\ mm$), manufactured using PIC 153 piezoelectric material (PI Ceramic). Figure 1 shows the experimental setup. The plate is mounted on a steel frame through $0.5\ mm$ aluminum strips, which provide sufficient longitudinal stiffness to prevent transverse displacement while offering low flexural rigidity to approximate free rotational boundary conditions.

The model was validated against the analytical natural frequencies of the simply supported plate. According to classical plate theory, the natural frequencies are given by

$$f_{(m,n)} = h_s \left(\frac{m^2}{l_x^2} + \frac{n^2}{l_y^2} \right) \frac{\pi}{4} \sqrt{\frac{Y_s}{3\rho_s \left(1 - \nu_s^2\right)}}, \tag{4}$$

where $f_{(m,n)}$ is the natural frequency of the (m, n) mode, h_s is the plate thickness, l_x and l_y are the plate dimensions along the x and y directions, respectively, m and n are the half-wave numbers in the x and y directions, Y_s is the Young's modulus, ρ_s is the density, and ν_s is the Poisson's ratio.

The accuracy of the numerical model was assessed by comparing its natural frequencies with those obtained analytically and experimentally. As shown in Figure 3, the three sets of results are in close agreement, with discrepancies consistently below 8%, and typically around 4% for the experimental and numerical cases. These differences are mainly attributed to the bonded piezoelectric patches, which are not considered in the analytical formulation but are included in both the numerical model and the experimental setup, as well as to slight inconsistencies in reproducing the boundary conditions in the experimental configuration. A detailed description of the setup is provided in [21].

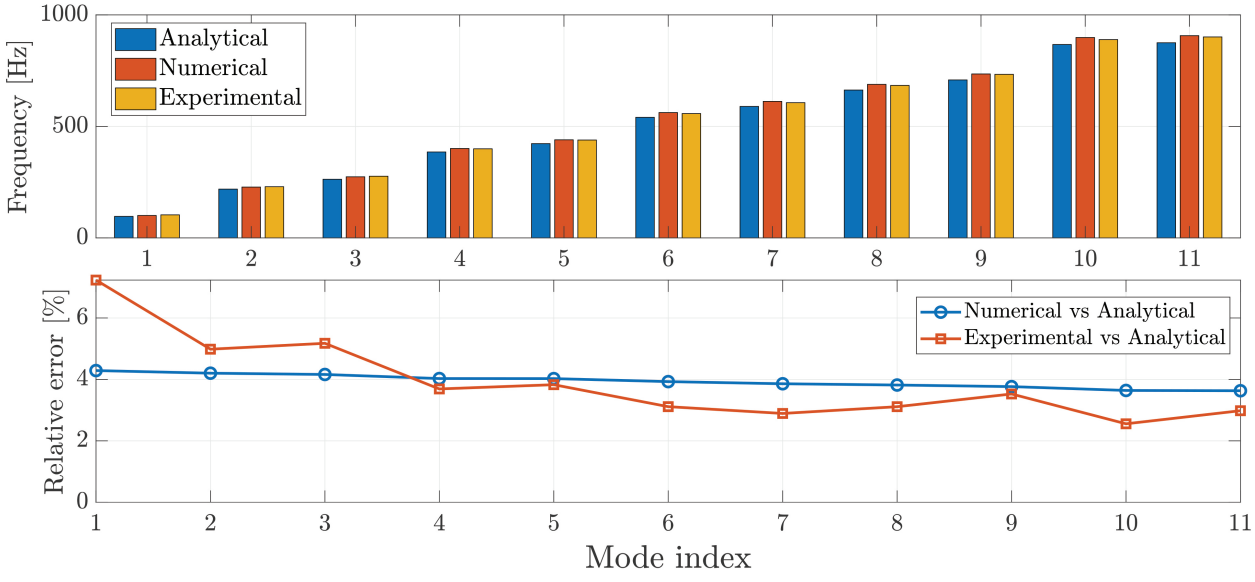

Fig. 3 Comparison of the first eleven natural frequencies from analytical, numerical, and experimental results, with discrepancies below 8% due to the presence of piezoelectric patches not included in the analytical model

Methodology

The proposed detection algorithm is based on the voltage response of the piezoelectric sensors, which is proportional to the average in-plane deformation of the plate. These measurements are used to reconstruct the curvature mode shapes. In this study, up to 11 vibration modes were considered within the 0–1000 Hz frequency range.

To minimize variability, the reconstructed curvature mode shapes were normalized by dividing each sensor's response by that of a reference sensor (Patch 11 in Figure 5), selected to ensure non-zero output across all modes. Subsequently, the

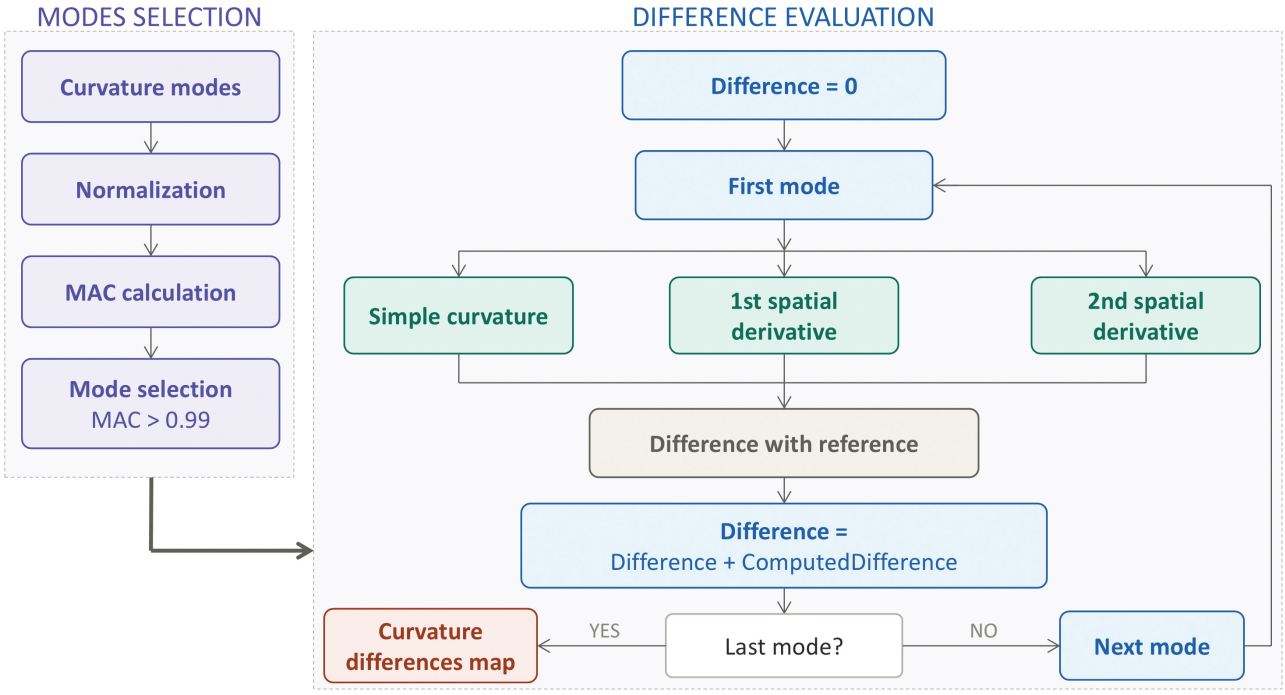

Fig. 4 Block scheme of the algorithm in the three cases when curvature differences are considered and when the first and second derivative of the curvature is employed



Fig. 5 Layout of the 42 piezoelectric transducers mounted on the plate. Transducer 11 was selected as the reference sensor for the normalization procedure, while transducer 35 was used as the actuator during the experimental tests

second spatial derivative of the curvature mode shapes was computed to assess whether higher-order derivatives improve ice localization performance.

For the iced configurations, the extracted modes were compared with those of the ice-free reference case using the Modal Assurance Criterion (MAC). Only modes with a MAC greater than 0.99 were retained for analysis, ensuring that the comparison focused on modes strongly consistent with the reference case. This filtering minimizes the impact of discrepancies and highlights modal shape variations specifically induced by ice accretion. Localization was carried out by summing, for each sensor, the deviations between the reference and current curvature mode shapes across the selected modes.

The methodology was tested on six different ice configurations, varying in size, thickness, and position (Figure 2, Table 1). Case 6 represents full-surface icing, whereas Cases 1–5 correspond to localized patches of different geometries. The overall algorithmic workflow is summarized in Figure 4.

To quantitatively assess the performance of the localization algorithm, an index was introduced that evaluates how well the most significant portion of the localization map overlaps with the true patch. Let $H(x, y)$ denote the localization map normalized in $[0, 1]$, and let Ω be the set of all pixels (or sensor positions). The pixels are first ranked in descending order according to the values of $H(x, y)$, and the subset $\Omega_k \subset \Omega$ containing the top $k\%$ of pixels is selected. The localization index is then defined as

$$T_k = \frac{\left|\Omega_k \cap P\right|}{\left|\Omega_k\right|}, \tag{5}$$

where P denotes the set of pixels belonging to the actual patch.

In this work, the value $k = 10\%$ was chosen, so that the index measures the fraction of the 10% most activated pixels of the map that are located inside the true patch. By construction, $T_k \in [0, 1]$: values close to 1 indicate that the most relevant part of the localization map is concentrated within the actual patch, thus reflecting a good localization, whereas values close to 0 correspond to cases in which the algorithm's strongest response lies outside the true patch. Compared to centroid-based measures, this formulation directly assesses the spatial consistency between the detected high-intensity region and the actual patch, while remaining insensitive to distortions or multiple maxima in the map.

It is worth noting that this index is meaningful for all test cases except for the last one (Case 6), where the ice patch completely covers the plate surface. In such a situation, T_k would trivially take the value 1 regardless of the localization map, and thus provides little information on the actual performance of the algorithm. For this specific case, a qualitative graphical evaluation was therefore preferred.

Numerical Analysis

The numerical investigation was conducted using COMSOL Multiphysics. The aluminum plate and the ice patches were modeled as perfectly bonded, forming a single composite domain. Modal analysis was performed to extract the mode shapes and corresponding voltages at each piezoelectric patch (Figure 6 illustrates representative results for the second and seventh modes).

When the curvature mode shapes were directly employed as input to the localization algorithm, the method was able to provide a satisfactory indication of the iced regions in all six test cases (Figure 7, first column). The identified areas generally overlapped with the actual patch locations, which are indicated in the figures, demonstrating the capability of curvature-based indicators to capture the main alterations induced by the ice. Nonetheless, the resolution of the results was not always optimal: in Case 4, the presence of two distinct patches modified the global response of the plate, leading to a more diffuse localization, while in Case 5, the irregular geometry of the ice layer produced a broader and less defined affected region.

The introduction of spatial derivatives enhanced the performance of the method. The first derivative of curvature (Figure 7, second column) yielded slightly sharper contours of the localized regions compared to curvature alone, but the improvement remained marginal, and in some cases the results were comparable.

By contrast, the second derivative of curvature (Figure 7, third column) produced a significant improvement in localization accuracy. The detected regions appeared more compact and better aligned with the actual patches. For Cases 1–3, where the ice coverage followed simple geometries, the iced areas were reconstructed with higher precision and reduced spatial spreading. In Case 5, the irregular patch was captured more reliably, with the algorithm reproducing its main shape and extension. In Case 6, characterized by uniform ice coverage, the method correctly highlighted the distributed nature of the modification across the entire plate. Table 2 provides the quality index accordingly to Equation 5 for the numerical case.

Experimental Analysis

For the experimental investigation, one of the 42 piezoelectric transducers mounted on the plate was used as an actuator (transducer 35 in Figure 5), while the voltages induced in the remaining 41 sensors were recorded. The transducer selected for excitation was chosen to ensure effective activation of all eleven target modes. The input signal consisted of a linear chirp ranging from 20 to 1000 Hz. The acquisition system provided the frequency response functions (FRFs) of each sensor

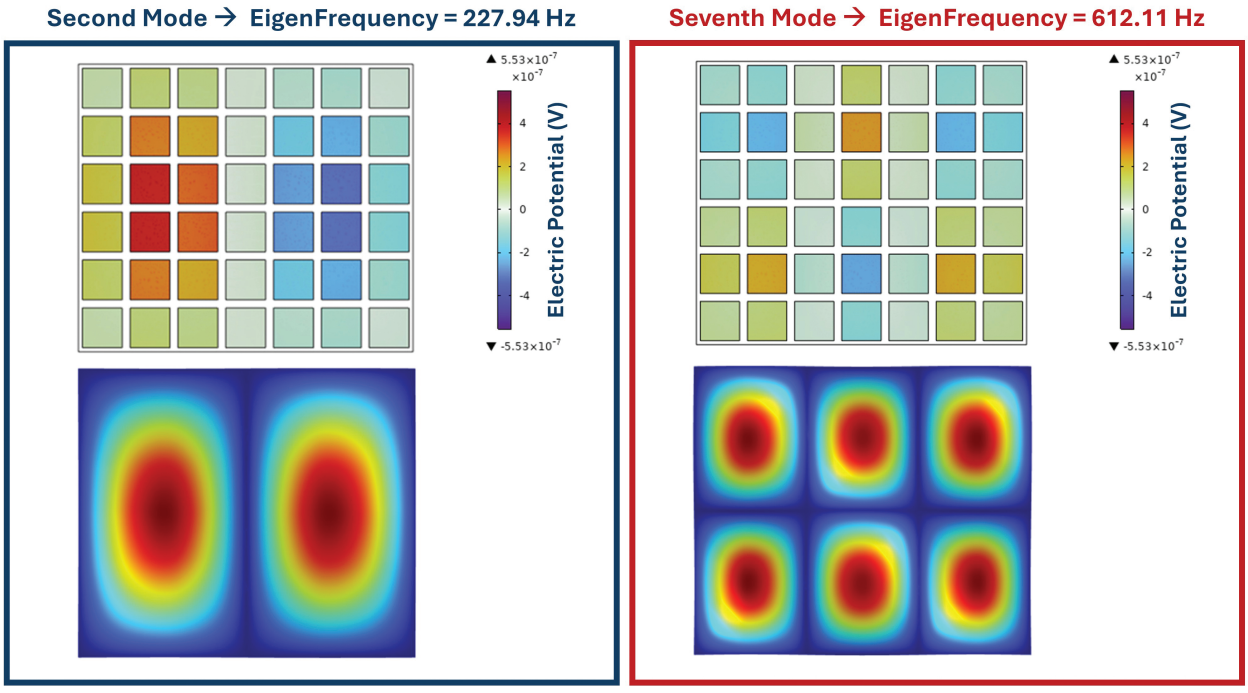

Fig. 6 Voltages measured from each piezoelectric patch for the numerical analysis. In the figure, the cases for the second and seventh modes are reported, in the figures above the voltages, and in the plots below the mode shapes

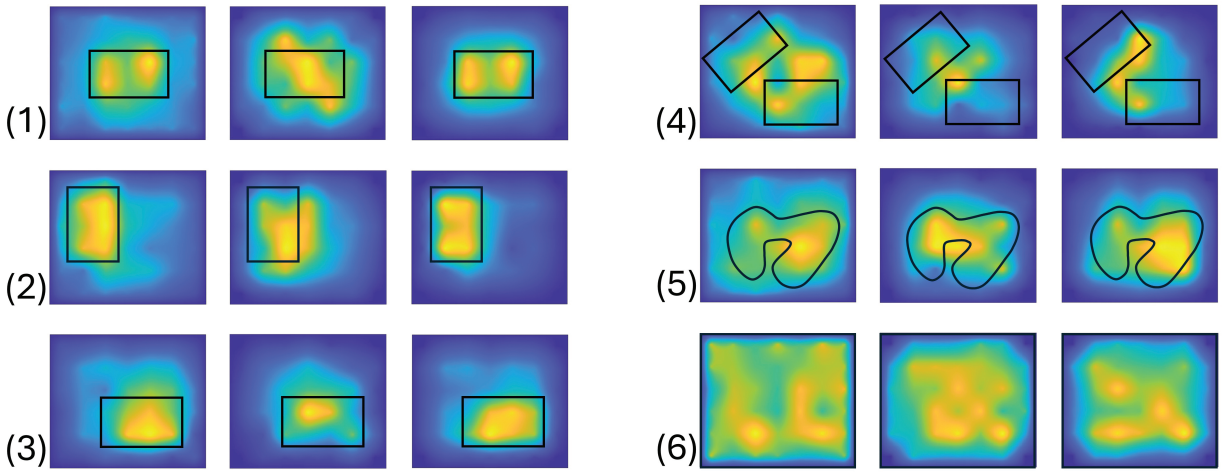

Fig. 7 Ice localization maps for the six analyzed configurations. Each row corresponds to a different ice scenario (Cases 1–6, see Table 1), while the three columns represent the localization algorithm applied to: (left) curvature mode shapes, (center) first spatial derivative of curvature mode shapes, and (right) second spatial derivative of curvature mode shapes. For each case, the actual patch location is indicated in the figures. Warmer colors indicate stronger deviations from the ice-free reference, highlighting the regions most affected by ice accretion

directly. To reduce measurement noise, five repeated acquisitions were performed for each configuration, and the corresponding FRFs were averaged prior to further processing.

The exported FRFs were analyzed using operational modal analysis techniques to estimate the natural frequencies and mode shapes. The Least-Squares Complex Exponential algorithm [22] was employed to extract modal parameters directly from the frequency responses. Since the measured voltages are proportional to structural curvature, the resulting identified mode shapes correspond to curvature mode shapes. Subsequently, point-by-point differences between the reference and

Table 2 Quantitative evaluation of the localization performance for different ice conditions. The reported values correspond to the proposed indices computed from curvature, first derivative, and second derivative features

Ice Condition	1	2	3	4	5	6
Curvature	0.985	0.998	0.929	0.492	0.782	*Graph*
First Derivative	0.787	0.615	0.789	0.504	0.826	*Graph*
Second Derivative	1.000	1.000	1.000	0.556	0.796	*Graph*

modified configurations were computed, and the contributions of the selected modes were summed, following the same procedure adopted in the numerical analysis.

During the campaign, ice was substituted with a paraffin layer, selected for its ease of use. While paraffin has a density comparable to ice, its Young's modulus is significantly lower, being between 40 and 100 times smaller. Accordingly, the tested configurations predominantly reproduce a mass effect rather than the stiffness increase that would result from ice. Six different paraffin patches were prepared, replicating the size and location of the numerical simulations with two exceptions: in Case 5 the patch exhibited a different irregular shape, and in Case 6 it was not possible to obtain a uniform thickness of 5 mm across the entire plate.

Figure 8 reports the experimental results obtained by applying the proposed localization algorithm to the six investigated configurations. Each row corresponds to a different paraffin patch, while the three columns display the outcomes obtained when using the curvature (first column), its first derivative (second column), and its second derivative (third column) as the input field for the algorithm.

A general trend can be observed across all cases. When curvature alone is employed, the localization is possible but relatively diffuse, and the estimated affected regions tend to spread over larger areas than the actual patch. The use of the first derivative of curvature does not improve the localization significantly; in fact, in most cases, the results are comparable to those obtained with curvature.

In contrast, the second derivative of curvature systematically provides clearer and more accurate results. The identified regions are more compact, better aligned with the actual paraffin patches, and less affected by spurious responses outside the damaged zones. This improvement is particularly evident in configurations 1, 2, and 3. In these cases, the second derivative highlights the modifications more sharply, reducing the influence of background variability.

The results reported in Table 3 confirm the numerical findings discussed in the previous section, showing that the second derivative of curvature constitutes the most effective indicator for experimental patch localization.

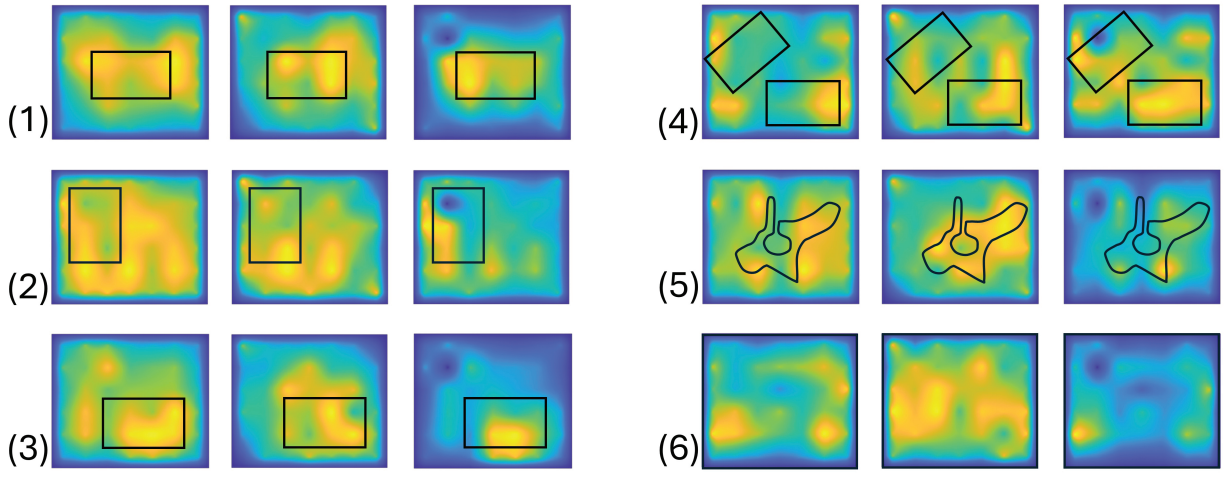

Fig. 8 Patch localization maps for the six analyzed configurations. Each row corresponds to a different scenario (Cases 1–6, see Table 1), while the three columns represent the localization algorithm applied to: (left) curvature mode shapes, (center) first spatial derivative of curvature mode shapes, and (right) second spatial derivative of curvature mode shapes. For each case, the approximate patch location is indicated in the figures. Warmer colors indicate stronger deviations from the reference, highlighting the regions most affected by paraffin accretion

Table 3 Experimental results of the localization performance index for the different conditions of paraffin. For Condition 6, where the patch covers the entire plate surface, the index is not informative and a qualitative graphical evaluation is reported instead

Ice Condition	1	2	3	4	5	6
Curvature	0.617	0.143	0.888	0.510	0.781	*Graph*
First Derivative	0.834	0.211	0.660	0.601	0.794	*Graph*
Second Derivative	0.889	0.789	0.911	0.884	0.713	*Graph*

Conclusion

This work presents a curvature-based approach, reconstructed through a network of piezoelectric sensors, for localizing ice on plate-like structures. Both numerical and experimental analyses have demonstrated that utilizing spatial derivatives of curvature enhances the method's sensitivity. In particular, the second derivative proved to be the most effective indicator, providing more compact, accurate, and robust reconstructions of the iced regions.

However, the use of the second derivative also introduces a significant drawback: it amplifies measurement noise. While this does not undermine the validity of the results obtained under controlled conditions, it limits the direct applicability of the algorithm in operational scenarios characterized by higher levels of disturbance. Therefore, the proposed method appears most suitable for applications where adequate noise control can be ensured, while further developments will be required to improve its robustness in real-world conditions.

Overall, the results confirm the potential of piezoelectric networks as a multifunctional platform for ice monitoring and autonomous management, paving the way for integrated sensing and de-icing solutions.

Acknowledgments This research was funded by the European Union – NextGeneration EU, Mission 4 Component 2 Investment 3.3 CUP B53C23001500004

References

1. Barber, S., Wang, Y., Jafari, S., Chokani, N., and Abhari, R.S. "The impact of ice formation on wind turbine performance and aerodynamics" (2011).
2. Lynch, F.T. and Khodadoust, A. "Effects of ice accretions on aircraft aerodynamics". *Progress in Aerospace Sciences*, 37(8):669–767 (2001).
3. Jarvinen, P. "Aircraft ice detection method". In *45th AIAA Aerospace Sciences Meeting and Exhibit*, page 696 (2007).
4. Wang, Y., Xu, Y., and Huang, Q. "Progress on ultrasonic guided waves de-icing techniques in improving aviation energy efficiency". *Renewable and Sustainable energy reviews*, 79:638–645 (2017).
5. Zhang, X., Zhou, W., and Li, H. "Electromechanical impedance-based ice detection of stay cables with temperature compensation". *Structural Control and Health Monitoring*, 26(9):e2384 (2019).
6. Maio, L., Memmolo, V., Christophel, N., Kohl, S., and Moll, J. "Electromechanical admittance method to monitor ice accretion on a composite plate". *Measurement*, 220:113290 (2023).
7. Wiedemann, J., Meyer, P., Feder, J., Sinapius, M., Riemenschneider, J., and Hühne, C. "Electromechanical deicing of helicopter structures with integrated ice detection by impedance measurement". *Journal of Aerospace Engineering*, 37(1):04023094 (2024).
8. Hongerholt, D.D., Willms, G., and Rose, J.L. "Summary of results from an ultrasonic in-flight wing ice detection system". In *AIP conference proceedings*, volume 615, pages 1023–1028. American Institute of Physics (2002).
9. Cuc, A., Giurgiutiu, V., Joshi, S., and Tidwell, Z. "Structural health monitoring with piezoelectric wafer active sensors for space applications". *AIAA journal*, 45(12):2838–2850 (2007).
10. Giurgiutiu, V., Bao, J., and Zhao, W. "Piezoelectric wafer active sensor embedded ultrasonics in beams and plates". *Experimental mechanics*, 43(4):428–449 (2003).
11. Giurgiutiu, V. "Tuned lamb wave excitation and detection with piezoelectric wafer active sensors for structural health monitoring". *Journal of intelligent material systems and structures*, 16(4):291–305 (2005).
12. Zhang, Y., Zhang, H., XIONG, J., et al. "Analysis method and experimental study of ice accumulation detection signal based on lamb waves". *Chinese Journal Of Aeronautics*, 37(8):388–403 (2024).
13. Pohl, M. "A lamb wave-based icing sensor for aircraft ice detection". In *Proceedings–Int. Workshop on Atmospheric Icing of Structures* (2022).
14. Zhao, X. and Rose, J.L. "Ultrasonic guided wave tomography for ice detection". *Ultrasonics*, 67:212–219 (2016).
15. Gantasala, S., Luneno, J.C., and Aidanpää, J.O. "Influence of icing on the modal behavior of wind turbine blades". *Energies*, 9(11):862 (2016).
16. Tsiapoki, S., Häckell, M.W., Grießmann, T., and Rolfes, R. "Damage and ice detection on wind turbine rotor blades using a three-tier modular structural health monitoring framework". *Structural Health Monitoring*, 17(5):1289–1312 (2018).

17. Pandey, A., Biswas, M., and Samman, M. "Damage detection from changes in curvature mode shapes". *Journal of sound and vibration*, 145(2):321–332 (1991).
18. Wahab, M.A. and De Roeck, G. "Damage detection in bridges using modal curvatures: application to a real damage scenario". *Journal of Sound and vibration*, 226(2):217–235 (1999).
19. Song, Z., Wei, J., and Li, F. "An accurate deicing method by utilizing the piezoelectric materials based on the active mode control theory". *Mechanical Systems and Signal Processing*, 158:107804 (2021).
20. Whalen, T.M. "The behavior of higher order mode shape derivatives in damaged, beam-like structures". *Journal of sound and vibration*, 309(3-5):426–464 (2008).
21. Robin, O., Chazot, J.D., Boulandet, R., Michau, M., Berry, A., and Atalla, N. "A plane and thin panel with representative simply supported boundary conditions for laboratory vibroacoustic tests". *Acta Acustica united with Acustica*, 102(1):170–182 (2016).
22. Brandt, A. *Noise and vibration analysis: signal analysis and experimental procedures*. John Wiley & Sons (2023).

Chapter 7
High-precision Modal Parameter Identification Algorithm Based on QR Decomposition

J. M. Liu and F. Liu

Abstract Modal parameters include modal frequency, damping ratio, modal shapes and participation factors. Traditional modal parameter identification algorithms do not yield the optimal result in least square sense, meaning that the error between the synthesized frequency response function (FRF) and measured FRF is not the least. By optimizing the identified modal parameters, theoretically, the unique modal parameters with the highest fitting accuracy can be obtained despite different modal parameter identification algorithm is used. When the number of modal parameters is large, optimizing all the modes simultaneously requires solving extremely large-scale linear equations, which is time-consuming and impractical in engineering applications. The algorithm proposed in this paper concentrates the parameters of modal frequency, damping ratio and participation factors in the latter part of the optimization equation through QR decomposition. This approach allows for considering all variables during each optimization, only calculating the optimized frequency, damping ratio and participation factors, without needing to solve extremely large-scale linear equations. The optimized modal shapes can be extracted point by point using linear equations from single measurement points' FRF or half power spectra. The proposed algorithm significantly improves computational speed, enabling the rapid acquisition of experimental modal parameters with the highest fitting accuracy.

Keywords Modal testing · High-precision · Modal parameter identification · QR decomposition · Optimization

Introduction

Modal testing is divided Experimental Modal Analysis(EMA) with measurable excitation force and Operational Modal Analysis(OMA) with unmeasurable excitation force. The modal parameters of EMA can be identified by FRF (Frequency domain) or impulse response function (Time domain), while in OMA, it is obtained by half power spectrum (Frequency domain) or by cross-correlation coefficients with positive time delay (Time domain). To identify close modes or to obtain accurate modal shapes for all orders, Multi-Input and Multi-Output (MIMO) experimental methods are often used. There are two types of MIMO in EMA, the first involves multiple excitations (the number of excitation points is equal to the number of reference points), measuring all responses; the second involves multiple fixed responses (the number of response points is equal to the number of reference points), exciting all measurement points. MIMO in OMA involves selecting multiple reference points. Sensors in these reference points should keep in the same position if the number of sensor is not enough to measure all points at one time.

The commonly used parameter identification algorithms in EMA include Eigensystem Realization Algorithm (ERA)[1], the PolyMAX[3] algorithm in frequency domain and the PolyIIR[4] algorithm in time domain Based on the Unified Matrix Polynomial Approach(UMPA)[2]. The commonly used parameter identification algorithms in OMA include Data-Driven Stochastic Subspace Identification (Data_Driver SSI)[5] based on the original data, the SSI(COV)[6] algorithm based on the half-spectrum, the Enhanced Frequency Decomposition (EFDD)[7]algorithm.as well as the PloyMAX algorithm in the frequency domain and the PolyIIR algorithm in the time domain based UMPA. All these algorithms except EFDD require the calculation of a stabilization graph, manual or automatic selection of physical poles to avoid mathematical poles, and

J.M.Liu · F. Liu
China Orient Institute of Noise & Vibration, Beijing 100085, China
e-mail: liujm@coinv.com; liuf@coinv.com

© The Author(s), under exclusive license to River Publishers 2026

Kristin B. Zimmerman, PhD (eds.), *Topics in Modal Analysis & Parameter Identification in Structural Dynamics, 2026, Vol. 8*,
Conference Proceedings of the Society for Experimental Mechanics Series, https://doi.org/10.13052/rp-9788743814191

then to extract the modal shapes of each mode. The obtained modal parameters are not the optimal result in least square sense, meaning that the error between the measured and synthesized FRF(EMA) or half spectrum (OMA) is not in the least.

By optimizing the modal parameters base on the initial result of different algorithms, the best result in least square sense can be obtained. In this way, the result of different algorithms can be unified, the precision of parameters will be greatly improved[8].

Modal parameters include poles (modal frequency and modal damping ratio), with a quantity of twice the total number of modes (including conjugate modes); modal participators, with a quantity of twice the total number of modes multiplied by the number of reference points; and modal shapes, with a quantity of twice the total number of modes multiplied by the number of measurement points.

Optimization algorithms can be divided into three types.

1. Fix modal shapes and participators, optimize to obtain new modal poles. Caculate the participators base on the new poles. Extract modal shapes point by point. Then, proceed to the next optimization cycle. This method can be realized very easily, but the efficiency of optimization is very low and cannot reach the optimal result, often stop at the initial result.
2. fix the modal shapes, optimize to obtain modal participators and the new poles. extract new modal shapes point by point. Then, proceed to the next optimization cycle. This method is easier to implement the algorithm 1 can be realized easily, optimization efficiency is better than method 1, but still can't reach the optimal solution.
3. Optimize all modal parameters simultaneously to obtain the optimized participators, poles and modal shapes. This algorithm can obtain the optimal solution. However, when the product of modal measurement points and the total number of modal order is large, solving extremely large-scale linear equations is required, which is very time consuming, making it impractical.

The algorithm proposed in the paper improves algorithm 3 by optimizing all modal parameters simultaneously. It concentrates the modal poles and participator in the latter part of the optimization equation, performs QR decompose on the linear equations, and firs solves for the optimized modal poles. Then, for each reference points, the optimized modal poles are used to establish equations containing participators and modal shapes, and QR decomposition is performed again to separately obtain the participator corresponding to each reference point. After obtaining the optimized modal poles and participator, the optimized modal shapes can be extracted point by point. Then, proceed to the next optimization cycle. By avoiding solve large dimension linear equations, This approach can significantly improve the computational speed.

Theory

The optimization algorithm has a premise, which is that the current solution is close to the optimal state and all parameters change slightly during the optimization process. Therefore, it is required that the initial solution obtained through the stability diagram includes all physical modal poles without missing any modes.

QR optimization algorithm for modal parameters

For MIMO modal parameters with normalized mass, assuming the number of exciting point is$p$, responding point is q, mode orders is$n$, and the initial solution of the modes is known. For responding point$i$, exciting point(or reference point)j, the theoretical function of FRF(EMA Test)or Half spectrum(OMA Test) is

$$\hat{H}_{ij}(s) = \frac{a_{ij}}{s} + b_{ij} + \sum_{r=1}^{2n} \frac{\phi_r^i L_r^j}{s - s_r} \tag{1}$$

Where the first term of right side of equation (1) is the low frequency garbage term, which can be seen as the influence of 0Hz, $a_{ij}$is a real number; the second term is the high frequency garbage term, which can be seen as the influence of$+\infty$.$b_{ij}$is a real number. ϕ_r^i,L_r^j and s_r are complex numbers, $\phi_r^i$is the modal shape of point $i$and mode order$r$,L_r^j is the participator of reference point $j$and mode order r,s_r is the pole of mode order$r$. There are n orders as well as corresponding conjugate orders. For OMA test, if test is measured by multiple groups, L_r^j is different in each group. To extract vibration shape, need to compute by group.

Taking the derivative of equation (1), we get:

$$H_{ij}(s) - \hat{H}_{ij}(s) = \frac{\Delta a_{ij}}{s} + \Delta b_{ij} + \sum_{r=1}^{2n} \frac{L_r^j}{s - s_r} \Delta \phi_r^i + \sum_{r=1}^{2n} \frac{\phi_r^i}{s - s_r} \Delta L_r^j + \sum_{r=1}^{2n} \frac{\phi_r^i L_r^j}{(s - s_r)^2} \Delta s_r \tag{2}$$

Where $H_{ij}(s)$ is obtained from actual measurements.
Define:

$$\sigma_r^j(s) = \frac{L_r^j}{s - s_r} \tag{3}$$

$$\psi_r^i(s) = \frac{\phi_r^i}{s - s_r} \tag{4}$$

Then we have

$$\begin{bmatrix} \frac{1}{s} & 1 & A_j & B_i & C_{ij} \end{bmatrix} \begin{bmatrix} \Delta a_{ij} \\ \Delta b_{ij} \\ \Delta \hat{\phi}_i \\ \Delta \hat{L}_j \\ \Delta \hat{\mathrm{s}} \end{bmatrix} = [\Delta H_{ij}(s)] \tag{5}$$

$$A_j = \begin{bmatrix} \sigma_1^j(s) & \sigma_2^j(s) & \cdots & \sigma_{2n}^j(s) \end{bmatrix} \tag{6}$$

$$B_i = \begin{bmatrix} \psi_1^i(s) & \psi_2^i(s) & \cdots & \psi_{2n}^i(s) \end{bmatrix} \tag{7}$$

$$C_{ij} = \begin{bmatrix} \psi_1^i(s)\sigma_1^j(s) & \psi_2^i(s)\sigma_2^j(s) & \cdots & \psi_{2n}^i(s)\sigma_{2n}^j(s) \end{bmatrix} \tag{8}$$

$$\Delta \hat{\phi}_i = \begin{bmatrix} \Delta \phi_1^i \\ \Delta \phi_2^i \\ \vdots \\ \Delta \phi_{2\mathrm{n}}^i \end{bmatrix} \tag{9}$$

$$\Delta \hat{L}_j = \begin{bmatrix} \Delta L_1^j \\ \Delta L_2^j \\ \vdots \\ \Delta L_{2\mathrm{n}}^j \end{bmatrix} \tag{10}$$

$$\Delta \hat{s} = \begin{bmatrix} \Delta s_1 \\ \Delta s_2 \\ \vdots \\ \Delta s_{2n} \end{bmatrix} \tag{11}$$

Equation (5) can be written in the form of a real coefficient equation as:

$$\begin{bmatrix} 0 & 1 & A1_j^{re} & -A2_j^{im} & B1_i^{re} & -B2_i^{im} & C1_{ij}^{re} & -C2_{ij}^{im} \\ \frac{-1}{\omega} & 0 & A1_j^{im} & A2_j^{re} & B1_i^{im} & B2_i^{re} & C1_{ij}^{im} & C2_{ij}^{re} \end{bmatrix} \begin{bmatrix} \Delta a_{ij} \\ \Delta b_{ij} \\ \Delta \hat{\phi}_i^{re} \\ \Delta \hat{\phi}_i^{im} \\ \Delta \hat{L}_j^{re} \\ \Delta \hat{L}_j^{im} \\ \Delta \hat{s}^{re} \\ \Delta \hat{s}^{im} \end{bmatrix} = \begin{bmatrix} \Delta H_{ij}^{re}(j\omega) \\ \Delta H_{ij}^{im}(j\omega) \end{bmatrix} \tag{12}$$

For n modes, their poles, participators and modal shapes all appear in conjugate forms. Equation (12) can be simplified to solve for the optimization parameters of modes by making slight adjustments to the matrix in equation (12).

$$A1_j^{re} = \begin{bmatrix} rea_1^j(s) & rea_2^j(s) & \cdots & rea_n^j(s) \end{bmatrix},$$

Where $rea_{\mathrm{r}}^{j}(s)$ is the real part of $\frac{L_r^j}{s-s_r}+\frac{(L_r^j)^*}{s-s_r^*}$

$$A1_j^{im}=\left[\begin{array}{cccc} ima_1^j(s) & ima_2^j(s) & \cdots & ima_n^j(s) \end{array}\right],$$

Where $\mathrm{i}ma_{\mathrm{r}}^{j}(s)$ is the imaginary part of $\frac{L_r^j}{s-s_r}+\frac{(L_r^j)^*}{s-s_r^*}$

$$B1_i^{re}=\left[\begin{array}{cccc} reb_1^i(s) & reb_2^i(s) & \cdots & reb_n^j(s) \end{array}\right],$$

Where $reb_{\mathrm{r}}^{i}(s)$ is the real part of $\frac{\phi_r^i}{s-s_r}+\frac{(\phi_r^i)^*}{s-s_r^*}$

$$B1_i^{im}=\left[\begin{array}{cccc} imb_1^i(s) & imb_2^i(s) & \cdots & imb_n^i(s) \end{array}\right],$$

Where $imb_{\mathrm{r}}^{j}(s)$ is the imaginary part of $\frac{\phi_r^i}{s-s_r}+\frac{(\phi_r^i)^*}{s-s_r^*}$

$$C1_{ij}^{re}=\left[\begin{array}{cccc} rec_1^{ij}(s) & rec_2^{ij}(s) & \cdots & rec_n^{ij}(s) \end{array}\right],$$

Where $rec_{\mathrm{r}}^{ij}(s)$ is the real part of $\frac{\phi_r^i L_r^j}{(s-s_r)^2}+\frac{(\phi_r^i)^*(L_r^j)^*}{(s-s_r^*)^2}$

$$C1_{ij}^{im}=\left[\begin{array}{cccc} imc_1^{ij}(s) & imc_2^{ij}(s) & \cdots & imc_n^{ij}(s) \end{array}\right],$$

Where $imc_{\mathrm{r}}^{ij}(s)$ is the imaginary part of $\frac{\phi_r^i L_r^j}{(s-s_r)^2}+\frac{(\phi_r^i)^*(L_r^j)^*}{(s-s_r^*)^2}$

Each element of $A2_j^{re}$ is the real part of $\frac{L_r^j}{s-s_r}-\frac{(L_r^j)^*}{s-s_r^*}$. The other matrix with 2 is similar, the operation sign from "+" change to "-".

Equation (12) simplify as

$$[X(j\omega)]_{2\times(2+6n)}\,\theta_{(2+6n)\times 1}=[Y(j\omega)]_{2\times 1} \tag{13}$$

Equation (13) holds for spectral lines of N, Equation (13) is expanded to

$$\left[\begin{array}{c} X(j\omega_1) \\ X(j\omega_2) \\ \vdots \\ X(j\omega_N) \end{array}\right]_{2N\times(2+6n)} \theta_{(2+6n)\times 1}=\left[\begin{array}{c} Y(j\omega_1) \\ Y(j\omega_2) \\ \vdots \\ Y(j\omega_N) \end{array}\right]_{2N\times 1} \tag{14}$$

Perform QR decomposition on the coefficient matrix of the left side of equation (14), we get:

$$\left[\begin{array}{c} X(j\omega_1) \\ X(j\omega_2) \\ \vdots \\ X(j\omega_N) \end{array}\right]=[Q_{ij}]_{2N\times 2N}\left[\begin{array}{cc} R_{11}^{ij} & R_{12}^{ij} \\ 0 & R_{22}^{ij} \\ 0 & 0 \end{array}\right]_{2N\times(2+6n)} \tag{15}$$

The decomposition R is illustrated in figure 1

Dimension of $[R_{22}^{ij}]$ is$2n\times 2n$, $[R_{11}^{ij}]$ is $(2+4n)\times(2+4n)$, $[R_{12}^{ij}]$ is $(2+4n)\times 2n$

Substitute (15) into (14) to obtain:

$$\left[\begin{array}{cc} R_{11}^{ij} & R_{12}^{ij} \\ 0 & R_{22}^{ij} \\ 0 & 0 \end{array}\right]\left[\begin{array}{c} \vdots \\ \Delta\hat{s}^{re} \\ \Delta\hat{s}^{im} \end{array}\right]=[Q_{ij}]^T\left[\begin{array}{c} Y(j\omega_1) \\ Y(j\omega_2) \\ \vdots \\ Y(j\omega_N) \end{array}\right]=\left[\begin{array}{c} S_{ij} \\ P_{ij} \\ T_{ij} \end{array}\right] \tag{16}$$

We can get:

$$[R_{22}^{ij}]\left[\begin{array}{c} \Delta\hat{s}^{re} \\ \Delta\hat{s}^{im} \end{array}\right]=P_{ij} \tag{17}$$

P_{ij} is the row of $3+4n$ to $2+6n$ in equation (16).

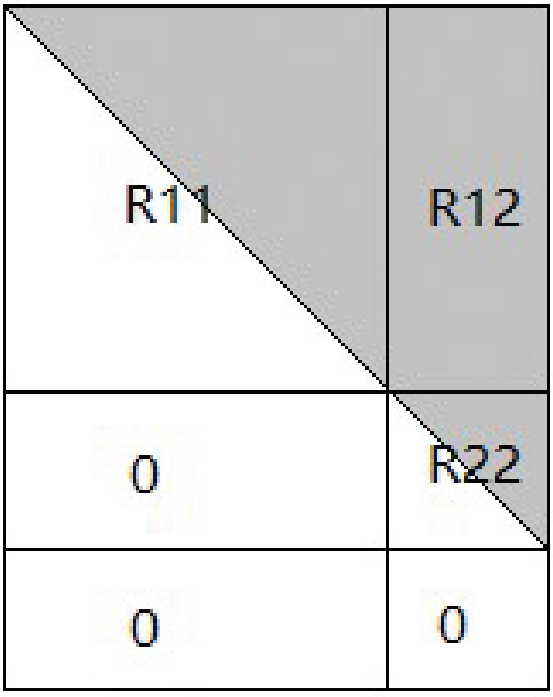

Fig. 1 QR decomposition illustration

Each excitation point(reference point) corresponds to q FRF or half spectrum curves for all response points. There are p excitation points, equation (17) is expanded to:

$$\begin{bmatrix} R_{22}^{11} \\ R_{22}^{21} \\ \vdots \\ R_{22}^{qp} \end{bmatrix}_{2pqn\times 2n} \begin{bmatrix} \Delta\hat{s}^{re} \\ \Delta\hat{s}^{im} \end{bmatrix} = \begin{bmatrix} P_{11} \\ P_{21} \\ \vdots \\ P_{qp} \end{bmatrix} \tag{18}$$

Thus

$$\left(\sum_{i=1}^{q}\sum_{j=1}^{p}\left[R_{22}^{ij}\right]^T\left[R_{22}^{ij}\right]\right)\begin{bmatrix} \Delta\hat{s}^{re} \\ \Delta\hat{s}^{im} \end{bmatrix} = \sum_{i=1}^{q}\sum_{j=1}^{p}\left[R_{22}^{ij}\right]^T[P_{ij}] \tag{19}$$

The least squares solution of the pole correction amount can be obtained from equation (19). After the pole correction is known, the calculation of the modal participator correction amount requires all curves corresponding to the same exciting point.

From equation (2), get

$$\frac{\Delta a_{ij}}{s} + \Delta b_{ij} + \sum_{r=1}^{2n}\frac{L_r^j}{s-s_r}\Delta\phi_r^i + \sum_{r=1}^{2n}\frac{\phi_r^i}{s-s_r}\Delta L_r^j = H_{ij}(s) - \hat{H}_{ij}(s) - \sum_{r=1}^{2n}\frac{\phi_r^i L_r^j}{(s-s_r)^2}\Delta s_r \tag{20}$$

(12) is rewritten as

$$\begin{bmatrix} 0 & 1 & A_j^{re} & -A_j^{im} & B_i^{re} & -B_i^{im} \\ \frac{-1}{\omega} & 0 & A_j^{im} & A_j^{re} & B_i^{im} & B_i^{re} \end{bmatrix}\begin{bmatrix} \Delta a_{ij} \\ \Delta b_{ij} \\ \Delta\hat{\phi}_i^{re} \\ \Delta\hat{\phi}_i^{im} \\ \Delta\hat{L}_j^{re} \\ \Delta\hat{L}_j^{im} \end{bmatrix} = \begin{bmatrix} J_{ij}^{re}(j\omega) \\ J_{ij}^{im}(j\omega) \end{bmatrix} \tag{21}$$

Simplify as

$$[V(j\omega)]_{2\times(2+4n)}\,\theta_{(2+4n)\times 1} = [J(j\omega)]_{2\times 1} \tag{22}$$

Equation (22) holds for spectral lines of N, equation (22) is expanded to:

$$\begin{bmatrix} V(j\omega_1) \\ V(j\omega_2) \\ \vdots \\ V(j\omega_N) \end{bmatrix}_{2N\times(2+4n)} \theta_{(2+4n)\times 1} = \begin{bmatrix} J(j\omega_1) \\ J(j\omega_2) \\ \vdots \\ J(j\omega_N) \end{bmatrix}_{2N\times 1} \tag{23}$$

Perform QR decomposition on the coefficient matrix of the left side of equation (23) to obtain:

$$\begin{bmatrix} V(j\omega_1) \\ V(j\omega_2) \\ \vdots \\ V(j\omega_N) \end{bmatrix} = [Q_{ij}]_{2N\times 2N} \begin{bmatrix} R_{11}^{ij} & R_{12}^{ij} \\ 0 & R_{22}^{ij} \\ 0 & 0 \end{bmatrix}_{2N\times(2+4n)} \tag{24}$$

The dimension of $[R_{22}^{ij}]$ is $2n \times 2n$, $[R_{11}^{ij}]$ is $(2+2n)\times(2+2n)$, $[R_{12}^{ij}]$ is $(2+2n)\times 2n$
Substitute into (23) to obtain:

$$\begin{bmatrix} R_{11}^{ij} & R_{12}^{ij} \\ 0 & R_{22}^{ij} \\ 0 & 0 \end{bmatrix} \begin{bmatrix} \vdots \\ \Delta\hat{L}_j^{re} \\ \Delta\hat{L}_j^{re} \end{bmatrix} = [Q_{ij}]^T \begin{bmatrix} J(j\omega_1) \\ J(j\omega_2) \\ \vdots \\ J(j\omega_N) \end{bmatrix} = \begin{bmatrix} S_{ij} \\ P_{ij} \\ T_{ij} \end{bmatrix} \tag{25}$$

We can get:

$$[R_{22}^{ij}] \begin{bmatrix} \Delta\hat{L}_j^{re} \\ \Delta\hat{L}_j^{re} \end{bmatrix} = P_{ij} \tag{26}$$

P_{ij} is the row of $3+2n$ to $2+4n$ in equation (25)
For each exciting point, there are q curves, equation (24) is expanded to:

$$\begin{bmatrix} R_{22}^{1j} \\ R_{22}^{2j} \\ \vdots \\ R_{22}^{qj} \end{bmatrix}_{2qn\times 2n} \begin{bmatrix} \Delta\hat{L}_j^{re} \\ \Delta\hat{L}_j^{re} \end{bmatrix} = \begin{bmatrix} P_{1j} \\ P_{2j} \\ \vdots \\ P_{qj} \end{bmatrix} \tag{27}$$

Therefore, we have

$$\left(\sum_{i=1}^{q} \left[R_{22}^{ij}\right]^T \left[R_{22}^{ij}\right]\right) \begin{bmatrix} \Delta\hat{L}_j^{re} \\ \Delta\hat{L}_j^{re} \end{bmatrix} = \sum_{i=1}^{q} \left[R_{22}^{ij}\right]^T [P_{ij}] \tag{28}$$

The least squares solution of the participator correction amount for the excitation point j can be obtained from equation (28).

After obtaining the optimized modal frequencies, damping ratios and participators, modal shapes can be extracted point by point, considering the influence of high frequency and low frequency garbage responses.

Finally, the optimization algorithm of parameters of MIMO modal test is surmised as bellow:

1. In each optimization process, modal frequencies, damping ratios, participators and modal shape should be optimized at the same time. The influence of low and high frequency garbage terms need to be considered.
2. To obtain the correction amount of modal frequencies and damping ratios, all curves should be considered. A single spectral line equation is constructed according to equation (12),and multiple spectral line equations are constructed through equation (14). After QR decomposition, we get the R matrix illustrated as figure 1, from which we can obtain equation (17) containing only the modal pole correction amount. Considering all curves, equation (18) is obtained, the optimized poles will be get in least square meaning.

3. To obtain the correction amount of modal participators, all curves corresponding to same excitation point are required. Equation (23) is obtained from equation (22), and equation (25) is obtained from the same excitation point corresponding to all response point curves. Equation (27) is extended using all response point curves, and the least squares method is used to obtain the correction amount of the participator.
4. Extract modal shapes point by point, considering the influence of low and high frequency garbage terms.
5. Caculate the fitting error coefficient to decide whether to continue the next loop of optimization.

Application

A MIMO test of a car brake disc was conducted to verify the optimization algorithm. The brake disc is shown as figure 2.

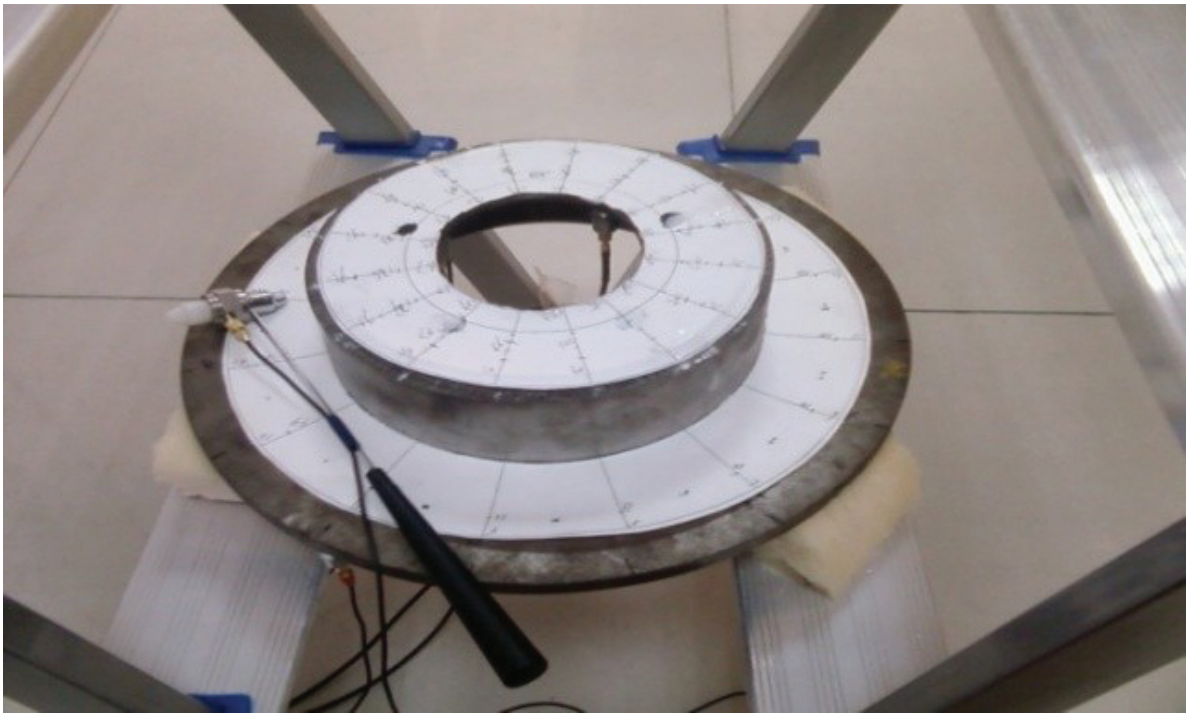

Fig. 2 The break disc of a car

The size of the break disc is as follows:

Outside diameter: R = 15cm, Inside diameter: R = 9cm, Innermost inner diameter R = 4cm, Height: 6cm, Bottom thickness: 1cm, Wall thickness: 0.7cm, Top thickness: 0.5cm. There are 5 evenly spaced small holes and one small hole near the edge on the top. Its mass is 5.18 kg.

A total of 160 measurement points were set, and four piezoelectric accelerometer weighing 8 grams were placed at point 1,7,15 and 22. By moving the excitation point with a hammer. 4 groups of FRFs with 8193 spectral lines are obtained for MIMO modal analysis. The analysis frequency is 6400Hz.

The initial solution was obtained by PolyIIR algorithm, with a total of 32 orders. The last two modes are used to ensure the stability and convergence of the optimization calculation process within the entire frequency band.

Three algorithms were used for Optimization. Algorithm 1 can't proceed, the initial result is the best result. Algorithm 2 reached the optimal result after 7 optimizations. Algorithm 3 can be optimized hundreds of times, but its optimization efficiency decreases evidently. The first 19 optimization data were taken to compare with algorithm 2. The optimization efficiency of different algorithm is illustrated in figure 3.

In the figure 3, the fitting error is the ratio of total root of mean square of error spectrum to measured spectrum.

The result of first loop of algorithm 3 is near the optimal result of algorithm 2, the result of second loop of algorithm 3 is better than the optimal result of algorithm 2.

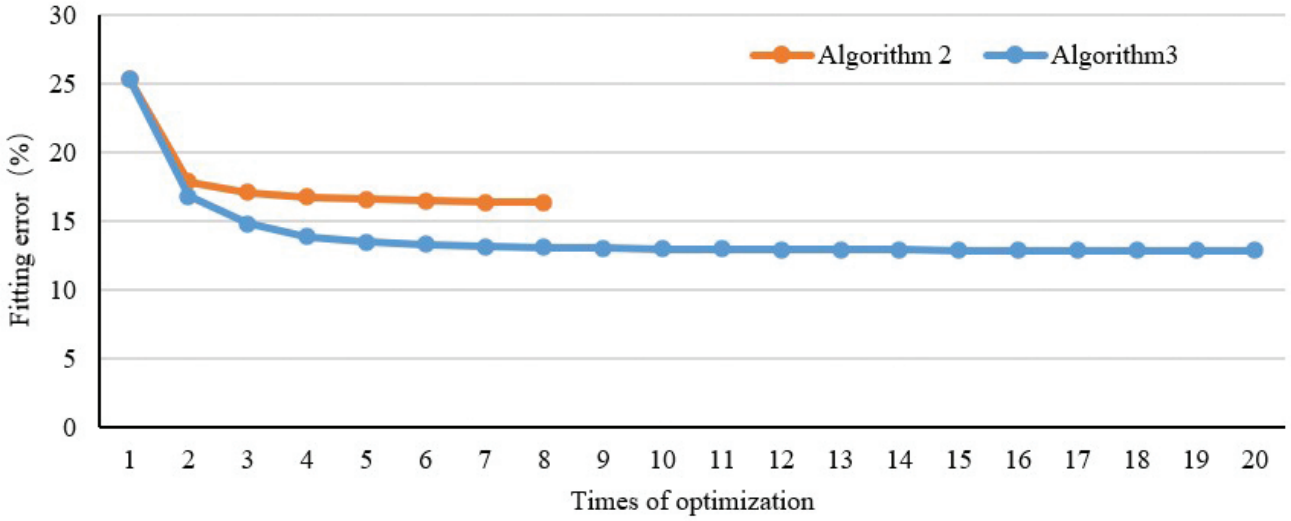

Fig. 3 Optimization efficiency of different algorithm

The foremost 30 modal shapes before optimization are illustrated in figure 4. The modal shapes after optimization by algorithm 2 are shown in figure 5. The modal shapes after optimization by algorithm 3 are shown in figure 6.

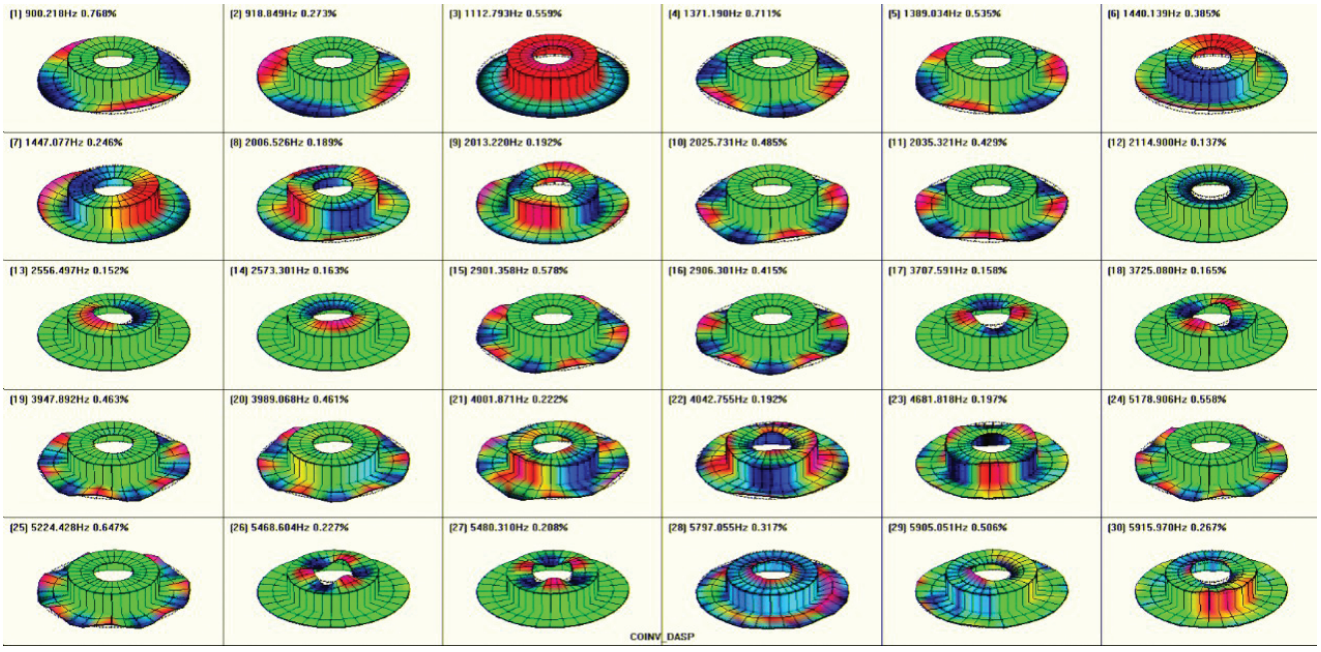

Fig. 4 Modal shapes before optimization

The modal frequencies, damping ratios and fitting errors before optimization and after optimization are listed in table 1.

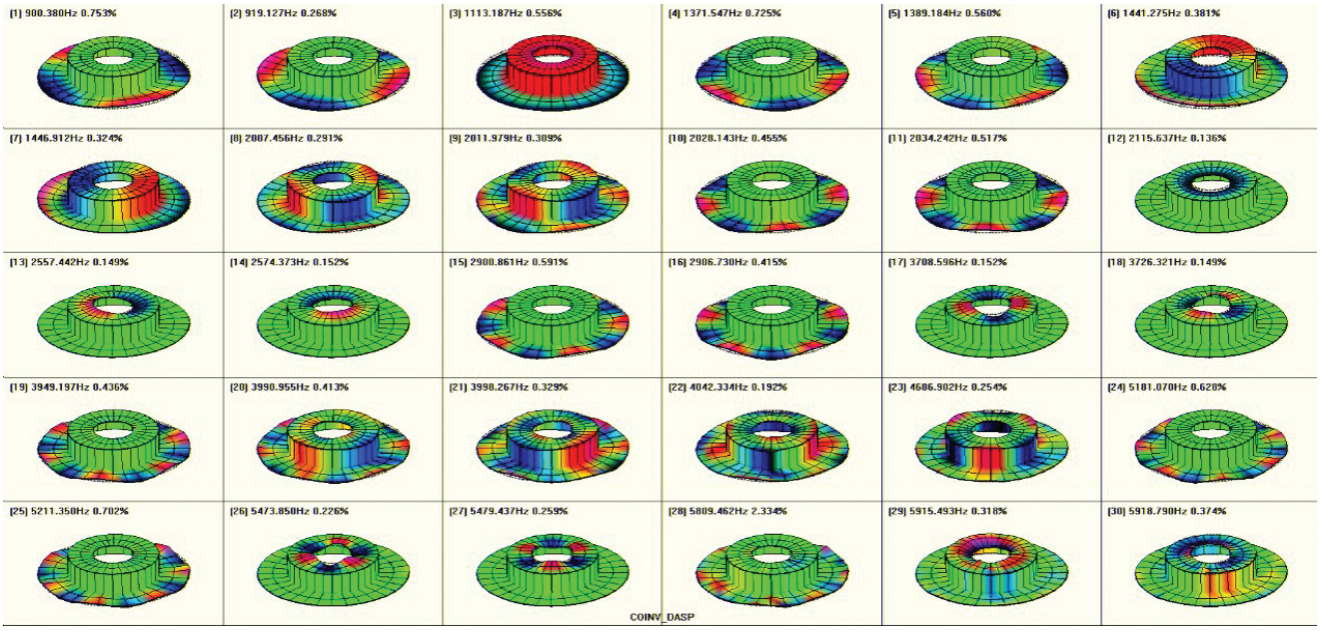

Fig. 5 Modal shapes optimized by algorithm 2

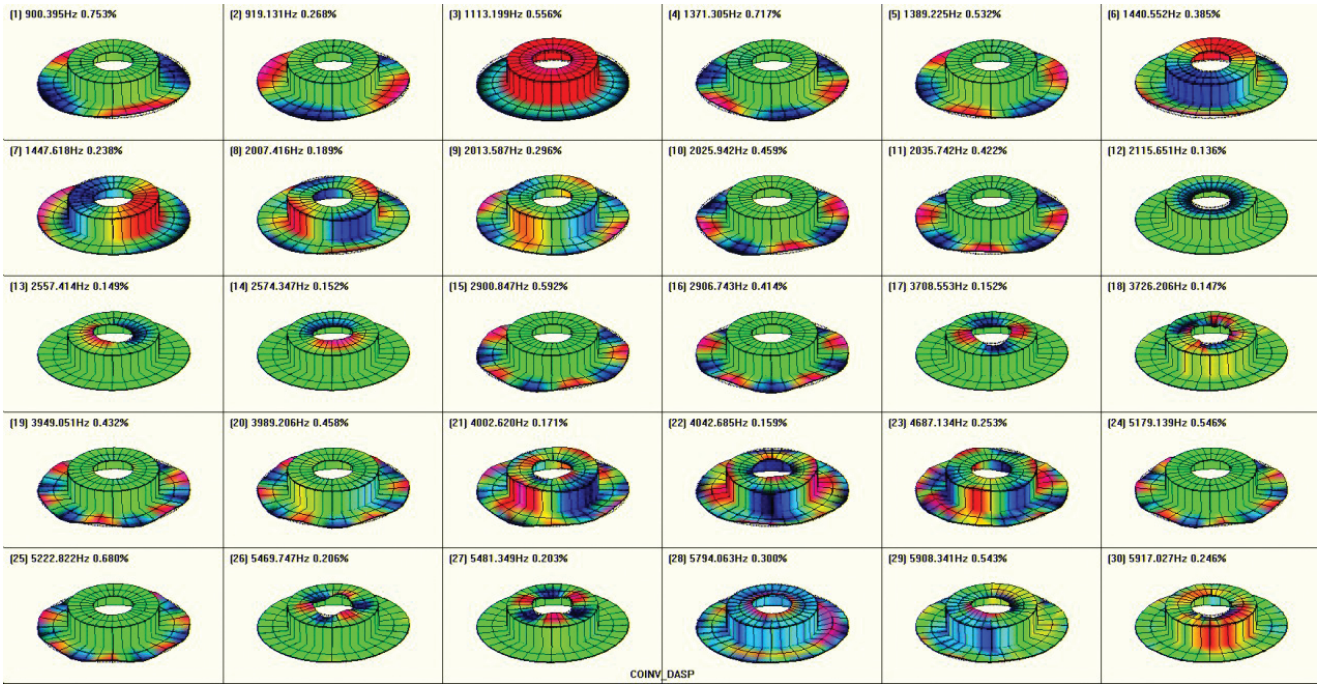

Fig. 6 Modal shapes optimized by algorithm 3

Discussion

Using the identified modal parameters as the initial solution and performing optimization can obtain the optimal solution that can best matches the synthesized FRF or half spectrum with the measured results in the least square sense. Optimization can unify the result of different parameter identification algorithms, and also can improve the accuracy of parameter identification. However, all modal frequencies, damping ratios, participators and modal shapes need to be optimized at the same time. If the number of measuring points and excitation points (EMA) or reference points (OMA) in MIMO test is large, extremely

Table 1 Fitting error comparison before and after optimization

Method	Initial Result		Algorithm 2		Proposed algorithm	
No.	Frequency(Hz)	Damping ratio(%)	Frequency(Hz)	Damping ratio(%)	Frequency(Hz)	Damping ratio(%)
1	900.218	0.273	900.380	0.753	900.395	0.753
2	918.849	0.559	919.127	0.268	919.131	0.268
3	1112.793	0.711	1113.187	0.556	1113.199	0.556
4	1371.190	0.535	1371.547	0.725	1371.305	0.716
5	1389.034	0.385	1389.184	0.560	1389.225	0.532
6	1440.139	0.246	1441.275	0.381	1440.552	0.384
7	1447.077	0.189	1446.912	0.324	1447.618	0.238
8	2006.526	0.192	2007.456	0.291	2007.416	0.189
9	2013.220	0.485	2011.979	0.309	2013.587	0.296
10	2025.731	0.429	2028.143	0.455	2025.942	0.459
11	2035.321	0.137	2034.242	0.517	2035.742	0.422
12	2114.900	0.152	2115.637	0.136	2115.651	0.136
13	2556.497	0.163	2557.442	0.149	2557.414	0.149
14	2573.301	0.578	2574.373	0.152	2574.347	0.152
15	2901.358	0.415	2900.861	0.591	2900.847	0.592
16	2906.301	0.158	2906.730	0.415	2906.743	0.414
17	3707.591	0.165	3708.596	0.152	3708.553	0.152
18	3725.080	0.463	3726.321	0.149	3726.206	0.147
19	3947.892	0.461	3949.197	0.435	3949.051	0.432
20	3989.068	0.222	3990.955	0.413	3989.206	0.457
21	4001.871	0.192	3998.267	0.329	4002.620	0.171
22	4042.755	0.197	4042.334	0.192	4042.685	0.159
23	4681.818	0.558	4686.902	0.254	4687.134	0.253
24	5178.906	0.647	5181.070	0.628	5179.139	0.547
25	5224.428	0.227	5211.350	0.702	5222.822	0.680
26	5468.604	0.208	5473.850	0.226	5469.747	0.206
27	5480.310	0.317	5479.437	0.259	5481.349	0.203
28	5797.055	0.506	5809.462	2.334	5794.063	0.300
29	5905.051	0.267	5915.493	0.318	5908.341	0.543
30	5915.970	0.655	5918.790	0.374	5917.027	0.246
31	6111.458	1.262	6258.083	2.836	6270.213	2.682
32	6164.628	0.273	6299.032	2.708	6292.603	2.790
Fitting error(%)	25.3953		16.3522		12.8469	

large-scale linear equations need to be solved in each loop of optimization, resulting in a long calculation time and making it impractical.

The optimization algorithm based on QR decomposition proposed in this paper first performs QR decomposition on the error data of each point separately, placing modal frequencies and damping ratios at the last part of the equation. Then all the data are combined into equation containing only modal frequency and damping ratio, the optimized modal frequencies and damping ratios are obtained using least squares method. Then, optimized participator can be solved with all curves of same excitation points or reference point, with similar QR decomposition method. The optimized modal shapes can be extract point by point with optimized poles and participators. The proposed optimization algorithm improves the optimization speed by hundreds or thousands of times for large number of measuring points in MIMO test with high orders, which make the optimization algorithm practical in engineering.

The feasibility of the new algorithm was verified with an engineering example, In the example of break disc modal test, the fitting error was reduced from 25.3953% to 12.8469%. All modal shapes after optimization are in accordance with the initial results.

References

1. Juang, J.-N., and Pappa, R.S. An Eigensystem Realization Algorithm for Modal Parameter Identification and Mode Reduction, Journal of Guidance, Control, and Dynamics, Vol 8, No. 1, 1985, pp 620-627

2. Allemang, R J, Brown, DL, and Fladung, W, Modal Parameter Estimation: A Unified Matrix Polynomial Approach, Proc. of the 12th IMAC,1994, pp. 501-514.
3. Bart Peeters, Patrick Guillaume, Herman Van der Auweraer, etc, Automotive and aerospace applications of the PolyMAX modal parameter estimation method. Proc. of 22th IMAC, 2004
4. J. M. Liu, S. W. Dong, M. Ying, S. Shen.Dynamic Parameters Identification Technology in Bridge Health Monitoring, Proceeding of the 14th ASIA PACIFIC VIBRATION CONFERENCE, 2011, Dec. HongKong
5. . van Overschee P, de Moor B. Subspace identification for linear systems: theory-implementation-applications[M]. Dordrecht, Netherlands: Kluwer Academic Publishers, 1996: 15−101.
6. B. PEETERS AND G. DE ROECK. Stochastic system identification for operational modal analysis: a review. ASME Journal of Dynamic Systems, Measurement, and Control, 123(4):659-667, 2001.
7. R.Brincker, L.Zhang, P.Andersen, Modal identification from ambient responses using frequency domain decomposition, Proceedings of the 18th IMAC, 2000
8. J. M. Liu, S. Shen, M. Ying and S. W. Dong, The Optimization and Autonomous Identification of Modal Parameters, Modal Analysis Topics, Volume 3,Conference Proceedings of the Society for Experimental Mechanics Series, 2011, Volume 6, 203-214.

Chapter 8
Expanding the Versatility of Resonant Ultrasound Spectroscopy

Andres Garcia, Kayleigh Hanlon, Matthew Luci, Mentors: Paul Geimer, Mathew Hayne, and Georgios Koutsakis

Abstract Resonant Ultrasound Spectroscopy (RUS) is used for the experimental characterization of materials. This method is traditionally performed in a free vibrating regime which requires that parts are removed from production which increases labor cost and analysis time. This project aims to expand RUS to accommodate non-ideal experimental boundary conditions. By integrating Finite Element Analysis (FEA) with RUS, we seek to explore the possibility of extracting accurate elastic property measurements of metallic samples that are clamped or otherwise constrained. Our experimental methods involve comparing the extracted material properties from freely vibrating metallic samples with those from constrained samples to determine the limitations of current RUS data extraction methods. While our team successfully extracted accurate material properties for freely vibrating samples, we encountered challenges with constrained samples due to RUS's limitations in handling transient terms and complex boundary conditions. Despite this setback, we gained valuable insights into the effects of boundary conditions, including damping produced at the contact interface and frequency shifts. Our results reveal the current limitations of RUS in scenarios involving constrained samples and highlight the need for further research and algorithm development. These advancements are necessary to overcome the existing constraints and enhance RUS's capabilities for more diverse experimental conditions.

Keywords Resonant ultrasound spectroscopy (RUS) · Acoustic excitation · Modal analysis · Finite element analysis (FEA) · Nondestructive testing · Boundary conditions

Introduction

RUS is a non-destructive testing method used to determine the mechanical properties of materials. It works by actively exciting a sample and measuring the natural resonance frequencies at which it vibrates. Researchers can then work backwards (via an "inversion" problem) to determine the material's elastic properties.

Figure 1 provides a detailed illustration of the typical RUS workflow [1]. Table 1 outlines fundamental RUS characteristics, while our research focused on modifications to boundary conditions, frequency spectra, and mode shapes. Traditional

Andres Garcia
Texas A&M University, College Station, TX 77843
e-mail: andresgar@lanl.gov

Kayleigh Hanlon
University of Illinois Urbana-Champaign, Urbana, IL 61801
e-mail: khanlon@lanl.gov

Matthew Luci
Rose-Hulman Institute of Technology, Terre Haute, IN 47803
e-mail: luci.m@lanl.gov

Paul Geimer · Mathew Hayne
Los Alamos National Laboratory, Los Alamos, NM 87545
e-mails: pgeimer@lanl.gov, mhayne@lanl.gov

Georgios Koutsakis
University of New Mexico, Albuquerque, NM 87131
e-mail: kousakis@unm.edu

© The Author(s), under exclusive license to River Publishers 2026

Kristin B. Zimmerman, PhD (eds.), *Topics in Modal Analysis & Parameter Identification in Structural Dynamics, 2026, Vol. 8*,
Conference Proceedings of the Society for Experimental Mechanics Series, https://doi.org/10.13052/rp-9788743814191

RUS assumes the sample is freely vibrating and a simple geometry that is precisely shaped, but this limits what types of samples can be tested. To overcome this, researchers integrate FEA along with RUS. FEA helps simulate vibrations for samples with more complex shapes or boundary conditions, like partial constraints or supports. This combined method improves the flexibility of RUS and makes it more applicable to real-world situations. These real-world applications can range from identifying nonconformance in complex additive manufactured parts to determine the characteristics of an unknown material. However, while FEA has helped extend RUS to new shapes, less experimental and theoretical validation has been done for how well RUS works when boundary conditions (like clamping or supports) are applied.

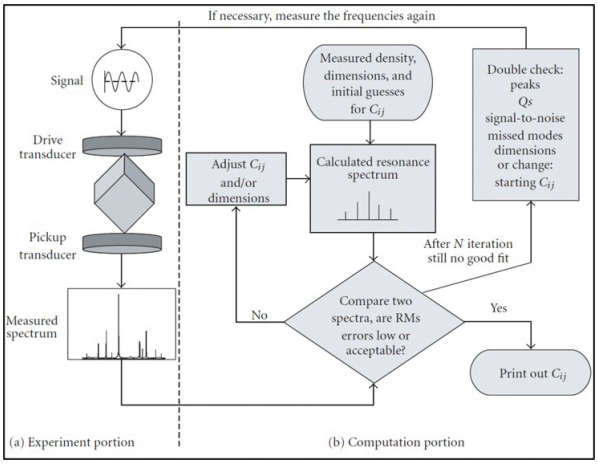

Fig. 1 The figure from [1] shows a traditional workflow output for a RUS experiment

Table 1 Experimental Factors for RUS Study

Conventional RUS	FEA with RUS
Swept Sine Input	Swept Sine Input
Free-Free Boundary	Prescribed Boundary
Frequency Spectra	Frequency Spectra
Simple Geometries	Complex Geometries
Single Point Excitation	Multi Point Excitation

This study aimed to validate RUS's ability to identify characteristics for metallic samples with boundary conditions to boost its reliability for advanced material applications. Comparing free and constrained vibration data from metallic samples allowed assessment of RUS accuracy and reliability when boundary conditions are introduced. Our goal was to evaluate the performance of RUS for determination of material properties under fixed boundary conditions. We specifically tested this through comparison of RUS experiments on an high purity aluminum rod under free-free and applied cantilever boundary conditions.

Background

This project aimed to expand RUS to accommodate non-idealized experimental boundary conditions. Validating performance for these boundary conditions would enhance RUS reliability for advanced material manufacturing applications and extend its capabilities to real-world manufacturing environments. This development could benefit on-machine inspection throughout

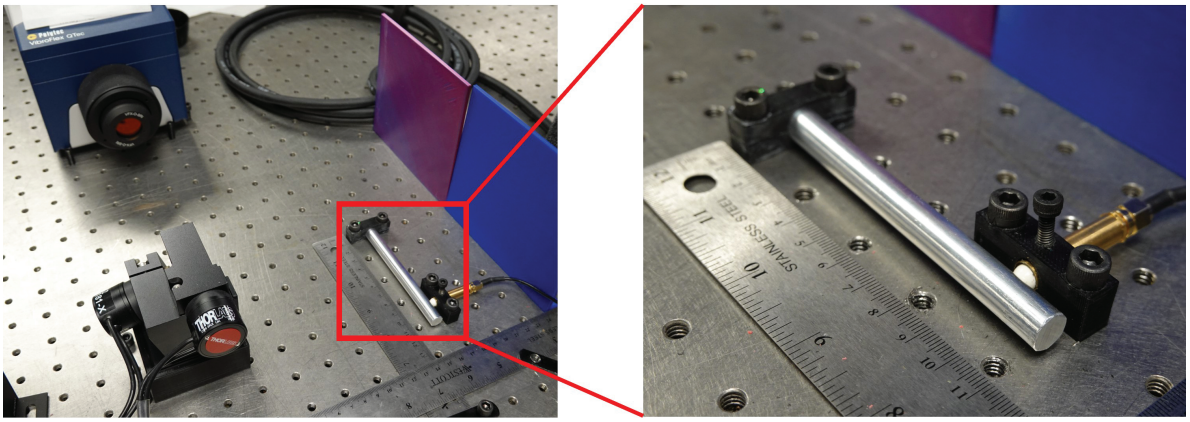

Fig. 2 Experimental apparatus for boundary conditioned RUS

the production process, significantly reducing handling risks and improving quality control. A key example of such non-ideal conditions is found in lathe operations, which our group explored in this study. The boundary condition in a lathe scenario is closely associated with a surface area prescribed boundary contact - to examine the lathe-inspired boundary condition, we devised an experimental setup that simulates these conditions, as shown in Figure 2. This setup allowed us to analyze how such boundary conditions affect RUS measurements and thus material property extraction, thereby bridging the gap between laboratory-based RUS and its practical application in manufacturing settings.

Our experimental setup featured a clamshell design with 3D printed PLA detachable top and bottom halves. This design prioritizes simplicity, utilizing just two protruding bolts for secure mounting. The streamlined configuration offered multiple benefits, including improved signal-to-noise ratio, enhanced laser scan results, and clearer mode shape visualization. A key feature of the setup is the 3D printed transducer stand, intentionally designed to be separate from the sample holder. This strategic separation minimizes the transmission of external vibrations to the clamp, thereby reducing unwanted noise and preventing the excitation of undesired mode shapes. Together, these design elements contribute to more accurate and reliable measurements in our RUS experiments.

Table 2 illustrates our mode shape extraction process. To obtain accurate mode shapes, we employed a Polytec 1D Qtec LDV connected to a Polytec VibroFlex Connect Front-End (max. frequency bandwidth of 24 MHz), coupled with a dual-axis galvanometer mirror system from Thorlabs to enable scanning. This technique allowed us to extract detailed 2D modal data, providing a comprehensive view of the material's vibrational behavior under various conditions. Table 3 shows a representative example of the difference between free-free and cantilever boundary for an experimental mode. The color distribution along the sample represents the displacement of the specimen. Red locations mean there is high displacement, and blue locations represent low displacement areas.

Table 2 Mode Shapes Extracted Using LDV

Mode Shape	Mode	Frequency (kHz)
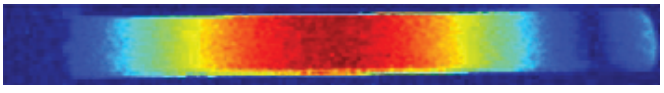	2	2.83
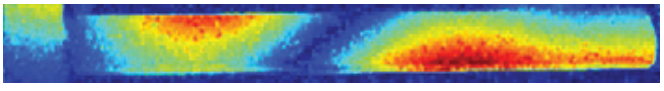	11	9.81
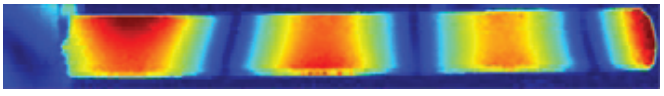	14	16.98
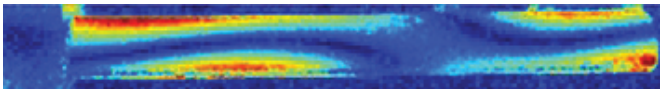	18	21.36
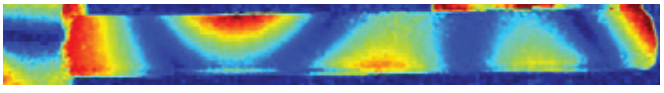	21	24.49

Table 3 Comparison between a free-free and cantilever mode shape

Free-Free	Cantilever
	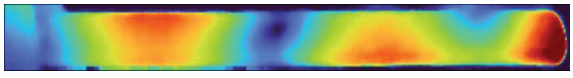

Experimental Methods

Figure 3 illustrates our project's experimental workflow. The process began with data extraction using the RUS holder under two conditions: free vibration and fixed boundaries. To collect the frequency spectrum from a specimen we placed our high

purity aluminum bar between the two clamshell PLA holders and bolted it directly into the optical table. We tightened the bolts to 2 N-m of torque for each trial to ensure repeatability and full contact. After this the LDV was aimed at the aluminum specimen at the 8 cm point from the fixed end, that was determined from an optimization study, at which point the frequency excitation began. We used previously determined settings to collect data which was then exported to begin the mode experimental mode shape scans. The resonant peaks were identified and then utilized in the laser scan software to obtain the mode shapes of the specimen. After this the frequency and mode shape data were exported into python scripts for processing. This experimental data was qualitatively compared against the scanned mode shapes to validate our approach. We then assessed the accuracy of the extracted data relative to our theoretical model, evaluating RUS's capability to determine material properties under various boundary conditions.

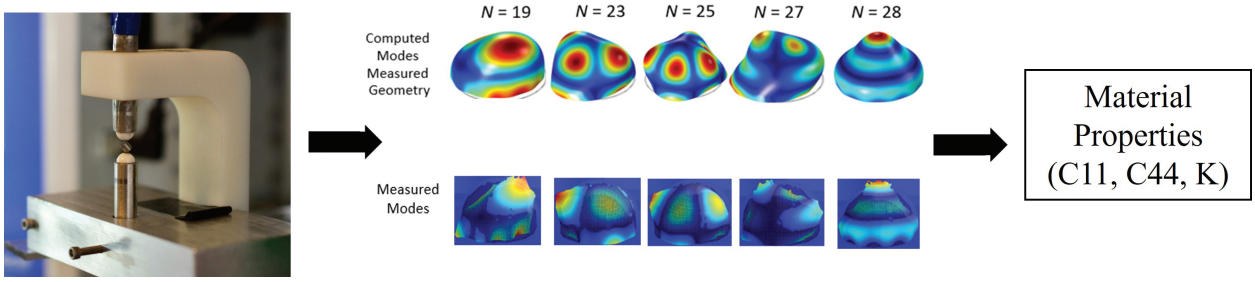

Fig. 3 Setup from LA-UR-23-22399 [2]. Mode shape images from [3]

Experimental Apparatus

Table 4 outlines the control group and variables for our experiment. To ensure the reliability and validity of our results, we carefully controlled key factors including material selection, specimen geometry, transducer and clamping locations, and clamping force. By maintaining consistency in these control variables, we aimed to isolate the effects of our independent variables on the resonant behavior of the specimens.

Table 4 Experimental Control Groups

Variable type	Factors
Independent	Boundary Conditions (fixed vs free) Specimen and Fixture Contact type (point vs surface) Fixture location (point, edge, corner)
Dependent	Resonance Frequencies (Hz) Mode Shapes Q factor/Damping Inversion Error
Control	Material Selection Geometry Transducer/Clamping location Clamping force

This experimental design allowed us to evaluate the sensitivity of the RUS technique to various boundary conditions and contact configurations, providing insights into its robustness and applicability in different scenarios. In our experimental apparatus there were a variety of devices that were utilized to perform RUS experimentation. In Table 5 you can see a list of the devices used as well as the role the device played in our experiments.

Evaluation of different experimental setups required experimental repeatability from run to run. This was partially accomplished through control over parameters and settings. Sample excitation was controlled via a consistent transducer drive amplitude of 5 Vpp to ensure that the high purity aluminum specimen was fully excited. The frequency range that we collected data over was from 100 Hz to 60 kHz. Starting at 100 Hz ensured that low frequency modes and shifted modes would

Table 5 Experimental Equipment and Setup

Equipment	Function
Piezoelectric transducers	Vibration input/excitation
Function Generator/Oscilloscope	Sweep through frequency range
Mounting apparatus / Frame	To position sample freely or constrained
Laser Doppler Vibrometer (LDV)	Contactless measurement of velocities
FEM software (Abaqus)	Simulate and invert modes
Calipers and Scale	Precise sample measurement
Environmentally Controlled Lab	Indirect control of temperature, humidity, and vibration isolation

be captured. The final frequency of 60 kHz was chosen after doing a sensitivity analysis which determined that modes after the 18th mode, which occurred at roughly 58 kHz, provided no new meaningful data. A frequency step of 2 Hz was selected to maintain the true center-to-center peak width for attenuation analysis. The ring-up time and acquisition time were set to 40 ms and 20 ms to ensure that full excitation was reached and captured. Given these settings, each run took approximately 40 minutes.

LDV parameters were optimized and then held constant during the experiments. The bandwidth was chosen to be 100 kHz, to ensure that we were fully capturing the full range of frequencies that were swept through during testing. Once the LDV was set, we maximized the instrument sensitivity by minimizing the velocity range. A range of 5 mm/s resulted in a sensitivity of, 2.5 mm/s/V. For our testing, we found that these settings provided sufficient sensitivity and produced reliable results.

There were five key criteria for choosing a metal sample for RUS experimentation. The first was elastic isotropy which was important for ease of analysis. The next criterion was homogeneity. While RUS can easily characterize alloys in a free-free regime we wanted to minimize the complexity of the specimen in a cantilevered regime. The next factor considered was a material that had high Q factors, which pointed us in the direction of metal specimens. The next two criterion are less restrictive as they can be easily characterized for each material. Having known specimen size and geometry ensure that models and RUS inversions are accurate. Based on this criterion, we chose a polycrystalline isotropic high purity aluminum sample for our RUS experiments due to its optimal properties. Its high purity minimizes internal defects, while its isotropic nature ensures uniform elastic properties (C11, C44) across all directions. The material's low natural damping and high Q factor result in sharp, easily identifiable frequency peaks. These characteristics collectively simplify analysis, improve measurement accuracy, and enhance the overall reliability of our RUS studies.

The 3D printing parameters utilized in our experiment were carefully selected to ensure the specimen fixtures were consistent and maximally rigid. The 100 percent infill density ensures that the fixture will be solid throughout, providing maximum stiffness and stability. At lower infill densities, the reduced stiffness allows the specimen to have increased motion which could reduce the quality of the frequency response. This is crucial for modal analysis as it minimizes any potential interference or unwanted vibrations from the fixture itself, allowing for more accurate measurements of the test subject's natural frequencies and mode shapes. Printing with a 100 percent infill also allows for the approximation of isotropic material properties. Although this assumption is not quite true as layer to layer interactions, internal voids, and other factors make the plastic anisotropic; these effects are minimized for small parts like our holders.

There are a variety of infill structures that can be used when printing with an FDM printer. The gyroid pattern provides isotropic strength properties, meaning it has similar strength in all directions. This is particularly advantageous for a modal analysis fixture, as it helps to distribute forces evenly and minimize any directional bias in the fixture's response. Additionally, the gyroid structure offers a good balance between strength and weight, which can be beneficial in reducing the overall mass of the fixture while maintaining its structural integrity.

The contact interfaces between the plastic parts and the metallic components of our apparatus needed to be as smooth as possible to ensure uniform contact. As can be seen in Figure 4 the 3D printed parts had contact areas printed in the Z direction to eliminate the need for supports at those locations. The print orientation in tandem with a chemical smoothing performed in acetone produced very smooth interfaces. The print orientation is also beneficial as it optimizes the strength of the fixture along its primary axis of loading. This orientation takes advantage of the layer-by-layer printing process, aligning the layers perpendicular to the main forces experienced during testing, which enhances the fixture's overall structural integrity.

We chose to use PLA for multiple reasons. The first is that the plastic is easy to print, has dimensional stability, and relatively high stiffness when compared to other plastics. We performed a plastic analysis study to see if ABS would be

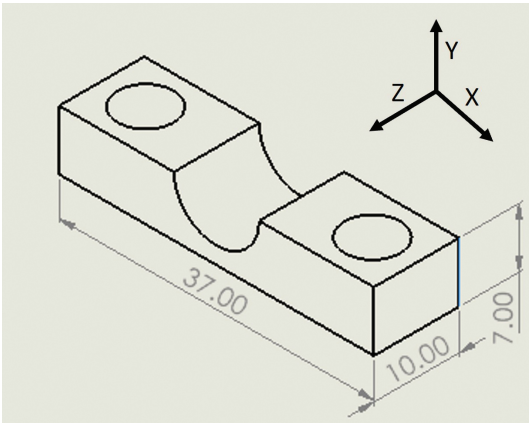

Fig. 4 Image of the print orientation of PLA components with units in mm

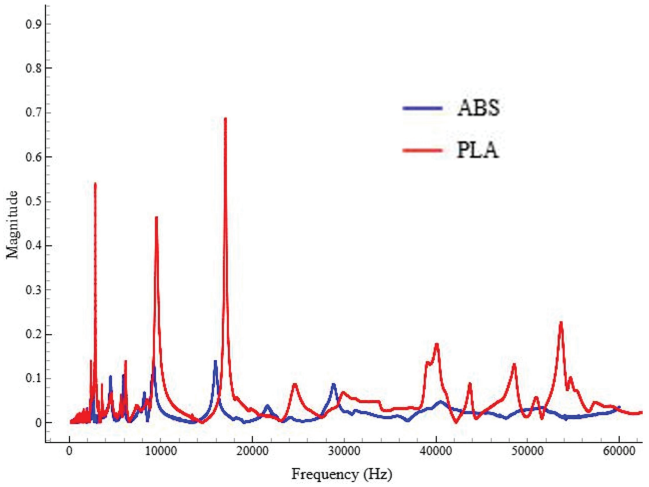

Fig. 5 Frequency response plot for the same frequency excitation sweep in the PLA and ABS holding fixtures

a more suitable material for our fixtures. ABS has a lower tensile strength than PLA but a higher flexural modulus and a larger elongation at break. We did this by testing six different aluminum samples in identical fixtures except for the plastic that it was made from. You can see in Figure 5 that the PLA holding fixture had a higher magnitude response which makes peak identification significantly easier. The ABS attenuated the signal response from all six specimens which increased the prevalence of noise in the response. There was a similar amount of peak shifting present in both holders due to stiffness and mass, which led us to the conclusion that PLA was the best material to use in our experimental apparatus.

After determining all the relevant parameters for the plastic and hardware, we moved on to finding the optimal location to have the laser beam on the specimen. This was done by placing the transducer 9 cm from the fixed end of the aluminum specimen. After this the LDV was aimed at a point 10 cm from the fixed end of the bar after which the specimen was excited. Following this, the laser was moved 2 cm down the bar closer to the fixed end, the measurement cycle was performed and this

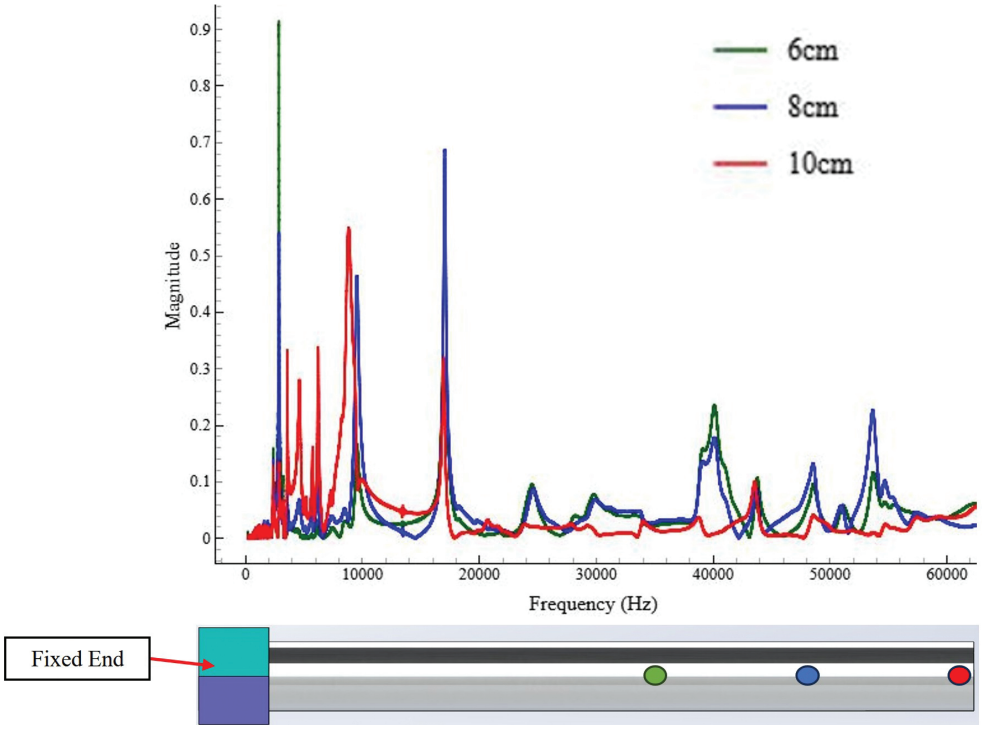

Fig. 6 Laser sweep study to determine the optimal laser location

process was repeated until the fixed end was reached. Figure 6 is a plot comparing the first three points along the specimen that were scanned. The largest difference that can be seen is in the amplitude of the magnitude for each response. The scan at the end of the bar had the lowest magnitude amplitude responses as it underwent the most motion and the LDV would have signal quality fluctuations that increased the level of noise recorded. The scan at 8 cm had the second highest signal to noise ratio with distinct peak amplitudes. As you moved past the 8 cm point, low frequency peaks had higher amplitudes. However, some mode loss occurred as some small amplitude modes were no longer visually present (e.g 14 kHz in the 6 cm scan). This led us to decide on a final position for the laser at the 8 cm point (0.5 cm repeatability) to maintain the highest signal strength.

Finite Element Model

To assess the accuracy of our experimental mode shape data, our group developed Finite Element models for both a freely vibrating aluminum sample and a sample with prescribed surface boundary conditions. This comparative approach allowed us to validate our experimental results against theoretical predictions. The Finite Element models were created using industry-standard software, Abaqus, using published material properties of aluminum and the specific dimensions of our samples [4, 5, 6]. We simulated various vibrational modes for both the free and constrained conditions, paying particular attention to the differences in mode shapes and resonance frequencies between the two configurations.

Initially we modeled our system with a simple fixed end boundary condition, however it was later determined that the effects of damping in our apparatus made this modeling method invalid. We then moved towards complex damping modeling but found that it was too difficult to directly quantify the damping in our system without doing computationally expensive non-linear modeling. We then modeled the cantilevered bar by developing a system of springs to replicate the motion of the bar when under the cantilever boundary condition. In Figure 7 you can see the full model of our 6 Degree of Freedom (DOF) spring ABAQUS model. In this model we make several key assumptions to create an intermediate linear representation of the system. We assume these springs behave linearly, neglecting potential nonlinear effects that may arise in real-world scenarios. This simplification allows for a more straightforward analysis while still capturing the essential dynamics of the system. As can be seen in purple, we utilize a Reference Point to define a single point that governs the motion of the entire rigid body, simplifying the analysis of the object's overall behavior. This point is internal to the volume of the bar and is radially connected to numerous nodes along the entirety of the clamped area. We used a kinematic coupling to ensure that the motion of the reference point was properly replicating the motion of the bar. We then modeled the stiffness of the holder by using a system of linear springs, representing each of the six degrees of freedom, which can be seen on the right. Three of these springs represent the translational degrees of freedom and the last three represent the rotational degrees of freedom. On the right we have another spring in the X direction that replicates the force that the transducer imparts during excitation of the specimen. This ensures that we capture the true dynamics of the system and replicate reality.

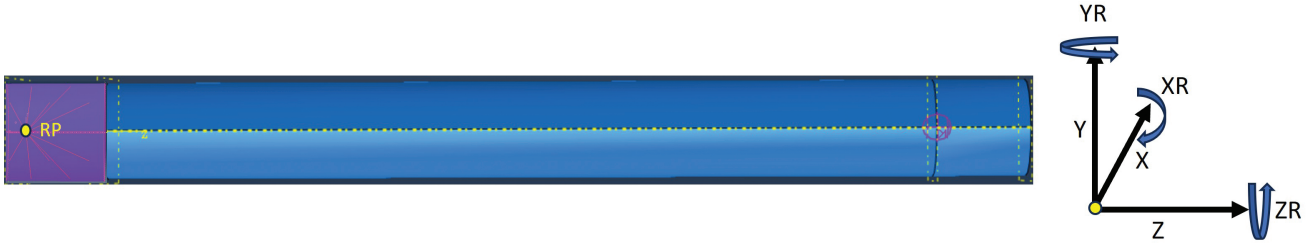

Fig. 7 This figure shows the full Abaqus model for the cantilevered specimen with the kinematic coupling shown in purple and the 6 translation and rotation springs to the right

By focusing on linear behavior, we created an intermediate model between free and prescribed boundary conditions that balances computational efficiency with a reasonable approximation of the system's response. This overall provides valuable insights into the specimen's vibrational characteristics without the added complexity of nonlinear analysis. A large part of this characterization was handled during the optimization of the spring stiffnesses. Since our model is somewhere between a free-free and fixed boundary condition the stiffness of each of the spring had to be manually tuned to match the experimental data.

The stiffness optimization was done manually through resonant frequency peak comparisons. As can be seen in Table 6 we tuned each spring stiffness for the first 15 modes to minimize the average percent error for the modes as well as maintaining a relatively distributed level of error across all the modes. Each spring was initially set to a value of 1e9 N/mm

Table 6 Spring Stiffness Optimization Table

Mode	Simulated Frequency (Hz)	Experimental Frequency (Hz)	Percent Difference (%)
1	3228	4266	27.7
2	3277	5936	57.7
3	7097	7338	3.4
4	8121	8222	1.2
5	9276	9152	1.4
6	10791	11346	5.0
7	12395	13398	7.8
8	17852	16536	7.7
9	18297	18272	0.1
10	21254	21962	3.3
11	26090	24520	6.2
12	28282	28018	0.9
13	34587	29494	15.9
14	35292	32746	7.5
15	37105	33172	11.2

which replicated a true fixed boundary condition. We started by characterizing each mode's sensitivity to each of the springs to see if the behavior was linear. Each mode had an initial linear response before converging to a constant frequency per mode. Each stiffness had a differing effect on the frequency response of the system. The stiffnesses with the highest effects were the X-translation DOF and the transducer spring. The next springs that had a significant effect on the response were the Y and Z translation degrees of freedom and the X and Z rotational degrees of freedom. The spring that had the smallest impact was the Y rotational DOF. In Table 7 you can see the final spring stiffness values that were utilized in the model.

Table 7 Final Spring Stiffness Values

X Stiffness (N/mm)	Y Stiffness (N/mm)	Z Stiffness (N/mm)	X Rotational Stiffness (N/mm)	Y Rotational Stiffness (N/mm)	Z Rotational Stiffness (N/mm)	Transducer Stiffness (N/mm)
1 E5	25 E5	75 E5	10 E5	250 E5	80 E5	5 E5

After this optimization was completed, we visually compared mode shapes for both the optimized modes, and modes outside the optimization selection. We found that we had qualitative agreement between the models which led us to do a final average percent difference calculation. The average value of 10.5% which was determined to be an adequate value as the model itself was accurately predicting the dynamic response of the system. Ignoring the first two modes as outliers, which we believe were unreliably captured by our experimental setup, reduced the average percent difference to 5.5%.

Results and Analysis

We conducted several experiments using free-free boundary conditions to verify both the material properties of our high purity aluminum and our capability to perform a RUS inversion. We extracted a range of values for the elastic tensor components C11 and C44 using the first 18 modes and used them to calculate the corresponding range for the Bulk Modulus of our material using Equation 1.

$$\mathrm{K} = C_{11} - \frac{4}{3}C_{44} \tag{1}$$

Figure 8 displays a frequency spectrum from our experimental free-free setup. Additionally, the results calculated from the free-free experiments were compared to literature to confirm their accuracy and are shown in Table 8.

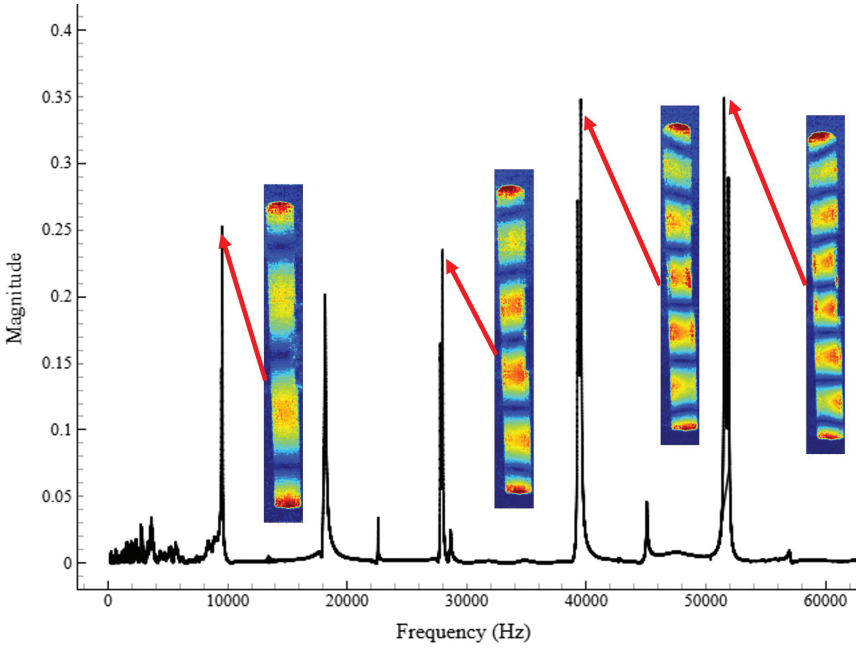

Fig. 8 Free-Free Frequency Spectrum

Table 8 Elastic Moduli for high purity aluminum. Literature values taken from sources -[4, 5, 6]

	C11 (GPa)	C44 (GPa)	Bulk Modulus (GPa)
Experimental	98.7 ± 5.3	25.9 ± 0.5	63.95 ± 4.45
Literature	91.9 – 104	23.3 – 26.3	60.8 – 68.9

The significant overlap between the experimental and literature values shown in Table 8 indicate that we were successful in measuring our material properties and ability to conduct a RUS inversion using a free-free boundary condition. We then proceeded to test our cantilever setup with prescribed boundary conditions.

We performed several tests in our cantilever setup after ensuring repeatability, and discovered a discrepancy in the modal data. An extra mode was occurring in the frequency spectrum at low frequencies caused by the transducer which was identified through analyzing the magnitude and phase plots of our mode shapes. To confirm this finding, we performed several tests using different aluminum samples to determine whether the resonance peak consistently reappeared in our frequency spectra. The data shown in Figure 9 confirms a recurring mode around 2.75kHz that was measured consistently across different aluminum sample tests. Table 9 provides supporting evidence, showing a false mode in the magnitude mode shape plot that doesn't appear in the phase plot of the aluminum sample. We confirmed that the mode originated from the transducer by taking mode shape scans on the transducer stand, specimen holder, and transducer. Because the transducer mode was not a characteristic of the high purity aluminum specimen, it was ignored in our analysis.

After all anomalies were identified, we performed a high fidelity scan of the cantilever setup to analyze for an inversion. Since established analytical methods to perform a RUS inversion assume free-free boundary conditions, we were unable to perform a traditional inversion to extract our material properties. Instead, we used a previously developed python script that used a finite element model as the forward solution with a genetic algorithm for the inversion. An initial finite element model was created in COMSOL using a fixed cantilever boundary condition. However, when attempting to match the experimental and simulated modes, resonance frequencies did not appear in the same regions and mode shapes did not correspond with each other. Additionally, we noticed immediate effects from the boundary conditions in the frequency spectrum of our cantilever experiment. RUS detects damping by measuring the full resonance response, including both the frequency and the

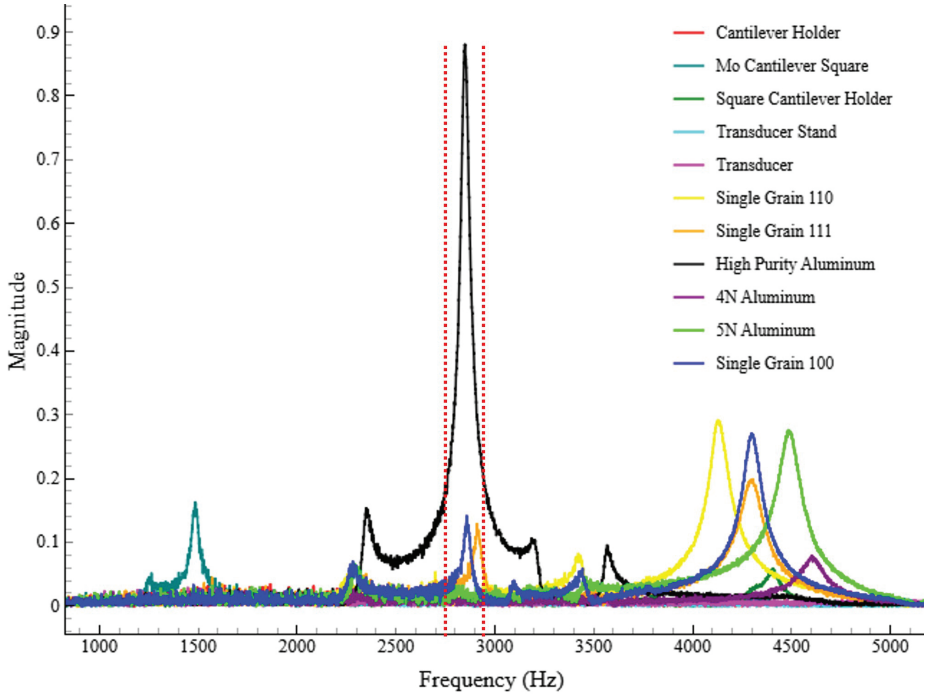

Fig. 9 Spectrum of Various Aluminum Samples

Table 9 Magnitude and Phase for Transducer Mode

Magnitude	Phase	Component
		
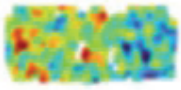		
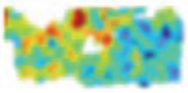		
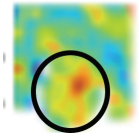		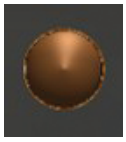

width of resonance peaks. Damping affects the accuracy of RUS measurements in several ways: it broadens peaks, making precise center frequency determination more difficult; it reduces signal amplitude, potentially lowering the signal-to-noise ratio; and in highly damped systems, resonance peaks may overlap, challenging the isolation of individual modes.

Figure 10 shows a comparison between the free-free and cantilever frequency spectrum where the damping effects are present. In the cantilever frequency response, the peaks were heavily attenuated by the holding fixture resulting in reduced signals. The peaks were also shifted left and right from the presence of added mass and stiffness. The effects of damping on our system were characterized as non-linear preventing us from performing a RUS inversion. As a result, we shifted our focus towards analyzing these non-linear effects through both quantitative measurements and qualitative comparisons. Q factors and frequency shifts were used for quantification, while mode shapes were used for qualitative analysis.

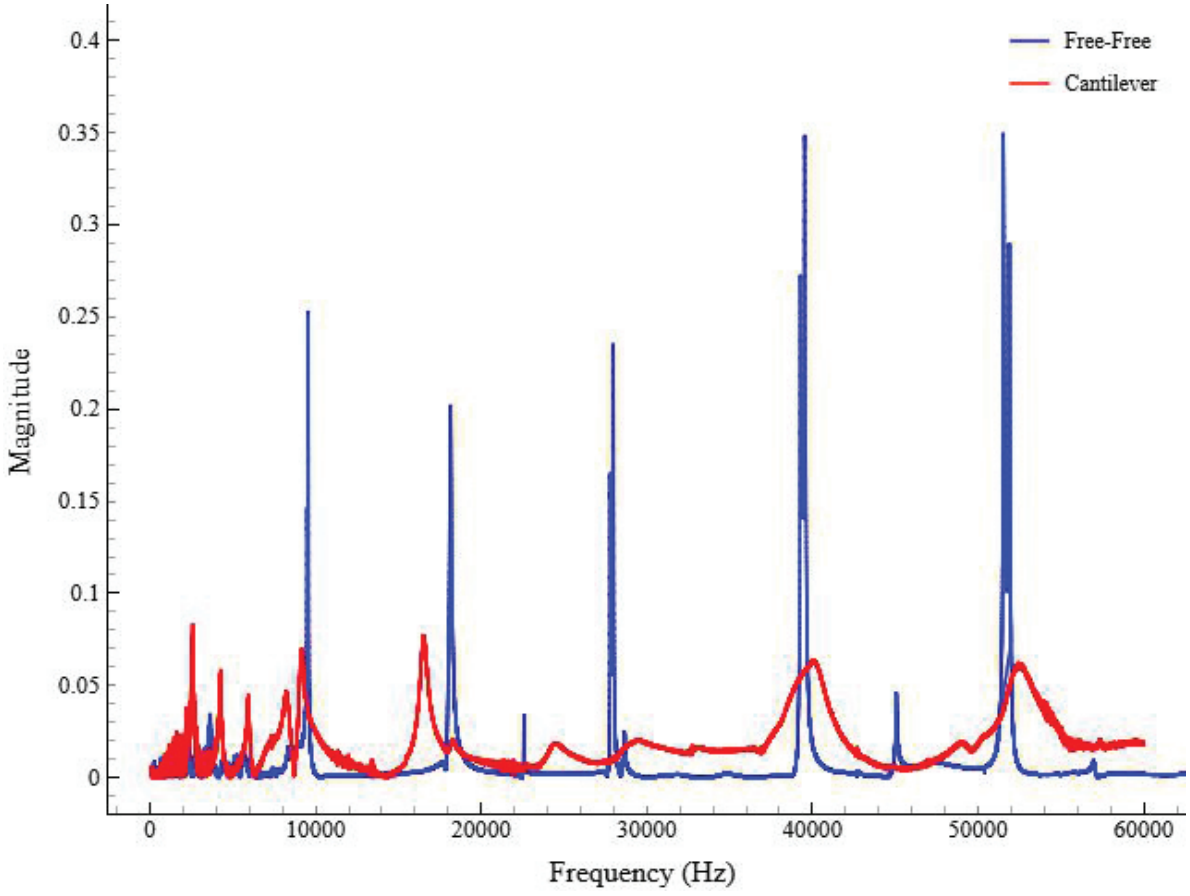

Fig. 10 Free-Free vs Cantilever Frequency Spectrum

We utilized our tuned finite element model to see if our model was closer to a free-free or fixed regime. As can be seen in Table 10 our specimen's response is closer to the response for a fixed specimen but not identical. The mode has the same shape but the actual magnitudes between the cantilever and fixed response are not the same. The most significant difference occurs at the clamping point where you can see in the cantilever response there is motion in the specimen that is not present in the fixed response. This motion is due to the specimen being stiffer than the holding fixture which allows for motion in the 6 degrees of freedom that we analyzed.

Q factors allow us to compare system damping where a higher Q factor indicates lower damping and good signal-to-noise ratio. High Q factors produce sharper resonance peaks and narrower bandwidths. We calculated our experimental Q factors using Equation 2 where f_o represents the resonance frequency and BW is the bandwidth of the peak, measured (in Hz) as the full width at half maximum (FWHM). The Q factors were then related to damping through Equation 2 where ζ represents the damping ratio. There is also an intrinsic impreciseness of frequency determination in dissipative systems, on the order of $1/Q^2$, stemming from the ambiguity in defining the resonance frequency due to damping [7].

$$\mathrm{Q} = \frac{f_o}{BW} = \frac{1}{2\zeta} \tag{2}$$

The Q factor for the free-free apparatus is 343.1 as compared to the Q factor for the cantilever apparatus of 18.76. We found the average Q decreased by 94.5% when compared with the free-free conditions, indicating significant damping effects in our system when applying prescribed boundary conditions. Additionally, there was a trend in the resonance frequency shift between the systems. While RUS can detect and measure damping, including friction damping, the presence of damping distinctly affects the accuracy of the measurements. The accuracy is primarily limited by the signal-to-noise ratio and the quality factor of the resonances, with an ultimate limit set by the intrinsic ambiguity in defining resonance frequencies in damped systems. The ability of RUS to achieve high signal-to-noise ratios can often offset some of the accuracy challenges posed by damping.

Table 10 Finite element simulation for Mode 6 in multiple loading scenarios

Free-Free	Cantilever	Fixed
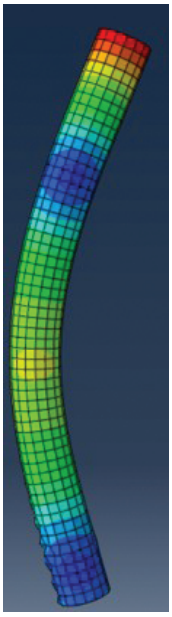	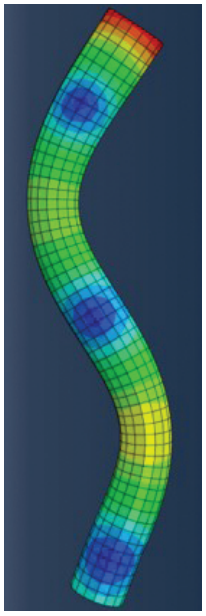	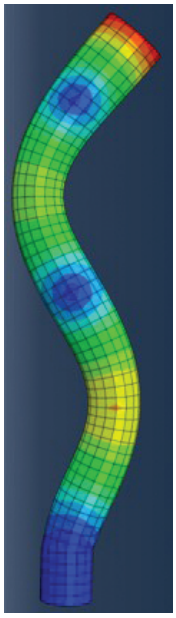

Conclusion

Our team successfully extracted and verified material properties for the high purity aluminum rod under free vibrating conditions using RUS. However, RUS's limitations in handling transient terms and complex boundary conditions necessitate further development to expand its applicability. Our team was able to extract information of the effects of boundary conditions, such as damping produced from the contact interface and frequency shifts. Future recommendations that can help advance this research involves changes to the experimental setup, data acquisition process, and inversion algorithm. Due to the lack of stiffness in our fixture, we were unable to fully qualify our boundary condition as fully cantilever. This leads us to recommending the use of a stiffer fixture such as a lathe or pipe vise to ensure that the specimen is fully fixed removing variability in the type of boundary condition being applied. Another limitation in our research was the ability to only measure out of place motion with our laser Vibrometer. Using other techniques such as Digital Image Correlation (DIC) would allow us to capture 3D displacement to identify any modes we might be missing compared to our signal point measurement technique. Additionally using triaxial accelerometer small enough for minimal mass loading could be another option to consider. As for inversion algorithms, we were unable to perform an inversion using established analytical methods as they are tailored for experiments that have free-free assumptions. Switching to a genetic algorithm which is a Stochastic evolutionary based algorithm, could help to converge to a global optimum rather than getting trapped in local minima. The genetic algorithm approach is particularly advantageous for our fixed-end cantilever configuration where the boundary conditions introduce additional complexity not accounted for in traditional analytical inversion techniques. Although our method was unsuccessful, we believe by pursuing these avenues, a RUS inversion can be successfully performed using boundary conditions.

Acknowledgments This research was funded by Los Alamos National Laboratory (LANL) through the Engineering Institute's Los Alamos Dynamics Summer School. The Engineering Institute is a research and education collaboration between LANL and the University of California San Diego's Jacobs School of Engineering. This collaboration seeks to promote multidisciplinary engineering research that develops and integrates advanced predictive modeling, novel sensing systems, and new developments in information technology to address LANL mission-relevant problems.

References

1. Li, G. and Gladden, J. “High temperature resonant ultrasound spectroscopy: a review”. *International Journal of Spectroscopy*, 2010(1):206362 (2010)ifnextchar.gobble.
2. Hayne Mathew Lindsay, e.a. “Error in rus measurements due to geometric uncertainties” (2023)ifnextchar.gobble.
3. Beardslee, L.B., Remillieux, M.C., and Ulrich, T. “Determining material properties of components with complex shapes using resonant ultrasound spectroscopy”. *Applied Acoustics*, 178:108014 (2021)ifnextchar.gobble.
4. Geimer Paul R, e.a. “Finite-element-based resonant ultrasound spectroscopy for measurement of multi-material samples”. *The Journal of the Acoustical Society of America*, 151(6):3633–3640 (2022)ifnextchar.gobble.
5. Kaufman, J.G. “Properties of pure aluminum” (2018)ifnextchar.gobble.
6. Hunsicker, H., Mondolfo, L., Tomblin, P., Carapella Jr, S., Hayduk, D., Carapella Jr, S., Hayduk, D., Westbrook, J., Marder, J., Stonehouse, A., et al. “Properties of pure metals”. In *Properties and Selection: Nonferrous Alloys and Special-Purpose Materials*, pages 1099–1201. ASM International (1990)ifnextchar.gobble.
7. Balakirev, F.F., Ennaceur, S.M., Migliori, R.J., Maiorov, B., and Migliori, A. “Resonant ultrasound spectroscopy: The essential toolbox”. *Review of Scientific Instruments*, 90(12) (2019)ifnextchar.gobble.

Appendix: Mesh Convergence and Q Factor Calculation

Table 11 Mesh Convergence Study: Relative Error in Natural Frequencies (Free-Free Vibration)

Number of Elements	Mode	Relative Error (%)			
		Mode 1	Mode 3	Mode 5	Mode 8
1819	1	0.014	0.028	0.036	0.000
2872	3	0.006	0.015	0.021	0.000
8924	5	0.000	0.002	0.000	0.000
29351	8	0.000	0.000	0.000	0.000

As shown in Table 11, the relative error decreases as the number of elements increases for free-free boundary condition vibration. The maximum relative error in natural frequencies compared to the finest mesh is 0.036%. This very small error indicates that even a coarse mesh is acceptable for this free-free vibration analysis.

Table 12 Mesh Convergence Study: Relative Error in Natural Frequencies (Cantilever Vibration)

Number of Elements	Mode	Relative Error (%)			
		Mode 3	Mode 7	Mode 10	Mode 14
7338	3	0.4635	0.4492	0.1744	0.4290
13398	7	0.2986	0.2898	0.0998	0.2776
21962	10	0.1472	0.1393	0.0404	0.1262
32746	14	0.0000	0.0000	0.0000	0.0000

As shown in Table 12, the relative error in natural frequencies decreases consistently as the number of elements increases for the cantilever boundary condition vibration analysis. The finest mesh (27,915 elements) is used as the reference for error calculation. The maximum relative error observed is approximately 0.4635% for Mode 1 with the coarsest mesh (2,133 elements), while the minimum error is 0.0404% for Mode 5 with 9,157 elements. This trend demonstrates clear mesh convergence, with even the coarsest mesh providing reasonably accurate results. The rapid decrease in error with increasing element count suggests that a moderately fine mesh offers a good balance between accuracy and computational efficiency for this cantilever vibration analysis.

$$\mathrm{Q} = \frac{Resonant Frequency}{Bandwidth} = \frac{27000Hz}{27256Hz - 26743Hz} = 52.63 \tag{3}$$

Chapter 9
Extraction of Boundary Impedance via Traveling Wave Analysis

William C. Rogers, Mohammad I. Albakri, and Pablo A. Tarazaga

Abstract Boundary conditions present in realistic environments are not often well represented by classical dynamic models. Extraction of accurate boundary conditions is necessary for substructuring applications and for meaningful environmental tests. The work herein addresses this problem via a novel method of boundary condition extraction utilizing traveling waves. Although it is possible to produce steady-state progressive waves in finite media, the excitation conditions required to do so are highly sensitive to the impedance of the boundary conditions. This study investigates the potential of leveraging this sensitivity to extract boundary conditions of a structure or a subsection of a larger structure. Traveling waves are generated using a modified two-point excitation, while boundary conditions are extracted by identifying excitation conditions corresponding to pure traveling waves. An example case is shown for an Euler-Bernoulli beam, where the boundary impedances are extracted with high accuracy.

Keywords Traveling waves · Impedance · Dynamic modeling

Introduction

Structure-bone traveling waves have been the subject of study for decades. All vibrating media experience wave propagation. The most common vibration behavior is standing waves, which is a steady-state phenomenon. These are often present in finite structures seen in modal analysis [1], these are the result of superimposed traveling waves in the structure. Generating propagating waves in finite media has been investigated in many studies, such as driving wave-driven motors [2, 3, 4], propelling particulates for high-precision pumps [5, 6], and replicating the behavior of the cochlear membrane in the human ear [7]. Of particular interest to this study is the influence of the boundary conditions on the wave propagation behavior of a finite structure. It has been noted by several authors that for finite media, ideal excitation conditions to generate dominantly traveling waves are sensitive to the boundary conditions of the structure [8, 9, 10]. This work is the first to demonstrate that this sensitivity allows for the extraction of the boundary impedance.

A pure traveling wave is one that propagates along a structure without reflection. There are three well-known methods of producing traveling waves in finite media with two exciters: active sink [11], impedance matching [12], and two-point (or two-mode) excitation [13]. Although only one of these methods includes the term “impedance,” all three can be described by exciting a wave at one point in the structure and matching the impedance at a later point, where the wave is absorbed.

William C. Rogers · Pablo A. Tarazaga
Fusion of Analysis, Simulation, and Testing (FAST) Lab, Texas A&M University, College Station, TX 77840, United States of America
e-mail: wcrogers42@tamu.edu; ptarazaga@tamu.edu

William C. Rogers · Mohammad I. Albakri
Smart Materials and Structures Research Lab College of Science and Engineering, Hamad Bin Khalifa University, Education City, Doha, Qatar
e-mail: wcrogers42@tamu.edu; malbakri@hbku.edu.qa

Mohammad I. Albakri
Texas A&M University at Qatar, Education City, Doha, Qatar
e-mail: malbakri@hbku.edu.qa

© The Author(s), under exclusive license to River Publishers 2026

Kristin B. Zimmerman, PhD (eds.), *Topics in Modal Analysis & Parameter Identification in Structural Dynamics, 2026, Vol. 8*, Conference Proceedings of the Society for Experimental Mechanics Series, https://doi.org/10.13052/rp-9788743814191

This is effectively achieved by exciting the structure at two points with a common frequency and a complex amplitude ratio between the two points. Both active sink and impedance matching allow these complex ratios to have different magnitudes. In contrast, two-point excitation forces have equal magnitude excitation with only a phase offset between the excitation points.

It was noted by Gabai and Bucher that the active sink method is susceptible to the boundary conditions of the structure [9]. In the original work presenting the active sink method, an Euler-Bernoulli beam was modeled as a waveform transforming along a waveguide. The excitation conditions necessary to produce a pure traveling wave were extracted from the formulation, but this requires an accurate model of the boundaries [11]. Later work by Gabai and Bucher [9] has shown that for cases of a single waveguide, this formulation can be written treating the forces as boundary elements and rearranging the characteristic equation to solve exactly for the complex forcing ratio. As noted in [9], even for this simplified case, the purity of the traveling waves generated by this predicted complex ratio is sensitive to the boundary conditions that must be known *a priori* for an exact calculation. Often, this shortcoming is accounted for with manual tuning of the complex ratio to achieve pure traveling waves.

This sensitivity of traveling waves to boundary conditions begs the question sought to be answered in this paper. Can the boundary conditions be extracted via the excitation conditions necessary for the generation of traveling waves? Understanding the boundary impedances of a structure is of particular interest for researchers in the area of vibration qualification testing [14], allowing for the design of better test apparatuses for environmental vibration testing. This approach is also convenient in that it does not require equally spaced measurement points and can extract properties using relatively low-magnitude excitation. These methods are scalable to higher dimensions and are agnostic to the direction of displacement included in the formulation.

Methodology

This section deals with the theoretical basis of the work. First, an analytical formulation for generating a pure traveling wave for an Euler-Bernoulli beam under fully generalized boundary conditions is presented. Next, the method for extracting boundary impedances based on the loading conditions required for pure traveling waves will be presented. Finally, a discussion is included on how the necessary information for this method is extracted in a realistic experimental environment.

Extraction of Boundary Impedances via Generation of Traveling Waves

To approximate a beam with generalized boundary conditions, consider a beam with springs and dampers acting linearly and torsionally in addition to masses acting on both sides of the beam (see Figure 1). The solution of the beam is assumed to be separable and of the form [15],

$$w(x,t) = W(x)e^{j\omega t} = \left[C_1 e^{-j\beta x} + C_2 e^{j\beta x} + C_3 e^{-\beta x} + C_4 e^{\beta x}\right] e^{j\omega t}. \tag{1}$$

For the case where forces are applied at the beam's ends, the boundary conditions for an Euler-Bernoulli beam of length L under these conditions are then [15],

$$\begin{aligned} EIw_{,xxx}(0,t) + k_1 w(0,t) + c_1 \dot{w}(0,t) + m_1 \ddot{w}(0,t) &= F_1 e^{j\omega t}, \\ -EIw_{,xxx}(L,t) + k_2 w(L,t) + c_2 \dot{w}(L,t) + m_2 \ddot{w}(L,t) &= F_2 e^{j\omega t}, \\ -EIw_{,xx}(0,t) + k_{t1} w_{,x}(0,t) + c_{t1} \dot{w}_{,x}(0,t) &= M_1 e^{j\omega t}, \\ EIw_{,xx}(L,t) + k_{t2} w_{,x}(L,t) + c_{t2} \dot{w}_{,x}(L,t) &= M_2 e^{j\omega t}. \end{aligned} \tag{2}$$

(3)

These boundaries can be rearranged into a system of equations,

$$\boldsymbol{A}\boldsymbol{c} = \boldsymbol{F}, \tag{4}$$

where $\boldsymbol{c} = \{C_1\ C_2\ C_3\ C_4\}^{\mathrm{T}}$, $\boldsymbol{F} = \{F_1\ F_2\ M_1\ M_2\}^{\mathrm{T}}$, and $\boldsymbol{A}$ is a 4×4 matrix. The steady-state solution then for the system can then be solved by inverting the $\boldsymbol{A}$ matrix to solve for the C_i terms. The terms of the $\boldsymbol{A}$ matrix can be written as,

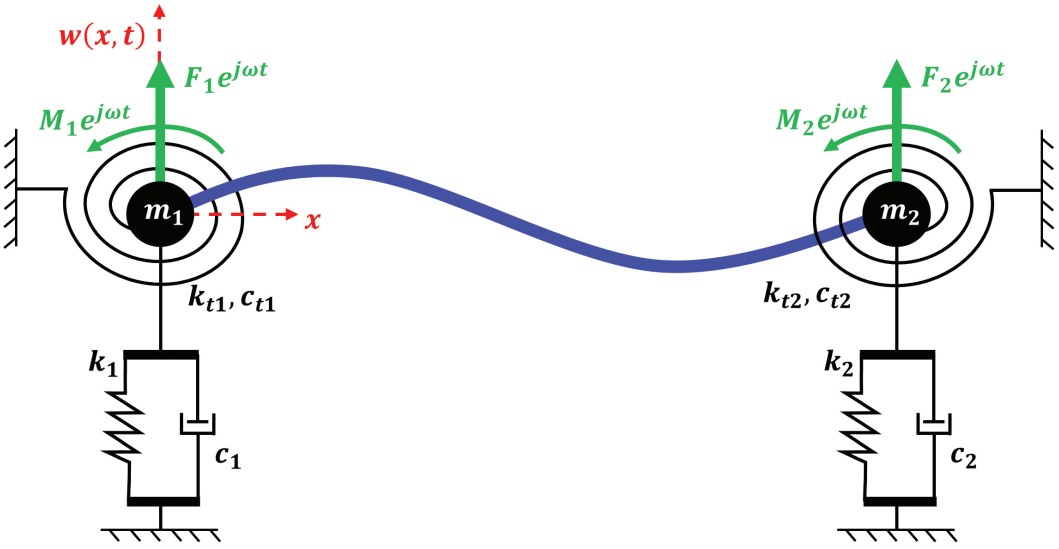

Fig. 1 Beam with generalized boundary conditions and applied loads

$$
\begin{aligned}
A_{11} &= j\omega Z_1 + j\omega Z_V, & A_{12} &= j\omega Z_1 - j\omega Z_V,\\
A_{13} &= j\omega Z_1 - \omega Z_V, & A_{14} &= j\omega Z_1 + \omega Z_V,\\
A_{21} &= (j\omega Z_2 - j\omega Z_V)e^{-j\beta L}, & A_{22} &= (j\omega Z_2 + j\omega Z_V)e^{j\beta L},\\
A_{23} &= (j\omega Z_2 + \omega Z_V)e^{-\beta L}, & A_{24} &= (j\omega Z_2 - \omega Z_V)e^{\beta L},\\
A_{31} &= \omega Z_{t1} - \omega Z_M, & A_{32} &= -\omega Z_{t1} - \omega Z_M,\\
A_{33} &= -j\omega Z_{t1} + \omega Z_M, & A_{34} &= j\omega Z_{t1} + \omega Z_M,\\
A_{41} &= (\omega Z_{t2} + \omega Z_M)e^{-j\beta L}, & A_{42} &= (-\omega Z_{t2} + \omega Z_M)e^{j\beta L},\\
A_{43} &= (-j\omega Z_{t2} - \omega Z_M)e^{-\beta L}, & A_{44} &= (j\omega Z_{t2} - \omega Z_M)e^{\beta L},
\end{aligned}
\tag{5}
$$

where the impedances of the boundaries are defined as $Z_i = c_i + jm_i(\omega^2 - \omega_i^2)/\omega$, $Z_{ti} = \beta(c_{ti} - jk_{ti}/\omega)$, and $\omega_i^2 = k_i/m_i$ and the impedances of the beam are $Z_V = EI\beta^3/\omega$ and $Z_M = -EI\beta^2/\omega$ for shear forces and moments respectively (where $i = 1, 2$). For this study, it is assumed that the properties and vibration behavior of the beam (Z_V, Z_M) are known. This is comparable to a case where a test specimen can be removed from its environment and tested independently.

The loading vector terms can be arranged to define the loading ratios

$$
\begin{aligned}
Q_F &\equiv \frac{F_1}{F_2}, & Q_{11} &\equiv \frac{F_1}{M_1}, & Q_{12} &\equiv \frac{F_1}{M_2},\\
Q_M &\equiv \frac{M_1}{M_2}, & Q_{22} &\equiv \frac{F_2}{M_2}, & Q_{21} &\equiv \frac{F_2}{M_1}.
\end{aligned}
\tag{6}
$$

These ratios are then analogous to the complex loading ratios for the active sink method [11]. Although only three of these terms are necessary to define the excitation conditions required for a pure traveling wave (since only three are independent), all six have been defined explicitly above for convenience. For the case of the pure right-moving traveling wave, it is known that $C_2 = C_3 = C_4 = 0$ and $C_1 \neq 0$. Given this, we can relate our loading ratios in Equation 6 to the terms in the first column of $\boldsymbol{A}$. These relations are then

$$
\begin{aligned}
Q_F^R &= \frac{A_{11}}{A_{21}}, & Q_{11}^R &= \frac{A_{11}}{A_{31}}, & Q_{12}^R &= \frac{A_{11}}{A_{41}},\\
Q_M^R &= \frac{A_{31}}{A_{41}}, & Q_{22}^R &= \frac{A_{21}}{A_{41}}, & Q_{21}^R &= \frac{A_{21}}{A_{31}}.
\end{aligned}
\tag{7}
$$

Each of these ratios in Equation 7 can be used to define an expression relating two of the boundary impedance terms to the impedance terms of the beam. Substituting the full expressions from the Equations in 5 into Equation 7 and rearranging the six equations into a new matrix yields the form,

$$
\boldsymbol{\Gamma}_R \boldsymbol{Z}_{BC} = \boldsymbol{\Omega}_R. \tag{8}
$$

The terms of Equation 8 are expanded as,

$$\boldsymbol{Z}_{BC} = \{Z_1 \quad Z_2 \quad Z_{t1} \quad Z_{t2}\}^{\mathrm{T}}, \tag{9}$$

$$\boldsymbol{\Gamma}_R = \begin{bmatrix} 1 & -Q_F^R e^{-j\beta L} & 0 & 0 \\ 0 & 0 & 1 & -Q_M^R e^{-j\beta L} \\ -j & 0 & Q_{11}^R & 0 \\ 0 & j & 0 & -Q_{22}^R \\ 0 & j & -Q_{21}^R e^{j\beta L} & 0 \\ j & 0 & 0 & -Q_{12}^R e^{j\beta L} \end{bmatrix}, \tag{10}$$

$$\boldsymbol{\Omega}_R = Z_V \begin{Bmatrix} -(1+Q_F^R e^{-j\beta L}) \\ 0 \\ j \\ j \\ j \\ -j \end{Bmatrix} + Z_M \begin{Bmatrix} 0 \\ (1+Q_M^R e^{-j\beta L}) \\ Q_{11}^R \\ Q_{22}^R \\ -Q_{21}^R e^{j\beta L} \\ Q_{12}^R e^{-j\beta L} \end{Bmatrix}, \tag{11}$$

where the superscript $(\cdot)^R$ and subscript $(\cdot)_R$ have been included to indicate that these ratios and matrices are defined in terms of a pure right traveling wave case. This matrix equation is overdefined, so an exact solution is not possible. An approximate solution is possible by calculating the pseudoinverse of the $\boldsymbol{\Gamma}_R$; however, the rank of $\boldsymbol{\Gamma}_R$ is 3, thus the pseudoinverse is ill-conditioned. The loading ratios in Equation 6 can also be related to a pure left-moving traveling wave case (where $C_1 = C_3 = C_4 = 0$ and $C_2 \neq 0$). Applying this condition, the ratios in Equation 6 are expressed as,

$$\begin{aligned} Q_F^L &= \frac{A_{12}}{A_{22}}, \quad & Q_{11}^L &= \frac{A_{12}}{A_{32}}, \quad & Q_{12}^L &= \frac{A_{12}}{A_{42}}, \\ Q_M^L &= \frac{A_{32}}{A_{42}}, \quad & Q_{22}^L &= \frac{A_{22}}{A_{42}}, \quad & Q_{21}^L &= \frac{A_{22}}{A_{32}}. \end{aligned} \tag{12}$$

The six ratios can again be rearranged into a matrix form,

$$\boldsymbol{\Gamma}_L \boldsymbol{Z}_{BC} = \boldsymbol{\Omega}_L, \tag{13}$$

where these terms are expanded

$$\boldsymbol{\Gamma}_L = \begin{bmatrix} -1 & -Q_F^L e^{j\beta L} & 0 & 0 \\ 0 & 0 & -1 & Q_M^L e^{j\beta L} \\ j & 0 & Q_{11}^L & 0 \\ 0 & j & 0 & Q_{22}^L \\ 0 & j e^{j\beta L} & Q_{21}^L & 0 \\ j & 0 & 0 & -Q_{12}^L e^{j\beta L} \end{bmatrix}, \tag{14}$$

$$\boldsymbol{\Omega}_L = Z_V \begin{Bmatrix} -(1+Q_F^L e^{j\beta L}) \\ 0 \\ j \\ -j \\ -j e^{j\beta L} \\ j \end{Bmatrix} + Z_M \begin{Bmatrix} 0 \\ (1+Q_M^L e^{j\beta L}) \\ -Q_{11}^L \\ Q_{22}^L \\ -Q_{21}^L \\ Q_{12}^L e^{-\beta L} \end{Bmatrix}, \tag{15}$$

where the superscript $(\cdot)^L$ and subscript $(\cdot)_L$ are introduced to indicate that these conditions are associated with the left-moving traveling wave. Equation 13 is similar to Equation 8 in that $\boldsymbol{\Gamma}_L$ is also rank 3, resulting in an ill-conditioned pseudoinverse. Although equations 8 and 13 alone are insufficient to extract the impedances accurately, these can be combined with far better success. The equations both relate the same boundary impedance vector $\boldsymbol{Z}_{BC}$, so the equations can be appended as

$$\boldsymbol{\Gamma}_{RL} \boldsymbol{Z}_{BC} = \begin{bmatrix} \boldsymbol{\Gamma}_R \\ \boldsymbol{\Gamma}_L \end{bmatrix} \boldsymbol{Z}_{BC} = \begin{Bmatrix} \boldsymbol{\Omega}_R \\ \boldsymbol{\Omega}_L \end{Bmatrix}. \tag{16}$$

By appending the $\boldsymbol{\Gamma}_R$ and $\boldsymbol{\Gamma}_L$ the resulting matrix, $\boldsymbol{\Gamma}_{RL}$, has a rank of 4 and a well-conditioned pseudoinverse. Thus, the impedance of the boundaries can be approximated from the loading ratios associated with pure traveling waves. The accuracy of this approximation will be evaluated for an example case in the Results section.

Results

This section will consider a case study where complex boundary impedances are extracted from a known Euler-Bernoulli beam. The beam under consideration in this study has dimensions 10 mm $\times$ 1 mm $\times$ 1 m, a Young's Modulus of 70 GPa, and a density of 2700 kg/m^3. The boundary impedances are calculated according to the boundary terms in Table 1. To extract the boundary impedances, the excitation conditions are identified for a pure right and left traveling wave for each frequency. Examples for a low and a high frequency case are shown in Figures 2 and 3. These waveforms have been generated using the associated forcing ratios that have been defined in Equations 7 and 12. For the benefit of the reader, the ideal loading ratios for these traveling wave examples are included in Table 2. These ratios are complex, so they have been reported in terms of their magnitude and their phase in degrees. These waveform examples are both calculated for $F_2 = 1$ kN, defining the other three loading terms using the calculated ratios in Table 2. The traveling waves have been plotted using a spatial resolution of 500 points to ensure no spatial aliasing and were sampled for 50 points temporally across one period T. The time axes have been normalized by their respective periods to improve readability.

Table 1 Boundary condition terms used for this case study

Intertial	Elastic	Dissapitive
$m_1 = 50$ g	$k_1 = 300$ N/m	$c_1 = 30$ N·s/m
$m_2 = 20$ g	$k_2 = 100$ N/m	$c_2 = 20$ N·s/m
	$k_{t1} = 70$ N·m/m	$c_{t1} = 5$ N·m·s/m
	$k_{t2} = 30$ N·m/m	$c_{t2} = 4$ N·m·s/m

Table 2 Loading ratios producing the pure traveling waves for frequencies 20 Hz and 2.5 kHz

	$\lvert Q_F^R\rvert$	$\lvert Q_{11}^R\rvert$	$\lvert Q_{12}^R\rvert$	$\lvert Q_F^L\rvert$	$\lvert Q_{11}^L\rvert$	$\lvert Q_{12}^L\rvert$
20 Hz	1.55	0.60	0.83	1.46	0.64	0.81
2.5 kHz	2.50	1.52	1.90	2.49	1.52	1.90
	$\angle Q_F^R$	$\angle Q_{11}^R$	$\angle Q_{12}^R$	$\angle Q_F^L$	$\angle Q_{11}^L$	$\angle Q_{12}^L$
20 Hz	172°	103°	−89.5°	−167°	−76°	111°
2.5 kHz	163°	177°	−19.4°	−160°	−1.84°	−165°

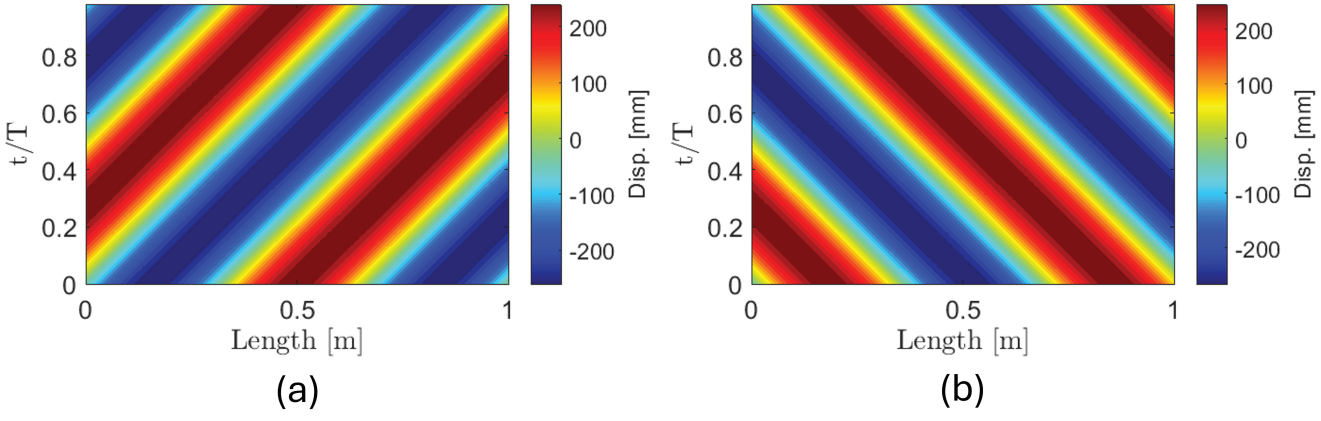

Fig. 2 Contour of a propagating wave for the pure (a) right-moving and (b) left-moving traveling waves associated with $\omega = 20$ Hz

It was mentioned in the Methodolgy that of the cases presented, only Equation 16 yields a well-conditioned pseudoinverse; thus, for brevity, only the results of this approximation are reported. The loading ratios to produce pure left and right traveling waves are calculated for a frequency range of $\omega \in (0, 5)$ kHz at 12 evenly distributed frequency lines. For each

frequency, the loading ratios are plugged into Equation 16 and the boundary impedances are extracted and are plotted against the exact values in Figures 4 and 5. The average error across all four of the boundary impedances is on the order of 10^{-15},

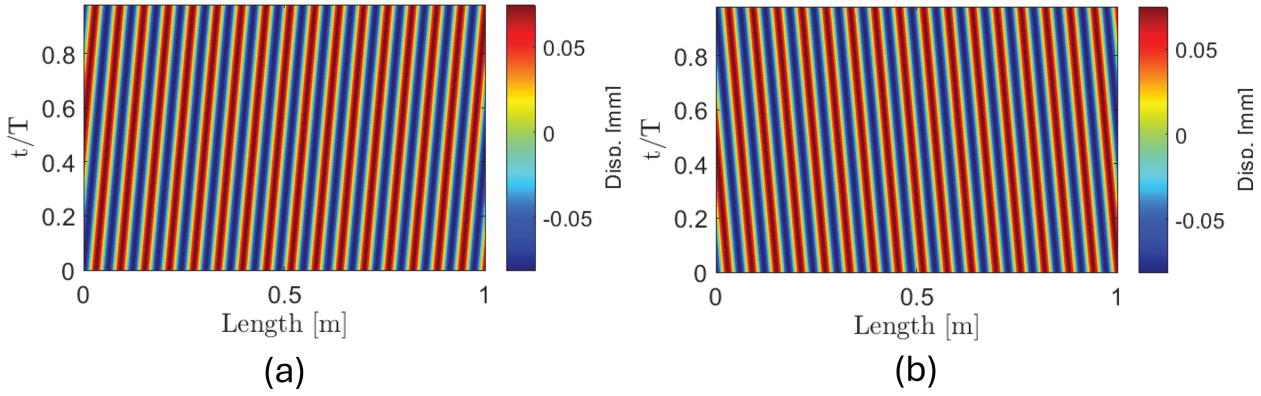

Fig. 3 Contour of a propagating wave for the pure (a) right-moving and (b) left-moving traveling waves associated with $\omega = 2.5$ kHz

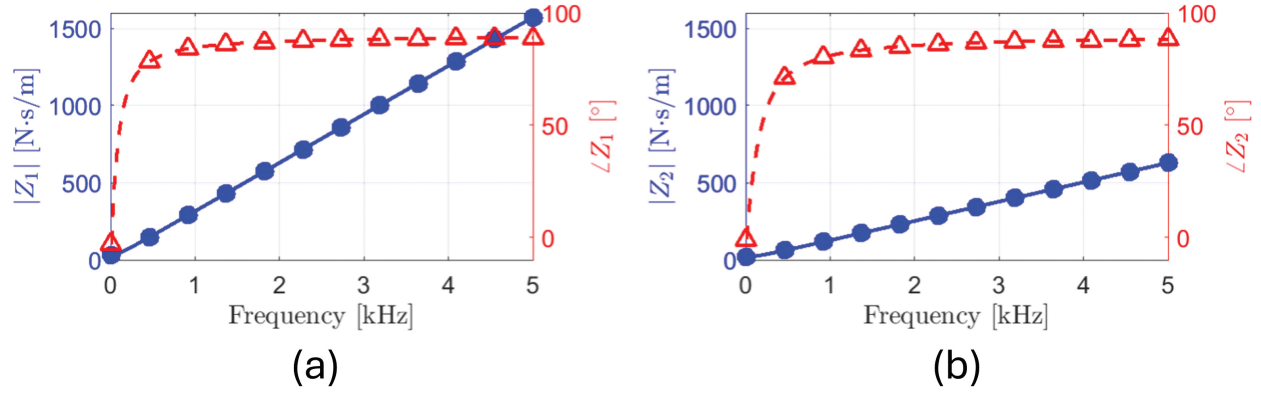

Fig. 4 Magnitude (blue) and phase (red) of the exact and approximated transverse impedances (Z_1, Z_2). Exact impedances for the (a) left and (b) right-hand sides of the beam are in solid blue and dashed red lines, while the approximated values are dotted for the magnitude and triangles for the phase

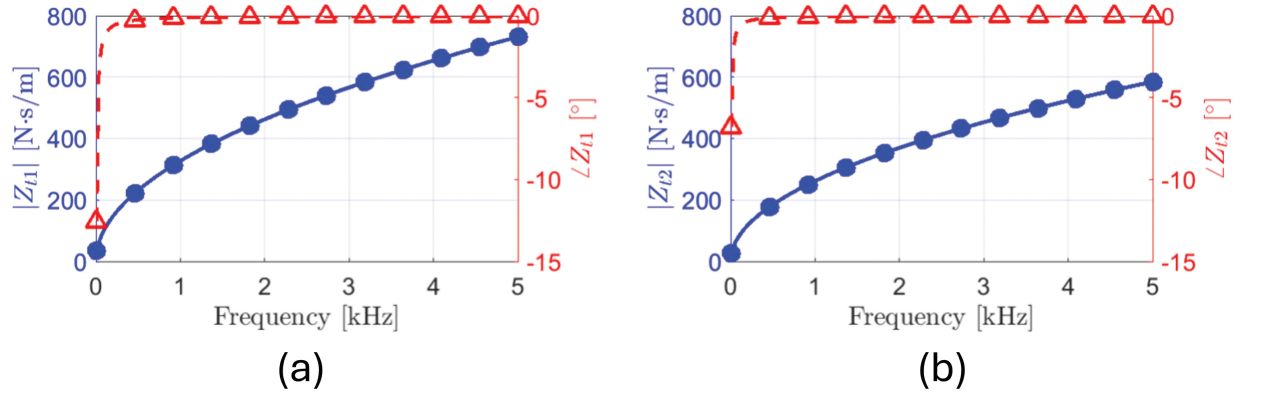

Fig. 5 Magnitude (blue) and phase (red) of the exact and approximated torsional impedances (Z_{t1}, Z_{t2}). Exact impedances for the (a) left and (b) right-hand sides of the beam are in solid blue and dashed red lines, while the approximated values are dotted for the magnitude and triangles for the phase

which is close to the scale of precision for double float variables and suggests that this method is capable of extracting the boundary impedances exactly within the parameters of the assumed information.

Conclusion

Decades of research in the area of steady-state traveling wave generation have stated that the necessary excitation conditions to produce a pure progressive wave have been sensitive to the boundary conditions of the structure. This work has shown that this sensitivity can be leveraged in the reverse direction: the excitation conditions can be used to approximate the impedance of the boundary conditions for a simple 1D Euler-Bernoulli beam. This has been done analytically, presuming that the user has complete knowledge of the structure's impedance and material properties.

Further work is necessary to fully implement this method experimentally. Namely, it is difficult to identify the loading ratios for exact excitation of traveling waves. Although there are many metrics to evaluate the quality of traveling waves, these most often consider the ratio of the left and right traveling waves ignoring the presence of the evanscent waves. Algorithmically identifying the loading ratios for these pure traveling waves is the next challenge that must be considered.

References

1. D. J. Ewins, *Modal testing: theory, practice, and application*, 2nd ed. Baldock, Hertfordshire, England ; Philadelphia, PA: Research Studies Press, 2000.
2. Z. Wen, D. Wu, and K. Nakamura, "A Miniature Traveling Wave Ultrasonic Linear Motor Utilizing Bimorph Transducers," *IEEE Transactions on Ultrasonics, Ferroelectrics, and Frequency Control*, vol. 71, no. 6, pp. 698–706, Jun. 2024. [Online]. Available: https://ieeexplore.ieee.org/document/10510491/
3. H. Hariri, Y. Bernard, and A. Razek, "Dual piezoelectric beam robot: The effect of piezoelectric patches' positions," *Journal of Intelligent Material Systems and Structures*, vol. 26, no. 18, pp. 2577–2590, Dec. 2015. [Online]. Available: https://journals.sagepub.com/doi/10.1177/1045389X15572013
4. V. Ruiz-Díez, J. Hernando-García, J. Toledo, A. Ababneh, H. Seidel, and J. L. Sánchez-Rojas, "Piezoelectric MEMS Linear Motor for Nanopositioning Applications," *Actuators*, vol. 10, no. 2, p. 36, Feb. 2021. [Online]. Available: https://www.mdpi.com/2076-0825/10/2/36
5. D. Fleishman, Y. Asscher, and M. Urbakh, "Directed transport induced by asymmetric surface vibrations: making use of friction," *Journal of Physics: Condensed Matter*, vol. 19, no. 9, p. 096004, Mar. 2007. [Online]. Available: https://iopscience.iop.org/article/10.1088/0953-8984/19/9/096004
6. S. Daniel, M. K. Chaudhury, and P.-G. de Gennes, "Vibration-Actuated Drop Motion on Surfaces for Batch Microfluidic Processes," *Langmuir*, vol. 21, no. 9, pp. 4240–4248, Apr. 2005. [Online]. Available: https://pubs.acs.org/doi/10.1021/la046886s
7. A. Omidi Soroor and P. A. Tarazaga, "Non-reflective traveling waves in finite thin beams: A parametric study," *Thin-Walled Structures*, vol. 208, p. 112839, Mar. 2025. [Online]. Available: https://linkinghub.elsevier.com/retrieve/pii/S0263823124012783
8. V. V. N. S. Malladi, D. Avirovik, S. Priya, and P. Tarazaga, "Characterization and representation of mechanical waves generated in piezo-electric augmented beams," *Smart Materials and Structures*, vol. 24, no. 10, p. 105026, Oct. 2015. [Online]. Available: https://iopscience.iop.org/article/10.1088/0964-1726/24/10/105026
9. R. Gabai and I. Bucher, "Excitation and sensing of multiple vibrating traveling waves in one-dimensional structures," *Journal of Sound and Vibration*, vol. 319, no. 1-2, pp. 406–425, Jan. 2009. [Online]. Available: https://linkinghub.elsevier.com/retrieve/pii/S0022460X08005609
10. R. Gabay and I. Bucher, "On Vibrating Traveling Waves Actuation, Sensing, and Tuning in Finite Structures," in *Design Engineering and Computers and Information in Engineering, Parts A and B*. Chicago, Illinois, USA: ASMEDC, Jan. 2006, pp. 809–817. [Online]. Available: https://asmedigitalcollection.asme.org/IMECE/proceedings/IMECE2006/47675/809/322339
11. N. Tanaka and Y. Kikushima, "Active Wave Control of a Flexible Beam : Proposition of the Active Sink Method," *JSME international journal. Ser. 3, Vibration, control engineering, engineering for industry*, vol. 34, no. 2, pp. 159–167, 1991.
12. M. Kuribayashi, S. Ueha, and E. Mori, "Excitation conditions of flexural traveling waves for a reversible ultrasonic linear motor," *The Journal of the Acoustical Society of America*, vol. 77, no. 4, pp. 1431–1435, Apr. 1985. [Online]. Available: https://pubs.aip.org/jasa/article/77/4/1431/785595/Excitation-conditions-of-flexural-traveling-waves
13. Y. Tomikawa, K. Adachi, H. Hirata, T. Suzuki, and T. Takano, "Excitation of a Progressive Wave in a Flexurally Vibrating Transmission Medium," *Japanese Journal of Applied Physics*, vol. 29, no. S1, p. 179, Jan. 1990. [Online]. Available: https://iopscience.iop.org/article/10.7567/JJAPS.29S1.179
14. P. M. Daborn, "Smarter Dynamic Testing of Critical Structures," Ph.D. dissertation.
15. S. S. Rao, *Vibration of continuous systems*. Hoboken, N.J: Wiley, 2007, oCLC: ocm65301593.

Chapter 10
Operational Modal Analysis of the Bear Mountain Bridge and Comparisons with Finite Element Model

CDT Gautam Namjoshi, CDT Ethan Espinosa, CDT Philip Williams, Courtney Clark, Dr. Qian Chen, and Dr. Thomas J. Matarazzo

Abstract The Bear Mountain Bridge is a historic suspension bridge that spans the width of the Hudson River in New York State. A wired sensor network of six uniaxial accelerometers was installed along the south side of the main suspended span to collect vibration data for use in operational modal analysis. This paper analyzes recently collected data to experimentally identify operational modes of the suspension bridge. Cross-validation of results from the system identification methods SSI-COV, ERA-NExT, and AFDD is used to determine modal frequencies. Stabilization diagrams from SSI-COV and ERA-NExT are compared to validate estimates of modal frequencies and mode shapes within individual datasets. Analysis of the identified modal frequencies, in conjunction with comparisons of associated mode shapes, found nine vertical modes for the bridge below 2.5 Hz. These results are then compared with estimates computed by a detailed finite element model of the bridge. This comparison shows good agreement between the experimentally identified modes and computationally identified modes.

Keywords System identification · Bridge · Modal properties · Sensor network · Structural health monitoring

Introduction

In recent decades, various vibration-based structural health monitoring techniques have been developed to identify dynamic properties in attempts to assess structural health. Ambient modal analysis involves recording structural vibrations during normal operation and analyzing these data to estimate modal properties [1]. There are a variety of well-established system identification methods capable of estimating structural modal properties based on ambient vibration data. Output-only system identification methods have been used historically to identify modes of large bridges based on the structure's dynamic response. For instance, modal analysis of the Golden Gate Bridge using an Autoregressive model accurately identified 67 different modes of the structure between 0 and 5 Hz [12]. These insights are highly valuable for calibration of physics-based models, damage detection, condition evaluation, and other applications [2].

Opened in 1924, the Bear Mountain Bridge has served as a landmark of cultural and economic value to New York State's lower Hudson Valley [3]. Its construction as a suspension bridge allows many comparisons to be made with other long-span, cable-supported structures, such as the Golden Gate Bridge, where analyses have previously been conducted [3][4]. In this study, accelerometer data is used to estimate the bridge's vertical and torsional modal frequencies, as well as its mode shapes. These modal characteristics establish a baseline that enables the detection of future structural changes. To improve

CDT Gautam Namjoshi · CDT Ethan Espinosa · Dr. Thomas J. Matarazzo
Department of Civil and Environmental Engineering, United States Military Academy, West Point, NY
e-mail: gautam.namjoshi@westpoint.edu; ethan.espinosa@westpoint.edu; thomas.matarazzo@westpoint.edu

CDT Philip Williams · Dr. Thomas J. Matarazzo
Department of Mechanical and Aerospace Engineering, United States Military Academy, West Point, NY
e-mail: philip.williams@westpoint.edu; thomas.matarazzo@westpoint.edu

Courtney Clark · Dr. Qian Chen
Thornton Tomasetti, New York, NY, United States Military Academy, West Point, NY 10997
e-mail: cclark@thorntontomasetti.com; qchen@thorntontomasetti.com

© The Author(s), under exclusive license to River Publishers 2026

Kristin B. Zimmerman, PhD (eds.), *Topics in Modal Analysis & Parameter Identification in Structural Dynamics, 2026, Vol. 8*,
Conference Proceedings of the Society for Experimental Mechanics Series, https://doi.org/10.13052/rp-9788743814191

accuracy, this baseline must be adjusted for environmental influences, such that variations in structural behavior can be more confidently attributed to shifts in the bridge's structural health.

Acquisition of Data

Modal identification in this study is based on the measurements of a network of six accelerometers installed on a main girder on the south side of the bridge, as shown in Figure 1. Spread across the 1632-foot-long main span, the sensors capture spatial dynamics of the bridge [3]. The uniaxial accelerometers are clamped to a flange underneath catwalk-access panels on the sidewalk. All accelerometers were hard-wired to a base station data acquisition system on the West side of the bridge. Sensors were affixed to the girder using a combination of mounting adhesive and clamps and positioned in such a way to resist detrimental environmental conditions.

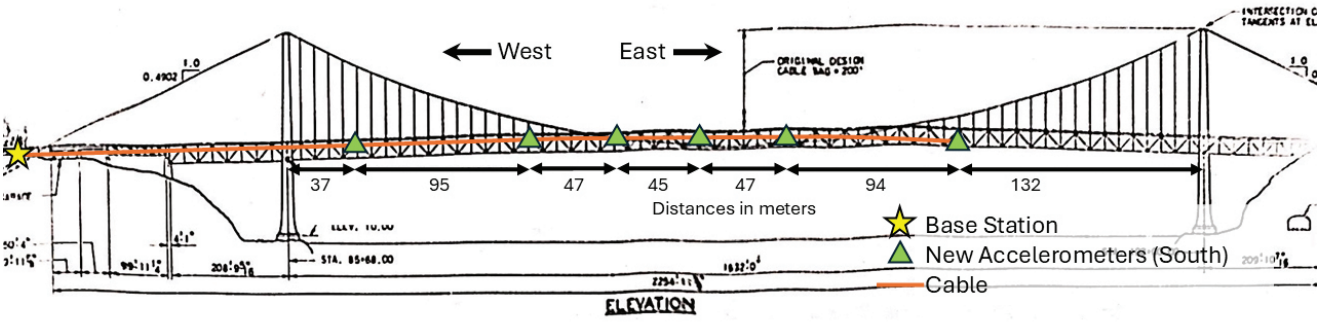

Fig. 1 Overview of Sensor Network Layout

Data collected from the "fixed" set of sensors requires on-site personnel to collect data, and so the data set was restricted to the bridge's working hours of 0800-1600. Initial datasets were collected in 2022 between the months of May and August with a previous sensor network. After the installation of this most recent network, data was collected in the months of November 2024, April 2025, and May 2025. The sensors are sensitive to a large band of low frequencies, including the expected range of 0-2.5 Hz for the relevant modal frequencies of the bridge.

Methods for Identification of Operational Modes

In order to conduct operational modal analysis on the Bear Mountain Bridge, output-only system identification methods are necessary. Prior analysis of the bridge identified three different output-only systems as appropriate for use with the data collection setup available. Automated Frequency Domain Decomposition (AFDD) [5], Eigensystem Realization Algorithm-Natural Excitation Techniques (ERA-NExT) [6], and Covariance-driven Stochastic Subspace Identification (SSI-COV) [7] are used as in past research to identify the operational modes of the bridge. The operational modal analysis of the structure uses stabilization diagrams with both SSI-COV and ERA-NExT to identify stable modes. Stabilization diagram results were further validated by comparing methods with representative datasets to ensure cooperating results. Technical issues with certain sensors required that some datasets be discarded altogether. In addition to output-only methods, a Finite Element Model (FEM) provided by an engineering firm was used to identify the modes of the model. Comparisons between these experimental and computational results were used to verify the accuracy of the Finite Element Model.

Stabilization Diagrams

Stabilization diagrams offer improved validation of results for operational modal analysis. Modes are initially identified through a base method—in this paper, SSI and ERA-NExT. Results are gathered for a range of model orders between 19 and 119; stable results exhibit similar frequencies (within 0.01 Hz), damping ratios (within 4%), and mode shapes (MAC value within 0.5%) across those multiple orders. These resulting stable poles are then clustered and averaged to identify a final frequency and mode shape. Stabilization diagrams also provide a visual guide for identifying the prominence of real modal

frequencies. Vertical lines of results indicate a trend of stability for that frequency, indicating a high likelihood of real modes. This method reduces the risk of mischaracterizing computational artifacts as real modes, allowing for better validation of results. While a lack of access to precision accelerometers was a cause for a lack of results in the ultra-low frequency range, the available sensors proved sensitive enough to obtain a representative set of results at low frequencies.

Both SSI-COV and ERA-NExT were used to identify the operational modes of the Bear Mountain Bridge. The novelty of ERA-NExT is that it allows for output-only estimation of modes through an assumption of a uniform white-noise set of input parameters [8]. Frequencies and Mode Shapes at different model orders are identified by the eigenvalues and vectors evaluated through iteratively increasing Hankel Matrix size. The resulting modal frequencies, damping ratios, and mode shapes are then used to identify the stability of the pole and construct stabilization diagrams, as seen for a representative dataset in Figure 2. SSI-COV constructs a Toeplitz matrix of the covariance matrices of the structure's response, with singular value decomposition used to identify the modes [9]. Once again, the results are used to identify the stability of each pole and construct appropriate stabilization diagrams as seen in Figure 3.

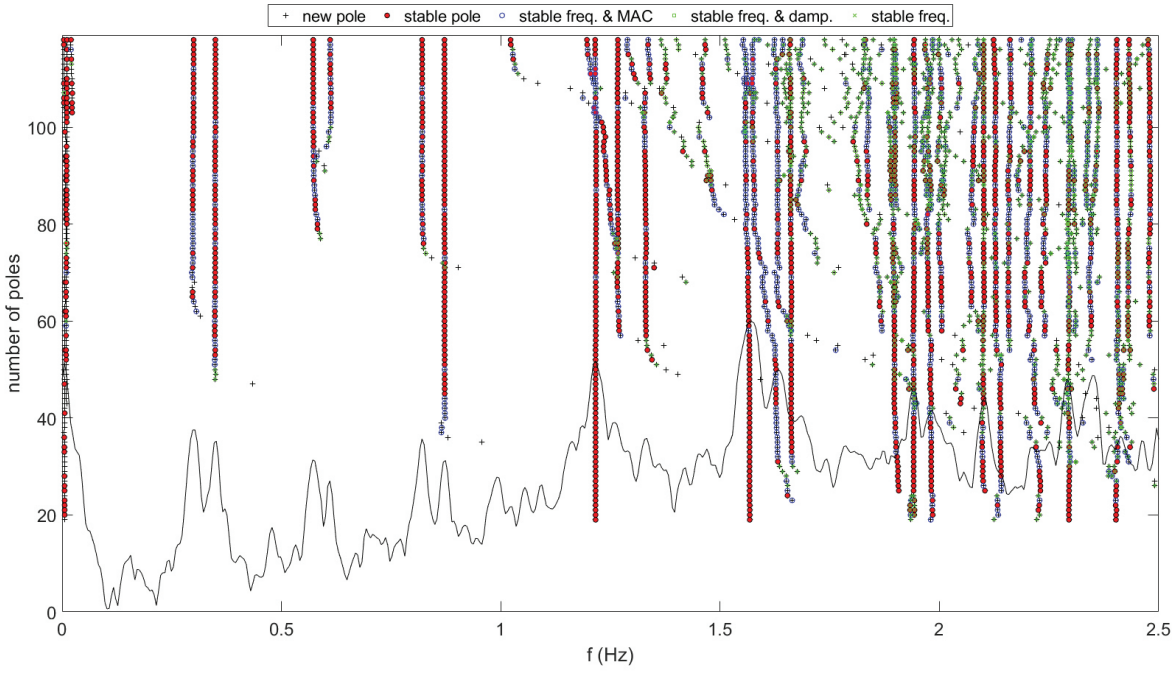

Fig. 2 Stabilization Diagram for ERA-NExT from a Representative Dataset (02MAY2025), Model orders 19 through 119

Finite Element Modeling of the Bridge

A three-dimensional global model of the suspended span of the Bear Mountain Bridge was developed in CSiBridge v24.2.0[17], as shown in Figure 4. The model includes the main cables, suspenders, towers, stiffening trusses, floor trusses, lateral bracings, stringers, concrete deck, tower saddles and other nonstructural components. Main cables and suspenders are modeled by cable elements that incorporate tension-stiffening and large-deflections nonlinearity in the element formulation. Towers, stiffening trusses, floor trusses, lateral bracings and stringers are modeled with beam elements. Shell elements are used for modeling decks, and link elements are used to simulate connections between the stiffening trusses and tower, as well as the stringer bearings. The main cables were anchored to the ground and modeled by pin support. At the top of the bridge tower, the main cable was supported through the tower saddles, joint constraints were defined for the main cable nodes and the tower saddle nodes. At the tower leg, the lateral only restraint provided by the tower to the upper and lower chord members of the stiffening truss were modeled by 1-D link elements. The entire model of the Bear Mountain Bridge consists of about 11,704 nodes, 7961 beam elements, 294 cable elements, 4224 shell elements and 1232 link elements.

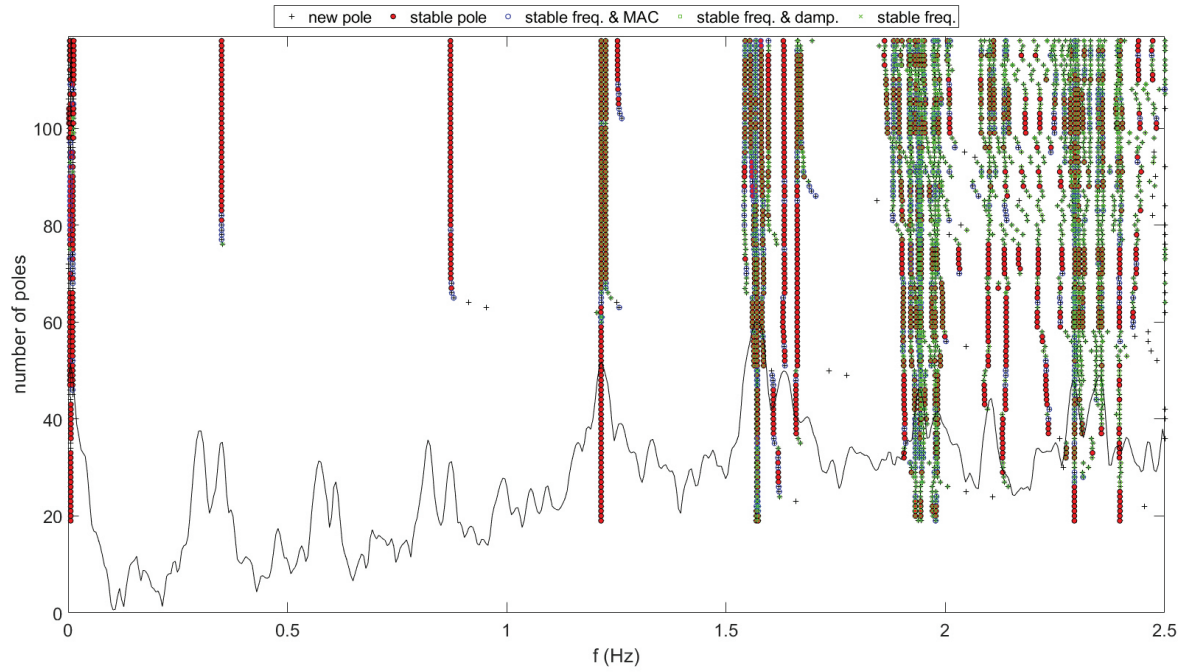

Fig. 3 Stabilization Diagram for SSI-COV from a Representative Dataset (02MAY2025), Model orders 19 through 119

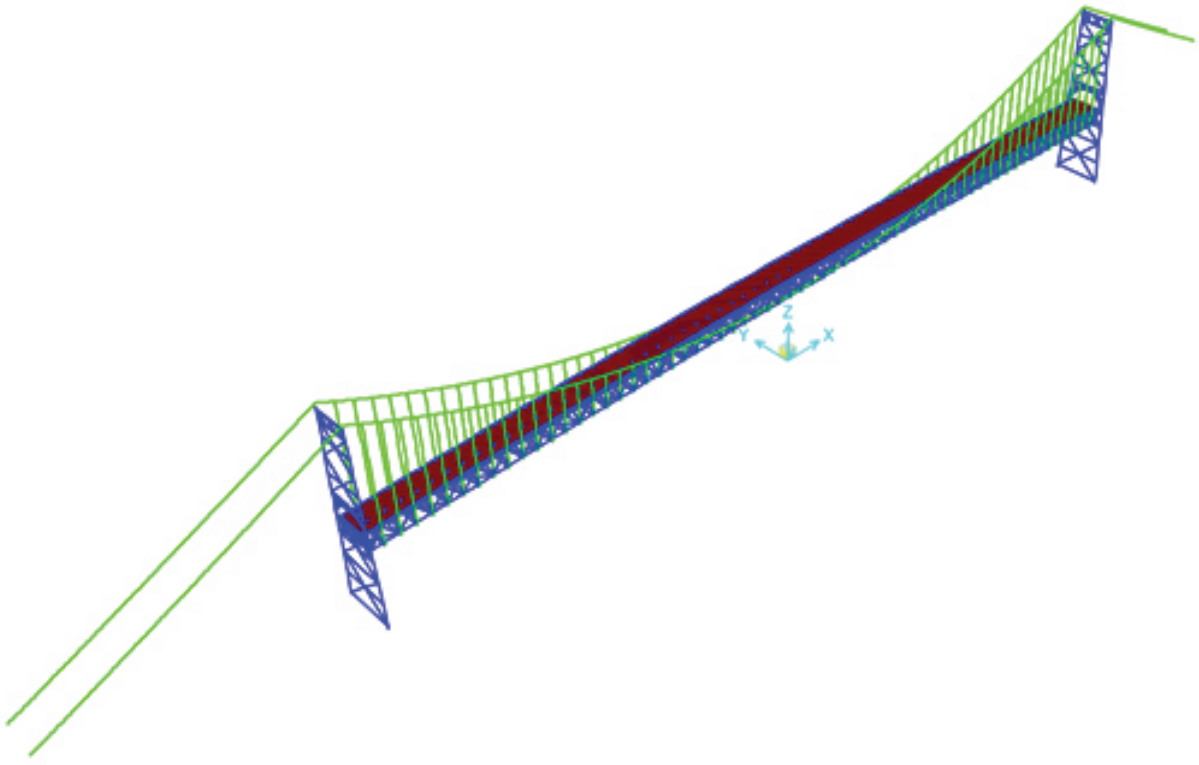

Fig. 4 The three-dimensional FEM model of the Bear Mountain Bridge

The modeling process began with a baseline model representing the bridge as it was originally constructed in the 1920s. Subsequently, a staged construction approach was adopted to simulate the deck replacement and strengthening undertaken in the 1970s, thereby representing the bridge's current existing condition. Model analysis was then conducted based on the stiffness at the end of nonlinear analysis of the dead load condition of the bridge in its current state.

Comparison of Results

The results from stabilization diagram analysis of the bridge are compared against the FEM-identified frequencies. For the Finite Element Model, the first 100 global modes of the bridge were extracted and compared with those identified from the field measurements. The corresponding mode shapes and frequencies obtained from the finite element model are presented in Figure 5 and Table 1. The results from the stabilization diagram come from a representative dataset. The stabilization diagram results for ERA-NExT identified 9 modes between 0 and 2.5 Hz, with the SSI-COV method identifying 5 modes, all of which align with the results from ERA-NExT. As shown in Table 1, the experimentally identified frequencies are in good agreement with the FEM results. Identifying concurring results with the results of the FEM model gives reasonable certainty that those modes are real modal frequencies. The concurring frequencies also lend credence to the accuracy of the FEM.

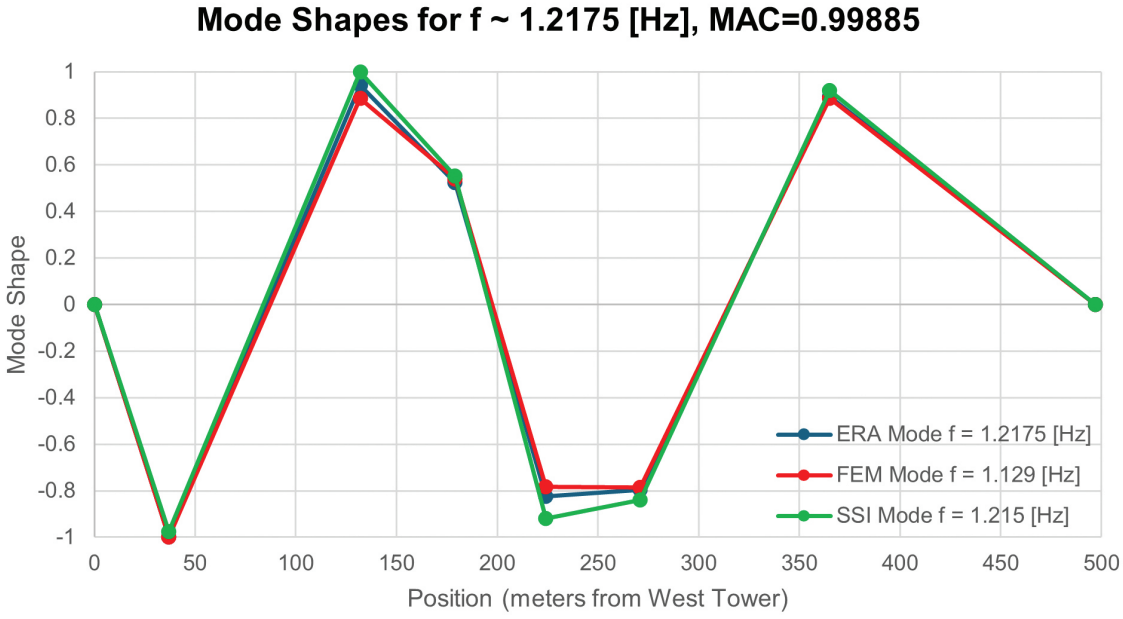

Fig. 5 Mode Shape Comparison for Mode 6

Once modal frequencies have been identified, their associated mode shapes can be analyzed. Comparisons of mode shapes from different methods at similar frequencies are used to validate the mode as a likely real mode. Modal Assurance Criterion or MAC values are computed for each pair of mode shapes from the three different methods and then averaged to give a quantitative evaluation of their correlation. MAC values close to 1 are indicative of concurrence between the different methods. For all nine identified modes, the average MAC values between the FEM, ERA-NExT, and SSI-COV methods remained close to 1, with mode shape concurrence decreasing as the modal frequencies increased. Due to high MAC values, reasonable certainty is gained that these identified modes are accurate, and that the mode shapes are representative of the dynamic response of the structure.

An example of the mode shape comparison is given in Figure 5 for Mode Six, a vertical mode, where the MAC value was computed to be 0.999. It is important to note the inherent limitation in spatial resolution of the estimated mode shape based on the limited number of fixed sensors. With six sensors, it is only possible to reconstruct mode shapes that have five or fewer points of inflection. Mode shape ordinates from the FEM model were selected at distances to match those of the sensors in order to demonstrate the concurrence between the mode shapes.

Table 1 Frequency Results from Stabilization Diagrams

Mode Number	Mode Type (V,T,?)	Modal Identification Results (02MAY25 Dataset)		FEM Results	Average MAC Values
		ERA-NExT	SSI-COV		
1	V	0.300	–	0.275	0.9988
2	?	0.349	0.350	0.340	0.9983
3*	?	0.572	–	0.526	0.9893
4	V	0.821	–	0.719	0.9989
5*	?	0.872	0.872	0.797	0.9995
6	V	1.217	1.215	1.129	0.9989
7	V	1.943	–	1.832	0.9839
8	T	2.101	2.101	2.050	0.8730
9*	?	2.478	2.358	2.510	0.8239

V = vertical mode, T = torsional mode, ? = unverified mode type. * = New Modes identified by Stabilization Diagrams.

Conclusion

This paper presents a continued analysis of the modal properties of the Bear Mountain Bridge based on vibration measurements from a network of six accelerometers. Through the use of stabilization diagrams for multiple methods, operational modes were calculated and validated by cross-checking modal frequency values and mode shapes through MAC value analysis, with operational modes identified by stabilization diagrams compared to modes identified from a finite element model. A total of nine modes were identified by ERA-NExT with five of those modes also identified by SSI-COV. All nine modes from ERA-NExT were also identified by the FEM out of the first 100 global modes of the model. Modal frequencies ranged from 0.3 to 2.5 Hz.

Mode estimation of the Bear Mountain Bridge through the use of stabilization diagrams further validates previously identified modes and establishes the usability of stabilization diagrams for future structural health monitoring. The strong concurrence between experimental results and FEM results highlights the accuracy of the FEM developed. With the Bear Mountain Bridge undergoing major renovations in 2026, this baseline modal analysis for the existing structure also offers the opportunity to identify in the future the impact of changing the bridge deck on its modal properties.

Acknowledgments We would like to thank the New York State Bridge Authority and the staff of the Bear Mountain Bridge for their help in planning, installing, and maintaining the sensor network used in this work. We would also like to thank Courtney Clark and Dr. Qian Chen for their work in providing the results from a Finite Element Model of the structure allowing us to compare results.

References

1. Reynders, E. “System Identification Methods for (Operational) Modal Analysis: Review and Comparison.” *Arch Computat Methods Eng* 19, 51–124 (2012). https://doi.org/10.1007/s11831-012-9069-x
2. Farrar, Charles R., and Keith Worden. Structural health monitoring: a machine learning perspective. John Wiley & Sons, 2012.
3. New York State Bridge Authority, *The Bear Mountain Bridge*. https://nysba.ny.gov/bridge/bear-mountain_
4. Pakzad, S. N. and Fenves, G. L., *Statistical Analysis of Vibration Modes of a Suspension Bridge Using Spatially Dense Wireless Sensor Network.* J. Struct. Eng., vol. 135, no. 7, pp. 863–872, 2009, doi: 10.1061/(asce)st.1943-541x.0000033.
5. Brincker, R., Zhang, L., Andersen, P., *Modal Identification of Output-Only Systems using Frequency Domain Decomposition*. Proceedings of the European COST F3 Conference on System Identification & Structural Health Monitoring, June 2000.
6. James III, George H., Carne, Thomas G., and Lauffer, James P., *The natural excitation technique (NExT) for modal parameter extraction from operating wind turbines*. Sandia National Labs, No. SAND-92-1666, Albuquerque, NM (United States), 1993.
7. Reynders, E., *Uncertainty Quantification in Data-driven Stochastic Subspace Identification*. Mechanical Systems and Signal Processing, 151, April 2021.
8. Caicedo, J., *Practical Guidelines for the Natural Excitation Technique (NExT) and the Eigensystem Realization Algorithm (Era) For Modal Identification Using Ambient Vibration*. Experimental Techniques, July/August 2011.
9. F. Magalhães, Á. Cunha, and E. Caetano, “Online automatic identification of the modal parameters of a long span arch bridge,” *Mechanical Systems and Signal Processing*, vol. 23, no. 2, pp. 316–329, Feb. 2009, doi: https://doi.org/10.1016/j.ymssp.2008.05.003.

10. Farrar, Charles R., and Keith Worden. Structural health monitoring: a machine learning perspective. John Wiley & Sons, 2012.
11. New York State Bridge Authority, *The Bear Mountain Bridge*. https://nysba.ny.gov/bridge/bear-mountain_
12. Pakzad, S. N. and Fenves, G. L., *Statistical Analysis of Vibration Modes of a Suspension Bridge Using Spatially Dense Wireless Sensor Network.* J. Struct. Eng., vol. 135, no. 7, pp. 863–872, 2009, doi: 10.1061/(asce)st.1943-541x.0000033.
13. M. Pourgholi, M. Mohammadzadeh Gilarlue, T. Vahdaini, and M. Azarbonyad, "Influence of Hankel Matrix Dimension on System Identification of Structures Using Stochastic Subspace Algorithms," *Mechanical Systems and Signal Processing*, vol. 186, p. 109893, Mar. 2023, doi: https://doi.org/10.1016/j.ymssp.2022.109893.
14. Al-Rumaithi, Ayad. *NExT-ERA* (https://www.mathworks.com/matlabcentral/fileexchange/72170-next-era). MATLAB Central File Exchange.
15. Cheynet, Etienne, Jakobsen, J. B., and Snæbjörnsson, J., *Damping estimation of large wind-sensitive structures.* Procedia Engineering, vol. 199, pp. 2047–2053, January 2017, doi: https://doi.org/10.1016/j.proeng.2017.09.471.
16. Cheynet, Etienne, *Operational modal analysis with automated SSI-COV algorithm.* April 2020, doi: https://doi.org/10.5281/zenodo.3774061.
17. CSI. CSI Analysis Reference Manual for SAP2000, ETABS, SAFE, and CSiBridge. Computers and Structures, Inc., Berkeley, CA, 2017.

Chapter 11
Experimental System Identification and Tower-Top Dynamic Response of Monopile-Supported Offshore Wind Turbines During Installation

Saravanan Bhaskaran, Max Kruse, Andrew Goupee and Amrit Verma

Abstract The upscaling of offshore wind turbines (OWTs) in pursuit of improved efficiency introduces new structural dynamics challenges during the installation phase due to large hub heights. The blade–hub mating process, in particular, demands high precision, and unpredictable tower-top motion during this phase can result in damage to blades or guide pins. This paper presents a scaled experimental study on the dynamic response of monopile-supported OWTs based on the International Energy Agency (IEA) 10 MW and 15 MW reference turbines fabricated at 1:70 Froude-scale. System identification tests were conducted for both models to extract modal parameters such as natural frequencies, damping ratios, mode shapes, and stiffness distributions. The tower-top motions of the 10 MW model were subsequently measured under regular waves in a controlled flume environment. This work provides benchmark data to support predictive modeling, digital twin development, and control strategies for future offshore wind turbine installations.

Keywords Offshore · Turbine · Dynamics · Modal · Installation

Introduction

Offshore wind energy is expanding worldwide as the demand for large-scale renewable power grows, leading to the deployment of increasingly larger turbines. Monopile-supported offshore wind turbines (OWTs) have become the predominant foundation solution for the deployment of wind energy infrastructure in shallow to intermediate water depths due to their structural simplicity and cost-effectiveness. The installation phase of OWTs presents significant engineering challenges distinct from their operational state, as the system experiences a variety of dynamic loads that include wind, wave, and installation-induced forces prior to commissioning. A fundamental barrier to the robust and safe deployment of OWTs lies in understanding and quantifying their dynamic response during installation. The blade–hub mating process represents one of the most critical junctures in the installation of OWTs, as it requires precise alignment under dynamic environmental conditions. At this stage, the monopile, tower and nacelle are already installed in the hammerhead configuration, while the blades are lifted to the hub height by a crane vessel for attachment. OWTs are known to exhibit complex elliptical orbits with rapidly changing directions at the tower top in the hammerhead configuration [1], which can lead to damage at the blade root or the guide pins. Such risks underscore the potential to compromise equipment integrity, jeopardize personnel safety, and disrupt project schedules, making it essential to thoroughly investigate and characterize these responses.

A practical and cost-effective approach to investigating the underlying physics of complex engineering systems is through carefully designed scaled model tests conducted under controlled laboratory conditions [2]. Several studies have investigated the dynamic behavior of monopile-supported offshore wind turbines during their design and operational phases, employing scaled laboratory experiments and numerical simulations to evaluate modal properties and soil–structure interaction [3, 4, 5, 6, 7, 8]. These works have provided valuable insights into the long-term performance of monopile foundations under combined environmental loading conditions, including the effects of scour, soil stiffness, and nonlinear vibrations in waves. However, the majority of these efforts have focused on fully operational turbines, where the structural configuration and

Saravanan Bhaskaran · Max Kruse · Andrew Goupee · Amrit Verma
Department of Mechanical Engineering, University of Maine, USA
e-mail: saravanan.bhaskaran@maine.edu; max.kruse@maine.edu; agoupe91@maine.edu; amrit.verma@maine.edu

© The Author(s), under exclusive license to River Publishers 2026

Kristin B. Zimmerman, PhD (eds.), *Topics in Modal Analysis & Parameter Identification in Structural Dynamics, 2026, Vol. 8*,
Conference Proceedings of the Society for Experimental Mechanics Series, https://doi.org/10.13052/rp-9788743814191

boundary conditions differ significantly from those encountered during installation. As a result, there remains a lack of experimentally validated data capturing the unique dynamic responses that occur in the hammerhead configuration during installation.

This paper presents an experimental study focused on the design and testing of fully flexible 1:70 scale models of the International Energy Agency (IEA) 10 MW [9] and 15 MW [10] reference turbines in the hammerhead configuration. The natural frequencies, damping ratios, mode shapes, and stiffness distributions of both models were derived through a series of free-decay tests, roving accelerometer modal tests, and pull-out tests. The experimental findings were compared with high-fidelity numerical predictions to validate the modeling assumptions and highlight the sensitivities critical to installation planning. The 10 MW model was later installed in a wave flume where tower top motions were recorded for various regular wave conditions.

Methodology

This study focuses on the design and experimental testing of fully flexible 1:70 Froude-scaled models of the IEA 10 MW and 15 MW reference turbines in the hammerhead configuration, developed to replicate the dynamic response characteristics of the corresponding full-scale systems. Firstly, the approach used to obtain the experimental models is illustrated in Fig. 1, which depicts the progression from the full-scale distributed springs numerical model (baseline) to the final fabricated experimental model.

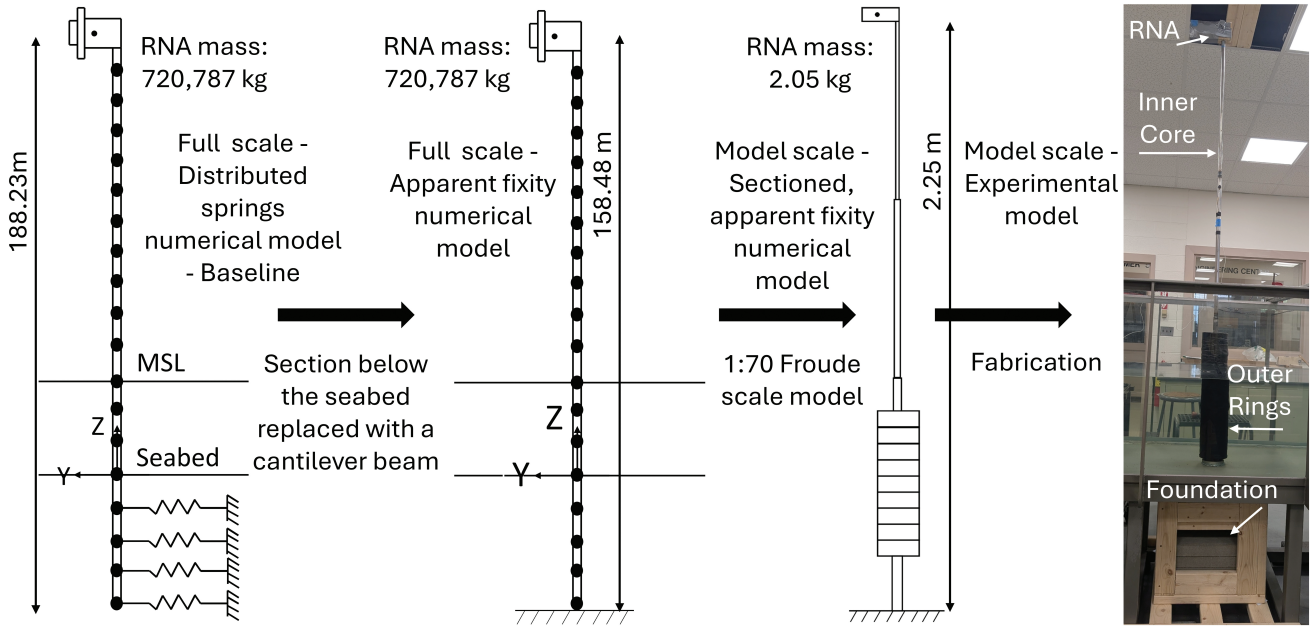

Fig. 1 Development of the 1:70 Froude-scale experimental model of the IEA 10 MW turbine

The numerical models used in this study were developed using the ASHES software package [11], a finite element analysis tool specifically designed for dynamic analyses of wind turbines. In the baseline representation, soil–structure interaction was modeled using a series of linear springs distributed along the embedded section of the monopile. Each node below the seabed was assigned three translational and three rotational stiffness constraints, with stiffness values calculated according to the equations provided in the IEA 15 MW turbine reference document [10]. The shear modulus of the soil was selected to represent dense sand conditions. The monopile and tower were modeled using Timoshenko beam elements, while the rotor–nacelle assembly (RNA) was represented as a lumped point mass with an eccentric offset relative to the tower axis. While the distributed springs model provides an accurate representation of the real soil–structure interaction, it is difficult to reproduce experimentally. Therefore, the apparent fixity method is adopted to simplify the soil representation by replacing the embedded section with an equivalent cantilever beam. The equivalent cantilever section below the seabed is required to produce the same deflection and rotation at the mudline as obtained from the baseline model. To achieve this, the 50-year return period load case was applied to the baseline model, assuming the turbine location along the U.S. East Coast near

New York. The resulting forces and bending moments were thereafter used to determine the equivalent bending stiffness and apparent fixity length, as described in [12]. The Froude scaling method was then used to reduce the structure to model-scale in order to preserve dynamic similarity between the model and the prototype. Froude scaling was chosen because wave–structure interactions are governed primarily by gravity, making the Froude number the controlling non-dimensional parameter. The primary Froude scaling relationships applied in this study are: length with λ, time with $\lambda^{0.5}$, mass and force with λ^3, and bending stiffness with λ^5, where λ is the scale factor. Since the full-scale structure features a varying diameter along its height, the model was divided into three uniform-diameter sections above the seabed and one section below the seabed to represent the embedded portion. The bending stiffness of the three sections above the seabed was averaged to match the overall stiffness distribution of the prototype, while the stiffness of the section below the seabed was accounted for using the apparent fixity method. The effectiveness of this sectioning approach in replicating the stiffness distribution of the prototype is shown in Fig. 2, where the modeled piecewise distribution of bending stiffness (EI) is compared with the baseline distributed springs representation for both turbines. This sectioning approach simplifies fabrication while retaining the essential dynamic fidelity of the prototype.

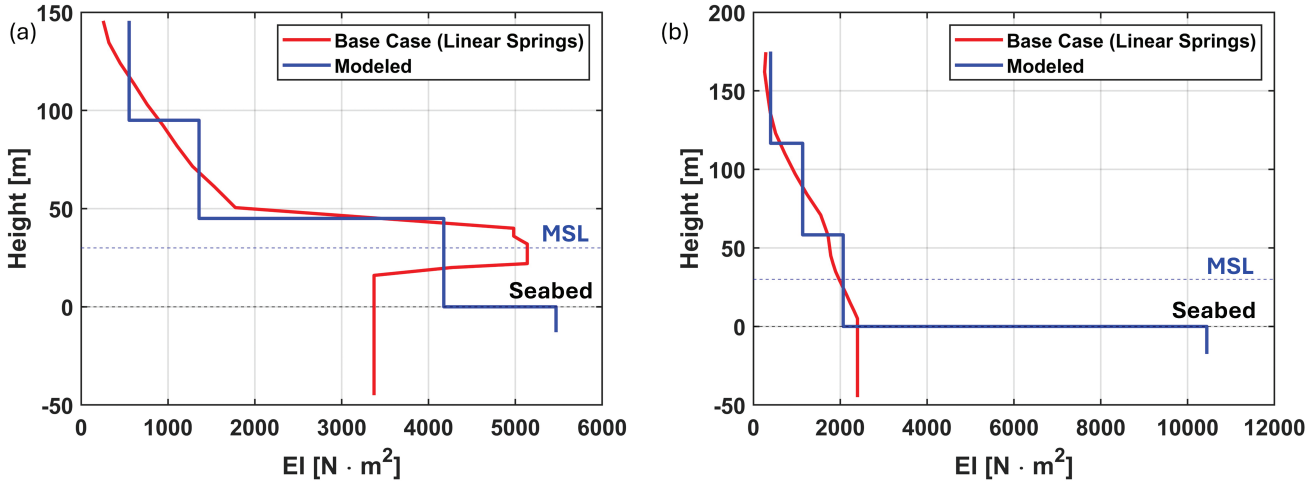

Fig. 2 Comparison of bending stiffness distributions: (a) IEA 10 MW (b) IEA 15 MW *Note: all values are reported in full-scale*

The experimental structure was assembled by welding four steel tube sections, each selected to achieve the required bending stiffness. An outer ring made of lightweight plastic was attached to the first section above the seabed to match the correct hydrodynamic diameter. The section below the seabed was clamped to a foundation containing heavy concrete slabs to enforce the fixed-end boundary condition at the base.

Results

System identification tests

Free decay tests

Free-decay tests were performed to identify the natural frequencies and damping ratios of the scaled turbine models. In these tests, the tower was excited using a rubber mallet, allowing the structure to oscillate freely. The resulting acceleration time histories were recorded with a piezoelectric accelerometer, and logarithmic decrement analysis was applied to estimate the damping ratios.

Two sets of modes were identified in both the fore–aft (FA) and side–side (SS) directions for the scaled turbine models. The corresponding natural frequencies and damping ratios for the 10 MW and 15 MW turbines are summarized in Tables 1 and 2, respectively. To align the first set of natural frequencies with the baseline model, the RNA mass was artificially increased by approximately 13% for the 10 MW model and 8% for the 15 MW model. This study focuses primarily on the first set of modes, as they are the most critical for capturing tower-top motions.

Table 1 Comparison of natural frequencies for the 10 MW turbine model

Mode	Baseline [Hz]	Modeled [Hz]	Experiment [Hz]	Damping [%]
Mode 1 (SS)	0.296	0.293	0.295	0.092
Mode 1 (FA)	0.297	0.294	0.297	0.175
Mode 2 (FA)	1.606	2.437	2.235	0.365
Mode 2 (SS)	1.622	2.498	2.309	0.316

Table 2 Comparison of natural frequencies for the 15 MW turbine model

Mode	Baseline [Hz]	Modeled [Hz]	Experiment [Hz]	Damping [%]
Mode 1 (SS)	0.185	0.185	0.185	0.279
Mode 1 (FA)	0.185	0.185	0.185	0.308
Mode 2 (FA)	1.182	1.604	1.548	0.244
Mode 2 (SS)	1.208	1.633	1.582	0.229

Mode shapes

Mode shapes for both turbine models were obtained using roving accelerometer tests. An impulse force hammer was used to excite the tower at both hub height and mid-height in order to capture the first and second sets of modes. Measurements were taken at 18 elevations along the tower height in both the fore–aft and side–side directions. The acceleration time histories and the impact forces were recorded for each case. Frequency response functions (FRFs) were computed, and the modal displacements were normalized with respect to the maximum value. Multiple hammer strikes were performed at each sensor location to account for variability in the manual excitation. To ensure consistency, only normalized displacements that deviated by less than 5% from the baseline results were retained for analysis. Out of the eight mode shapes extracted, two representative cases are shown in Fig. 3, and these exhibit good agreement with the baseline results, indicating that the scaled models capture the dynamic behavior of the prototypes.

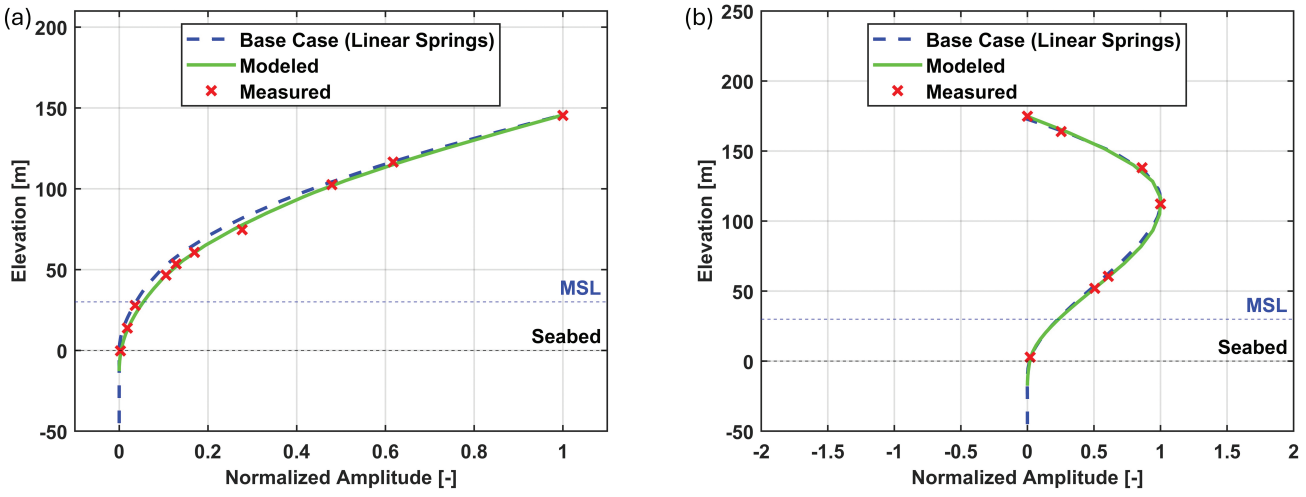

Fig. 3 Representative mode shapes (a) 10 MW 1st SS mode (b) 15 MW 2nd FA mode *Note: all values are reported in full-scale*

Pull-out tests

The stiffness of the physical models was evaluated through pull-out tests. Six measurement points were marked along the elevation of the tower, and varying known weights were applied near the tower top using a string and pulley arrangement to simulate static horizontal loading. The resulting displacements were measured with a high-speed camera. A reference image with a ruler was used to establish a pixel-to-millimeter conversion ratio, and the displacement of each marked point was determined by comparing images taken before and after the application of the loads. Tests were performed in all four

directions by rotating the foundation 90° for each iteration. Stiffness was calculated as the ratio of applied force to measured displacement, and the inverse (flexibility) was also derived, as shown in Fig. 4.

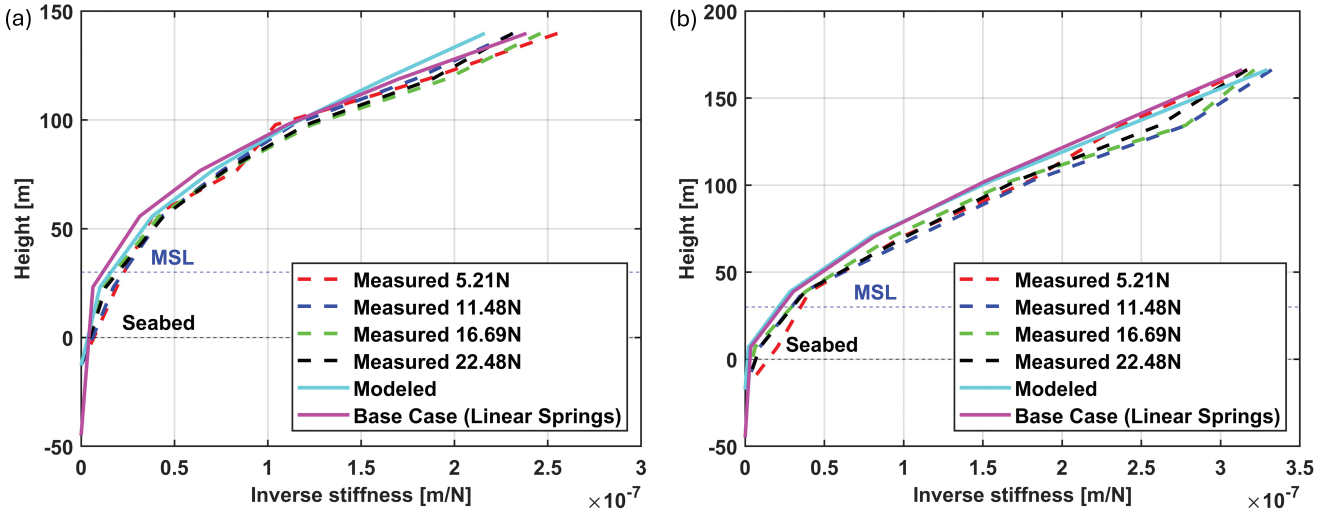

Fig. 4 Inverse stiffness distributions (a) 10 MW -X direction (b) 15 MW +X direction *Note: all values are reported in full-scale*

The results indicate strong linearity in stiffness and good agreement between the baseline and experimental observations.

Tower top motions

The 10 MW model was installed in a 10 m long wave flume to characterize its tower-top motion response under regular wave conditions. Two single-axis accelerometers were mounted on the nacelle to record motions in the X and Y directions at the tower-top. The tests were conducted at a model-scale wave height of 30 mm with periods of 0.4 s and 0.5 s, and an incident wave angle of 45°. Each load case was repeated six times, resulting in a total of 12 motion recordings. Each recording was approximately 1.25 minutes in duration, corresponding to about 10 minutes at full-scale. The recorded acceleration time histories were subsequently integrated twice, with appropriate filtering, to obtain the tower-top displacement trajectories in both the X and Y directions. Figure 5a illustrates the two-dimensional (2D) motion path at the tower top for a resonance case,

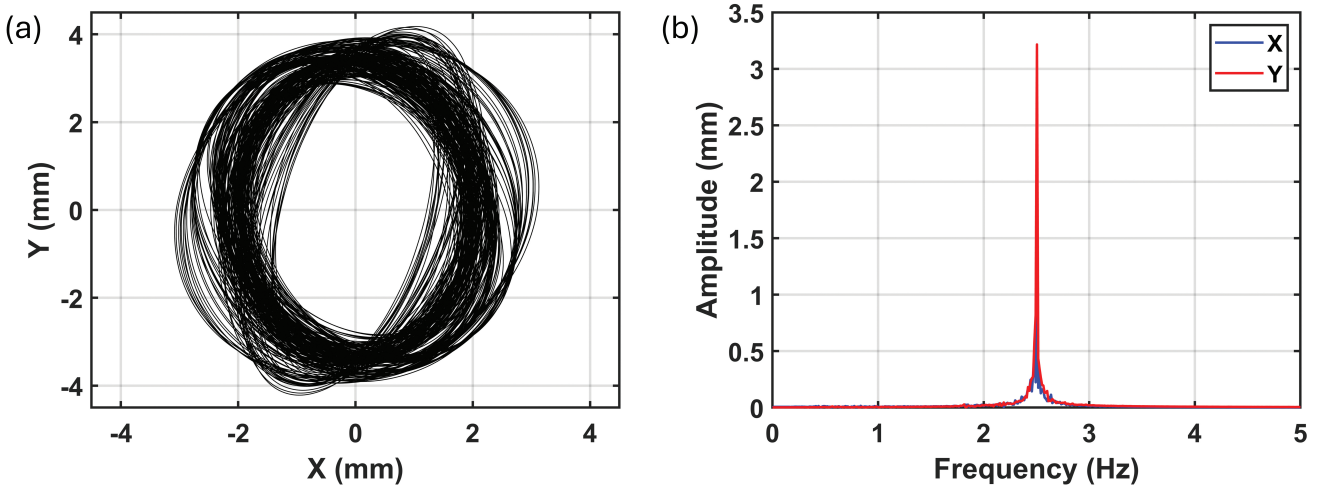

Fig. 5 (a) 2D motion path at the tower-top for H = 30 mm, T = 0.4 s θ_{wv} = 45° (b) frequency-domain response *Note: all values are reported in model-scale*

where the wave period of 0.4 s is close to the fundamental natural period of the system. In the frequency-domain response (Fig. 5b), a single sharp peak is observed at the resonant frequency of approximately 2.5 Hz. The time-domain trajectory reveals pronounced elliptical orbits that continuously change orientation. Such motions present significant challenges during the blade–hub mating phase, as the instability and rapid variation in orbital direction can hinder precise alignment.

Figure 6a shows the 2D motion trajectory at the tower top for the non-resonant case with a wave period of 0.5 s. The motion amplitude is significantly smaller compared to the resonant case, and the orbit remains consistently aligned with the incident wave angle of 45°. In the frequency-domain response (Fig. 6b), the dominant peak corresponds to the wave frequency of 2 Hz, accompanied by a smaller peak at the structural resonant frequency. Two additional secondary peaks are observed near the wave frequency, which result from reflected waves interacting to form a standing wave with a frequency offset of approximately 0.11 Hz. Minor noise contributions from the accelerometers are also visible, particularly due to the small displacement amplitudes.

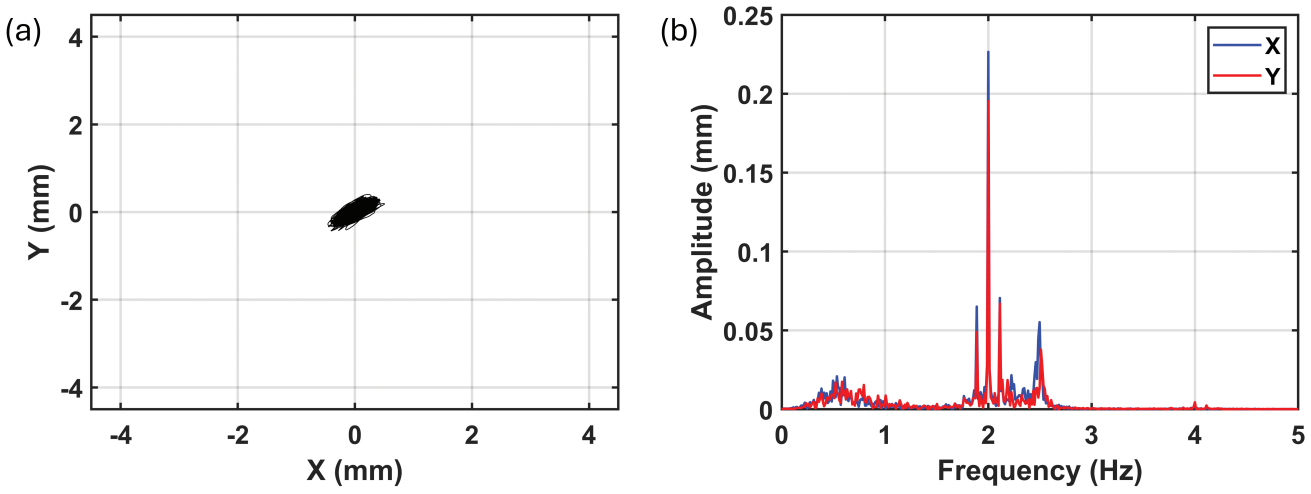

Fig. 6 (a) 2D motion path at the tower-top for H = 30 mm, T = 0.5 s $\theta_{wv} = 45°$ case (b) frequency-domain response *Note: all values are reported in model-scale*

Conclusions

This study presented fully flexible 1:70 scale models of the IEA 10 MW and 15 MW turbines in the hammerhead configuration, with system identification tests showing close agreement with numerical predictions of key dynamic properties. These results confirm the validity of the modeling approach and the suitability of the scaled structures for dynamic investigations. Tower-top motions of the 10 MW model were further characterized under regular wave forcing in a controlled wave flume. Resonant excitation produced complex elliptical orbital motions with rapidly changing orientations, while non-resonant conditions yielded small, stable orbits aligned with the wave direction. Such results highlight the dynamic instabilities that can occur during the blade–hub mating phase and underscore the importance of accounting for tower-top orbital motions in installation planning. Overall, the findings provide benchmark experimental data and validated modeling strategies that can support predictive tools, digital twin development, and improved risk management practices for offshore wind turbine installation.

Acknowledgments This research is funded by the National Science Foundation (NSF) through the Division of Chemical, Bioengineering, Environmental and Transport Systems (CBET) under Grant No. 2343210.

References

1. A. Sander, A. F. Haselsteiner, K. Barat, M. Janssen, S. Oelker, J.-H. Ohlendorf, and K.-D. Thoben, "Relative motion during single blade installation: Measurements from the north sea," in *International Conference on Offshore Mechanics and Arctic Engineering*, vol. 84416, p. V009T09A069, American Society of Mechanical Engineers, 2020.

2. S. Bhattacharya, G. Nikitas, and S. Jalbi, "On the use of scaled model tests for analysis and design of offshore wind turbines," in *Geotechnics for Natural and Engineered Sustainable Technologies: GeoNEst*, pp. 107–129, Springer, 2018.
3. L. Kerner, J.-C. Dupla, G. Cumunel, P. Argoul, J. Canou, and J.-M. Pereira, "Experimental study on a scaled model of offshore wind turbine on monopile foundation," in *Models, Simulation, and Experimental Issues in Structural Mechanics*, pp. 249–267, Springer, 2017.
4. R. Mayall, R. McAdam, B. Byrne, H. Burd, B. Sheil, P. Cassie, and R. Whitehouse, "Experimental modelling of the effects of scour on offshore wind turbine monopile foundations," in *Physical Modelling in Geotechnics, Volume 1*, pp. 726–730, CRC Press, 2018.
5. A. Buljac, H. Kozmar, W. Yang, and A. Kareem, "Concurrent wind, wave and current loads on a monopile-supported offshore wind turbine," *Engineering structures*, vol. 255, p. 113950, 2022.
6. S. Tian, C. Zhang, and Z. Wang, "Experimental study on the dynamic response of monopile supported offshore wind turbines in sand," *Ocean Engineering*, vol. 326, p. 120913, 2025.
7. S. Wu, H. Zhang, Z. Chen, X. Liu, L. Zheng, M. Du, R. Li, and D. Li, "Experimental study on nonlinear vibrations of flexible monopile-foundation offshore wind turbines in regular waves," *Water*, vol. 17, no. 8, p. 1176, 2025.
8. E. E. Bachynski, M. Thys, and F. Dadmarzi, "Observations from hydrodynamic testing of a flexible, large-diameter monopile in irregular waves," in *Journal of Physics: Conference Series*, vol. 1669, p. 012028, IOP Publishing, 2020.
9. P. Bortolotti, H. C. Tarres, K. Dykes, K. Merz, L. Sethuraman, D. Verelst, and F. Zahle, "Iea wind tcp task 37: Systems engineering in wind energy-wp2. 1 reference wind turbines," 2019.
10. E. Gaertner, J. Rinker, L. Sethuraman, F. Zahle, B. Anderson, G. Barter, N. Abbas, F. Meng, P. Bortolotti, W. Skrzypinski, *et al.*, "Definition of the iea 15-megawatt offshore reference wind turbine," 2020.
11. L. Suja-Thauvin, P. Thomassen, and A. Simis, "Engineering features summary,"
12. E. Bush and L. Manuel, "Foundation models for offshore wind turbines," in *47th AIAA aerospace sciences meeting including the new horizons forum and aerospace exposition*, p. 1037, 2009.

Chapter 12
Verification and Convergence of Multi-Harmonic Balance Algorithms for Future Application in Sierra/SD Finite Element Code

Oliver Khan, Dalton L. Stein, Nathan Schill, Robert J. Kuether, and David M. Day

Keywords Harmonic balance · Numerical continuation · Forced response curves · Nonlinear vibrations

Background

Engineered structures are frequently subjected to cyclic loading. Examples include rotating compressor blades in aircraft engines [1], buildings subjected to alternating heating and cooling cycles [2], and materials that are periodically stretched and compressed during testing [3]. Since cyclic loading is so prevalent, engineering industries have sought tools for predicting a structure's steady-state response to time-periodic forcing, particularly in the presence of nonlinearities. A common approach is to discretize a structure into a finite element model and use numerical time integration (TI) to compute the response over time. Although TI captures stable periodic orbits with high accuracy, small time-steps are needed to resolve high-frequency oscillations and long integration times are often required for the response to converge to a steady state. As an alternative to TI, the method of multi-harmonic balance (MHB) is increasingly adopted in mechanics and dynamics research to approximate the steady-state response of a nonlinear system to a time-periodic input. MHB represents the response as a finite Fourier series in time, and then applies a Fourier–Galerkin projection to the spatially-discretized governing equations from a finite element model. This yields a set of nonlinear algebraic equations for the Fourier coefficients of the response, which are solved using iterative techniques such as the Newton–Raphson method [4]. This approach offers efficiency by directly solving for the steady-state response, unlike TI which must process transient dynamics before reaching the steady state. When combined with numerical continuation [5], MHB can also compute a curve of periodic solutions as a parameter is varied. A notable example is the forced response curve (FRC), which shows the amplitude of a steady-state response as a (possibly multivalued) function of the forcing frequency. While TI only captures stable periodic orbits, MHB computes both stable and unstable solutions along an FRC, providing a more complete picture of a system's dynamics [4].

Despite its promise, the computational cost of MHB can increase significantly with the number of Fourier harmonics used, particularly for large-scale models. This occurs because the number of algebraic equations to be solved scales as $(2N_h + 1)n$, where N_h is the number of Fourier harmonics and n is the number of degrees of freedom in the finite element

Oliver Khan
Stanford University, Department of Mechanical Engineering
e-mail: ogkhan@stanford.edu

Dalton L. Stein
University of Rhode Island, Department of Mechanical, Industrial and Systems Engineering
e-mail: daltonstein98@uri.edu

Nathan Schill
Brigham Young University, Department of Mathematics
e-mail: schilln@mathematics.byu.edu

Robert J. Kuether · David M. Day
Sandia National Laboratories*
e-mail: rjkueth@sandia.gov; dmday@sandia.gov

*Sandia National Laboratories is a multimission laboratory managed and operated by National Technology and Engineering Solutions of Sandia, LLC., a wholly owned subsidiary of Honeywell International, Inc., for the U.S. Department of Energy's National Nuclear Security Administration under contract DE-NA-0003525.

© The Author(s), under exclusive license to River Publishers 2026

Kristin B. Zimmerman, PhD (eds.), *Topics in Modal Analysis & Parameter Identification in Structural Dynamics, 2026, Vol. 8*,
Conference Proceedings of the Society for Experimental Mechanics Series, https://doi.org/10.13052/rp-9788743814191

model. Understanding the convergence properties of MHB and determining the necessary Fourier basis for accurate solutions are crucial. While MHB is popular in research, its integration into commercial software remains limited, though some advancements have been made in MSC Nastran [6] and ANSYS [7]. The objective of the present work was to expand the utility of MHB in large-scale commercial codes by preparing an MHB algorithm for implementation in Sierra/Structural Dynamics (SD) finite element code at Sandia National Laboratories. Building upon an existing MATLAB implementation of MHB with pseudo-arclength continuation [4], an improved MHB algorithm was written in Sierra/SD's native language, C++. This C++ implementation and the original MATLAB implementation were verified by comparing FRCs with those computed using TI. It was important to verify both codes because the C++ algorithm was intended for future use in Sierra/SD and the MATLAB algorithm formed the basis of the C++ algorithm. After verification, the convergence of the C++ and MATLAB MHB algorithms was assessed for varying numbers of harmonics. The error metrics used in the convergence study were then used to create an adaptive algorithm that automatically selected the harmonics included in the response. In the future, this work will lay the groundwork for further MHB developments in Sandia's finite element codes, aimed at addressing challenges such as frictional damping and nonlinear viscoelastic behavior.

Implementation of Multi-Harmonic Balance

The multi-harmonic balance (MHB) algorithms in C++ and MATLAB required knowledge of spatially-discretized governing equations of the form

$$\mathbf{M}\ddot{\mathbf{x}} + \mathbf{C}\dot{\mathbf{x}} + \mathbf{K}\mathbf{x} + \mathbf{f}_{\text{nl}}(\mathbf{x}, \dot{\mathbf{x}}) = \mathbf{f}_{\text{pre}} + \mathbf{f}_{\text{ext}}(t), \tag{1}$$

where $\mathbf{M}, \mathbf{C}$, and $\mathbf{K}$ were the linear mass, damping, and stiffness matrices, respectively; $\mathbf{f}_{\text{nl}}(\mathbf{x}, \dot{\mathbf{x}})$ was the vector of nonlinear internal forces; $\mathbf{f}_{\text{pre}}$ was the constant preload force; and $\mathbf{f}_{\text{ext}}(t)$ was the time-periodic external force with fundamental frequency ω. The displacement vector $\mathbf{x}(t) \in \mathbb{R}^n$ was approximated by the truncated Fourier series,

$$\mathbf{x}(t) = \frac{\mathbf{c}_0^x}{\sqrt{2}} + \sum_{k=1}^{N_h} [\mathbf{c}_k^x \cos(k\omega t) + \mathbf{s}_k^x \sin(k\omega t)], \tag{2}$$

which converged based on the number of harmonics, N_h, included in the expansion. Substituting Eq. (2) into Eq. (1) and performing a Fourier-Galerkin projection onto the first N_h harmonics yielded a system of nonlinear algebraic equations for the Fourier coefficients $\mathbf{z} = \begin{bmatrix}(\mathbf{c}_0^x)^\top & (\mathbf{c}_1^x)^\top & (\mathbf{s}_1^x)^\top & \cdots & (\mathbf{c}_{N_h}^x)^\top & (\mathbf{s}_{N_h}^x)^\top\end{bmatrix}^\top$ of the displacement $\mathbf{x}$:

$$\mathbf{r}(\mathbf{z}, \omega) = \mathbf{A}(\omega)\mathbf{z} + \mathbf{b}_{\text{nl}}(\mathbf{z}) - \mathbf{b}_{\text{pre}} - \mathbf{b}_{\text{ext}} = \mathbf{0}. \tag{3}$$

In Eq. (3), $\mathbf{A}(\omega)$ encompassed the linear dynamics obtained from Fourier-Galerkin projection; $\mathbf{b}_{\text{nl}}$, $\mathbf{b}_{\text{pre}}$, and $\mathbf{b}_{\text{ext}}$ were Fourier coefficients of the nonlinear, preload, and time-periodic external forces, respectively; and $\mathbf{r}(\mathbf{z}, \omega) \in \mathbb{R}^m$ was the frequency domain residual with $m = (2N_h + 1)n$ being the problem dimension. In the numerical continuation procedure, ω was unknown at each step beyond the initial starting frequency. In order to solve for both $\mathbf{z}$ and ω at subsequent locations along an FRC, an additional constraint equation was appended to Eq. (3) such that the residual function became

$$\tilde{\mathbf{r}}(\mathbf{y}) = \begin{bmatrix} \mathbf{A}(\omega)\mathbf{z} + \mathbf{b}_{\text{nl}}(\mathbf{z}) - \mathbf{b}_{\text{pre}} - \mathbf{b}_{\text{ext}} \\ \mathbf{V}^\top(\mathbf{y} - \mathbf{y}^{(k=1)}) \end{bmatrix} = \mathbf{0}, \tag{4}$$

where $\mathbf{y} = \begin{bmatrix}\mathbf{z}^\top & \omega\end{bmatrix}^\top \in \mathbb{R}^{m+1}$ was the augmented vector of unknowns. Equation (4) was solved using Newton-Raphson iterations to a specified tolerance, ε_h.

Distinct Features of C++ Multi-Harmonic Balance Algorithm

The existing MATLAB MHB implementation utilized direct solves of the linear systems arising in the predictor-corrector scheme, which was known to be a substantial bottleneck in MHB continuation [4]. This work aimed to extend the work done in [4] and develop a code specifically tailored to large-scale systems. Therefore, the new C++ implementation utilized Krylov subspace methods to iteratively solve the linear systems during each continuation step. A known challenge for iterative methods in path-following problems was that the constraint equation could only be approximately satisfied due to the tolerance set for the iterative solver. To overcome this, the non-augmented Jacobian derived from Eq. (3) was mapped through a linear transformation matrix, $\mathbf{Q} \in \mathbb{R}^{m+1 \times m}$, such that the constraint equation was enforced on the iterates of the Krylov method. The construction of $\mathbf{Q}$ was based on Householder transformations, as outlined in [8]. The iterative solver used here was the bi-conjugate gradient stabilized method (BiCGSTAB) [9].

Verification

The C++ and MATLAB MHB implementations were verified on two related benchmark systems shown in Fig. 1. The cantilever beam in Fig. 1a was meshed with 10 Euler–Bernoulli beam elements, yielding 10 rotational and 10 translational degrees of freedom. Table 1 contains further details on the spatial geometry and material properties of the beam, as well as the cubic nonlinear spring attached to the beam's free end.

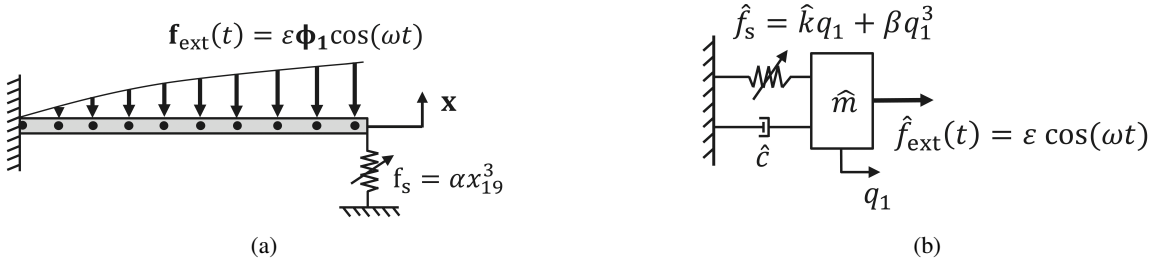

Fig. 1 (a) Model of the cantilever beam with cubic spring and (b) the Duffing oscillator obtained by projecting the beam-spring model onto its first linear normal mode.

Table 1 Parameters for Cantilever Beam Finite Element Model

Length × Width × Thickness [m]	$1 \times 0.00635 \times 0.003175$
Young's Modulus [GPa]	70
Density [kg m^{-3}]	2880
Modal Damping Ratio, ζ [%]	0.75
Nonlinear Spring Stiffness, α [N m^{-3}]	518.7

The Duffing oscillator in Fig. 1b was a single-degree-of-freedom reduced-order model of the beam-spring system obtained by projecting the full-order model onto its first linear normal mode, ϕ_1. The Duffing oscillator's governing equation was given by

$$\ddot{q}_1 + 2\zeta\omega_1\dot{q}_1 + \omega_1^2 q_1 + \beta q_1^3 = \varepsilon\cos(\omega t), \tag{5}$$

where q_1 was the modal displacement of ϕ_1, $\zeta = 0.0075$, $\omega_1 = 15.9$ rad s^{-1}, $\beta = 10^6$, and $\varepsilon = 0.025$.

Convergence

Three approaches were taken to assess the convergence of the C++ and MATLAB MHB codes: (i) a residual equation defined in the time domain, (ii) a residual equation defined in the frequency domain, and (iii) the magnitudes of individual harmonics in the computed displacement $\mathbf{x}$. The time-domain and frequency-domain residuals were defined by Eq. (6) and Eq. (7), respectively, and measured how well $\mathbf{x}$ and $\mathbf{z}$ satisfied the system dynamics:

$$\mathbf{R}(t) = \mathbf{M}\ddot{\mathbf{x}} + \mathbf{C}\dot{\mathbf{x}} + \mathbf{K}\mathbf{x} + \mathbf{f}_{\text{nl}}(\mathbf{x}, \dot{\mathbf{x}}) - \mathbf{f}_{\text{pre}} - \mathbf{f}_{\text{ext}}(t) \tag{6}$$

$$\mathbf{r}_{N_h^r}(\mathbf{z}, \omega) = \mathbf{A}(\omega)\mathbf{z} + \mathbf{b}_{\text{nl},N_h^r}(\mathbf{z}) - \mathbf{b}_{\text{pre}} - \mathbf{b}_{\text{ext}}. \tag{7}$$

Equation (7) is re-written distinct from Eq. (3) to emphasize the role of N_h^r, the number of harmonics assumed in the discrete Fourier transform when computing the Fourier coefficients of the nonlinear forcing, $\mathbf{b}_{\text{nl}}$, using the alternating frequency/time method [1, 4]. When first computing the solution $\mathbf{z}$ during the numerical continuation procedure, N_h^r was set equal to N_h, meaning that the number of harmonics in the nonlinear force vector, $\mathbf{b}_{\text{nl}}$, was the same as the number of harmonics included in the response, $\mathbf{z}$. However, when assessing the convergence of the MHB algorithms, N_h^r was set larger than N_h to study the change in the frequency domain residual, $\mathbf{r}_{N_h^r}$, when additional harmonics were accounted for in the nonlinear force vector but not in the response. This provided a relative metric to assess the increase or decrease in accuracy of a solution $\mathbf{z}$ that accounted for more or fewer of the higher harmonics introduced by the nonlinear forcing. After solving

for $\mathbf{R}$ and $\mathbf{r}_{N_h^r}$ in Eqs. (6)–(7), dimensionless error metrics were defined by normalizing the magnitudes of the time and frequency domain residuals by the magnitudes of the external forces:

$$E_{\mathbf{x}} = \frac{\|\mathbf{R}\|_{L^2([0,\,2\pi/\omega])}}{\|\mathbf{f}_{\text{pre}} + \mathbf{f}_{\text{ext}}\|_{L^2([0,\,2\pi/\omega])}} \tag{8}$$

$$E_{\mathbf{z}} = \frac{\|\mathbf{r}_{N_h^r}\|_2}{\|\mathbf{b}_{\text{pre}} + \mathbf{b}_{\text{ext}}\|_2}. \tag{9}$$

For a given fundamental forcing frequency ω, the L^2 norm of the time domain residual $\mathbf{R}(t)$ (and analogously, the external forces) over a single oscillation period was:

$$\|\mathbf{R}\|_{L^2([0,\,2\pi/\omega])} = \sqrt{\int_0^{2\pi/\omega} \mathbf{R}^\top(t)\mathbf{R}(t)\,dt}. \tag{10}$$

Separate from the error metrics $E_{\mathbf{x}}$ and $E_{\mathbf{z}}$ defined above, the magnitudes of the coefficients of the solution $\mathbf{z}$ were examined for different values of ω. Following [10], the coefficient magnitudes were normalized by the norm of the solution $\mathbf{z}$, such that $|\hat{\mathbf{z}}_i|/\|\mathbf{z}\| := \sqrt{\|\mathbf{c}_i^x\|^2 + \|\mathbf{s}_i^x\|^2}/\|\mathbf{z}\|$ represented the fraction of the solution's spectral energy contained in the i-th harmonic. Together, the error metrics given by Eq. (8) and Eq. (9), along with the spectral energy contained in the i-th harmonic, were used to explore an adaptive harmonic selection algorithm, which will be discussed in the presentation.

Results

For brevity, verification and convergence results are only shown for the cantilever beam. Analogous results for the Duffing oscillator will be provided in the presentation. Figure 2a shows forced response curves (FRCs) computed with time integration (TI), as well as the C++ and MATLAB multi-harmonic balance (MHB) algorithms with five harmonics included in the response (denoted H_5). All three methods showed strong agreement with each other, providing evidence that the C++ and MATLAB algorithms were implemented correctly. Figure 2b, meanwhile, shows the normalized L^2 norm of the time domain residual as a function of forcing frequency for odd numbers of harmonics. (Even harmonic orders are not shown because the cubic nonlinearity of the spring caused odd harmonics to dominate the response.) As the number of harmonics

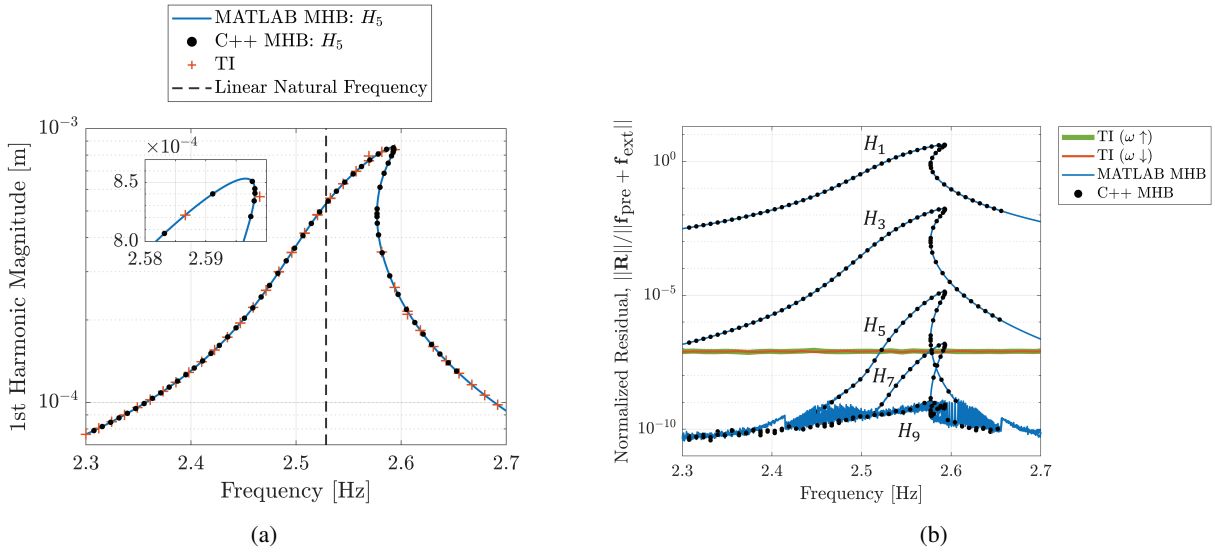

(a) (b)

Fig. 2 (a) First harmonic of the beam tip displacement, x_{19}, vs. forcing frequency and (b) normalized L^2 norm of the time domain residual vs. forcing frequency, for time integration (TI) and multi-harmonic balance (MHB) implementations in C++ and MATLAB. The notation H_j means that $N_h = j$ harmonics were included in the Fourier series expansion of the response in MHB. Note that in (a), the plus markers represent TI for both increasing and decreasing ω, while in (b), the TI data is separated based on whether ω was increasing ($\uparrow$) or decreasing ($\downarrow$).

included in MHB increased from one (H_1) to nine (H_9), the residual magnitude decreased, indicating that the approximation to the response became more accurate with more harmonics. The largest residual magnitudes coincided with the peak of the FRC. This higher error near the peak helped explain the small discrepancy between TI and the MHB algorithms in Fig. 2a near a forcing frequency of 2.595 Hz (see inset). Furthermore, the C++ and MATLAB MHB algorithms had nearly identical residual magnitudes in Fig. 2b for all harmonic orders. This agreement between the C++ and MATLAB residuals served as another form of verification, as it suggested that both algorithms were computing the same solutions at each harmonic order. It was also important to observe that the C++ and MATLAB normalized residual magnitudes in Fig. 2b saturated near 10^{-10}. This represented the limit of maximum possible accuracy given the C++ algorithm's linear solve tolerance and the MATLAB algorithm's residual tolerance. Increasing the harmonic order beyond nine had diminishing returns on accuracy unless the tolerances of the MHB solvers were lowered.

Acknowledgments This research was conducted at the 2025 Nonlinear Mechanics and Dynamics Research Institute hosted by Sandia National Laboratories and the University of New Mexico. Sandia National Laboratories is a multimission laboratory managed and operated by National Technology and Engineering Solutions of Sandia, LLC., a wholly owned subsidiary of Honeywell International, Inc., for the U.S. Department of Energy's National Nuclear Security Administration under contract DE-NA-0003525.

References

1. Y. Colaïtis and A. Batailly, "The harmonic balance method with arc-length continuation in blade-tip/casing contact problems," Journal of Sound and Vibration, vol. 502, p. 116070, 2021.
2. A. Athienitis, "A methodology for integrated building–HVAC system thermal analysis," Building and Environment, vol. 28, no. 4, pp. 483–496, 1993.
3. S. Patra, P. M. Ajayan, and T. N. Narayanan, "Dynamic mechanical analysis in materials science: The Novice's Tale," Oxford Open Materials Science, vol. 1, p. itaa001, Jan. 2021.
4. R. Kuether and A. Steyer, "Large-scale harmonic balance simulations with Krylov subspace and preconditioner recycling," Nonlinear Dynamics, vol. 112, pp. 1–22, 2024.
5. R. Seydel, *Practical Bifurcation and Stability Analysis*, vol. 5, Springer Science & Business Media, 2009.
6. D. Najera-Flores and R. J. Kuether, "Application of multi-harmonic balance for nonlinear frequency response analysis in MSC Nastran," presented at the 40th International Modal Analysis Conference (IMAC XL), 2022.
7. M. Kwarta, "An overview of ANSYS harmonic balance method: Current capabilities and future directions," presented at the 43rd International Modal Analysis Conference (IMAC XLIII), 2025.
8. H. F. Walker, "An Adaptation of Krylov Subspace Methods to Path Following Problems," SIAM Journal on Scientific Computing, vol. 21, no. 3, pp. 1191–1198, 1999.
9. H. A. van der Vorst, "Bi-CGSTAB: A fast and smoothly converging variant of Bi-CG for the solution of nonsymmetric linear systems," SIAM Journal on Scientific and Statistical Computing, vol. 13, no. 2, pp. 631–644, 1992.
10. A. Grolet and F. Thouverez, "On a new harmonic selection technique for harmonic balance method," Mechanical Systems and Signal Processing, vol. 30, pp. 43–60, 2012.

Chapter 13
Quantification of Vibrational Power Dissipation in a Coupled Panel System Using Experimental Modal Analysis

Karsten Hilgarth, Yeongeun Ki, Daniel Litowitz, Eric Williamson, Karthik Boddapati, Hongcheng Tao, Charlotte Moss, Greg Shaver, John T. Evans, Andres F. Arrieta, and James M. Gibert

Abstract To quantify the vibrational energy available in composite panels used in the construction of semi-truck trailers, this work investigates the power dissipated through internal damping as these panels undergo dynamic loading during road travel. Modal impact testing of a single 1.24 m x 2.49 m panel was conducted to extract the structure's natural frequencies, mode shapes, and damping ratios. Using this modal model, operational acceleration data collected during road testing were projected into modal coordinates and integrated to obtain modal velocities. These velocities, combined with the previously identified modal parameters, were used to estimate the instantaneous power dissipated in the dominant modes. The resulting average power dissipation reflects the rate at which vibrational energy is lost through internal damping and serves as a minimal upper bound for the mechanical energy that could be harvested using passive devices. Results across 19 road segments show that the average dissipated power ranges from $\sim$ 0.5–20 W, with peak values exceeding 6 kW during transient events. These results support the future development of piezoelectric or triboelectric energy harvesters integrated into trailer panels to help reduce the alternator load in heavy vehicles.

Keywords Experimental modal analysis · Operational data · Vibrations · Power dissipation · Energy scavenging

Introduction

Commercial vehicle manufacturers are investigating methods to reclaim energy that is typically wasted during operation to enhance efficiency. A viable method involves extracting vibrational energy from trailer sidewall panels, which are frequently stimulated by uneven road surfaces, powertrain vibrations, and wind during transit. As a result these lightweight composite panels waste energy through continuous vibrations, and partial recovery of this energy could decrease alternator demand, enhancing fuel efficiency and reducing emissions [1]. Nevertheless, a significant knowledge gap exists due to the absence of quantification of the panel's vibrational energy. Quantifying the available vibrational energy and comprehending its dissipation within panel structures is crucial for the design and integration of energy harvesters. This effort aims described here outlines the development evaluation of a framework for quantifying the vibrational energy wasted in trailer panels through experimental modal analysis and in-situ road testing.

This work provides a framework for assessing the energy available for different transduction methodologies ranging from electromagnetic to piezoelectric [2, 3] to triboelectric harvesting [4]. The results from this study provide an estimate of dissipated energy, advancing both the understanding of trailer panel dynamics and the development of technologies aimed at increasing the energy efficiency of heavy vehicles.

Karsten Hilgarth · Yeongeun Ki · Daniel Litowitz · Eric Williamson · Karthik Boddapati · Hongcheng Tao · Charlotte Moss · Greg Shaver · John T. Evans · Andres F. Arrieta · James M. Gibert
Ray W. Herrick Laboratories, School of Mechanical Engineering, Purdue University, West Lafayette, IN 47096
e-mail: khilgart@purdue.edu; yki@purdue.edu; dlitowit@purdue.edu; will1904@purdue.edu; kboddapa@purdue.edu; taoh@purdue.edu; moss66@purdue.edu; gshaver@purdue.edu; jevansiv@purdue.edu; aarrieta@purdue.edu; jgibert@purdue.edu

John T. Evans
Department of Agriculture and Biological Engineering, Purdue University, West Lafayette, IN 47096
e-mail: jevansiv@purdue.edu

© The Author(s), under exclusive license to River Publishers 2026

Kristin B. Zimmerman, PhD (eds.), *Topics in Modal Analysis & Parameter Identification in Structural Dynamics, 2026, Vol. 8*,
Conference Proceedings of the Society for Experimental Mechanics Series, https://doi.org/10.13052/rp-9788743814191

The remainder of this paper is organized as follows: the methodology integrating experimental modal analysis with operational road testing is described first, followed by details of the experimental setup and data collection procedures. The subsequent section presents the framework for estimating vibrational power dissipation in modal coordinates, with results from multiple road segments provided for comparison. A discussion of the implications for energy harvesting applications is then given, and the paper concludes with key findings and directions for future research.

Methodology

This study's methodology combines experimental modal analysis with operational observations to assess vibrational energy dissipation in trailer panels. First, modal properties, i.e., natural frequencies, damping ratios, and mode shapes, are identified from controlled impact testing. These parameters establish a reduced-order modal model of the panel. Next, *in-situ* acceleration data are collected under real driving conditions and projected into modal coordinates, enabling the estimation of modal velocities. Finally, the damping related power dissipation is computed in the modal domain, taking advantage of the invariance of power under the transformation between physical and modal coordinates. This combined framework provides a consistent means of linking laboratory based modal characterization with field measurements, thereby allowing reliable estimates of the energy available for harvesting in operational environments.

Experimental Modal Analysis (EMA)

In order to determine the energy dissipated by the panels, the modal properties of the panel were first obtained experimentally. Figure 1 (a) shows the experimental setup used for the modal analysis. The modal analysis is performed on the first full panel from the rear of the trailer. The panel has a width, height, and thickness of approximately 1.24 m x 2.49 m x 0.05 m (≈ 48.8 in × 98.0 in × 2.0 in), and a weight of 38 kg (≈ 83.8 lb). In order to facilitate non-contact measurement, reflective tape is placed on the panel at each of the 25 defined measurement points, as shown in Figure 1 (b). The vibration at each point is measured using a PSV 400-Laser Doppler Vibrometer (LDV), which provides velocity measurements without mass-loading the lightweight panel structure. The system is excited by an instrumented modal hammer (PCB Model 086D20) to provide a broadband, measurable force input, $F(t)$. The hammer is used to excite the panel from inside the trailer at location 13.

For each impact, the LDV records the velocity response of the sample as a function of time, $v(t)$. This time-domain data is then processed to determine the system's frequency response characteristics. Fast Fourier Transform (FFT) is applied to both the input force signal and the output velocity signal to transform them into the frequency domain, yielding the spectra $F(f)$ and $V(f)$.

From these spectra, the Frequency Response Function (FRF) is calculated. The H_1 estimator is typically used for this analysis, as it is formulated to minimize the effect of noise on the output (response) measurement, which is common in experimental setups. The H_1 FRF is calculated as the ratio of the cross-spectrum (G_{fv}) to the auto-spectrum of the input (G_{ff}):

$$H_1(f) = \frac{G_{fv}(f)}{G_{ff}(f)} = \frac{V(f)F^*(f)}{F(f)F^*(f)}, \tag{1}$$

where $F^*(f)$ is the complex conjugate of the force spectrum. Figure 2 shows the plots of Equation 1 for all 25 measurement points and the single excitation point. The quality and linearity of the measurement at each frequency are assessed using the coherence function, $\gamma^2(f)$. A coherence value close to 1.0 indicates a strong linear relationship between the input force and the output response, signifying the structure has sufficient energy to respond at that frequency. Conversely, drops in coherence can indicate noise contamination or nonlinear behavior. In this study $\gamma^2(f) > 0.9$ from 3 to 179 Hz for most points.

Once a set of FRFs is collected for all measurement points on the panel, modal parameter estimation algorithms are employed. These algorithms fit a theoretical modal model to the experimental FRF data to extract the key dynamic properties of the panel as installed: its natural frequencies (ω_n), modal damping ratios (ζ_n), and the corresponding mode shapes ($\vec{\psi}_n$).

Using the FRFs collected for all measurement points on the panel, modal parameters are extracted [5]. Since modal frequency and damping are global properties of the structure, a Global Curve Fitting approach is employed, as described by Richardson and Formenti [6]. This method leverages the entire set of FRF measurements simultaneously to yield a single, consistent set of modal parameters that is more robust than fitting each measurement individually.

The Rational Fraction Polynomial (RFP) method [6] is used to extract modal frequencies and damping ratios from the experimentally obtained frequency response functions. The method fits a ratio of two polynomials to the experimental FRF

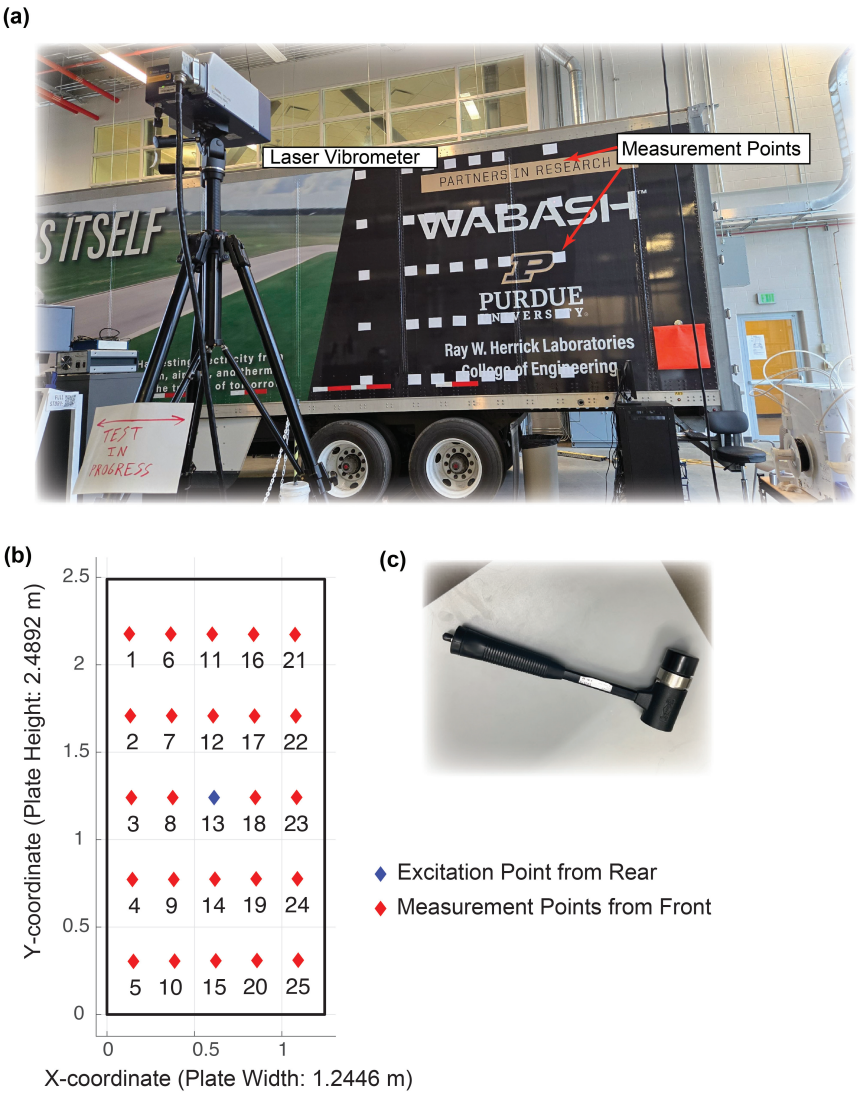

Fig. 1 Experimental setup to measure modeshapes of an individual panel: (a) photo of test setup (b) schematic of sensor locations, and (c) modal impact hammer (PCB Modal 086D20)

data. The roots of the denominator polynomial, known as the system poles, are identified. Each complex-conjugate pair of poles corresponds to a single mode of vibration. For each mode n, the pole p_n is given by:

$$p_n = -\sigma_n + j\omega_{dn}, \tag{2}$$

where σ_n is the damping factor and ω_{dn} is the damped natural frequency. The undamped natural frequency, ω_n, and the modal damping ratio, ζ_n, are then calculated from these pole values:

$$\omega_n = \sqrt{\sigma_n^2 + \omega_{dn}^2} \quad \text{and} \quad \zeta_n = \frac{\sigma_n}{\omega_n}. \tag{3}$$

This global estimation process yields a single, consistent value for the natural frequency and damping ratio for each mode.

The unscaled mode shape amplitudes at the discrete measurement points are estimated by taking the imaginary component of the FRF at each respective modal frequency. Biharmonic spline interpolation is then used to visualize the continuous mode shape across the panel surface, as shown in Figure 3. The first mode at 4.0 Hz is a simple bending mode along the panel's long axis. The second mode at 12.63 Hz exhibits a torsional or twisting motion. The third (24.6 Hz) and fourth (44.88 Hz) modes show higher-order bending and combined bending-torsion shapes, respectively. The fifth mode at 130 Hz is a

Table 1 Modal Frequencies and Damping Ratios of Wall Panel

Mode No. (n)	**Modal Frequencies** (ω_n)	**Damping Ratios** (ζ_n)
1	4.00 Hz	0.033
2	12.63 Hz	0.014
3	24.60 Hz	0.008
4	44.88 Hz	0.006
5	130.00 Hz	0.006

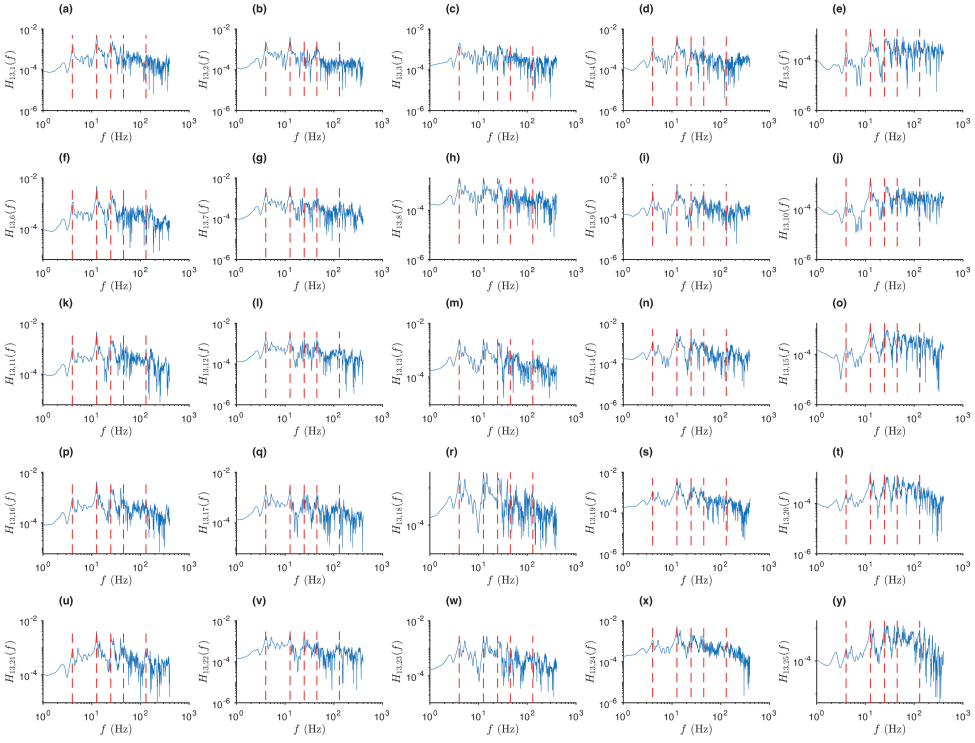

Fig. 2 Frequency Response Function magnitudes for all 25 measurement points relative to the excitation at point 13. The consistency of peak locations across all plots confirms the presence of global structural modes. Red dashed lines indicate the first five modal frequencies identified and used for subsequent power dissipation analysis. The consistency of peaks across FRFs enables a robust global fit

more complex, higher-order plate mode. These five modes were mass normalized and form the basis of the modal model used for subsequent analysis.

Operational Analysis During Road Transport

Figure 4 a) shows the experimental setup used for the operational analysis. The analysis was again conducted on the first full panel from the rear. To capture the panel's response under real-world conditions, five accelerometers (PCB 352C04 and PCB 352A60) are placed on the inside of the panel at key locations. The accelerometers are connected to a Keyence NR-X data logger with an Accelerometer (NR-CA04) module, which records their outputs.

The purpose of this test is to measure the panel's absolute acceleration time histories, $a_k(t)$, while the semi-trailer is driven on public roads. This provides a set of response data that results from the true broadband random excitation input from the road surface, suspension dynamics, and aerodynamic forces. This operational acceleration data serves as the input to the modal model, allowing the projection of the measured physical response onto the previously identified modal coordinates.

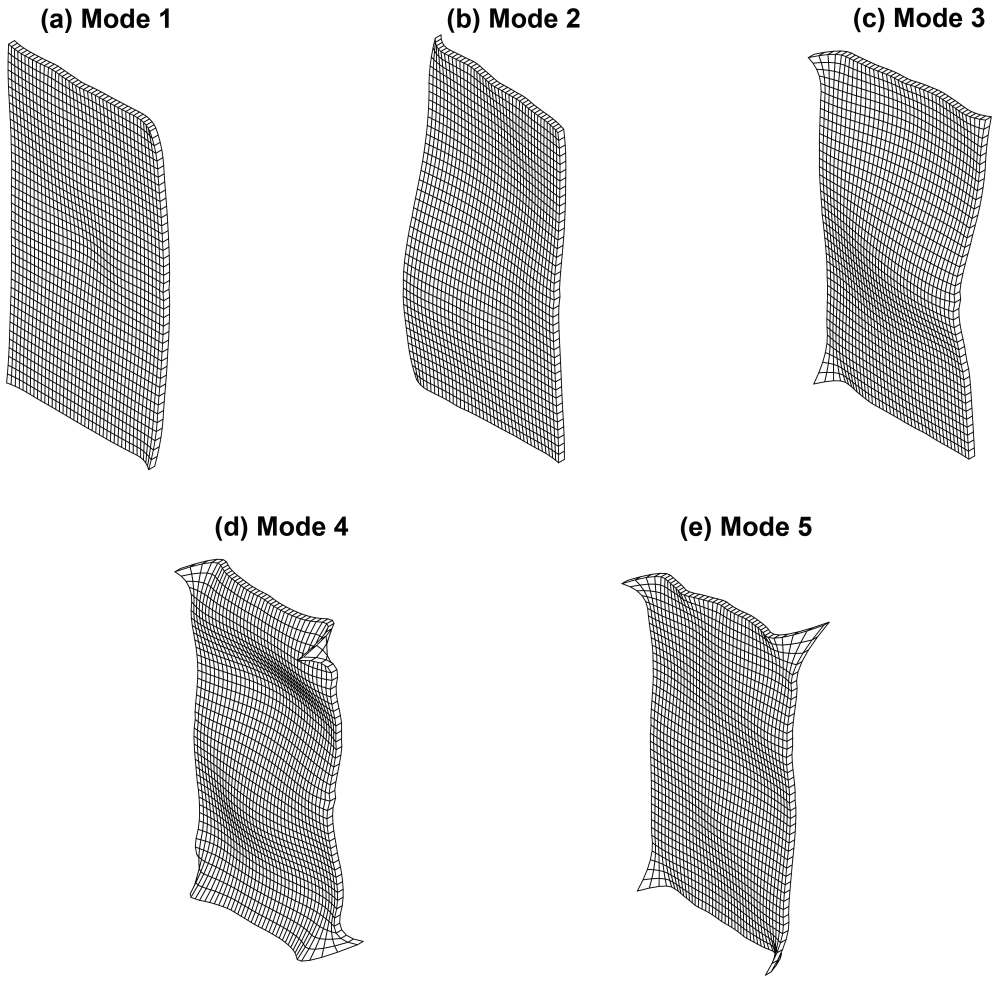

Fig. 3 Five modeshapes of rear panel used in this study: (a) first mode is 4 Hz, (b) second mode is 12.63 Hz, (c) third mode is 24.63 Hz, (d) fourth mode is 44.88 Hz and (e) fifth mode is 130 Hz

The route taken by the trailer in West Lafayette, Indiana is shown in Figure 5. The route consisted of 19 different road segments, named in Figure 5. Figure 6 plots the Power Spectral Density (PSD) for an accelerometer (S1) across the 19 different road segments revealing several consistent patterns in the vibrational environment experienced by the trailer panels. Power spectral density (PSD) estimates were obtained using Welch's method. Unless otherwise noted, the MATLAB pwelch function was applied with parameters: a Hamming window of 256 samples, 50% overlap (128 samples), and a 768-point FFT. With the sampling frequency of $f_s = 1000$ Hz, this configuration provides a frequency resolution of approximately 3.9 Hz based on 256 samples. PSD results are reported in units of power per Hz, using a one-sided spectrum since all signals were real-valued. Across nearly all roads, the dominant spectral energy is concentrated in the low frequency range below 20 Hz, which is typical of road induced base excitation where long-wavelength surface irregularities excite suspension and structural modes. While all roads show broadband excitation extending up to 50–60 Hz, certain segments, such as SR43, SR26, and I65, exhibit notably higher PSD amplitudes, indicating more aggressive vibrational input likely due to surface roughness, speed, or joint transitions. In contrast, roads like US421 show relatively lower energy levels, suggesting smoother or better-maintained pavement. Importantly, the PSDs do not exhibit sharp resonant peaks, implying that structural modes are either well-damped or not strongly excited during typical driving conditions. This behavior suggests that energy harvesting strategies should focus on broadband response within the 2–20 Hz range, rather than tuning to narrowband resonances. These observations also support the classification of roads by excitation severity, providing a basis for fatigue, damage, or energy harvesting analysis under representative operational loading conditions.

To assess whether the acceleration signals could be treated as broadband random processes suitable for power spectral analysis, statistical descriptors were computed in 30-s windows across the full I-65 dataset. For the acceleration signal $a(t)$

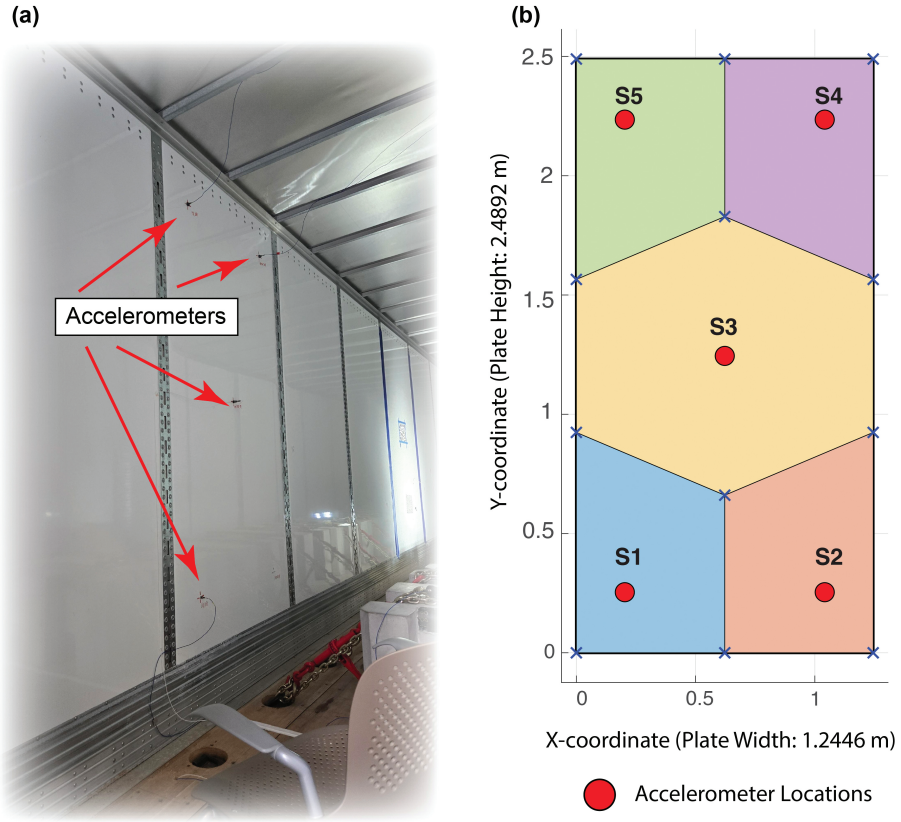

Fig. 4 Experimental setup to perform operational analysis: (a) location of accelerometer, and (b) accelerometer locations and Voronoi tesselation of mass for modal analysis

sampled at N points, the time-domain statistics were computed as:

$$\text{RMS} = \sqrt{\frac{1}{N}\sum_{i=1}^{N} a_i^2}, \quad \text{Crest Factor} = \frac{\max|a_i|}{\text{RMS}}, \quad \text{and} \quad \text{Kurtosis} = \frac{\frac{1}{N}\sum_{i=1}^{N}(a_i - \bar{a})^4}{\left(\frac{1}{N}\sum_{i=1}^{N}(a_i - \bar{a})^2\right)^2}, \tag{4}$$

where $\bar{a}$ is the sample mean.

The results indicate non-stationary but predominantly random-like behavior. RMS values varied from 0.18 to 0.80 m/s^2, with occasional peaks as high as 7.9 m/s^2. Crest factors typically ranged between 4 and 6, though extreme values above 12 were observed, suggesting intermittent impulsive events. Kurtosis values were generally near Gaussian expectations (3–6) but reached as high as 19–24 in isolated windows, further confirming the presence of rare, heavy-tailed transients.

Table 2 Summary statistics for I-65 acceleration data (30-s windows)

Metric	Typical Range	Extreme Values	Interpretation
RMS (m/s^2)	0.18–0.80	–	Varies with road roughness
Peak (m/s^2)	1–3	7.9	Rare large impulses
Crest Factor	4–6	12.9	Broadband with transients
Kurtosis	3–6	19–24	Heavy-tailed distribution

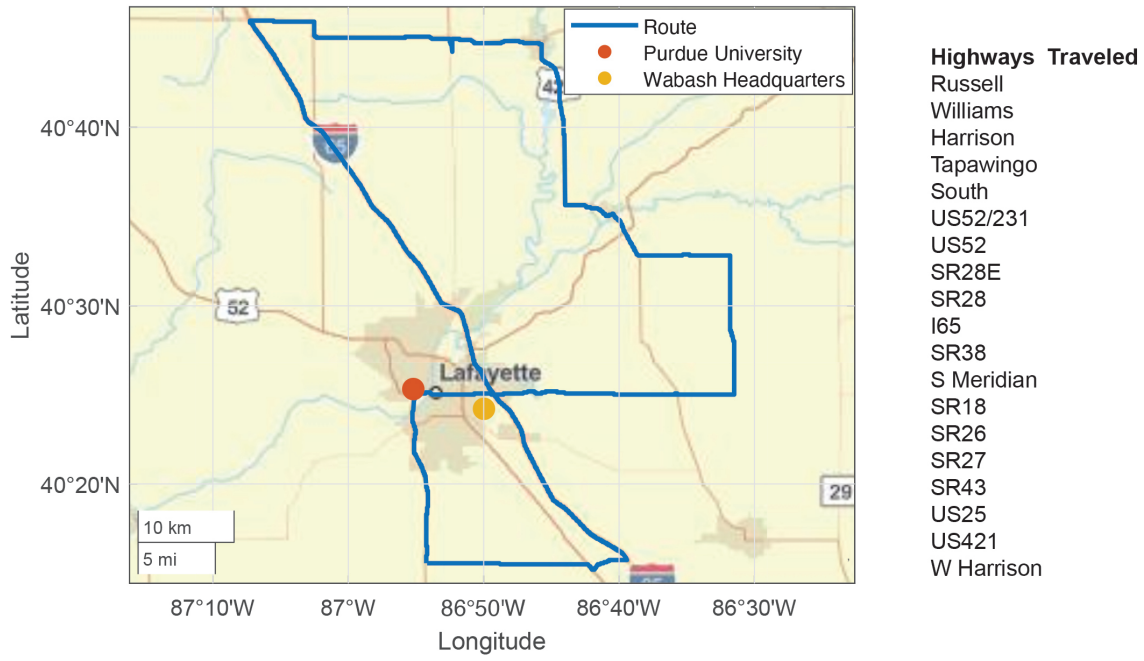

Fig. 5 Route driven in West Lafayette, Indiana by the semi-truck trailer during operational testing to collect panel acceleration data. The loop incorporated 19 distinct road segments, ranging from local streets to interstate highways, providing a diverse set of excitation environments. These segments form the basis for the comparative power and energy dissipation analysis presented in Table 3

Methodology for Energy Dissipation

The following analysis focuses on a single instrumented panel within a larger assembly of 12 coupled panels. The boundary conditions are addressed implicitly; by measuring the modal parameters *in situ*, the stiffening and mass-loading effects of the adjacent panels are inherently captured in the measured mode shapes ($\vec{\psi}_n$) and natural frequencies (ω_n). The calculated power, P_{measured}, represents the energy converted to heat (dissipated) within this single panel due to its internal damping. This calculation is based on the panel's net response, which is the result of all energy inputs from the frame and adjacent panels. It is important to note that this dissipated power is only one of two primary energy pathways for the panel. The second pathway is the net power transmitted across its boundaries to its neighbors, $P_{\text{transmitted}}$. While this analysis does not directly calculate $P_{\text{transmitted}}$, it uses this physical understanding to establish justifiable lower and upper bounds for the energy dissipation of the entire 12-panel system that composes one wall.

Time Domain Modal Velocity Approach

The dissipated vibrational power of the panel is estimated by transforming measured accelerations into modal coordinates and computing the associated damping losses. The procedure consists of four main steps: (i) identification of modal parameters, (ii) estimation of effective mass distribution, (iii) transformation of physical accelerations into modal accelerations and velocities, and (iv) computation of instantaneous and average power. This analsyis is conducted in the time domain since accelerometer signals exhibit quasi-stationary behavior with intermittent transients, as indicated by windowed statistics in Table 2, i.e., RMS variation across windows, crest factors frequently exceeding 6, and occasional high-kurtosis windows). Welch PSD estimates assume in a wide-sense stationarity thus a purely spectral approach can dilute the contribution of short-duration, high-amplitude events. In contrast, our time-domain formulation computes instantaneous modal power and cumulative power and retains the effects of transients. The derivation of the method can be found in the Appendix.

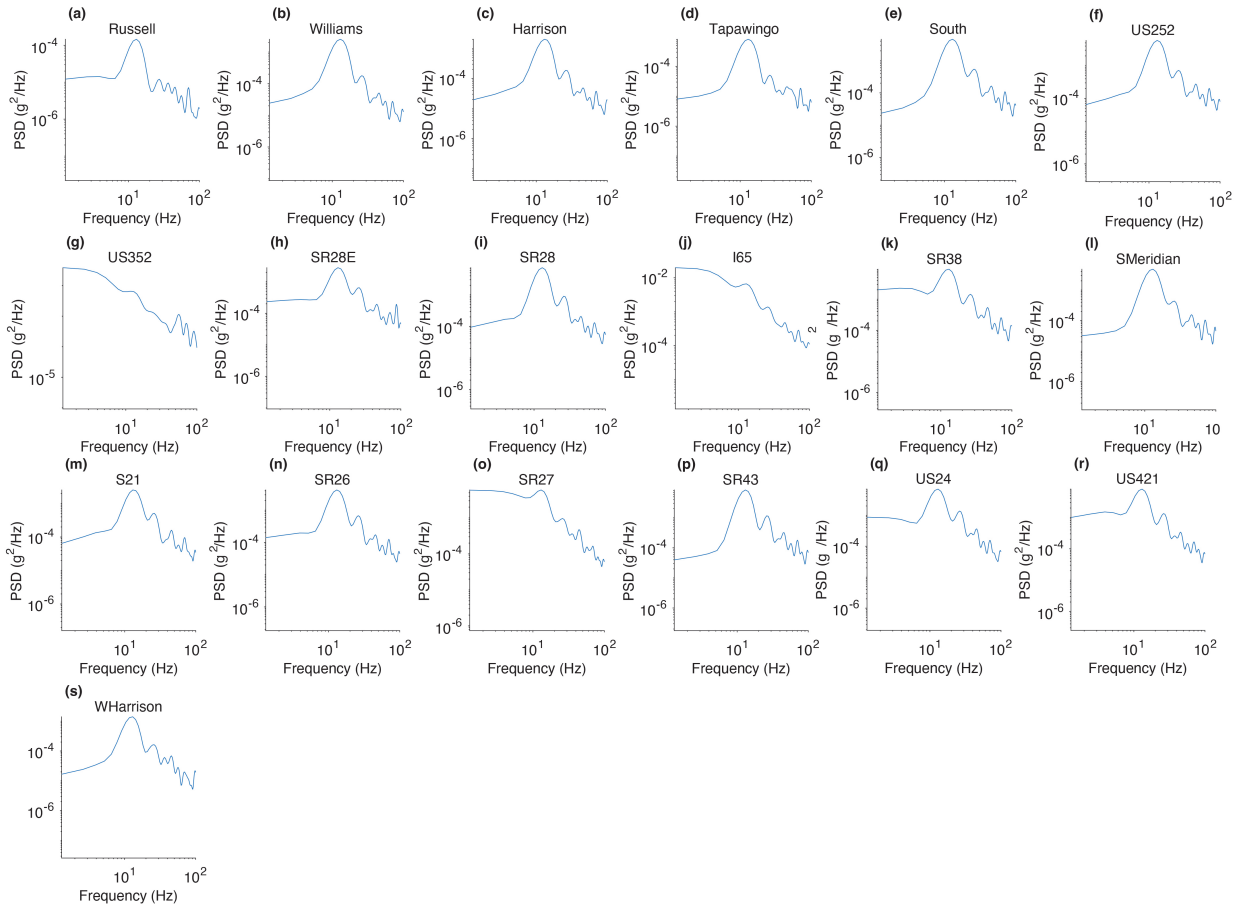

Fig. 6 Power spectral density (PSD) of trailer panel acceleration measured at sensor S1 across 19 road segments. Dominant vibrational content is concentrated below 20 Hz, with broadband excitation extending up to 50–60 Hz. PSDs were estimated using Welch's method (256-sample Hamming window, 50% overlap, 768-point FFT, f_s = 1000 Hz), yielding a frequency resolution of 3.9 Hz. Variations in the number of spectral points across curves reflect differences in road segment duration, as shorter segments contain fewer data samples

Modal Parameter Identification

The experimental modal analysis provided the natural frequencies ω_n, mass-normalized mode shapes $\vec{\psi}_n$, and damping ratios ζ_n for each mode $n = 1, \ldots, N_m$ where N_m is the number of modes retained, i.e, $N_m = 5$ in this study. Because the mode shapes were mass-normalized, the modal mass is unity ($m_n = 1$), and the modal damping coefficient simplifies to

$$c_n = 2\zeta_n\omega_n. \tag{5}$$

Lumped Mass Matrix via Voronoi Tessellation

To account for the spatial distribution of the panel's mass, the physical mass matrix $\mathbf{M}$ is approximated as diagonal with entries M_k representing the effective mass at each measurement location. These lumped values are obtained by partitioning the panel area into Voronoi cells based on sensor positions, clipping the cells to the panel boundary, and scaling by the areal mass density $\rho_A = M_{\text{total}}/A_{\text{total}}$:

$$M_k = \rho_A A_k, \tag{6}$$

where A_k is the area of the clipped cell associated with sensor k. The resulting mass matrix is

$$\mathbf{M} = \text{diag}(M_1, \ldots, M_{N_p}), \tag{7}$$

where N_p defines the number of Voronoi partitions [7]. This method assigns a region of mass to each accelerometer based on proximity. This ensures that every point on the panel is mathematically associated with its nearest sensor, providing an objective basis for the lumped mass matrix.

Transformation to Modal Coordinates

Operational acceleration measurements $a_k(t)$ at N_p points are collected during road tests and assembled into the vector $\vec{a}(t)$. Modal accelerations are then obtained through projection onto the mode shapes:

$$\ddot{q}_n(t) = \vec{\psi}_n^T \mathbf{M} \vec{a}(t) = \sum_{k=1}^{N_p} (\vec{\psi}_n)_k M_k a_k(t). \tag{8}$$

Integration yields the modal velocities,

$$\dot{q}_n(t) = \int \ddot{q}_n(t)\, dt, \tag{9}$$

with appropriate high pass filtering to mitigate drift.

Computation of Dissipated Power

The transformation from physical to modal coordinates preserves the fundamental energy relationships of the system. In particular, the instantaneous power, defined as the inner product of velocity and force, is invariant under this transformation *provided that a sufficiently complete set of modes is retained to represent the motion*; with truncated modal bases, the invariance holds only for the projected component of the response. Thus, whether expressed in the physical coordinates of the measurement points or in the reduced modal coordinates, the computed power remains identical. This invariance ensures that the subsequent analysis of dissipated and transmitted power can be carried out entirely in the modal domain without loss of physical fidelity. The dissipated power per mode n is expressed as

$$P_n(t) = c_n[\dot{q}_n(t)]^2 = 2\zeta_n \omega_n [\dot{q}_n(t)]^2. \tag{10}$$

Summing across modes gives the total dissipated power,

$$P_{\text{dissipated}}(t) = \sum_{n=1}^{N_m} P_n(t). \tag{11}$$

The time-averaged dissipation over a duration T is

$$\overline{P}_{\text{dissipated}} = \sum_{n=1}^{N_m} 2\zeta_n \omega_n \langle [\dot{q}_n(t)]^2 \rangle, \tag{12}$$

where $\langle [\dot{q}_n(t)]^2 \rangle$ denotes the mean-square modal velocity. For the bounding analysis, a factor of $\beta = 3$ was assumed. The accumulated dissipated energy is obtained by integrating power over time,

$$E_{\text{dissipated}}(t) = \int_0^t P_{\text{dissipated}}(\tau)\, d\tau. \tag{13}$$

To bound the total vibrational energy exchange, we assume a boundary transmission factor β such that

$$P_{\text{transmitted}} = \beta\, P_{\text{dissipated}}. \tag{14}$$

Hence the bound on instantaneous power, average power, and cumulative energy are

$$P_{\text{bound}}(t) = (1+\beta)\, P_{\text{dissipated}}(t), \quad \overline{P}_{\text{bound}} = (1+\beta)\, \overline{P}_{\text{dissipated}}, \quad E_{\text{bound}}(t) = (1+\beta)\, E_{\text{dissipated}}(t), \tag{15}$$

with $\beta = 3$ in this work.

Coupling loss factors in structural assemblies are often comparable in magnitude to internal damping, and in cases of strong junctions or multiple coupling pathways the total loss factor can substantially exceed the internal component (Schiller, 2010) [8]. Studies in [9], and[10, 11] confirm that coupling loss factors vary widely with boundary conditions, motivating

the back-of-the-envelope estimate of β adopted in this work. From the estimates in Table 2, the modal damping ratios fall in the range $\zeta \sim 0.006-0.033$, corresponding to internal loss factors of $\eta \approx 2\zeta, \sim 0.012-0.066$. Using $\sum \eta_{ij} \approx 0.06$ for a panel connected to two neighbors plus the ceiling and floor, the resulting $\beta = \frac{\sum \eta_{ij}}{\eta_i}$ spans ~0.9–5 depending on the assumed internal loss factor.

The framework developed builds upon well-established practices in experimental modal analysis [5], including global curve fitting of frequency response functions [6] Alternative methods for estimating vibrational power flow include structural intensity approaches [12] and statistical energy analysis (SEA) [13], both of which require extensive spatial measurements or coupling loss factor data. In contrast, most energy harvesting research has focused on modeling specific transducers such as piezoelectric, electromagnetic, or triboelectric devices. By treating internal damping losses identified through EMA as an upper bound for harvestable energy, our method provides a harvester agnostic and operationally validated metric that can be applied consistently across different road environments.

Results and Discussion

Figure 7 show the modal velocity for the accelerometer S5, the total instantaneous power and the cumulative energy for the I-65 road segment. Note that the energy dissipated is cumulative with discontinuities at spikes in power. In order to quantify uncertainty in the mean dissipated power over I-65, the instantaneous power signal was aggregated into non-overlapping 30 s windows and the window-mean power was computed. The trip-average power was $\bar{P} = 1.565$ W per panel. A 95% confidence interval (CI) of $[1.448, 1.728]$ W was estimated in using a block bootstrap with 90 s contiguous windows (5000 resamples). The corresponding cumulative energy over the trip was $E_{\text{trip}} \approx 4.11 \times 10^3$ J per panel.

Table 3 are estimations for a full 24-panel trailer wall, calculated by multiplying the results from the single instrumented panel by 24, assuming similar vibrational behavior across all panels. The vibration energy data collected across 19 distinct road segments reveals substantial variation in both energy harvesting potential and power intensity, highlighting key opportunities and limitations for vibration-based energy systems. The interstate corridor I-65 stands out, generating the highest cumulative energy output (over 54.6 kJ) and extreme peak power levels (over 27.5 kW for 24 panels), making it the most promising candidate for high-yield energy harvesting. Other major corridors such as US52/31, US421, and SR26 also demonstrate considerable energy accumulation (ranging from approximately 6.5 to 10.3 kJ), suggesting that heavily trafficked, long-duration road segments are particularly well-suited for sustained energy recovery or self-powered infrastructure applications.

Table 3 Summary of Vibration-Based Power and Energy Estimates Across Road Segments (24 Panels). "+Bound" indicates inclusion of boundary transmission with $\beta = 3$, i.e., values are $(1 + \beta) = 4$ times the dissipated estimates

Road	Time (s)	Mean Power (W)	Peak Power (W)	Energy (J)	Mean+Bound (W)	Peak+Bound (W)	Energy+Bound (J)
Russell	182.12	0.568	5.13	103.51	2.273	20.54	414.04
Williams	93.99	5.231	18.93	491.69	20.93	75.70	1,966.76
Harrison	100.03	3.105	27.86	310.55	12.42	111.43	1,242.20
Tapawingo	101.99	0.548	3.29	55.92	2.193	13.17	223.67
South	583.96	11.42	51.19	6,668.72	45.68	204.77	26,674.89
US52/31	762.81	13.54	47.74	10,328.34	54.16	190.95	41,313.36
US52	98.98	9.20	1,874.90	910.47	36.80	7,499.60	3,641.88
SR28E	696.61	0.828	148.80	576.84	3.312	595.19	2,307.38
SR28	226.95	24.27	99.65	5,508.30	97.08	398.62	22,033.21
I65	2,626.54	20.81	6892.19	54,649.04	83.23	27,568.77	218,596.18
SR38	56.05	1.766	156.00	98.98	7.064	623.99	395.91
SMeridian	135.01	0.668	13.67	90.22	2.673	54.70	360.89
SR18	408.00	1.797	102.15	733.08	7.187	408.60	2,932.31
SR26	1,423.94	6.474	173.44	9,218.06	25.89	693.76	36,872.25
SR27	722.00	6.070	1,731.68	4,382.63	24.28	6,926.71	17,530.53
SR43	156.02	1.932	26.26	301.40	7.727	105.03	1,205.61
US24	1,852.94	2.999	1,122.63	5,556.12	11.99	4,490.52	22,224.47
US421	1,473.88	4.435	2,067.20	6,536.37	17.74	8,268.79	26,145.48
WHarrison	127.98	1.237	15.23	158.36	4.949	60.91	633.43

In contrast, several roads including SR38, Tapawingo and West Harrison produced minimal energy yields (below 150 J total), primarily due to short durations and lower vibrational intensity. These segments are unlikely to support active energy harvesting and may instead serve as control or baseline environments for vibration analysis. Notably, many roads exhibit

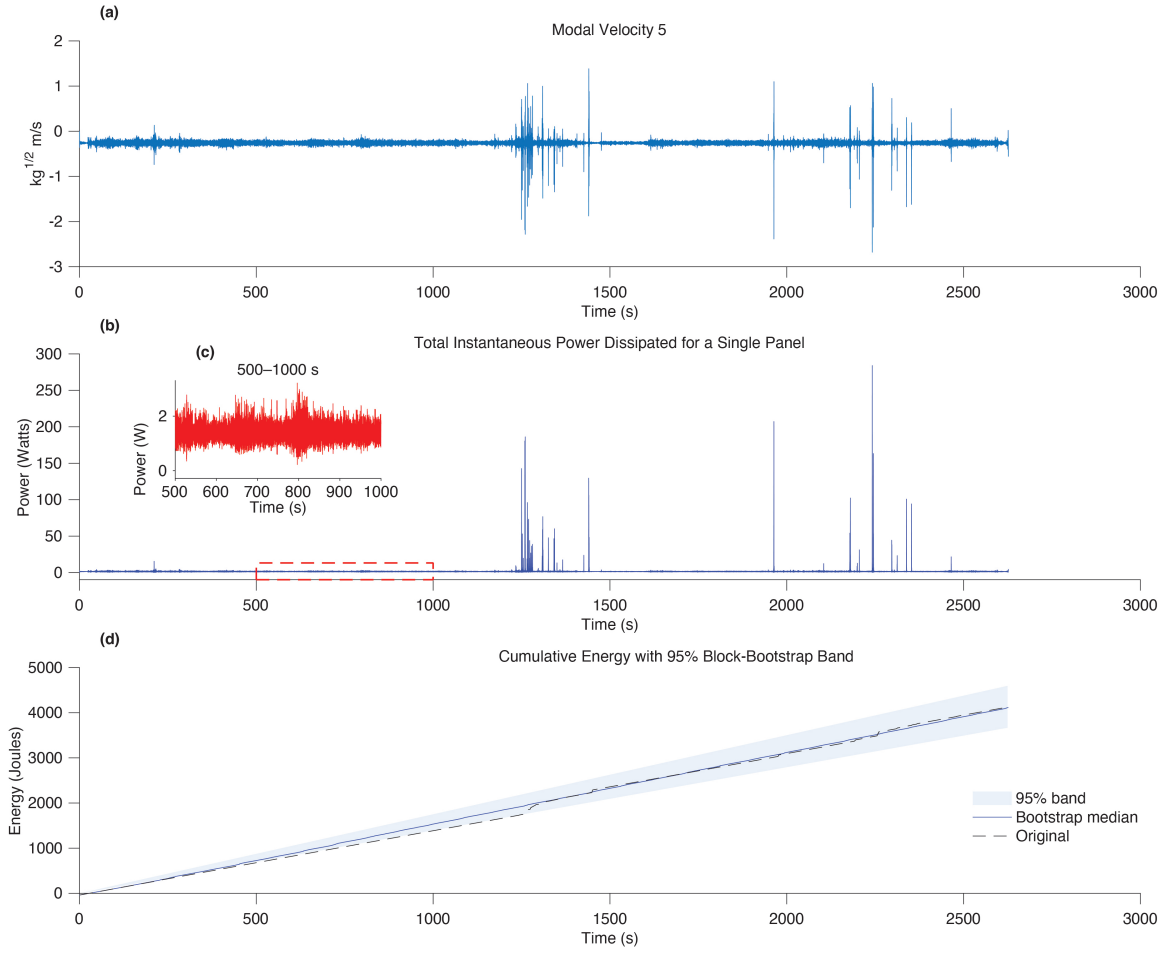

Fig. 7 Experimental energy in first rear panel for I-65: (a) modal velocity of mass 5, (b) instantaneous power, and (c) accumulated energy with 95% Block-Bootstrap band. The modal velocity has units of $kg^{1/2}m/s$, which is characteristic of modal coordinates derived from mass-normalized mode shapes where the modal mass is unity. Inset in (b) shows the power from 500 to 1000 s interval (red box in the main trace) on I-65. Note that energy increases monotonically with time, while the instantaneous power exhibits intermittent bursts tied to transient excitations

significant increases in RMS and peak power when boundary effects are included in the analysis. For instance, RMS power often increased by a factor of three to four when boundaries were modeled, indicating that edge effects or mechanical constraints on panel configurations play a nontrivial role in strain amplification and energy transduction.

Several roads, including US52, SR28E, and SR38, exhibit unusually high peak powers relative to their overall energy output, implying short-duration, high-intensity excitations such as bridge joints, pavement gaps, or surface anomalies. These conditions may be ideal for triggering threshold-based systems (e.g., damage detection or alert beacons) rather than continuous energy harvesting. Overall, the data indicate that deployment strategies should be differentiated based on road characteristics: highways and arterials with sustained vibrations are optimal for energy recovery, while urban and low-yield roads may benefit more from passive sensing systems or localized energy storage. The clear performance disparities across road types underscore the importance of site-specific design in energy harvesting applications.

Limitations

This work has several important limitations. First, modal truncation excludes the dissipative contributions of higher modes, so the present estimates should be regarded as a *conservative lower bounds* unless the retained modes capture a sufficiently

large fraction of the total effective modal mass. Second, not all modes were reliably excited across the different impact configurations; only those consistently identified in every modal test were retained. This restriction improves robustness but further reduces modal coverage and may bias the dissipation estimates downward by omitting intermittently excited modes. Another source of uncertainty is in the mass discretization; the lumped mass matrix is derived from a nonuniform Voronoi partition around the sensors. While a uniform partition is not feasible without repeating the experiment, increasing the number and uniformity of masses would systematically improve the quadrature accuracy of the modal projections and reduce discretization bias. Finally, this study assumes that the single panel tested is representative of the other trailer panels. In practice, the selected edge panel may deform differently than middle panels or opposite-side edge panels due to boundary conditions and asymmetric load paths. As such, the extrapolation of results to the full trailer should be viewed cautiously until validated by measurements on additional panel locations.

Conclusion

This study presented an integrated framework to quantify vibrational power dissipation in semi-trailer panels by combining experimental modal analysis with operational road testing. Using modal impact tests, the panel's natural frequencies, damping ratios, and mode shapes were identified and formed the basis of a reduced-order modal model. Operational accelerometer data collected across 19 road segments were then projected into modal coordinates, enabling estimation of modal velocities and subsequent calculation of dissipated vibrational power.

The results demonstrate that vibrational energy dissipation in trailer panels is dominated by broadband responses in the 2–20 Hz frequency range, rather than by isolated resonances. Among the tested conditions, interstate highway segments such as I-65 exhibited the highest energy accumulation (exceeding 54 kJ for 24 panels) and peak power levels (over 27 kW), while local or short road segments such as West Harrison and Russell produced negligible energy yields. These findings highlight the strong dependence of energy availability on road type and driving conditions, suggesting that deployment of energy harvesting devices should be tailored to specific operational environments.

Although this analysis focuses on a single panel, boundary effects and mass loading from neighboring panels were implicitly captured in the measured modal parameters, providing a lower bound estimate of energy dissipation. Nonetheless, additional work is required to explicitly quantify transmitted power across panel boundaries and to assess the collective response of the full trailer assembly.

Future research should extend this framework to multi-panel models, investigate fatigue and durability effects, and integrate prototype energy harvesting devices (piezoelectric, triboelectric, or electromagnetic) to validate practical performance. By establishing a physically consistent method for estimating vibrational energy dissipation, this work provides a foundation for designing next-generation trailer panels capable of harvesting ambient vibrations to reduce alternator load and improve the energy efficiency of heavy vehicles.

Acknowledgments The authors gratefully acknowledge the support of Wabash for providing access to the trailer panels used in this study and for funding this study. We extend special thanks to Andrzej Wylezinski and Michael Bodey for their guidance, technical input, and continued support throughout this work. Their collaboration and insights were essential to the successful execution of the research. We also thank Cody Bahler and Jose Romero for their assistance in operating the semi-truck during testing.

Appendix: Derivation of Power Quantification

The equations of motion of a trailer panel can be written in physical coordinates as

$$\mathbf{M}\,\ddot{\vec{x}}(t) + \mathbf{C}\,\dot{\vec{x}}(t) + \mathbf{K}\,\vec{x}(t) = \vec{f}(t), \tag{16}$$

where $\vec{x}(t)$ are nodal displacements, $\vec{f}(t)$ are applied forces, and $\mathbf{M}, \mathbf{C}, \mathbf{K}$ are the mass, damping, and stiffness matrices. The damping matrix is assumed to be proportional to $\mathbf{M}$ and $\mathbf{K}$.

Let $\mathbf{\Phi} = [\,\vec{\psi}_1 \;\cdots\; \vec{\psi}_{N_m}\,]$ denote the retained set of mass-normalized mode shapes identified from experimental modal analysis (EMA). The displacement and velocity fields are expressed as

$$\vec{x}(t) = \mathbf{\Phi}\,\vec{q}(t), \qquad \dot{\vec{x}}(t) = \mathbf{\Phi}\,\dot{\vec{q}}(t), \tag{17}$$

where $\vec{q}(t)$ are modal coordinates.

Substituting into the governing equations and premultiplying by $\mathbf{\Phi}^{\mathsf{T}}$ gives the decoupled modal equations of motion:

$$\ddot{q}_n(t) + 2\zeta_n\omega_n\dot{q}_n(t) + \omega_n^2 q_n(t) = g_n(t), \qquad n = 1, \ldots, N_m, \tag{18}$$

where ω_n and ζ_n are the natural frequency and damping ratio from EMA, and $g_n(t) = \vec{\psi}_n^{\mathsf{T}}\vec{f}(t)$ are modal forces.

In this case, the applied force vector is replaced by the equivalent damping forces, $\mathbf{C}\dot{\vec{x}}(t)$, so that the power expression reduces to the rate of energy dissipated through damping. This substitution leads directly to the modal form of the dissipated power, expressed as a sum over the modal damping contributions. The instantaneous mechanical power is preserved under this transformation:

$$P(t) = \dot{\vec{x}}^{\mathsf{T}}\vec{f}(t) = \dot{\vec{q}}^{\mathsf{T}}\vec{g}(t), \tag{19}$$

and using the damping forces $\vec{f}(t) = \mathbf{C}\,\dot{\vec{x}}(t) = \mathbf{C}\mathbf{\Phi}\dot{\vec{q}}(t)$, the dissipated power is

$$P_{\text{diss}}(t) = \dot{\vec{q}}^{\mathsf{T}}\mathbf{C}_m\dot{\vec{q}} = \sum_{n=1}^{N_m} c_n\,\dot{q}_n^2(t), \tag{20}$$

where $\mathbf{C}_m = \mathbf{\Phi}^T\mathbf{C}\mathbf{\Phi}$ and the cumulative dissipated energy over $[0, T]$ is

$$E_{\text{diss}}(T) = \int_0^T P_{\text{diss}}(t)\,dt. \tag{21}$$

In practice, operational accelerations $\vec{a}(t) = \ddot{\vec{x}}(t)$ are recorded during road testing, and the mass matrix $\mathbf{M}$ is approximated by lumped weights $\{M_k\}$ assigned via sensor-based partitioning. Modal accelerations are obtained from

$$\ddot{\vec{q}}(t) = \mathbf{\Phi}^{\mathsf{T}}\mathbf{M}\,\ddot{\vec{x}}(t), \tag{22}$$

and integrated to yield $\dot{\vec{q}}(t)$, which are then used to compute $P_{\text{diss}}(t)$ and $E_{\text{diss}}(T)$.

References

1. Ropovik, R., Hatala, M., and Dobransky, J. "Optimization of lighting for truck with lifting platform". *Manufacturing Technology*, 24(Special Issue):TEAM2024–00031 (2024)ifnextchar.gobble.
2. Arrieta, A.F., Wagg, D.J., and Neild, S.A. "A piezoelectric bistable plate for nonlinear broadband energy harvesting". *Applied Physics Letters*, 97(10):104102 (2010)ifnextchar.gobble.
3. Erturk, A. and Inman, D.J. *Piezoelectric Energy Harvesting*. John Wiley & Sons (2011)ifnextchar.gobble.
4. Tao, H. and Gibert, J. "Multifunctional mechanical metamaterials with embedded triboelectric nanogenerators". *Advanced Functional Materials*, 30(23):2001720 (2020)ifnextchar.gobble.
5. Ewins, D.J. *Modal Testing: Theory, Practice and Application*. Research Studies Press, 2nd edition (2000)ifnextchar.gobble.
6. Richardson, M.H. and Formenti, D.L. "Global curve fitting of frequency response measurements using the rational fraction polynomial method". In *Proceedings of the 3rd International Modal Analysis Conference (IMAC)*, pages 390–397, Orlando, Florida (1985)ifnextchar.gobble. Structural Measurement Systems, San Jose, California.
7. O'Rourke, J. *Computational Geometry in C*. Cambridge University Press (1998)ifnextchar.gobble.
8. Schiller, N.H. "Impact of damping uncertainty on sea model response". Technical Report NASA/TM–2010-216352, NASA Langley Research Center (2010)ifnextchar.gobble. Accessed: 2025-09-21.
9. Langley, R.S. "A derivation of the coupling loss factors used in statistical energy analysis". *Journal of Sound and Vibration*, 141(2):207–219 (1990)ifnextchar.gobble.
10. Park, W.S. and Kim, Y.H. "Variability of the coupling loss factor between two subsystems". *Journal of Sound and Vibration*, 279(1-2):357–371 (2005)ifnextchar.gobble.
11. Su, J. and Zheng, L. "An identification method for the effective coupling loss factor based on the hybrid fe–sea model". *Applied Sciences*, 13(6):3687 (2023)ifnextchar.gobble.
12. Booth, W. and Hammond, J.P. "Structural intensity and power flow techniques in vibration". *Journal of Sound and Vibration*, 150(3):319–335 (1991)ifnextchar.gobble.
13. Lyon, R.H. and DeJong, R.G. *Theory and Application of Statistical Energy Analysis*. Butterworth-Heinemann, 2nd edition (1995)ifnextchar.gobble.

Chapter 14
Guided Analysis Tools for Highly Efficient Impact Testing and Modal Parameter Estimation

Bart Peeters, Simone Manzato, and Mattia Dal Borgo

Abstract Impact testing is a widely used technique for measuring structural Frequency Response Functions (FRFs). Even though this testing methodology is already a few decades old and reached a very high level of maturity, modern industrial testing requirements and the continuous drive for increased efficiency, necessitated a (r)evolution in the way impact testing is performed and the "best" hits are selected for obtaining optimal-quality FRFs in a minimal amount of time with minimal involvement of human resources. This paper will highlight the new Smart Hit Selection (SHS) method that, in a fully automated way, assists the user in obtaining optimal measurement results. The methodology will be explained and illustrated by means of a measurement campaign.

The goal of impact testing is to understand the structural dynamics behaviour of a physical structure. After acquiring FRFs, often Experimental Modal Analysis (EMA) is applied to estimate the eigenfrequencies, damping ratios and mode shapes to gain additional quantified insights in the tested structure. As a second part of this paper, an innovative Hybrid AI method, incorporated in the EMA process, will be highlighted. Hybrid AI represents a significant advance in the field of artificial intelligence by bridging two distinct approaches: machine learning-based and rule-based methods. In the specific method discussed here, unsupervised learning is combined with domain expertise captured in rules. The Hybrid AI method has been designed to automatically estimate the modal parameters with the same level of quality as an expert in the modal analysis field would do. The innovative technology will be illustrated using FRF data obtained by SHS.

Keywords Impact testing · Experimental modal analysis

Smart Hit Selection (SHS)

Impact testing is a widely used technique to measure FRFs of a structure or component. Often a roving hammer approach is adopted in which the operator sequentially excites the structure at all locations of interest. A few fixed accelerometers are recording the structural responses due to impact excitation. At each location, multiple hits are applied and the data from multiple hits is "averaged" to reduce noise and bias errors on the FRFs. Not all hits are suited to be considered for the FRF calculations. Example of mishits are the following: too low force is applied resulting in noisy measurements; too high force is applied resulting in overload; impact is not applied at the right location or in the right direction; an acquisition is erroneously triggered e.g. by accidentally touching an object with the hammer. Also, in case of a highly resonating structure, it is sometimes difficult to avoid double or multiple impacts: the operator will hit unintentionally the structure multiple times. This is not necessarily problematic and such measurements do not have to be excluded a priori, but it may lead to higher noise levels as the force spectrum of a double/multiple impact will exhibit oscillating behaviour: some frequencies are better excited than others.

For all these reasons, it is important that the right hits are selected, i.e. the hits that are consistently applied at the same location and in the same direction and have a high signal-to-noise ratio (SNR). A manual, interactive process can be used, but this will considerably slow down the measurement campaign. Therefore, a fully automated, user-guided process has been developed called "Smart Hit Selection" (SHS). The main idea of SHS is to select the hits that are most similar to each other, assuming that these have been applied closest to the target location (Figure 1). Different metrics can be used to express such "similarity" and in the research leading to SHS, multiple metrics have been investigated such as correlation between

Bart Peeters · Simone Manzato · Mattia Dal Borgo
Siemens Industry Software NV, Leuven, Belgium
e-mail: bart.peeters@siemens.com; simone.manzato@siemens.com; mattia.dal_borgo@siemens.com

© The Author(s), under exclusive license to River Publishers 2026

Kristin B. Zimmerman, PhD (eds.), *Topics in Modal Analysis & Parameter Identification in Structural Dynamics, 2026, Vol. 8*,
Conference Proceedings of the Society for Experimental Mechanics Series, https://doi.org/10.13052/rp-9788743814191

instantaneous FRFs, coherence improvement ratio, correlation between instantaneous and averaged FRFs. However, it was found that the following 2 metrics lead to the highest overall coherence (and thus FRF quality) of the selected hits:

- "Pairwise similarity": a metric expressing the "similarity" between 2 instantaneous FRFs across a certain frequency range. Examples of such metric are presented in [1][2]. In the SHS method, the following is used:

$$S(H^{(1)}, H^{(2)}) = \frac{\left|H^{(1)} + H^{(2)}\right|^2}{2(\left|H^{(1)}\right|^2 + \left|H^{(2)}\right|^2)} \tag{1}$$

  where $H^{(i)}$ is the ith instantaneous (based on a single hit) FRF.

- "Pairwise coherence": the classical coherence between input (force) $u(t)$, $U(\omega)$, and output (acceleration, typically) $y(t)$, $Y(\omega)$, based on 2 averages (2 hits) only:

$$\gamma_{yu}^2 = \frac{|S_{yu}|^2}{S_{yy}S_{uu}} \ , \quad S_{yu} = \frac{1}{2}\sum_{i=1}^{2} Y^{(i)}U^{(i)^*} \tag{2}$$

Both metrics have a value between 0 and 1 for each spectral line. They are averaged across the frequency range of interest to obtain a single number quality indicator.

In the SHS method, the selected metric is calculated for all pairs of hits for all sensors. When applied in online mode, each additional hit will trigger immediately new metric calculations. The metric is compared to a user-defined target value and all hits above or equal to the target are retained as good hits. If the number of retained hits is lower than the minimum value of required hits, the best hits are selected up to this minimum number. At least 2 good hits are required, but it is recommended to set the minimum value of required hits a bit higher to have enough statistical confidence in the averaged FRF.

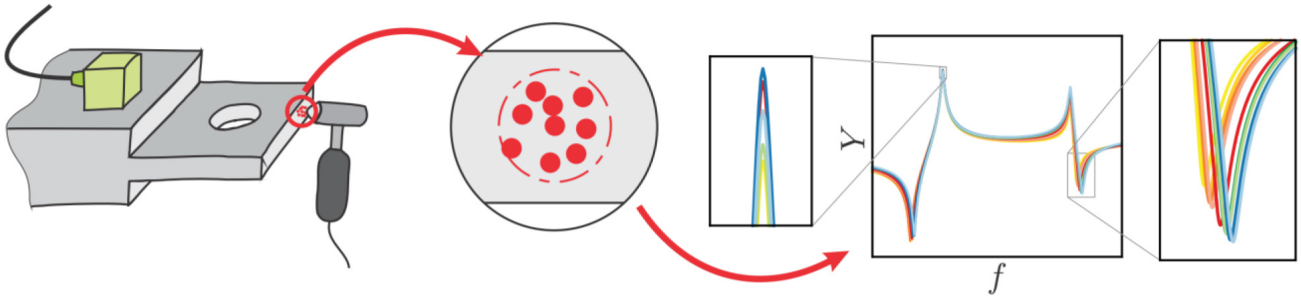

Fig. 1 Impact testing: it is challenging to always hit at the same location and in the same direction. Changes in location and orientation will lead to changes in the acquired FRF. SHS assists the user in selecting the hits that are most similar to each other, leading to high quality FRFs and high coherences

The SHS concepts are illustrated using data from a simple metal plate (Figure 2, Left). In Figure 3 and Figure 4, two hits at the same location are compared to each other (Figure 2, Right). The 1st hit is a good, single-impact hit, but with rather low excitation level, resulting in noisy data at higher frequencies. The 2nd hit is actually a double or even multiple-impact hit, but with a high excitation level, resulting in a good SNR even at high frequencies.

From Figure 3, it can be observed that the pairwise similarity is much noisier than the pairwise coherence. This is caused by the 1st hit which also shows a very noisy instantaneous FRF (Figure 4). The pairwise coherence is much less affected by the noisy hit (just like the averaged FRF is less affected – see Figure 4): lower-level signals contribute less to the averaged FRF (H1 estimator), which is not true for the instantaneous FRFs. This is also the reason why H1 estimators are used for averaging rather than simply taking the average of all instantaneous FRFs.

It should be noted that for other hit pairs, and in general, not so big differences are observed between both criteria: pairwise similarity and pairwise coherence, and both can be used with confidence to obtain the best hits.

In Figure 5, the benefits of SHS are made clear: there is a clear quality improvement when running SHS and retaining the 3 or 5 best hits compared to using all hits. The SHS method is able to improve the coherence considerably, leading to higher quality FRFs. Benefits of "Smart Hit Selection" include [3]:

- The operator can focus on testing, the algorithm will discard bad hits;

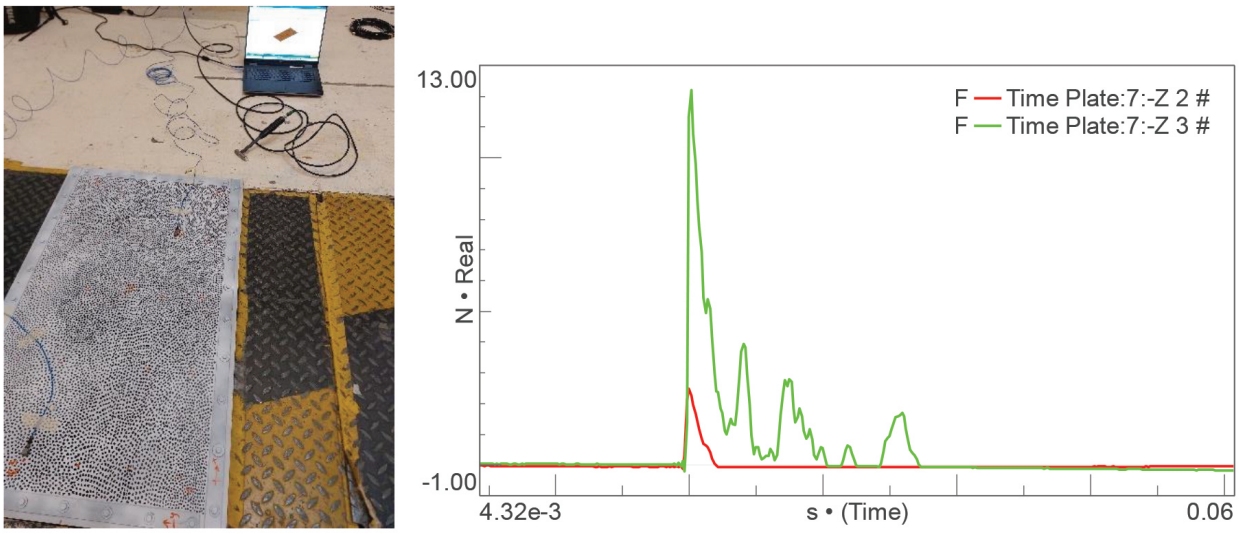

Fig. 2 (Left) Plate used to illustrate the SHS method. Plate is fuzzily supported, and roving hammer excitation has been applied in a rectangular grid. Two fixed accelerometers are capturing the plate response. (Right) Plate is highly resonating resulting in quite some double / multiple-impact hits as illustrated by the force measurements in time domain. A low-level single hit is shown together with a higher-level multiple-impact hit

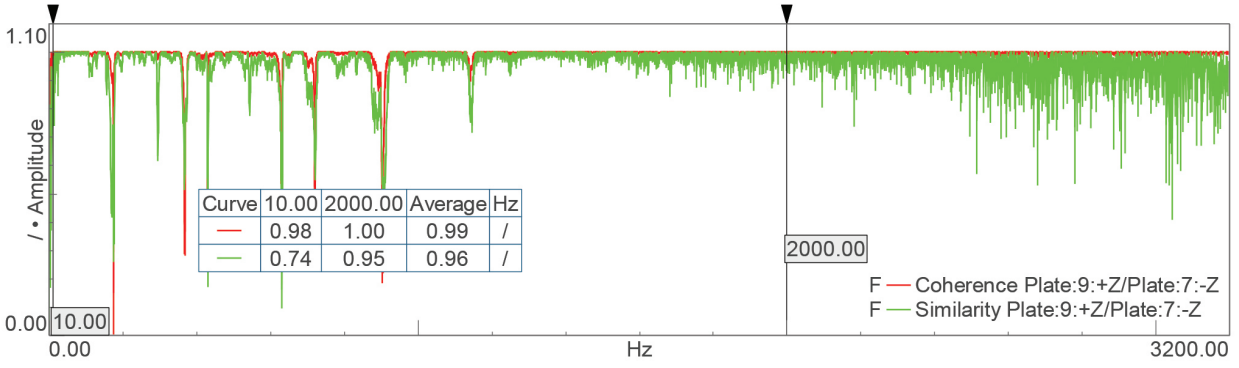

Fig. 3 Pairwise coherence and pairwise similarity of the same 2 hits

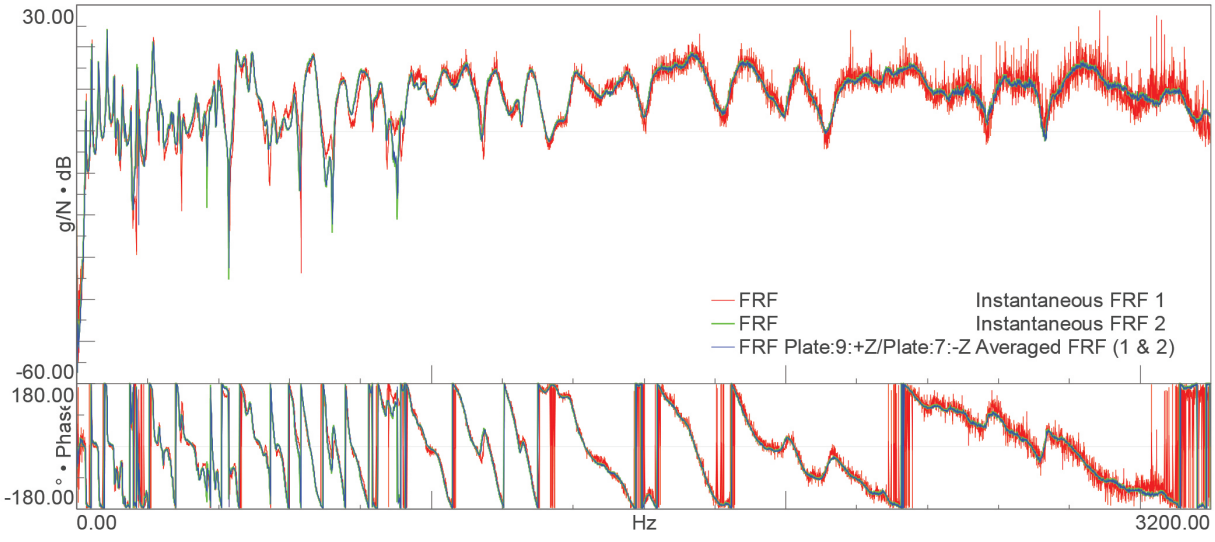

Fig. 4 Two instantaneous FRFs and the averaged (H1 estimator) FRF based on 2 hits

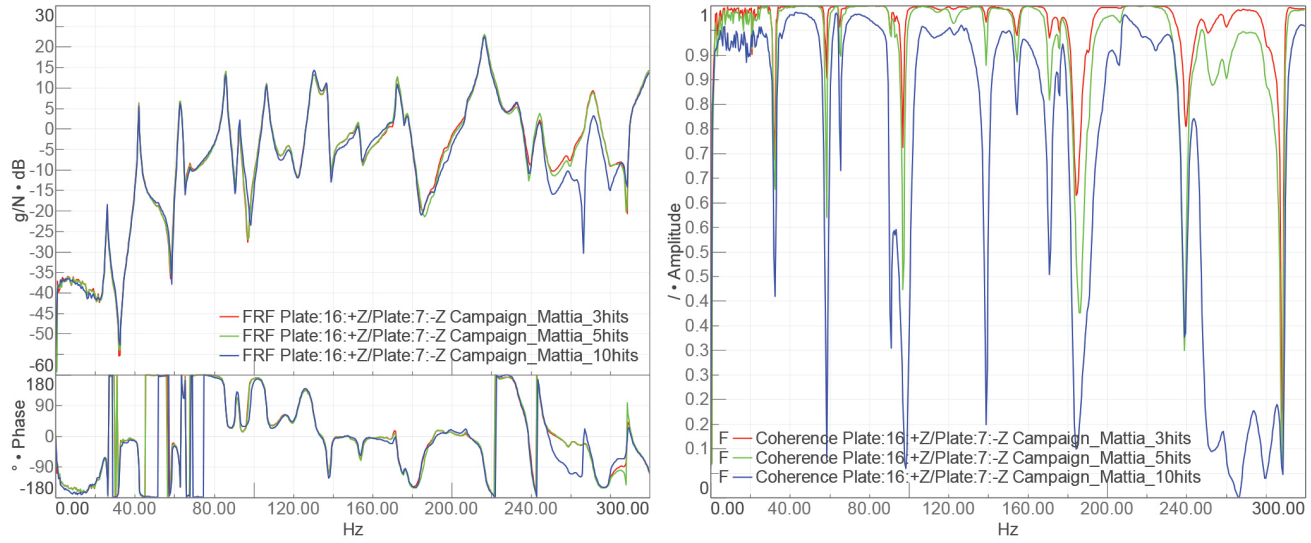

Fig. 5 (Left) FRFs obtained using SHS: all 10 hits, 5 best hits, 3 best hits; (Right) corresponding coherences

- There is less/no need to manually scan all data after the test;
- Highest quality FRFs are obtained from the available impacts;
- SHS can be applied online during the test and/or offline after the test. Parameters of the method (selected metric, frequency range, target value, ...) can be modified at any moment, allowing to tune the method to the particularities of the tested structure and inherent measurement quality.

The application of AI in the modal analysis process

Experimental Modal Analysis is the process of estimating structural modes (eigenfrequencies, damping ratios, and mode shapes) based on vibration measurements in either controlled experimental or operational conditions, respectively. This happens by so-called curve-fitting techniques where a modal model is fitted to the measurement data.

When trying to estimate the modal parameters from sometimes noisy data, it is generally a good idea to over-specify the model order considerably, i.e. to try to fit high-order models that contain much more modes than present in the data. Afterwards the true physical modes are separated from the spurious numerical ones by interpreting a so-called stabilisation diagram (Figure 6). The poles corresponding to a certain model order are compared to the poles of a one-order-lower model. If their differences are within pre-set limits, the pole is labelled as a stable one. The spurious numerical poles will not stabilise very well during this process and can be sorted out of the modal parameter data set more easily.

Nevertheless, the interpretation of stabilisation diagrams may be intimidating for the non-expert and the selection of the "right" poles can be a time-consuming and error-prone process. Therefore, the automation of pole selection in modal analysis is important to accurately process complex datasets without user-dependent interaction and with repeatability. Such automated modal analysis method was recently proposed in [5]: a so-called Hybrid AI method was developed using a Machine Learning (ML) density-based clustering technique, combined with domain knowledge of modal parameter selection. In contrast to other clustering algorithms, density-based clustering techniques have the capability of automatically neglecting spurious data points, which can be a useful capability for the analysis of poles in stabilization diagrams. More specifically, Density-Based Spatial Clustering of Applications with Noise (DBSCAN) has been selected as the clustering algorithm: it organizes points based on their density in the feature space, typically evaluated using a distance function [6]. Unlike many clustering methods, DBSCAN does not require a predefined number of clusters as a hyperparameter. Instead, it relies on two key hyperparameters: (1) epsilon distance (ε), which defines the neighborhood around a point, and (2) minimum points ($MinPts$) needed within that neighborhood to form a cluster.

To improve the effectiveness and as an integral part of the proposed Hybrid AI method, cluster verification steps are applied after DBSCAN, again without requiring any user interaction. The following verification steps, based on expert knowledge cast in rules, are performed:

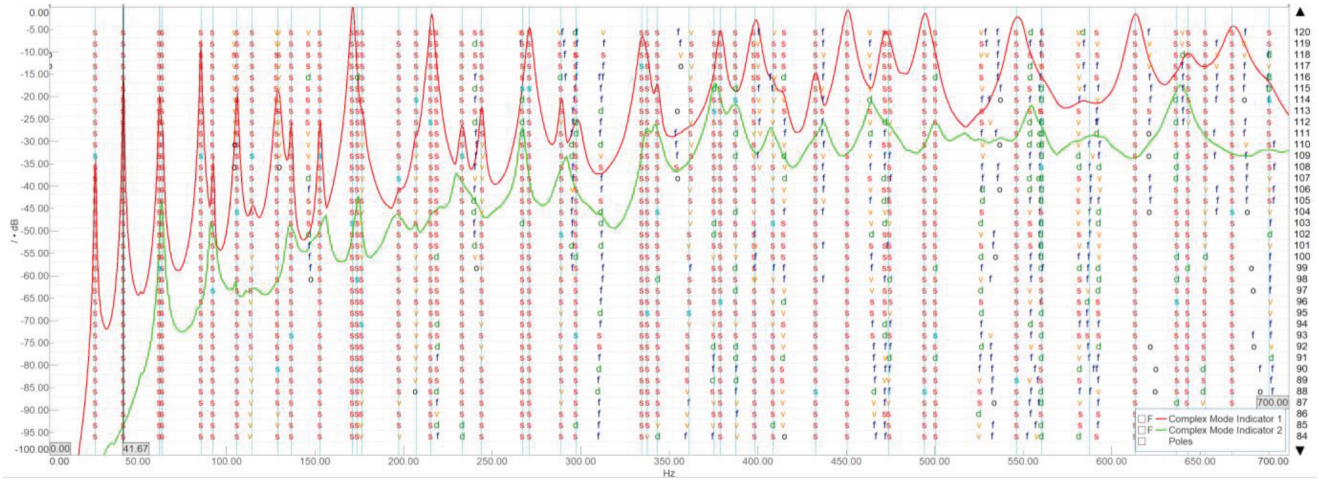

Fig. 6 Typical stabilisation diagram, allowing to select stable poles despite over-fitting. The FRF data from the plate introduced in previous section (Figure 2, Left) is used

- It may be necessary to join multiple clusters together that belong to the same physical pole but may have been separated by DBSCAN, due to high damping ratio differences.
- In case of very high model orders and complex data, sometimes too many clusters are obtained with representative poles that contribute very little to the measured data. Such low-contributing poles will be labelled as "numerical poles" and not retained in the final set of "physical poles".

The complete Hybrid AI method is represented in Figure 7. More details can be found in [5]. The result of the method applied to the stabilization diagram of Figure 6 is provided in Figure 8, where the different clusters are indicated and a single representative physical pole per cluster is selected. A view on the "dashboard" containing the full modal parameter estimation process within Simcenter Testlab Neo Modal Analysis is shown in Figure 9.

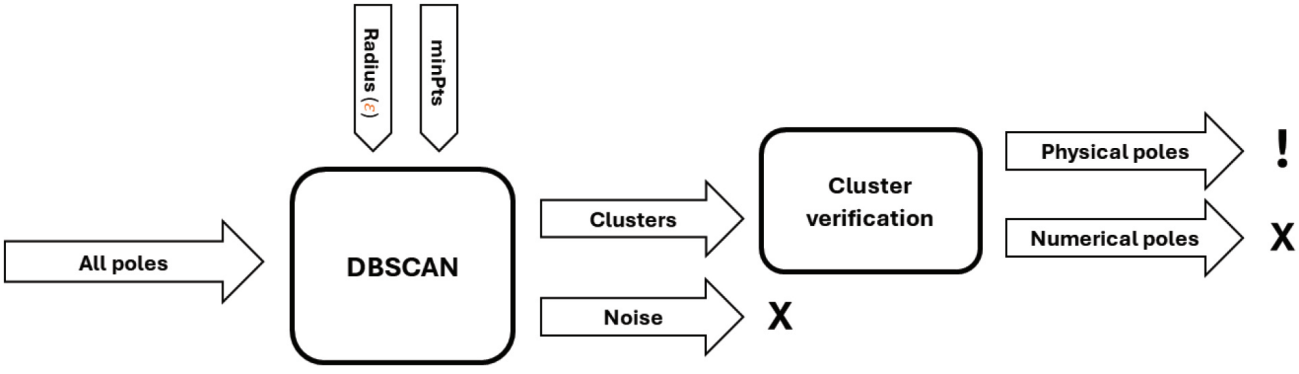

Fig. 7 Hybrid AI scheme adopted for automatic modal analysis: unsupervised learning (DBSCAN clustering) is combined with domain expertise (cluster verification)

Conclusions

This paper presented guided analysis tools for:

- highly efficient impact testing;
- AI-assisted modal parameter estimation.

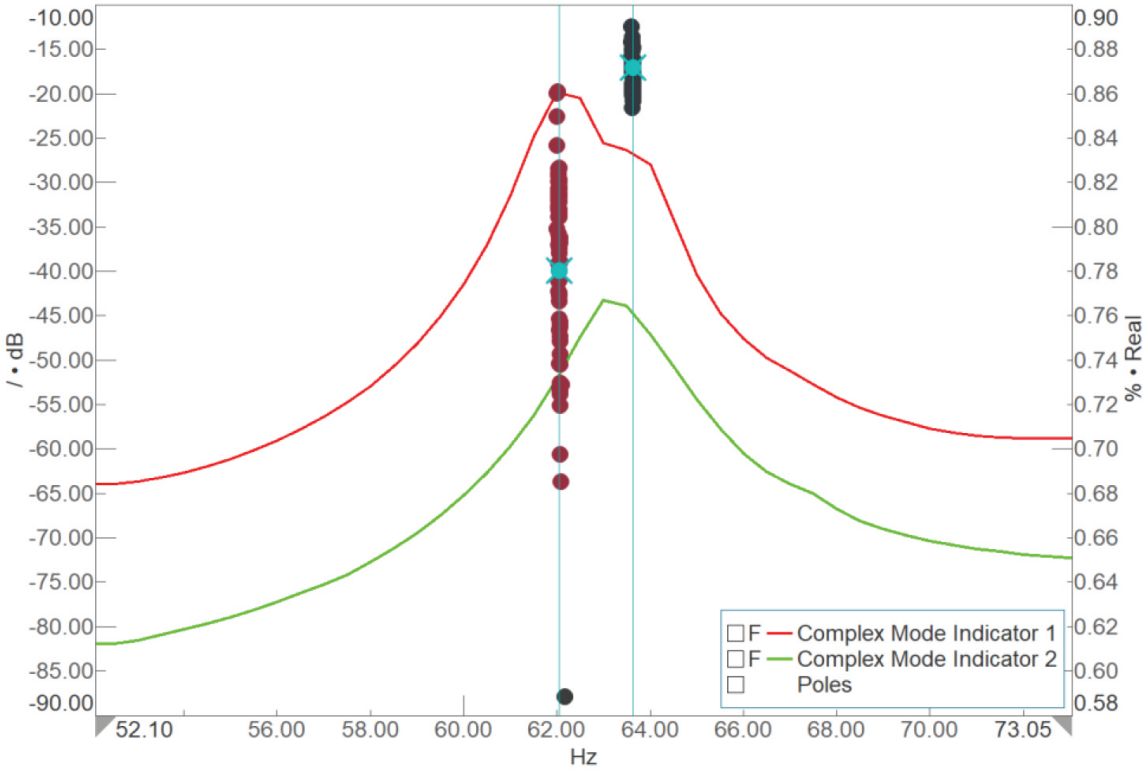

Fig. 8 Cluster representation of the stabilisation diagram from Figure 6, with poles selected by the Hybrid AI method, zooming in at 2 close poles

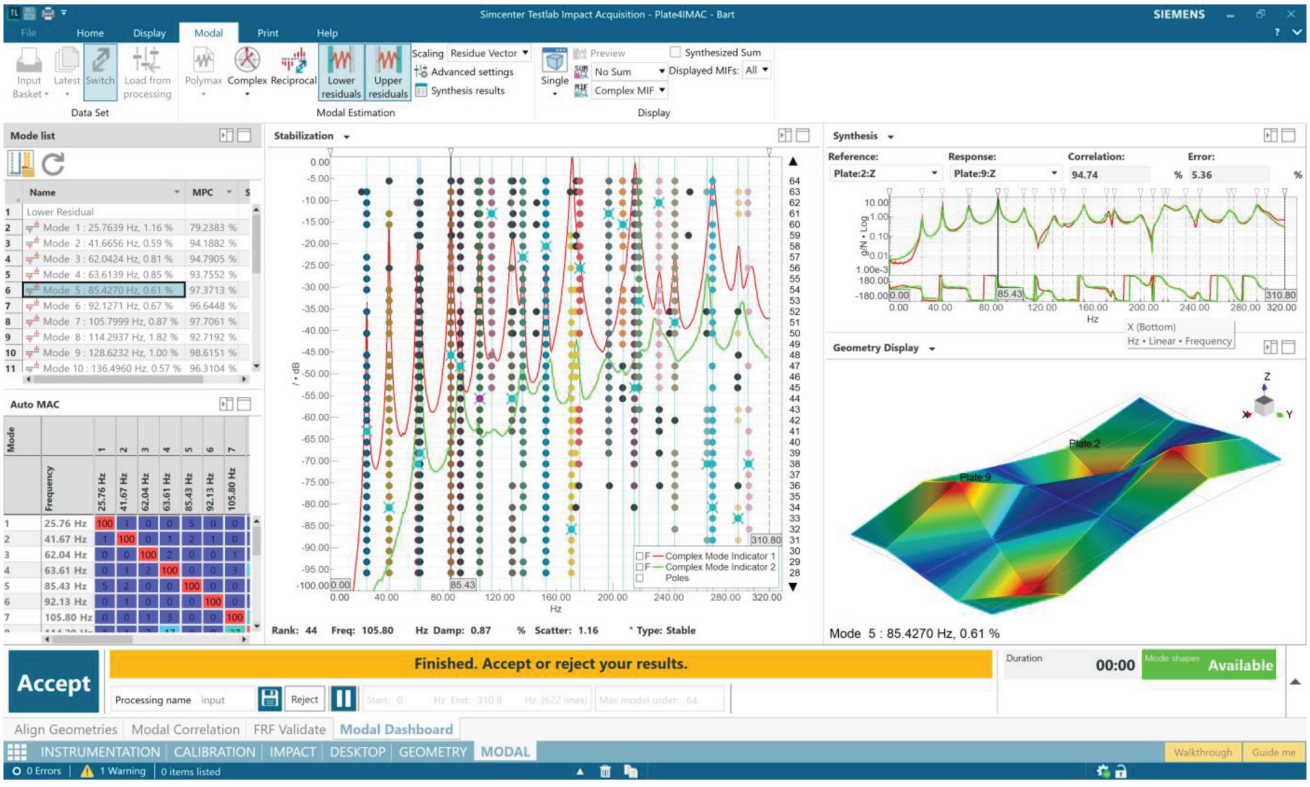

Fig. 9 Simcenter Testlab Neo Modal Analysis with embedded AI

Both methods aim to considerably facilitate the work of the experimentalist. The Smart Hit Selection (SHS) method allows the operator to focus on acquiring data in a highly efficient way, while SHS takes care of selecting the best hits resulting in optimal-quality FRFs and coherences, eliminating measurement errors and reducing noise propagation. AI-assisted modal parameter estimation combines advanced density-based clustering techniques with domain knowledge-driven mode validation. This integrated solution streamlines the time-intensive steps of experimental modal analysis, providing reliable and repeatable expert-level results with minimal user intervention.

References

1. Kodrič, M., Čepon, G., Boltežar M. (2021) Experimental framework for identifying inconsistent measurements in frequency-based substructuring. *Mechanical Systems and Signal Processing*, 154, DOI: 10.1016/j.ymssp.2020.107562.
2. van der Seijs, M., van den Bosch, D., Rixen, D., de Klerk, D. (2013) "An improved methodology for the virtual point transformation of measured frequency response functions in dynamic substructuring" in *Proc. COMPDYN 2013*, Kos Island, Greece.
3. Nelson, S. (2025) "Smart Hit Selection in Simcenter Testlab Neo". Available at: https://community.sw.siemens.com/s/article/Smart-Hit-Selection-in-Simcenter-Testlab-Neo [accessed September 30, 2025]
4. Dal Borgo, M., Manzato, S., Faignet, E., Di Lorenzo, E., Peeters, B. (2024) "Merging multiple hammer and shaker measurements to extend the FRFs frequency range" in *Proc. 4th RASD conference*, Southampton, UK.
5. Tavares, A.; Di Lorenzo, E.; Cornelis, B.; Manzato, S.; Peeters, B.; Desmet, W.; Gryllias, K. (2025) Automated experimental modal analysis with density-based clustering: A benchmark validation through jury testing. *Mechanical Systems and Signal Processing*, 232, DOI: 10.1016/j.ymssp.2025.112714.
6. Ester, M., Kriegel, H.-P., Sander, J., Xu, X. (1996) "A density-based algorithm for discovering clusters in large spatial databases with noise" in *Proc. 2nd Int. Conf. on Knowledge Discovery and Data Mining (KDD-96)*, Portland, Oregon, USA.

Chapter 15
Tips, Tricks, and Obscure Features for Operational Modal Analysis with Cross Spectra

William Fladung and Kevin Napolitano

Abstract While it has recently been proffered that cross spectra can be used for operational modal analysis, this alternative approach has revealed some unanticipated nuances in the modal parameter estimation process. This paper discusses some auxiliary procedures and obscure features that can be used to address these pertinent issues.

Keywords Operational modal analysis · Cross spectra

Introduction

In [1] it was demonstrated that using cross spectra for operational modal analysis (OMA) is a viable third option (in addition to correlations functions and positive power spectra), with just some slight alterations to algorithms that have traditionally estimated poles and shapes from frequency response functions (FRFs). However, as the authors gained some experience with this alternative approach for OMA, we discovered some new challenges that haven't usually been a consideration when using FRFs for experimental modal analysis (EMA). A few tips, tricks, and obscure features intended to redress these issues are discussed in this paper using data from a direct field acoustic noise (DFAN) test [2].

For a DFAN test, the tested structure is surrounded by an array of loudspeakers as an alternative to testing in a reverberant chamber for acoustic qualification tests. The test article for this DFAN test, shown in Fig. 1(a), was intended to represent a satellite with acoustically active panels mounted on an environmental shaker. There were 34 accelerometers mounted on the test article, as shown in Fig. 1(b), and the test article was surrounded by twelve Acoustic Research Systems (ARS) Neutron™ acoustic sources. The purpose of this test was to demonstrate that DFAN could be used for in situ acoustic qualification testing as well as for modal survey tests.

Virtual References in the Frequency Domain

When using cross spectra for OMA, there is a quartet of poles for each mode, which means that the model order of the modal parameter estimation (MPE) algorithm is double of what it would be for FRFs. The number of poles from a solution of an MPE algorithm is equal to the model order times the size of the polynomial matrix coefficients, which for a high-order model such as the Laplace-domain orthogonal polynomial (LDOP) algorithm [3] or the z-domain orthogonal polynomial (ZDOP) algorithm [4] is the number of references. For an FRF dataset from an EMA test, the number of references is typically between one and ten, which produces a manageable number of poles for moderate model orders. However, for a cross-spectra dataset from an OMA test, the number of references is the same as the number of responses, which could be several score to a few hundred. Clearly the references would need to be down-selected to a more reasonable number. This could be done by intuition, experience, and judgement based on the locations of the response degrees of freedom (DOFs) and the expected mode shapes or by inspection of the response data as exemplified in Fig. 2. The power spectral mode indicator functions (PSMIFs) for each reference, which is the summation of the cross spectra of all responses for each reference,

William Fladung · Kevin Napolitano
ATA Engineering, Inc., San Diego, California, 92128, USA
e-mail: bill.fladung@ata-e.com; kevin.napolitano@ata-e.com

© The Author(s), under exclusive license to River Publishers 2026

Kristin B. Zimmerman, PhD (eds.), *Topics in Modal Analysis & Parameter Identification in Structural Dynamics, 2026, Vol. 8*,
Conference Proceedings of the Society for Experimental Mechanics Series, https://doi.org/10.13052/rp-9788743814191

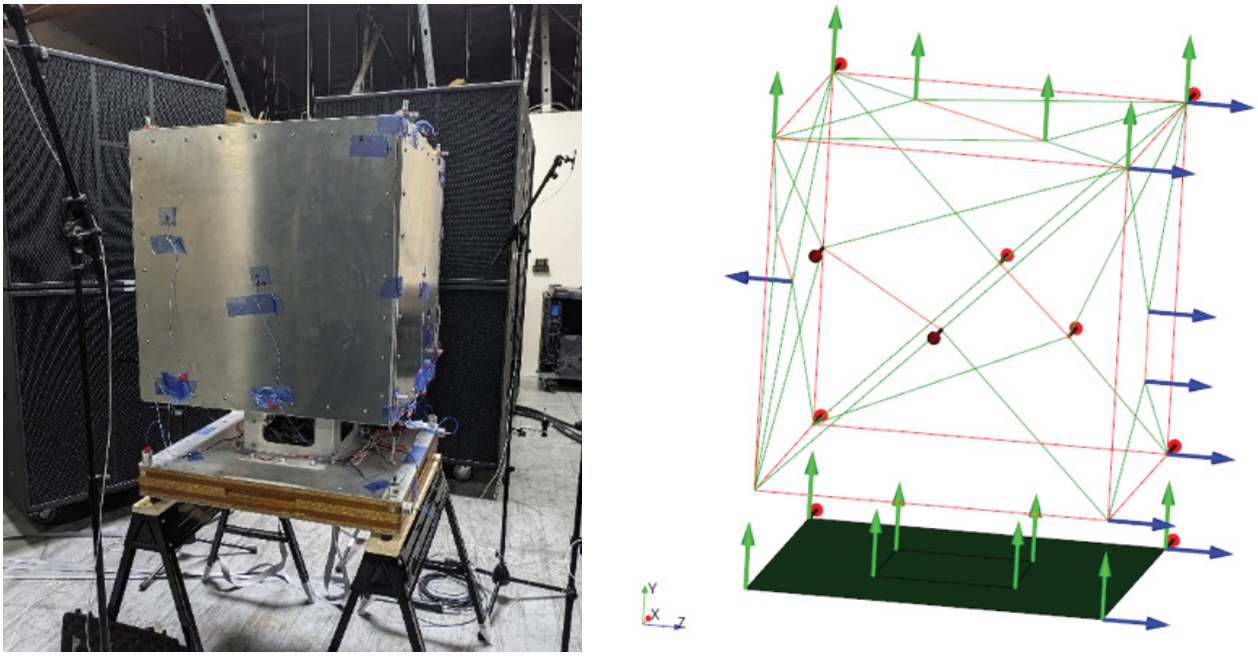

(a) (b)

Fig. 1 (a) Example DFAN test article; (b) test display model with accelerometer measurement degrees of freedom

are plotted in Fig. 2(a) and show which modes are observed by each DOF. The reference tracking (or color-coded [5]) complex mode indicator functions (CMIFs), which evaluate the right singular vectors to sort the functions according to each reference's relative ability to observe the modes, are plotted in Fig. 2(b).

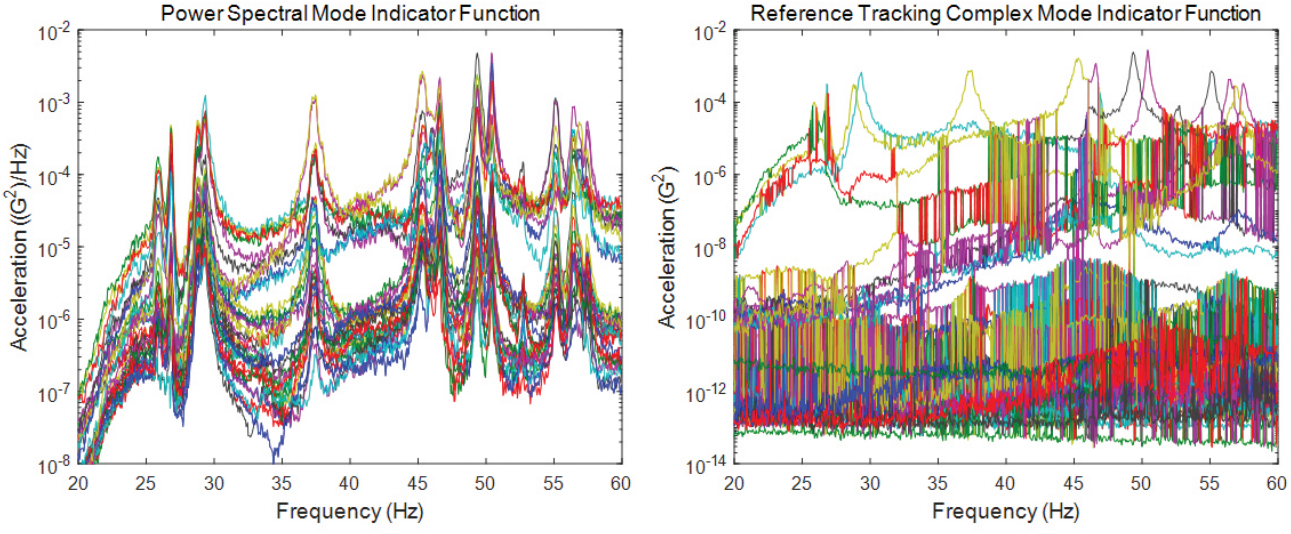

(a) (b)

Fig. 2 (a) PSMIF of all references; (b) reference tracking CMIF

After some tedious contemplation, you could probably decipher a reduced set of references that capture all of the modes of interest from either of these two plots. Or you could forgo the physical realm of the measured DOFs and condense the references into fewer *virtual references* instead. Transforming the $N_o \times N_o$ cross-spectra matrix G_{XX}, where N_o is the number of responses, into an $N_o \times N_v$ matrix with N_v virtual references starts with the singular value decomposition (SVD)

of a concatenated cross spectra array containing N_s spectral lines in a frequency band:

$$\underset{N_o N_s \times N_o}{\tilde{G}_{XX}} = \begin{bmatrix} G_{XX}(\omega_1) \\ G_{XX}(\omega_2) \\ \vdots \\ G_{XX}(\omega_{N_s}) \end{bmatrix} \tag{1}$$

Then the economy-size SVD of $\tilde{G}_{XX}$ results in

$$\underset{N_o N_s \times N_o}{\tilde{G}_{XX}} = \underset{N_o N_s \times N_o}{U} \sum_{N_o \times N_o} \underset{N_o \times N_o}{V^H} = \sum_{k=1}^{N_o} u_k \sigma_k v_k^H \approx \sum_{k=1}^{N_v} u_k \sigma_k v_k^H = \underset{N_o N_s \times N_v}{\tilde{U}} \underset{N_v N_v \times N_v}{\tilde{\Sigma}} \underset{N_v \times N_o}{\tilde{V}} \tag{2}$$

One of the popular usages of SVD is to represent the primary content of a matrix with fewer components by discarding those that contribute less to the first summation in Eq. (2), where the singular values are customarily sorted from the largest to the smallest. Thus, a subset of the right singular vectors in $\tilde{V}$ can condense the N_o columns of G_{XX} to N_v virtual references in $\tilde{G}_{XV}$:

$$\underset{N_o \times N_v}{\tilde{G}_{XX}}(\omega) = \underset{N_o \times N_o}{G_{XX}}(\omega) \underset{N_o \times N_v}{\tilde{V}} \tag{3}$$

In addition, virtual drive point responses, which are useful for evaluating which virtual reference best identifies particular modes, can also be created by using a subset of left singular vectors from a horizontally-concatenated array of $\tilde{G}_{XX}$ as spatial filters.

The number of virtual references (N_v) is determined from the number of significant singular values, which can be selected from a plot of the singular values. Two renditions of the singular values for the cross spectra in the frequency band of 23–59 Hz are shown in Fig. 3. The singular values normalized by the first (and largest) value are plotted in Fig. 3(a). Since there isn't always a distinctive knee in the curve demarcating the significant singular values, the successive ratio of the singular values, where each value is divided by the preceding value, is plotted in Fig. 3(b) for an alternative perspective. From this plot, eleven virtual references are the apparent choice, although seven or three might also be worth considering.

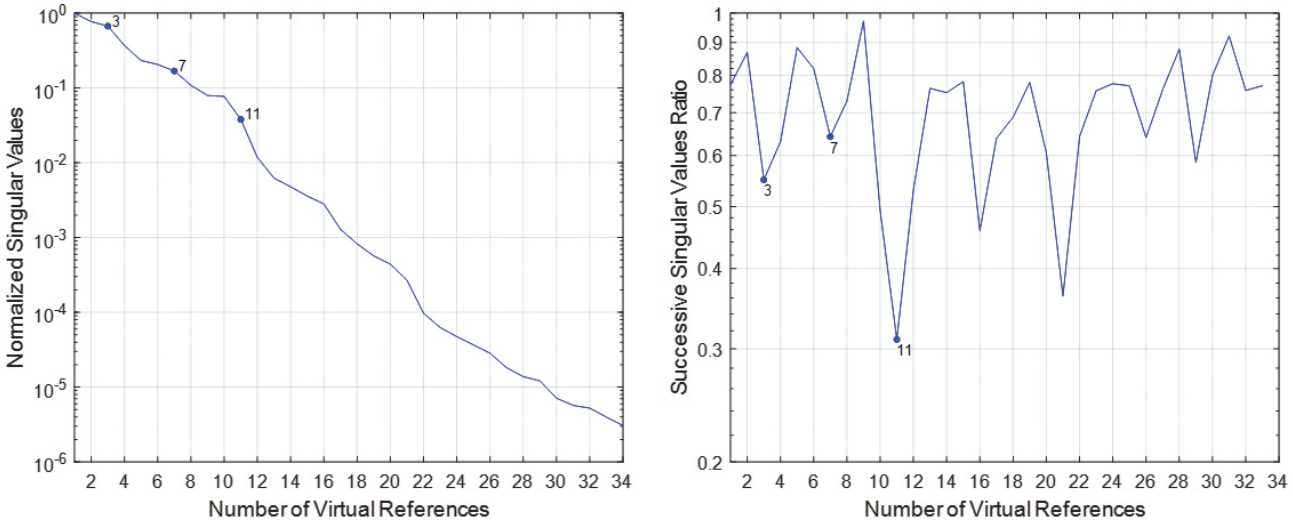

(a) (b)

Fig. 3 (a) Normalized singular values of cross spectra in 23–59 Hz frequency band; (b) successive ratio of singular values of cross spectra

To evaluate if any of these choices recreates the important aspects of the original data, cross spectra with virtual references, i.e., G_{XV} from Eq. (3), were generated for $N_v = 3$, 7, and 11. Fig. 4 compares the CMIF of the reduced number of virtual references to that of all of the original measured references (where only the first five CMIFs are plotted). The eleven virtual references match the original at all of the primary peaks, as do the seven virtual references, except with a slightly reduced amplitude for the peaks at 26 and 27 Hz. The three virtual references capture most of the primary peaks, although

with reduced amplitude for the peaks at 26, 27, 29, 37, and 55–57 Hz, but might be missing a mode at 28 Hz. The conclusion here would be that while eleven virtual references would certainly be a good choice, seven could also be sufficient.

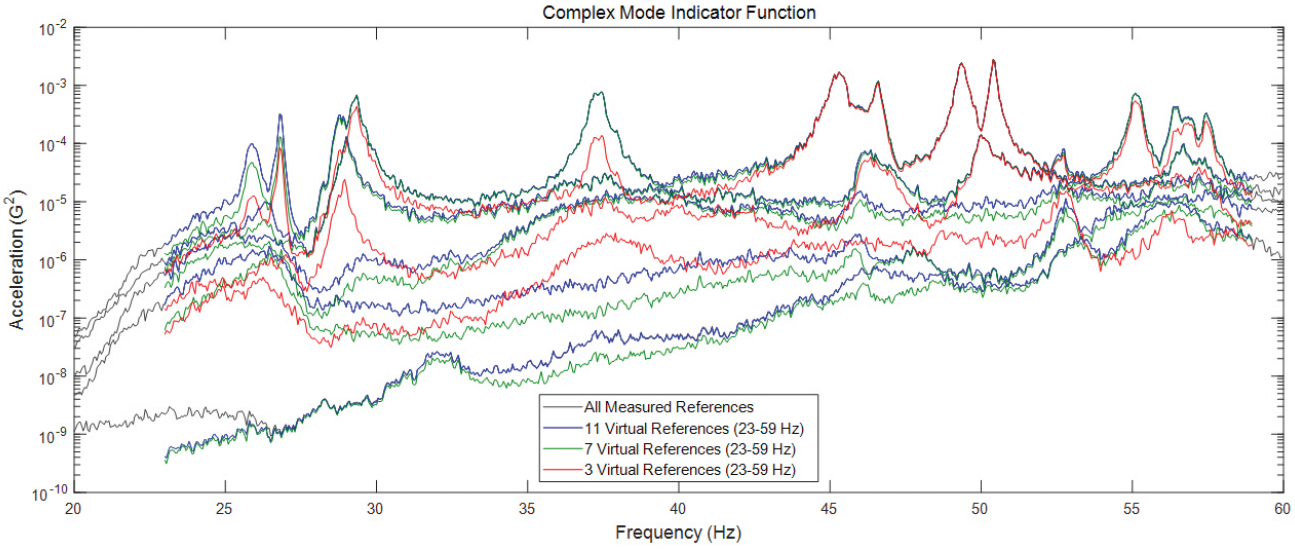

Fig. 4 CMIFs of cross spectra for 3, 7, and 11 virtual references in 23–59 Hz frequency band compared to CMIF of cross spectra for all measured references

In the preceding example, a set of virtual references was found for the entire 23–59 Hz frequency band. However, the example in Fig. 5 shows that it could be divided into several smaller frequency bands, with fewer virtual references for each band. In this case, three or four virtual references are sufficient to match the peaks in each of the three frequency bands.

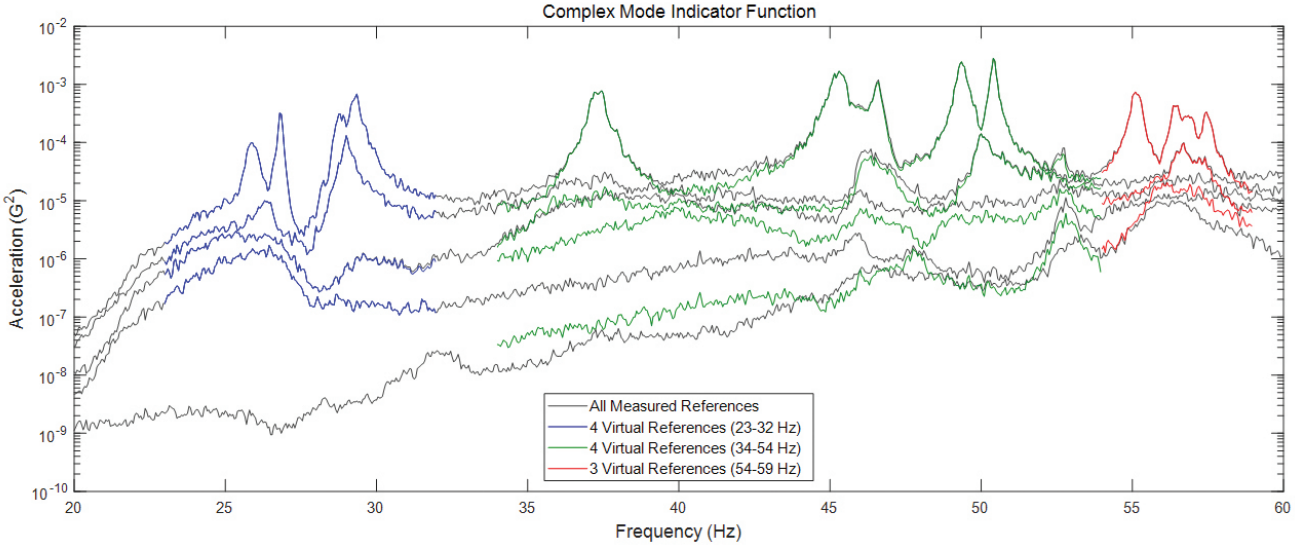

Fig. 5 CMIFs of cross spectra for virtual references in three frequency bands compared to CMIF of cross spectra for all measured references

Virtual References in the Time Domain

For the examples in the preceding section, we started with the 34×34 cross-spectra matrix from the DFAN test, which is not an excessive number of functions. However, for a larger number of responses, generating the entire $N_o \times N_o$ cross-spectra matrix could be avoided by creating the virtual references a few steps upstream in the time domain. To do this, you would first compute the response power spectral densities (PSDs) and plot a PSMIF of these functions to select the frequency bands, as shown in Fig. 6. Then bandpass-filter the time-response data to a frequency band. Virtual-reference time-response functions are generated by spatially filtering the measured time response with a subset of the singular vectors from the SVD of an $N_o \times N_p$ array of the measured time response, where N_p is the number of time points. Then compute the cross spectra between the measured responses and the virtual references.

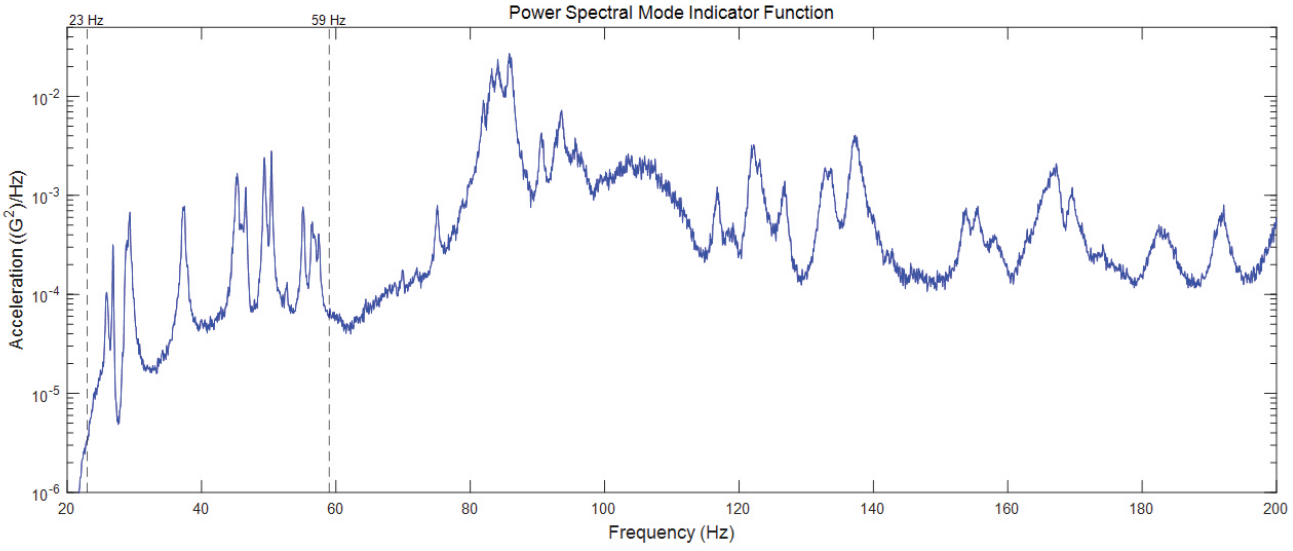

Fig. 6 PSMIF of response PSDs with the 23–59 Hz frequency band denoted by vertical, dashed lines

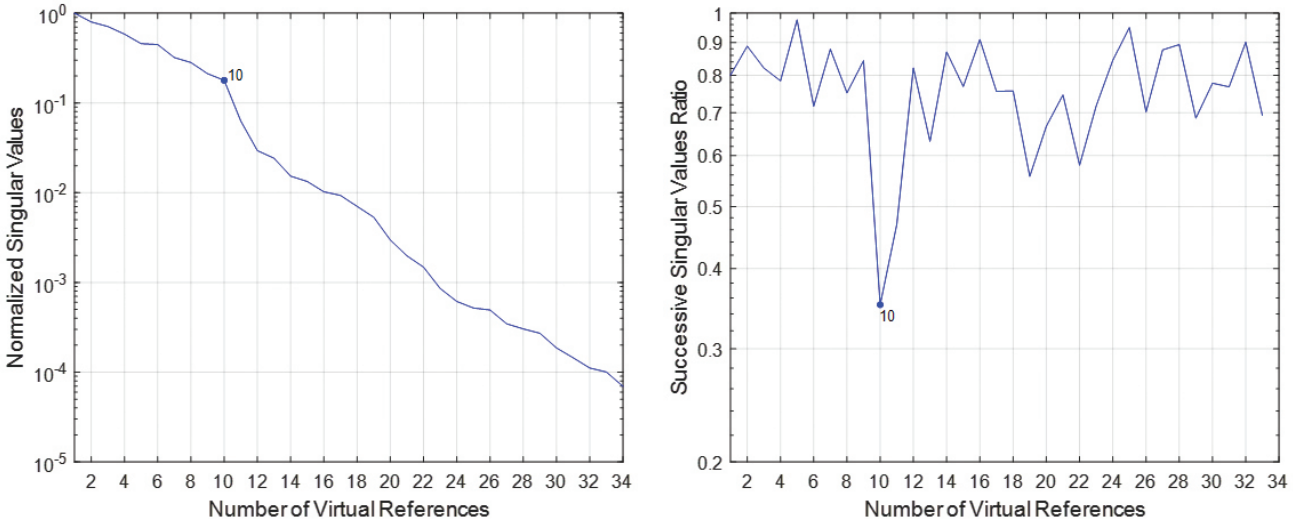

(a) (b)

Fig. 7 (a) Normalized singular values of 23–59 Hz bandpass-filtered time response; (b) successive ratio of singular values

Fig. 7 shows the singular values of the time response that has been bandpass-filtered to the 23–59 Hz frequency band. In this case, there is a distinct knee in the normalized singular values plot in Fig. 7(a) at ten virtual references, which is

confirmed by the successive ratio of the singular values in Fig. 7(b). Fig. 8 shows the CMIF of the cross spectra computed with ten virtual references, which compares very well with the CMIF of the original cross spectra with all the measured references. The deviation at the edges of the frequency band can be attributed to the roll-off of the filter.

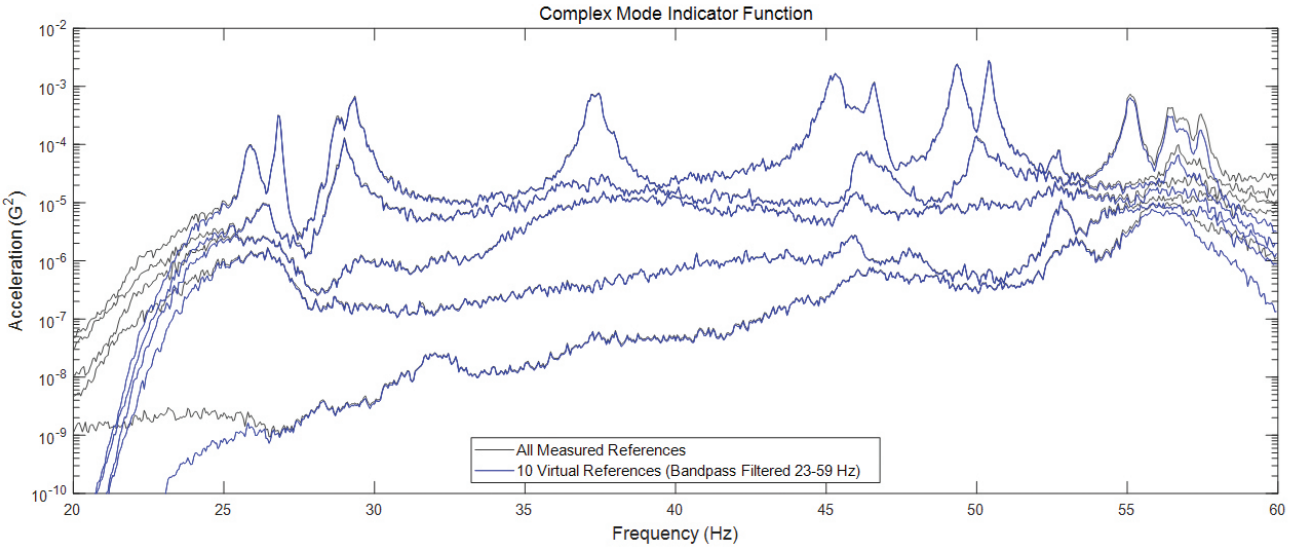

Fig. 8 CMIF of cross spectra for ten time-response virtual references for bandpass-filtered 23–59 Hz frequency band compared to CMIF of cross spectra for all measured references

Estimating Residues in Frequency Bands

When estimating residues, all of the spectral lines in the frequency range encompassing the selected poles are typically included, but as advocated in [6], sometimes it can be better to only use narrow frequency bands near the selected poles. This seems to be especially true for OMA with cross spectra, since the data in the valleys between the modes tend to be quite

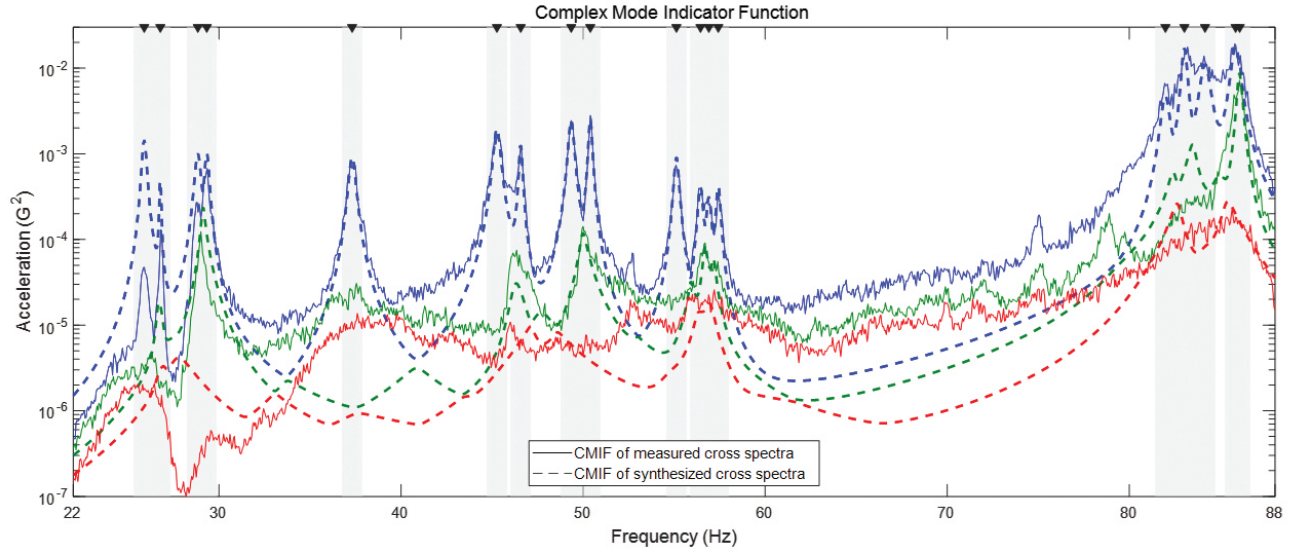

Fig. 9 CMIF for cross spectra synthesized from estimated modal parameters compared to CMIF for measured cross spectra when including all poles in residue solution

noisy. Additionally, we have found that including all the poles in the residues solution can sometimes adversely affect the estimates of some of them. In this case, better results can be obtained by estimating the residues as small groups in narrow frequency bands. An example of this occurrence is shown in Fig. 9, where the results for the four modes below 30 Hz are a cause for concern since the synthesized functions do not match the measured functions. For Fig. 10, the residues were estimated for the groups of poles in the vertical, gray bands, which greatly improved the results for those four modes. For both cases, the selected poles are designated by the triangular markers, and only the spectral lines in the vertical, gray bands were included in the residue estimation. While conclusive proof as to the cause of this phenomenon is not currently available, our prevailing conjecture is that the error in the residue estimation could be a result of violating a fundamental assumption of OMA—that the input spectrum is "broadband, smooth, and constant." For the DFAN test, the input spectra were controlled, but they were not completely flat over the entire frequency range and started to roll off below about 25 Hz (refer to Fig. 5 of [1]). Although this does invalidate the assumption, it's less invalid over small frequency spans, which might lessen the effect on the residue estimates.

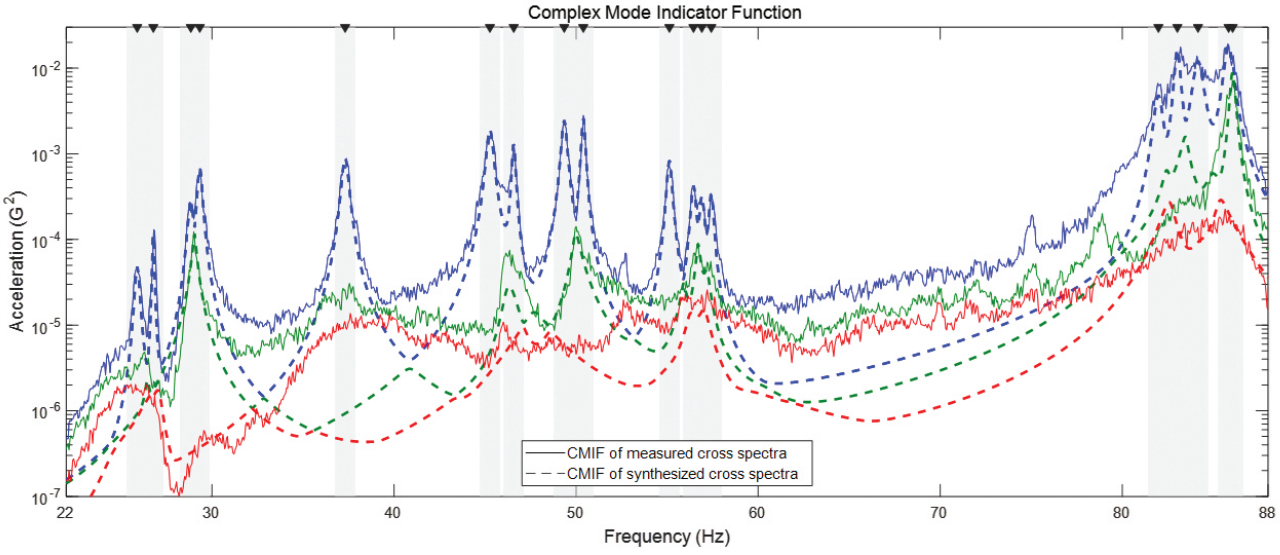

Fig. 10 CMIF for cross spectra synthesized from estimated modal parameters compared to CMIF for measured cross spectra when including narrow-frequency-band poles in residue estimation

Summary

When using cross spectra for OMA, the dataset is likely to have many more potential reference DOFs than are typically encountered when using FRFs for EMA. This paper has shown that the reference space can be reduced to something more amenable to a high-order algorithm by using virtual references instead of physical references. In the examples shown above, the transformation matrix to create the virtual references was derived from the SVD of the measured data from a frequency band (in either the frequency or time domain). However, other vectors, such as operating shapes or mode shapes from a finite element model, can also be used to create virtual references. By applying such a spatial filter, to either the cross spectra or the time response, with either a pseudo-inverse or mass-weighted-shape operation, those shapes can be emphasized in the frequency-domain functions. Doing so is advantageous when trying to extract a set of targets defined in a pretest analysis. Another obscure feature intended in the spirit of the "don't use data that doesn't help your cause" theme in [6] is to estimate the residues as small groups in narrow frequency bands if that improves your results.

References

1. Fladung, W., and Napolitano, K., "Why Don't We Just Use the Cross Spectra for Operational Modal Analysis?," *Proceedings of the 43rd International Modal Analysis Conference*, February 2025.

2. Napolitano, K., Yang, M., Friedlander, E., and Schick, D., "Mode Shape Extraction Using Direct Field Acoustic Noise Test Data," *Proceedings of the 43rd International Modal Analysis Conference*, February 2025.
3. Fladung, W., and Vold, H., "An Improved Implementation of the Orthogonal Polynomial Modal Parameter Estimation Algorithm Using the Orthogonal Complement," *Proceedings of the 33rd International Modal Analysis Conference*, February 2015.
4. Fladung, W., and Vold, H., "An Orthogonal View of the Polyreference Least-Squares Complex Frequency Modal Parameter Estimation Algorithm," *Proceedings of the 33rd International Modal Analysis Conference*, February 2015.
5. Mayes, R., and Rohe, D., "A Colored Complex Mode Indicator Function for Selecting a Final Mode Set," *Proceedings of the 36th International Modal Analysis Conference*, February 2018.
6. Fladung, W., and Napolitano, K., "Tips, Tricks, and Obscure Features for Modal Parameter Estimation," *Proceedings of the 41st International Modal Analysis Conference*, February 2023.

Chapter 16
Time-Reversed Vibration-Induced Particle Motion on an Elastic Plate

Abigail Smith, Sanchita Das, Samikhshak Gupta, and Vijaya V. N. Sriram Malladi

Abstract This study investigates the use of time-reversed vibration profiles to observe the motion of flat-surface beads on a two-dimensional elastic plate. Building on earlier demonstrations of object manipulation with time-reversal focusing, the present work examines how controlled flexural waveforms influence particle trajectories and displacement. An experimental setup with four modal shakers and a laser vibrometer is used to synthesize waveforms from measured impulse responses excited by chirp signals. By varying parameters such as frequency bandwidth, clipping threshold, excitation amplitude, particle position, and distance from the excitation source, energy is focused at prescribed locations on the plate. Particle motion is recorded with an overhead camera and analyzed to characterize displacement patterns and trajectory repeatability. Preliminary trials provide new insight into the feasibility of using tuned time-reversal profiles to study particle dynamics, advancing the foundation for vibration-based approaches to particle manipulation.

Keywords Time reversal · Vibration profile · Particle manipulation · Impulse response function · Flexural waveform

Introduction

The concept of reversing time has long fascinated scientists. In signal processing, time reversal (TR) has been studied since the 1960s [1], originally applied to underwater acoustic communication between submarines. TR enables wave fields to be refocused at a location distinct from their original source, allowing waves emitted from different source locations to amplify the response at a designated focal point. Initially termed *matched signal processing* [1], the concept was later popularized as *time-reversed acoustics* (or simply time reversal) in the 1990s by Fink and colleagues [2, 3]. Since then, its applications have expanded to medicine (e.g., lithotripsy for kidney stone treatment [4], transskull therapy [5]), hydrodynamics [6], nondestructive testing [7], and fundamental physics experiments [8]. In elastic media, TR has been used for structural health monitoring [7, 9], pipe communication [10], and seismic event localization [11]. A comprehensive overview is given in [12].

More recent demonstrations have popularized TR in laboratory environments. In 2017, BYU Acoustics visually illustrated TR focusing in a thin plate [13], followed by playful demonstrations using LEGO minifigures [14]. These studies showed the forward step—where an impulse is emitted from a source and recorded at a receiver—and the backward step, in which the recorded response is reversed in time and re-emitted to retrace the original path. This process results in the original source receiving a signal closely resembling the initial impulse. Extending this approach, multiple sources were employed with a single focal receiver: sequential emissions were recorded, time-reversed, and rebroadcast simultaneously. Constructive interference at the focal location produced a strong amplified response, validated in practical demonstrations such as knocking over small objects via localized TR focusing.

While TR in acoustics and elastic media has been widely studied, its application to *particle motion* remains limited. Early work in geophysics proposed TR imaging to investigate particle chaos and its suppression through wave propagation [15]. More recently, Anderson's group demonstrated elastic wave visualization using salt grains on a plate, showing that TR focusing could be achieved at pre-selected focal points. Building on this foundation, the present study investigates particle motion on an elastic plate to characterize the amplitude and effective radius of TR focusing. Elastic waves are introduced by

Abigail Smith · Sanchita Das · Samikhshak Gupta · Vijaya V. N. Sriram Malladi
Vibrations, Intelligent Testing, & Active Learning of Structures (ViTALS) Group, Department of Mechanical and Aerospace Engineering, Michigan Technological University, Houghton, MI 49931
e-mail: abrsmith@mtu.edu; sdas14@mtu.edu; sgupta14@mtu.edu; smalladi@mtu.edu

© The Author(s), under exclusive license to River Publishers 2026

Kristin B. Zimmerman, PhD (eds.), *Topics in Modal Analysis & Parameter Identification in Structural Dynamics, 2026, Vol. 8*, Conference Proceedings of the Society for Experimental Mechanics Series, https://doi.org/10.13052/rp-9788743814191

four modal shakers at the plate corners, and small beads placed on the plate surface serve as tracers of particle motion. The aim is to observe how TR focusing influences bead displacement and to determine the spatial extent of the focal region.

To this end, we developed an experimental setup that began with qualitative visualization (a splash of water), followed by a single bead, and later extended to grid-like arrangements of multiple beads. Initial results demonstrate the successful application of TR focusing for multi-particle motion. A more detailed analysis of individual particle trajectories and parameter effects is reserved for future work.

Overview of Time-reversal

Let $s(t)$ denote the source signal, $h(t)$ the impulse response of the medium between a source and a receiver, and $r(t)$ the received signal. Using Fourier transforms (denoted by capital letters), we write $X(\omega) = \mathbb{F}\{x(t)\}$. These derivations are followed from a book chapter called *Time Reversal Techniques* by Anderson *et al.* [16].

Forward step: The received signal is the convolution of the source with the medium response,

$$r(t) = (h * s)(t) = \int_{-\infty}^{\infty} h(\tau)\, s(t-\tau)\, d\tau, \tag{1}$$

which in the frequency domain becomes

$$R(\omega) = H(\omega)\, S(\omega). \tag{2}$$

Time reversal: The time-reversed signal is

$$y(t) = r_{\mathrm{TR}}(t) = r(-t), \tag{3}$$

which in the frequency domain corresponds to

$$Y(\omega) = R(-\omega), \quad \text{and if } r(t) \in \mathbb{R}, \quad Y(\omega) = R^*(\omega). \tag{4}$$

Backward step: Re-emitting $y(t)$ from the original source location forces multipath components to arrive in phase at the receiver (the focal point). The focal waveform is proportional to the autocorrelation of the impulse response:

$$p_{\mathrm{focus}}(t) \;\propto\; (h * h^-)(t) = \int_{-\infty}^{\infty} h(\tau)\, h(\tau - t)\, d\tau, \quad h^-(t) \equiv h(-t), \tag{5}$$

which has a sharp peak at $t = 0$. In the frequency domain,

$$P_{\mathrm{focus}}(\omega) \;\propto\; H(\omega)\, H^*(\omega) = |H(\omega)|^2. \tag{6}$$

These relations assume that the medium is linear, reciprocal, and time-invariant, with sufficient bandwidth and signal-to-noise ratio, and negligible change between forward and backward steps.

Finally, for discrete signals, if $r[n]$ has length N, then the time-reversed sequence is $r_{\mathrm{TR}}[n] = r[N-1-n]$, and for real-valued $r[n]$, the frequency-domain representation satisfies $R_{\mathrm{TR}}[k] = R^*[k]$.

Overview of Experimental Setup

The elastic medium employed in this study is a flexible aluminum plate with dimensions $9.5 \times 9.5 \times 0.06$ in^3, as shown in fig. 1a. The plate is supported at its four corners by nylon stingers that are coupled to modal shakers. Each shaker is mounted in a 3D-printed stand with bolt holes, allowing secure attachment to the test table or other fixtures. The entire assembly is stabilized by a rectangular frame constructed from 80/20 aluminum beams, which provides both portability and adjustable shaker placement. This mechanical configuration ensures that the excitation is applied in a repeatable and controlled manner.

The excitation signal is supplied by Douk Audio Nobsound power amplifiers, which are connected through custom-modified audio jacks to the data acquisition (DAQ) system. The output signals are delivered to the shakers and simultaneously looped back into the DAQ, which allows us to monitor the input and verify that any observed disturbances arise from the mechanical system rather than electrical interference. To further validate the input, PCB force sensors are positioned between the stingers and the plate, enabling direct measurement of the transmitted force. These measurements help us track the excitation as it passes through the system and isolate potential sources of noise.

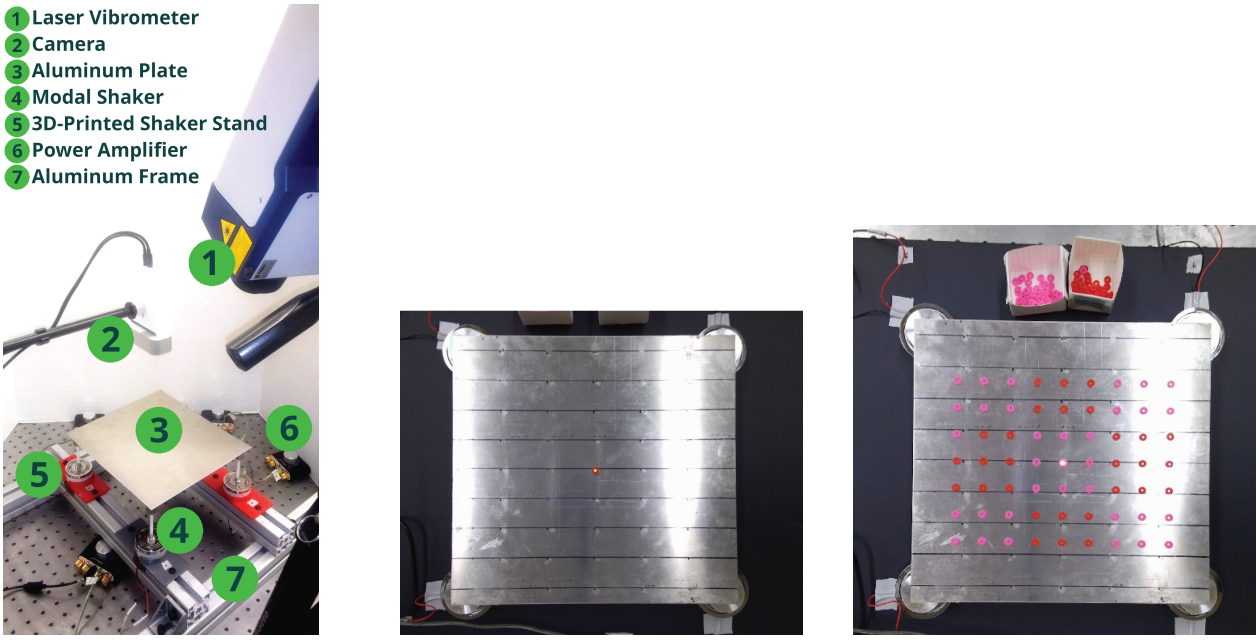

(a) (b) (c)

Fig. 1 Photographs of the experimental setup: (a) labeled view of components, (b) single particle, (c) grid-like layout of multiple particles

We record the vibrations of the plate using a Polytec MLV-100 laser vibrometer mounted on a tripod and directed toward predefined measurement points. The vibrometer output is processed by a Polytec OFV-5000 controller, which provides a velocity signal to the DAQ. To complement these measurements, we also monitor particle motion on the plate surface using a Microsoft Azure Kinect camera suspended overhead. The Kinect is connected to the control computer via USB and provides both images and videos of particle trajectories, giving us a visual record to correlate with vibrometer data.

The baseline testing procedure follows the two-step TR framework described in eqs. (1), (3) and (5). In the forward step, we generate a chirp signal in MATLAB and deliver it sequentially to the shakers while recording the response at the desired focal location using the vibrometer. This measurement provides the effective impulse response of the system, $h(t)$, convolved with the source signal. The recorded response is then processed: it is transformed into the frequency domain, windowed to reduce noise, and then time-reversed by spectral conjugation as expressed in eq. (4). In the backward step, the time-reversed signals are simultaneously re-emitted from all shakers. By reciprocity, the multipath components of the wave field retrace their original trajectories and arrive in phase at the focal point. The reconstructed waveform is therefore proportional to the autocorrelation of the impulse response, $(h * h^{-})(t)$, as in eq. (5), which produces a sharp focus in both time and space at the chosen measurement location. This two-step process provides a controlled basis for TR focusing on the plate.

With this baseline established, we extend the setup to investigate particle motion under TR focusing. The particles used are small, flat, disk-shaped rubber beads. For single particle motion (SPM), the setup requires only minor modification: as shown in fig. 1b, a single bead is placed at the focal point between the forward and backward steps. We then activate the backward step and observe the resulting displacement of the particle. For multiple particle motion (MPM), we place a total of 63 beads in a 7×9 grid layout using a plexiglass spacer to ensure precise and repeatable placement (fig. 1c). To improve clarity during analysis, beads in different regions are assigned contrasting colors.

Results and Discussion

Particle motion was further explored in a set of two trials, which were performed using the same parameters to test repeatability of the process. Each trial repeated the backward step of the TR focusing process multiple times without resetting the beads to their initial positions. This procedure was performed ten times in sequence for each trial, with the final bead positions captured after each iteration using the Microsoft Azure Kinect camera. The recorded images were processed through a

systematic pipeline: blob analysis was first applied to identify bead positions, an HSV color-thresholding method was used to create binary masks, and the Hungarian algorithm was employed to assign unique IDs and track each of the 63 beads across frames. For clarity, each processed image is referred to as a *frame*, with the initial configuration being Frame 1. Including the ten repeated backward steps, the dataset comprised 11 frames. Representative examples—Frames 1, 3, 5, 7, 9, and 11—from Trial 1 are shown in fig. 2.

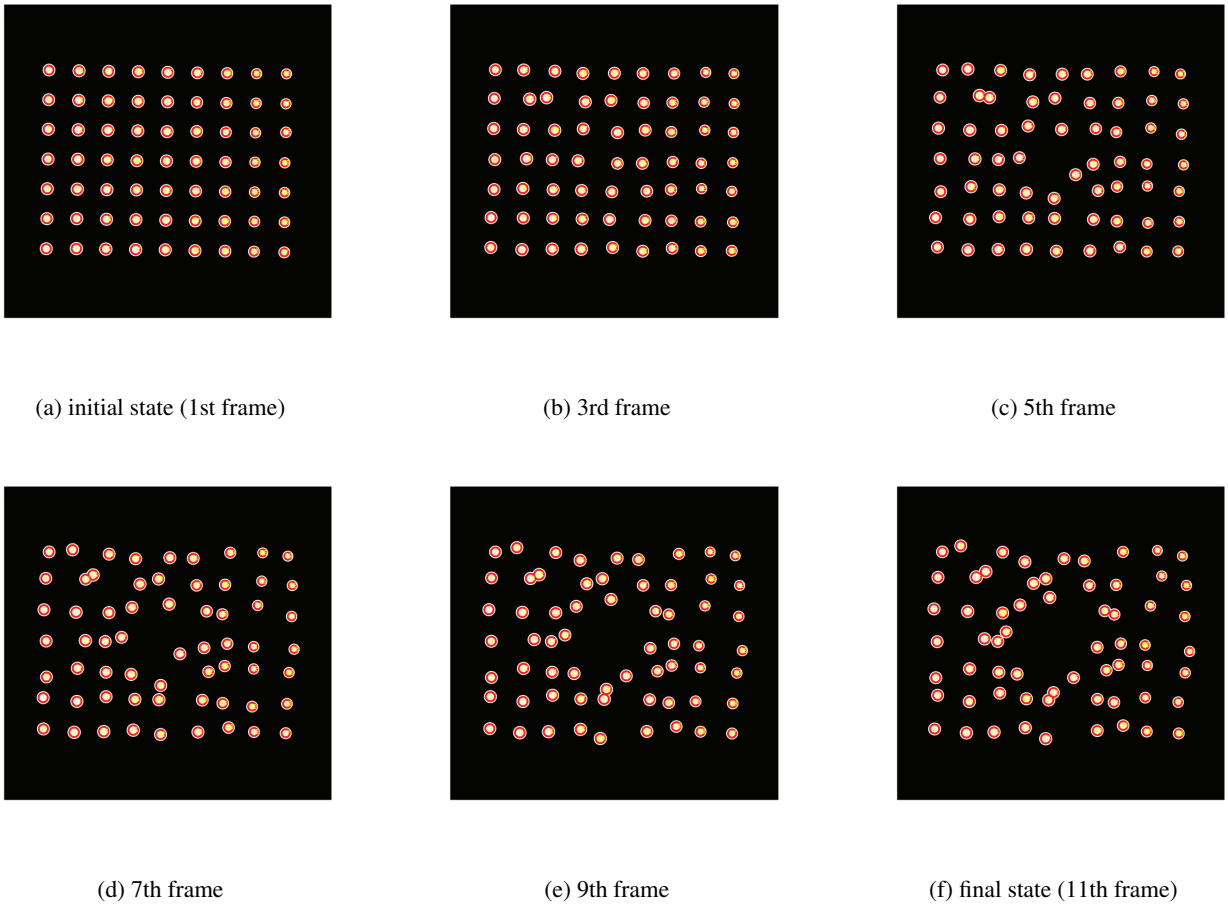

(a) initial state (1st frame) (b) 3rd frame (c) 5th frame

(d) 7th frame (e) 9th frame (f) final state (11th frame)

Fig. 2 Multiple particle motion at different stages (Trial 1)

The effect of the TR impulse is evident in these frames, where the focal region shows clear localized bead motion while beads farther away remain relatively undisturbed. Particle identity was preserved between frames using a nearest-neighbor tracking method, which enabled full trajectories to be reconstructed. The trajectories of all beads across the 11 frames are presented in fig. 3a and fig. 3d, while fig. 3b and fig. 3c compare bead displacement from the focal point, with data points color-coded by frame.

Analysis of the results highlights two important observations: First, beads located closer to the focal source consistently experienced larger displacements, confirming the localized nature of TR focusing. Second, the relationship between displacement and distance from the focal point was not strictly linear. As illustrated in fig. 3b and fig. 3c, displacement did not decrease smoothly with increasing distance; instead, localized variations were observed, where beads farther away still exhibited significant motion. Furthermore, the results from different trials indicate that the process is not strictly repeatable, as the maximum displacement reached by the center bead in the 11th frame of the first trial was already attained by the 8th frame in the second trial. These variations suggest that interference patterns and secondary reflections within the plate influence particle trajectories. The findings emphasize the complex dynamics of wave–particle coupling in elastic media and indicate that factors beyond distance alone, such as boundary conditions and scattering effects, contribute to the observed particle behavior.

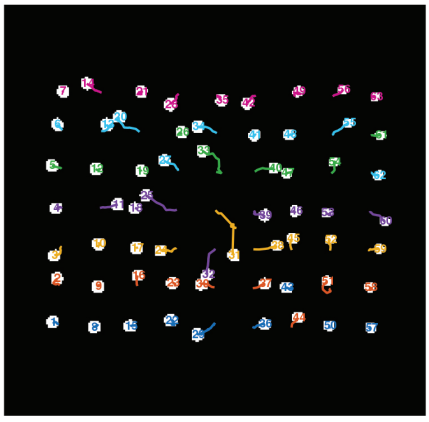

(a) Trial 1 trajectories

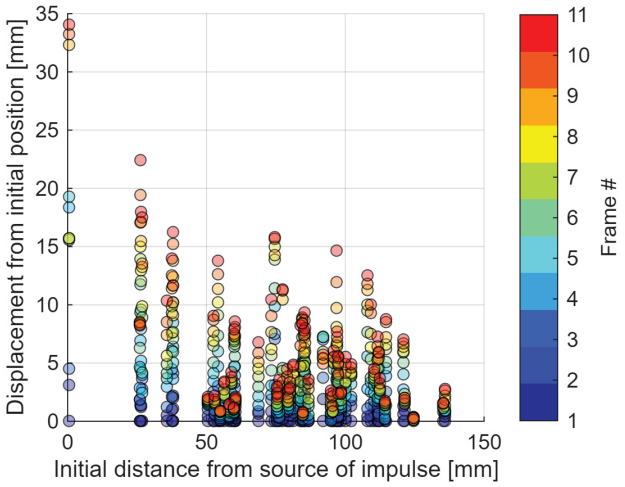

(b) Trial 1 displacement

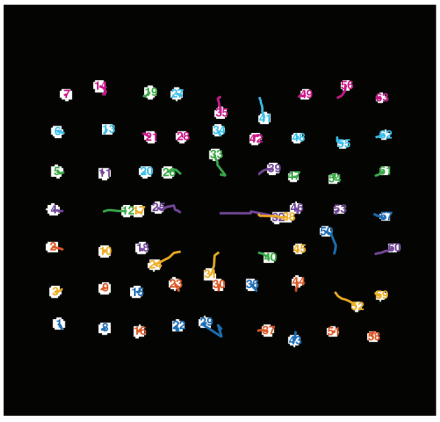

(c) Trial 2 trajectories

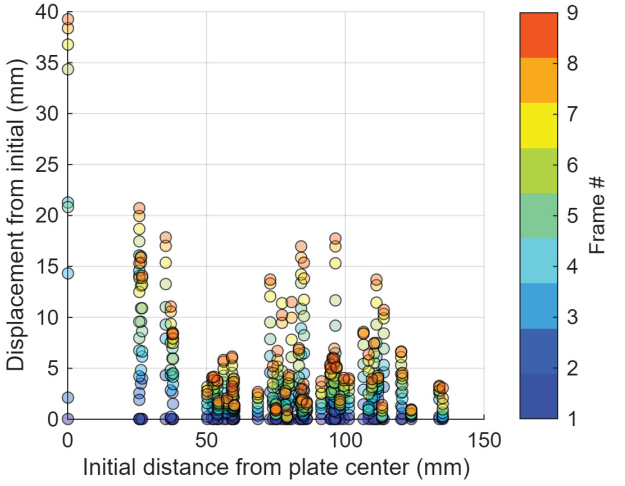

(d) Trial 2 displacement

Fig. 3 Overview of multiple particle motion: (left) reconstructed trajectories of individual beads across 11 frames, (right) displacement comparison as a function of distance from the impulse source

Conclusion

This work demonstrated the use of TR focusing to study vibration-induced particle motion on an elastic aluminum plate. The experimental setup, consisting of four modal shakers, a laser vibrometer, and an overhead camera system, successfully generated and observed TR focusing effects. Preliminary trials with a splash of water and a single bead confirmed the basic operation of the setup, while the extension to multiple particles provided a clearer view of how TR focusing influences ensembles of particles. The results showed that beads located near the focal region consistently experienced the largest displacements, confirming the localized nature of TR focusing. At the same time, the relationship between displacement and distance from the focal point was found to be non-linear, suggesting that interference patterns, reflections, and boundary effects strongly shape the observed motion.

While the experiments and modeling validate the feasibility of TR focusing for particle manipulation, several aspects remain open for further study. The model for TR focusing can be optimized by varying force and sensor locations, as well as by modifying the input signals, in order to achieve more precise and tunable focusing. The next stage of this research will include mounting the setup under a Scanning Laser Doppler Vibrometer (SLDV), which will provide a better angle for accurate measurements and yield detailed information about the vibration profile of the plate. In addition, different force positions will be simulated and tested to evaluate whether symmetry plays a role in system performance. Together, these efforts will help refine the experimental methodology and improve the control of particle motion using TR focusing.

In summary, this study establishes a foundation for applying TR-based vibration focusing to particle manipulation in elastic media. By combining experimental validation with numerical modeling, we have shown both the potential and the challenges of this approach, setting the stage for more systematic and optimized investigations in future work.

Acknowledgments This research was partially supported by the National Science Foundation through the grant CMMI-2301776.

References

1. Parvulescu, A. and Clay, C. "Reproducibility of signal transmissions in the ocean". *Radio and Electronic Engineer*, 29(4):223–228 (1965)ifnextchar.gobble.
2. Fink, M. "Time-reversed acoustics". *Scientific American*, 281(5):91–97 (1999)ifnextchar.gobble.
3. Fink, M., Cassereau, D., Derode, A., Prada, C., Roux, P., Tanter, M., Thomas, J.L., and Wu, F. "Time-reversed acoustics". *Reports on progress in Physics*, 63(12):1933 (2000)ifnextchar.gobble.
4. Fink, M., Montaldo, G., and Tanter, M. "Time-reversal acoustics in biomedical engineering". *Annual review of biomedical engineering*, 5(1):465–497 (2003)ifnextchar.gobble.
5. Thomas, J.L. and Fink, M.A. "Ultrasonic beam focusing through tissue inhomogeneities with a time reversal mirror: application to transskull therapy". *IEEE transactions on ultrasonics, ferroelectrics, and frequency control*, 43(6):1122–1129 (2002)ifnextchar.gobble.
6. Chabchoub, A. and Fink, M. "Time-reversal generation of rogue waves". *Phys. Rev. Lett.*, 112:124101 (2014)ifnextchar.gobble.
7. Prada, C., Kerbrat, E., Cassereau, D., and Fink, M. "Time reversal techniques in ultrasonic nondestructive testing of scatteringmedia". *Inverse problems*, 18(6):1761 (2002)ifnextchar.gobble.
8. de Rosny, J. and Fink, M. "Overcoming the diffraction limit in wave physics using a time-reversal mirror and a novel acoustic sink". *Phys. Rev. Lett.*, 89:124301 (2002)ifnextchar.gobble.
9. Anderson, B., Griffa, M., Ulrich, T., Le Bas, P.Y., Guyer, R., and Johnson, P. "Crack localization and characterization in solid media using time reversal techniques". In *ARMA US Rock Mechanics/Geomechanics Symposium*, pages ARMA–10. ARMA (2010)ifnextchar.gobble.
10. Anderson, B.E., Ulrich, T.J., Le Bas, P.Y., and Ten Cate, J.A. "Three-dimensional time reversal communications in elastic media". *The Journal of the Acoustical Society of America*, 139(2):EL25–EL30 (2016)ifnextchar.gobble.
11. Larmat, C.S., Guyer, R.A., and Johnson, P.A. "Time-reversal methods in geophysics". *Physics Today*, 63(8):31–35 (2010)ifnextchar.gobble.
12. Anderson, B.E., Griffa, M., Johnson, P.A., Larmat, C., and Ulrich, T.J. "Time reversal" (2008)ifnextchar.gobble.
13. Heaton, C., Anderson, B.E., and Young, S.M. "Time reversal focusing of elastic waves in plates for an educational demonstration". *The Journal of the Acoustical Society of America*, 141(2):1084–1092 (2017)ifnextchar.gobble.
14. Barnes, L.A., Anderson, B.E., Le Bas, P.Y., Kingsley, A.D., Brown, A.C., and Thomsen, H.R. "The physics of knocking over lego minifigures with time reversal focused vibrations for use in a museum exhibita)". *The Journal of the Acoustical Society of America*, 151(2):738–751 (2022)ifnextchar.gobble.
15. Draeger, C. and Fink, M. "One-channel time reversal of elastic waves in a chaotic 2d-silicon cavity". *Physical Review Letters*, 79(3):407 (1997)ifnextchar.gobble.
16. Kundu, T. *Nonlinear Ultrasonic and Vibro-Acoustical Techniques for Nondestructive Evaluation*. Springer International Publishing (2018)ifnextchar.gobble.

Chapter 17
Damping Identification Using FBG Sensors in Controlled Thermal and Pressure Conditions

Lorenzo Sclafani, Antonello Binni, Silvia Milana, Antonio Culla, and Antonio Carcaterra

Abstract

Low-intensity mechanical vibrations become critical in several domains of experimental physics, such as gravitational wave detection, the search for neutrinoless double beta decay, and quantum computing. In these contexts, extremely accurate measures require high isolation from external vibrational sources and challenging sensor sensitivity. In extreme working conditions, as cryogenic temperatures and high vacuum, the uncertainties in material properties represent a significant limitation for the stability and accuracy of measurements.

Although stiffness has been extensively studied, damping remains a significantly less understood phenomenon. Due to the poorly understood connection between macroscopic and microscopic effects, current models of damping are incomplete. While it is often approximated in practice as a constant parameter, experimental evidence suggests that damping is highly dependent on both temperature and frequency.

This work aims to provide a comprehensive characterization of damping across a wide range of environmental conditions, in order to investigate its behaviour and its intrinsic dependence on variables such as temperature and pressure. To this end, a novel experimental setup is proposed, employing Fiber Bragg Grating (FBG) sensors and a single-stage pulse tube cryostat, to extract the damping characteristics of a cantilever beam in controlled conditions. Unlike traditional approximations, a more sophisticated damping model is presented, distinguishing different damping contributions and highlighting their dependence on environmental variables.

The results of this study are expected to deepen the understanding of damping mechanisms under extreme conditions, thereby supporting the design and predictive modeling of dynamic systems operating in such environments.

Keywords Damping · Experimental identification · Fiber optics · FBGs · Cryogenics

Introduction

Damping refers to the mechanisms by which the vibratory energy of a system is irreversibly dissipated, closely linked to the thermodynamic concept of dissipation, i.e., the conversion of mechanical energy into heat. Together with stiffness and mass, it represents one of the fundamental parameters required to predict the dynamic response of a system [1]. In structural applications, the measured damping typically results from the superposition of different dissipation mechanisms [2], whose identification remains challenging and often leads to oversimplifications.

Existing dissipative models are essentially phenomenological [3, 4, 5, 6], and a comprehensive description of the process, as the transfer of energy from a macroscopic to a microscopic level (i.e., particles' kinetic energy, hence temperature), is still missing. Nevertheless, recent contributions, such as Carcaterra and Akay's [2, 7, 8] have shown the field's increasing interest towards physically motivated models.

Lorenzo Sclafani
Department of Physics and Astronomy "G. Galilei", University of Padua, Padua, Italy,
e-mail: lorenzo.sclafani@phd.unipd.it

Lorenzo Sclafani · Antonello Binni · Silvia Milana · Antonio Culla · Antonio Carcaterra
Department of Mechanical and Aerospace Engineering, Sapienza University of Rome, Rome, Italy
e-mail: lorenzo.sclafani@uniroma1.it; antonello.binni@uniroma1.it; silvia.milana@uniroma1.it;
antonio.culla@uniroma1.it; antonio.carcaterra@uniroma1.it

© The Author(s), under exclusive license to River Publishers 2026

Kristin B. Zimmerman, PhD (eds.), *Topics in Modal Analysis & Parameter Identification in Structural Dynamics, 2026, Vol. 8*,
Conference Proceedings of the Society for Experimental Mechanics Series, https://doi.org/10.13052/rp-9788743814191

A deeper understanding of damping would significantly improve the prediction of structural behavior, particularly under extreme conditions such as cryogenic temperatures and vacuum. These environments, driven by remarkable advancements in vacuum and cooling technologies, are central to applications in medicine, aerospace, and experimental physics. In particular, many modern large-scale fundamental physics experiments operating in cryogenics environments, such as gravitational wave detectors, neutrinoless double beta decay searches, and quantum computing systems, face significant challenges in sensor sensitivity when measuring small mechanical disturbances [9, 10]. A key issue is the limited knowledge of fundamental properties required for accurate system design, especially when leveraging amplification near resonance. While the mass is constant and stiffness is reasonably characterized, damping remains poorly understood, highlighting a significant gap in the literature.

In this context, this study aims to fill the crucial gap in the understanding of damping by proposing a novel experimental approach to characterize the damping of a simple cantilever beam over controlled temperature and pressure conditions. Firstly, the proposed theoretical model is briefly discussed. It accounts for both internal structural damping and fluid damping, explicitly introducing temperature dependence through constitutive relationships and fluctuation–dissipation arguments. Then, the experimental setup, leveraging a Pulse Tube cryocooler and Fiber Bragg Grating (FBG) optical sensors, is presented in detail.

Theoretical Damping Model

Slender continuous structures may be modeled as simple Euler–Bernoulli beams. When subjected to an external load $p(x,t)$, the beam's undamped transverse response $w(x,t)$ can be expressed as:

$$\frac{\partial^2}{\partial x^2}\left(EI\frac{\partial^2 w(x,t)}{\partial x^2}\right)+\rho A\frac{\partial^2 w(x,t)}{\partial t^2}=p(x,t) \tag{1}$$

where, E is the Young modulus, I the area moment of inertia, ρ the density and A the cross-section of the beam. Damping is often introduced into Equation 1 through an additional term proportional to the beam's velocity. This work, however, aims to find a more complete description of damping as a superposition of simultaneous phenomena.

The proposed damping model takes into account two fundamental dissipation mechanisms of structures: within the solid itself and due to the interaction with the surrounding fluid. The former, commonly referred to as internal or material damping, relates to the process by which the kinetic energy of a solid, subjected to periodic motion, is converted into heat due to many microscopic sources (e.g., dislocation motion and molecular friction). The latter, known as fluid damping, refers to the energy dissipation caused by a fluid's resistance to the relative motion of an object. This resistance, or drag, opposes motion and converts part of the mechanical energy into thermal energy in the fluid.

The internal structural damping is modelled following one of the latest works of Carcaterra and Akay [8]. The authors introduce a model based on a loss-free oscillator connected to a piston to describe dissipation as the degradation of energy from macroscale ordered energy (mechanical energy) to a microscale disordered form (kinetic energy of the particles). Employing their dissertation to highlight the temperature dependence, a dissipative constitutive relationship describing stress as a function of strain, strain rate, and temperature is obtained:

$$\sigma\left(\epsilon,\dot{\epsilon},T\right)=E\epsilon+\sigma_d\left(\dot{\epsilon},T\right) \tag{2}$$

On the other hand, the fluid damping is described using an older model of Akay and Carcaterra [2]. A piston in a cylinder filled with freely moving particles (representative of an ideal gas) is used to understand how the piston's energy irreversibly converts into the gas's thermal energy. By implementing the characteristic approach of the Fluctuation-Dissipation theorem, the net force resulting from the interaction with the surrounding gas can be expressed as the sum of two components. One, proportional to the velocity of the structure, can be interpreted as a damping term with a temperature-dependent damping coefficient $\gamma(T)$. While the other remains as a fluctuation $\tilde{f}(t)$, hence a random forcing term on the right-hand side of the system equation.

Therefore, by introducing these damping effects into Equation 1, the beam's damped equation of motion yields:

$$\frac{\partial^2}{\partial x^2}\left(EI\frac{\partial^2 w(x,t)}{\partial x^2}+\int\sigma_d\left(\dot{\epsilon}(z),T\right)z dA\right)+\rho A\frac{\partial^2 w(x,t)}{\partial t^2}+\gamma(T)\frac{\partial w(x,t)}{\partial t}=p(x,t)+\tilde{f}(t) \tag{3}$$

where the material damping effect appears as the integral term involving σ_d, resulting from the new constitutive relationship effect on the bending momentum. Both σ_d and γ can now be written explicitly as functions of temperature.

Experimental Set-up

To validate the theoretical model presented in the previous section, an experimental campaign was designed to investigate damping under controlled thermal and pressure conditions. The simultaneous control of variables was achieved using a single-stage cryostat, available at the Department of Mechanical and Aerospace Engineering (DIMA) of La Sapienza University. The system employs a Stirling-type single orifice pulse tube refrigerator (PTR), capable of reaching a temperature of around $70\,K$ on a limited surface, known as the *cold head*. Commonly referred to as cryocoolers, these machines consist of a few basic components (Figure 1): a compressor with a rotary valve, heat exchangers, a regenerator, a pulse tube, an orifice, and a buffer volume. In steady-state conditions, the working fluid (helium) is forced to oscillate by periodic pressure waves generated by the rotary valve, external to the system. These pressure variations induce an alternating motion of the fluid through the regenerator and in and out of the buffer through the orifice. This periodic motion activates a particular thermal exchange process as the gas flows through the regenerator: it cools down as it moves toward the cold-end heat exchanger (i.e. the cold head) and heats up on the way back. Finally, the pulse tube allows the fluid temperature to rise again, while the orifice and reservoir control the phase shift between pressure and mass flow, minimizing the heat transfer to the cold head. One of the key advantages of this system is its ability to achieve cryogenic temperatures with no moving components in the cold region [11, 12, 13].

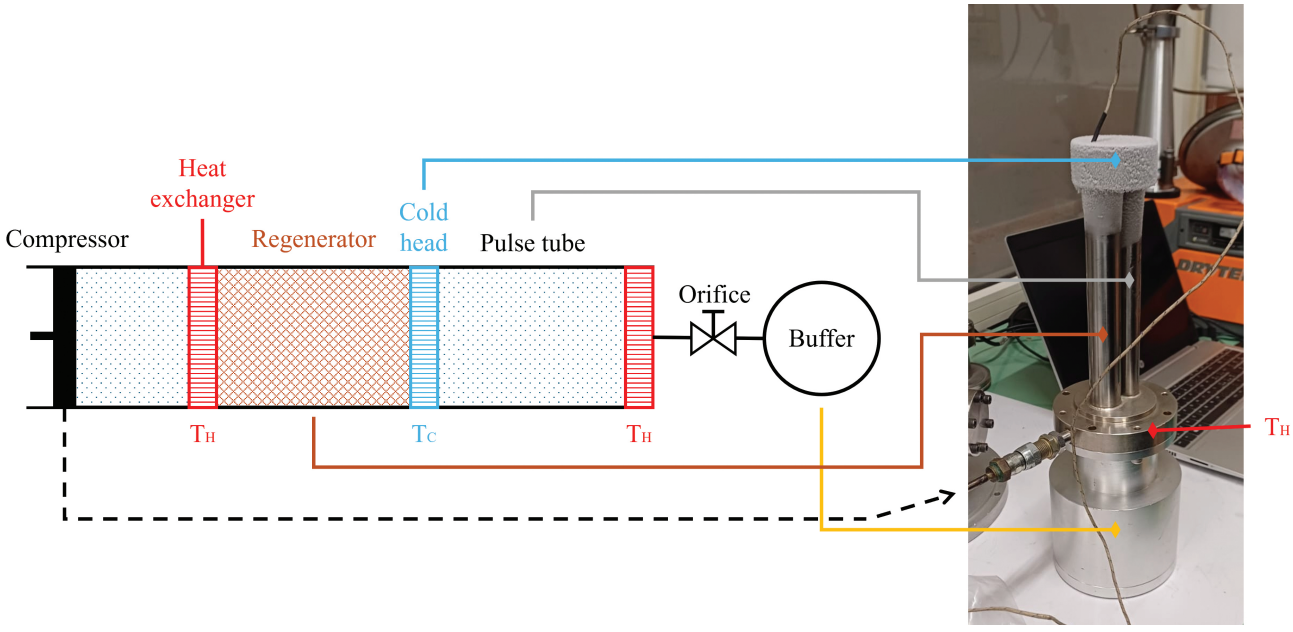

Fig. 1 Scheme of a typical PTR with reference to the cryocooler available at DIMA's lab, La Sapienza University

The PTR is inserted into the complementary vacuum chamber, creating a small experimental volume: a cylinder of approximately $100\,\text{mm}$ diameter and $60\,\text{mm}$ height. The pressure inside the chamber is controlled by a turbomolecular pump and measured with a FRG-700 Full Range Pirani Inverted Magnetron Gauge, reliable down to 5×10^{-9} mbar.

Within this controlled vacuum environment, the investigated system is a simple harmonic steel cantilever beam, directly fixed to the PTR's cold head. It has a length of $L = 40\,\text{mm}$, a width of $b = 10\,\text{mm}$, and a thickness of $h = 0.35\,\text{mm}$. An additional root length of $L_{\text{root}} = 15\,\text{mm}$ is included to ensure proper clamping conditions. Figure 2 shows the clamping system designed to place the beam parallel to the cold head surface. Two U-shaped plates grip the beam's root, while a disc of the same dimensions as the cold head presses them down. Since convection is ineffective under vacuum, this "sandwich" setup allows the beam to cool down through conduction at the fixed end, while enhancing radiative thermal exchange with the surrounding cold surfaces along its length.

Due to the small size of the beam and the high uncertainty in damping measurements, a non-contact excitation is preferred. In the proposed setup, the beam is excited by imposing a displacement on its fixed end through impact excitation of the outer shell of the cryostat. Such superimposed displacement, $u(t)$, on the fixture results in a uniform inertial load, $p(t)$, on the cantilever:

$$p(t) = -\rho A \ddot{u}(t), \tag{4}$$

where ρ is the beam's density and $A = h \cdot b$ is its cross-sectional area.

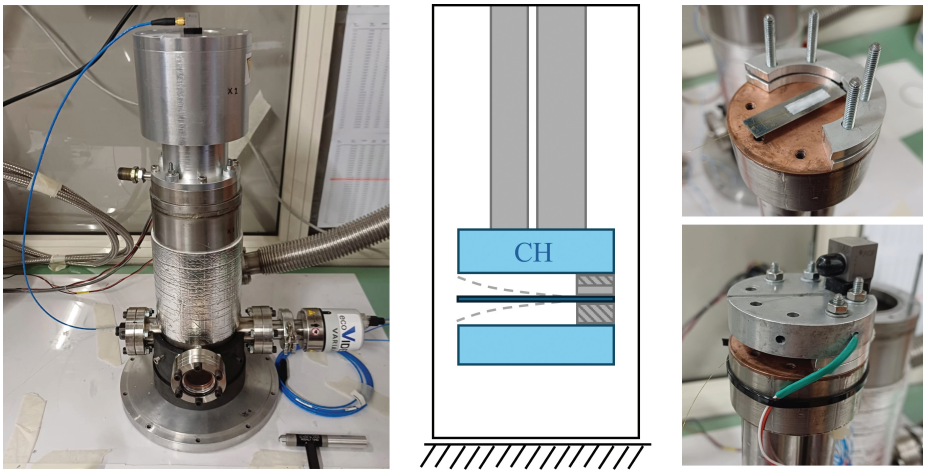

Fig. 2 Fully mounted cryostat with the sandwich clamping system, and schematic view of its interior

By preliminarily characterizing the cryostat through the transfer function between the outer shell and the fixture, the displacement at the fixed end can be inferred from the more accessible measurement of the outer cryostat response. For this purpose, triaxial accelerometers (PCB Piezotronics) and a Dewesoft Sirius acquisition system were employed.

Finally, the system response is measured in terms of strain using Fiber Bragg Grating (FBG) sensors. These optical sensors are an optimal choice thanks to their low invasiveness and well-documented ability to function in cryogenic environments [14, 15, 16, 17].

An FBG is a distributed Bragg reflector within an optical fiber, with periodic variations in the refractive index. This structure acts as an optical filter, reflecting a specific wavelength λ_B, called the Bragg wavelength, defined as:

$$\lambda_B = 2\, n_{eff}\, \Lambda \tag{5}$$

with n_{eff}, the effective refractive index, and Λ, the period of the grating.

External perturbations, such as temperature and strain, alter the grating period, shifting the reflected wavelength and enabling vibration sensing [17]. A schematic summary and visual representation of the FBG's working principle is given in Figure 3.

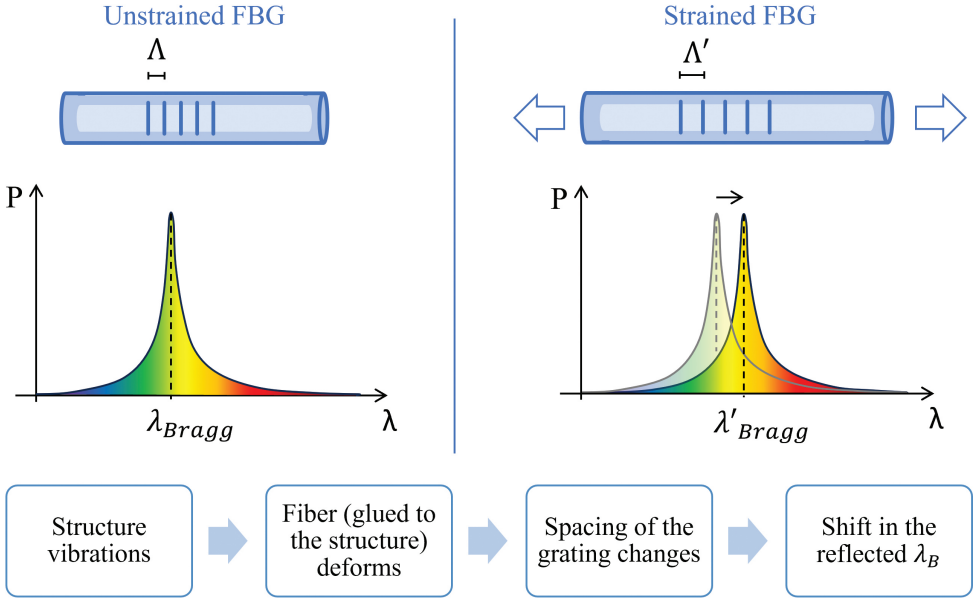

Fig. 3 Visual representation of FBG's working principle

Two FBGs are used in this experimental campaign. The first, glued to the beam using an equivalent of the Eccobond 286 A/B Epoxy suggested by [15], measures the strain. Its placement at $x_{FBG} = L/3$ is chosen so as not to coincide with the nodes of the first four modes of the cantilever. Meanwhile, the second FBG is left free to measure and compensate for thermal effects, as is common practice. From inside the cryostat, the fibers pass through a feedthrough and are connected to a Smartscan optical interrogator.

Figure 4 depicts the overall measurement setup.

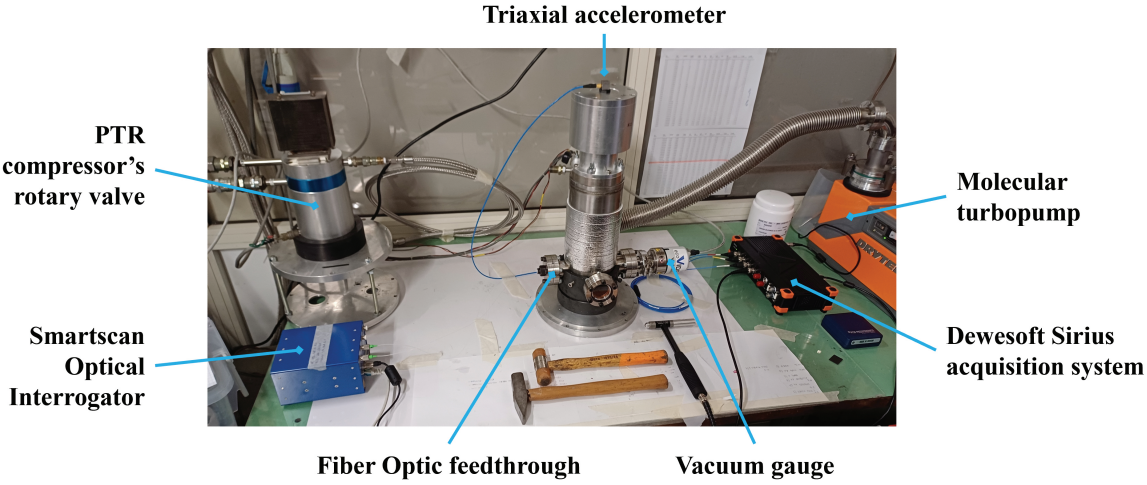

Fig. 4 Measurement setup

Conclusions

The experimental setup proposed in this study allows for the damping characterization of a cm-scale cantilever beam under controlled pressure and temperature conditions. Leveraging pulse tube cryocooler technology, it is possible to go down to cryogenic temperatures and mid-vacuum with minimal mechanical vibrations. Advanced optical sensors (FBGs) are used to measure the system, ensuring accurate and reliable data acquisition over time in such extreme conditions while avoiding the limitations of more intrusive techniques. The contemporary control over both temperature and pressure on the system is particularly relevant for the validation of advanced damping models that explicitly account for different dissipation mechanisms, such as the one proposed in this study. Indeed, control over the chamber pressure allows for neglecting the contribution of fluid–structure interaction, isolating the intrinsic internal structural damping. Meanwhile, the wide temperature range enables the investigation of the experimentally well-known damping-temperature relationship.

Although this work focuses on damping, the proposed setup could be implemented to characterize other fundamental properties (e.g., stiffness) and their relationship to environmental variables and extreme conditions. Nevertheless, many further improvements are possible. In particular, the design of the clamping system could be optimized to reduce uncertainties in boundary conditions and temperature gradients along the beam, while more sophisticated excitation methods could be introduced to expand the range and precision of the measurements.

Overall, the proposed methodology represents a promising step toward a more accurate and physically motivated characterization of damping, contributing to improving the design and prediction of dynamic systems under cryogenic and vacuum environments.

Acknowledgments This research was funded by the European Union – NextGeneration EU, Mission 4 Component 2 Investment 3.3 CUP C96E23000240005

References

1. Sestieri, A. and Carcaterra, A. "Vibroacoustic: The challenges of a mission impossible?". *Mechanical Systems and Signal Processing*, 34(1-2):1–18 (2013).

2. Akay, A. and Carcaterra, A. “Damping mechanisms”. In *Active and passive vibration control of structures*, pages 259–299. Springer (2014).
3. Levine, M.B. and White, C. “Material damping experiments at cryogenic temperatures”. In *Optical Materials and Structures Technologies*, volume 5179, pages 165–176. SPIE (2003).
4. Young Jr, C.P. and Buehrle, R.D. “Structural damping studies at cryogenic temperatures”. Technical report, National Aeronautics and Space Administration (NASA) (1994).
5. Le Bot, A., Carcaterra, A., and Mazuyer, D. “Statistical vibroacoustics and entropy concept”. *Entropy*, 12(12):2418–2435 (2010).
6. Tonazzi, D., Meziane, A., Culla, A., Biateau, C., Pepe, G., and Massi, F. “Material damping estimation within low-, medium-and high-frequency ranges”. *International Journal of Applied Mechanics*, 16(05):2450056 (2024).
7. Carcaterra, A. “New concepts in damping generation and control: theoretical formulation and industrial applications”. In *Variational Models and Methods in Solid and Fluid Mechanics*, pages 249–313. Springer (2012).
8. Carcaterra, A. and Akay, A. “Harmonic oscillator, dissipation, and thermodynamics”. *Journal of Applied Mechanics*, 92(4):041009 (2025).
9. Frasconi, F., Majorana, E., Naticchioni, L., Paoletti, F., and Perciballi, M. “A vertical accelerometer for cryogenics implementation in third-generation gravitational-wave detectors”. *Measurement Science and Technology*, 25(1):015103 (2013).
10. Chen, D., Naticchioni, L., Khalaidovski, A., Yamamoto, K., Majorana, E., Sakakibara, Y., Tokoku, C., Suzuki, T., Kimura, N., Koike, S., et al. “Vibration measurement in the kagra cryostat”. *Classical and Quantum Gravity*, 31(22):224001 (2014).
11. Park, J., Jeong, S., and Cha, J. “Development and experimental investigation of stirling-type pulse tube refrigerator (ptr) below 20 k; cold compressor and colder expander”. *International Journal of Refrigeration*, 75:64–76 (2017).
12. Richardson, R. and Evans, B. “A review of pulse tube refrigeration”. *International journal of refrigeration*, 20(5):367–373 (1997).
13. Wang, B., Chao, Y., Zhao, Q., Wang, H., Wang, Y., and Gan, Z. “A high efficiency stirling-type pulse tube refrigerator for cooling above 200 k”. *Energy*, 215:119120 (2021).
14. James, S.W., Tatam, R.P., Twin, A., Morgan, M., and Noonan, P. “Strain response of fibre bragg grating sensors at cryogenic temperatures”. *Measurement science and technology*, 13(10):1535 (2002).
15. Li, J., Neumann, H., and Ramalingam, R. “Design, fabrication, and testing of fiber bragg grating sensors for cryogenic long-range displacement measurement”. *Cryogenics*, 68:36–43 (2015).
16. Venkatesan, V. and Ramalingam, R. “Numerical and experimental investigation of fbg strain response at cryogenic temperatures”. In *IOP Conference Series: Materials Science and Engineering*, volume 171, page 012133. IOP Publishing (2017).
17. Wang, X., Guo, Y., Xiong, L., and Wu, H. “High-frequency optical fiber bragg grating accelerometer”. *IEEE Sensors journal*, 18(12):4954–4960 (2018).

Chapter 18
Experimental-Based Investigation of Standing and Traveling Waves in a Petri Dish using Piezoelectric Actuation

Rachel Cole, Samikhshak Gupta, Vijaya V. N. Sriram Malladi, Smitha Rao Hatti, and Adrienne Minerick

Abstract This study experimentally investigates the vibrational behavior of a circular Petri dish to characterize and control standing and traveling wave fields through piezoelectric actuation. Harmonic excitation was applied using four piezoelectric stacks, and out-of-plane surface motion was captured with a Scanning Laser Doppler Vibrometer (SLDV). The resulting frequency response functions (FRFs) were analyzed directly to extract modal parameters including natural frequencies, damping ratios, and mode shapes. Based on these experimentally derived characteristics, a two-point excitation scheme was developed in which actuator pairs were driven simultaneously with prescribed phase offsets. The results show that excitation at natural frequencies produced standing waves, while driving between resonances with a 90° phase difference yielded traveling waves. Additionally, the actuator configuration determined the wave type: adjacent actuators generated rotational traveling waves, whereas diagonally opposed actuators produced translational patterns. These findings demonstrate how FRF-based experimental modal analysis can be used to design phase-controlled excitation strategies that selectively generate and tune wave kinematics in thin circular structures. The outcomes establish a foundation for Petri-dish-based platforms capable of precision particle transport, fluid manipulation, and resonant sensing applications.

Keywords Traveling waves · Standing waves · SLDV · Two-point excitation · Petri-dish

Introduction

Mechanical waves are commonly categorized by how they transmit energy—either as traveling waves or standing waves. In standing waves, energy remains localized to specific spatial regions, whereas traveling waves transport energy through the medium. This distinction is crucial in dynamic systems analysis and has broad applicability across disciplines. In biological settings, many aquatic organisms and microorganisms employ traveling-wave kinematics for propulsion, reflecting principles shared with structural dynamics and fluid–structure interactions. Over more than five decades, wave-based locomotion has been extensively studied. Traveling waves underpin flagellar and ciliary motion in microorganisms [1, 2, 3, 4, 5, 6, 7] and undulatory swimming in fish [8, 9, 10, 11, 12, 13], inspiring engineered systems ranging from robotic locomotion [14, 15, 16, 17, 18, 19] and bio-inspired propulsion [20, 21, 22, 23] to biomechanical structures such as the cochlea [24, 25, 26, 27, 28, 29], where wave propagation is central to function. Beyond biological and bio-mimetic systems, traveling waves are also exploited to reduce skin-friction drag on aerodynamic surfaces [30, 31, 32, 33] and to enable non-prehensile transport at micro and macro scales via controlled surface actuation [34, 35]. Given this significance,

Rachel Cole, Samikhshak Gupta, Vijaya V. N. Sriram Malladi
Vibrations, Intelligent Testing, & Active Learning of Structures (ViTALS) Group, Department of Mechanical and Aerospace Engineering, Michigan Technological University, Houghton, MI 49931
e-mail: reole@mtu.edu; sgupta14@mtu.edu; smalladi@mtu.edu

Smitha Rao Hatti
Department of Biomedical Engineering, Michigan Technological University, Houghton, MI 49931
e-mail: smithar@mtu.edu

Adrienne Minerick
Department of Chemical Engineering, Michigan Technological University, Houghton, MI 49931
e-mail: minerick@mtu.edu

© The Author(s), under exclusive license to River Publishers 2026

Kristin B. Zimmerman, PhD (eds.), *Topics in Modal Analysis & Parameter Identification in Structural Dynamics, 2026, Vol. 8*,
Conference Proceedings of the Society for Experimental Mechanics Series, https://doi.org/10.13052/rp-9788743814191

multiple strategies have been developed to generate traveling waves in finite structures, including strings [36, 37, 38, 39, 40, 41, 42, 43], beams [44, 45, 46, 47, 48], plates [49, 50, 51, 52, 53, 54], rings [55, 56], and rigid-walled circular acoustic ducts [57, 58]. Bucher et al. [56] showed that exciting a structure at two locations with a 90° phase difference, at a mean frequency between adjacent modes, induces directional traveling waves. Malladi and Avirovik [34, 44, 46] extended this two-point approach to piezo-augmented one-dimensional beams under varied boundary conditions, demonstrating theoretically and experimentally that both frequency and phase govern wave formation, beyond a fixed 90° offset at the mean frequency. In parallel, alternative control strategies have been explored. Blanchard et al. [38, 39] investigated passive suppression in fixed strings using a spring–dashpot attachment, revealing localized damping that can yield coexisting traveling and standing components through complex modal behavior and enabling passive confinement via proper tuning. Motaharibidgoli et al. [47] proposed a one-point excitation with a spring–damper to generate hybrid modes in Euler–Bernoulli beams and to distinguish and optimize traveling versus standing response. While effective on linear beams, single-point actuation is less practical on small, symmetric platforms, where mounting and achieving consistent directionality from a single source are sensitive to alignment and coupling.

Complementing structural approaches, surface acoustic waves (SAWs) [59, 60, 61] and broader acoustofluidic platforms [62, 63] enable biocompatible manipulation of micro/nanoparticles and cells, achieving on-chip transport [64], focusing, separation [65], and mixing [66]. Acoustic tweezers—spanning standing/traveling, bulk/surface, and streaming-driven modes—offer precise trapping, patterning, and translation from extracellular vesicles to single cells and small organisms [67, 68, 60, 69]. Despite an extensive body of work, direct implementations on standard Petri dishes—ubiquitous in cell and microbiology laboratories—remain limited, owing to constraints imposed by their circular symmetry, small footprint, and requirements for mounting, sterility, and optical access. These gaps motivate Petri-dish-centric strategies that preserve biocompatibility while delivering reliable wave directionality.

This study adopts an experimental framework that leverages modal analysis to estimate the traveling-wave fields that can be generated on standard Petri dishes for *in situ* microparticle transport, separation, and mixing in culture-relevant media. Guided by identified mode shapes and resonance frequencies, we determine drive frequency and phase relationships; accordingly, a two-point excitation scheme is proposed to achieve stable phase control and reliable wave directionality on circular substrates. While full realization of the traveling-wave fields is not presented here, the methodology and design parameters established in this work specify the conditions under which such fields are achievable. This preliminary effort provides the foundation for future tasks involving both single- and multi-particle control, including targeted transport, selective separation, and programmable mixing.

Experimental Setup

In this study, a borosilicate glass Petri dish served as the test specimen for modal analysis. Four PiezoDrive stack actuators were positioned on a $5\mathrm{cm}$ grid, each mounted $2\mathrm{mm}$ off-center relative to the dish, which was supported by half-sphere holders. The actuators were powered by a PiezoDrive PD200X4 amplifier with a gain of $20\mathrm{V}\,/\,\mathrm{V}$ and were driven using OptoScan software, which simultaneously scanned the dish surface during testing. The Scanning Laser Doppler Vibrometer (SLDV) provided the chirp excitation signal to the actuators and used their voltage outputs as the reference channel (see

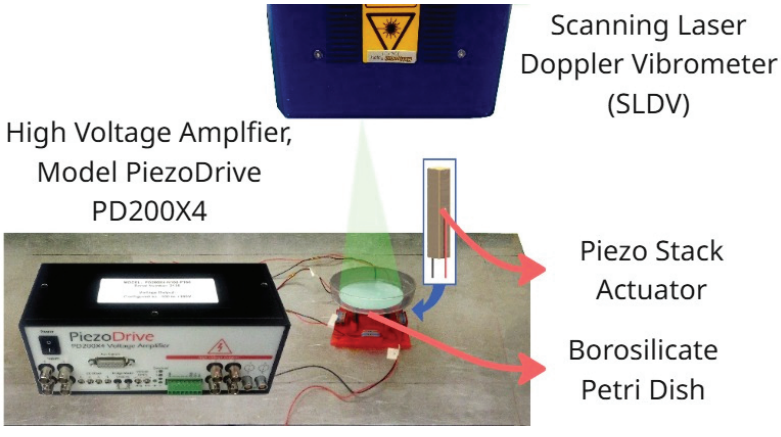

Fig. 1 Experimental setup for Petri dish modal analysis

Figure 1). The Petri dish was kept enclosed, with its lid secured to the base using double-sided tape. A circular piece of reflective tape was placed on the bottom surface to enable vibrometer measurements. For potential follow-up testing, an additional piezo actuator was fixed inside the dish. A 448-point circular mesh was defined in the OptoScan software on the dish base, consisting of 50 radial lines and 9 concentric rings. To account for the added actuator, three points were removed and nine were shifted. Modal data were collected at all 448 points for each stack actuator, resulting in four independent modal analyses.

The chirp input had an amplitude of 0.1 V, swept from 0–2000 Hz, and a duty cycle of 80%. Measurements were acquired at a maximum frequency of 50 kHz with 102,400 spectral lines, corresponding to a spectral resolution of 488.281 mHz and a sampling rate of 128 kS/s, satisfying the Nyquist criterion. Data collection was triggered at 0.05 V on the leading edge with a 1% pre-trigger factor. At each scan point, seven averages were recorded with a 0.01 s delay between acquisitions, and a rectangular window was applied during signal processing.

Data Driven Model for Traveling Wave Generation

After obtaining the frequency response functions (FRFs) of the petri-dish, each measurement point provides four responses, one from each stack actuator.

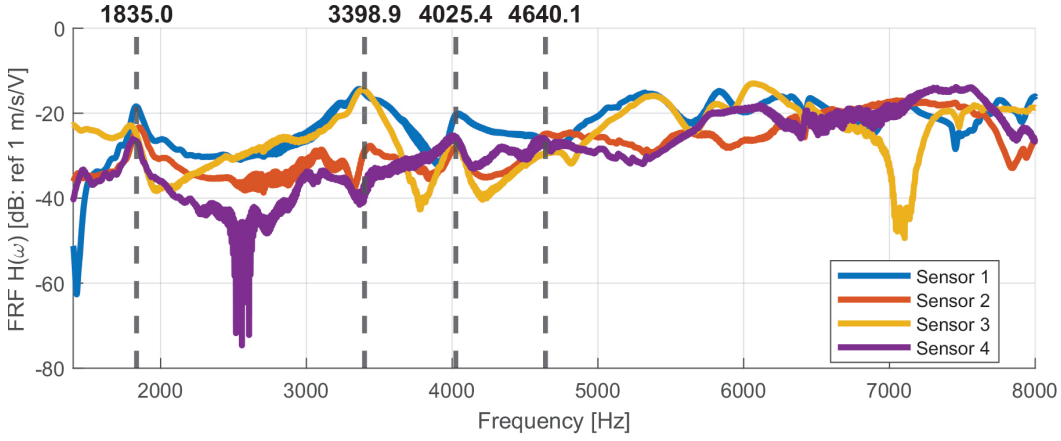

Fig. 2 Frequency response function (FRF) highlighting resonant peaks corresponding to natural frequencies

These FRFs can be arranged as

$$\mathbf{H}(x_i,\,\omega) = \begin{bmatrix}\mathbf{H_1} & \mathbf{H_2} & \mathbf{H_3} & \mathbf{H_4}\end{bmatrix}, \tag{1}$$

where $\mathbf{H}(x_i,\,\omega) \in \mathbb{C}$ denotes the FRFs at point x_i for a given frequency ω, and $\mathbf{H_1},\ \mathbf{H_2},\ \mathbf{H_3},\ \mathbf{H_4}$ represent the responses associated with actuators 1 through 4.

It is well established in prior work [56, 46, 70, 71] that traveling waves can be generated through two-point excitation. This is achieved by driving both actuators at a frequency located between two adjacent natural frequencies while maintaining a 90° phase difference. Under these conditions, the operational deflection shape (ODS) becomes a superposition of the individual actuator responses, with the enforced phase offset serving as the key mechanism that promotes traveling-wave formation.

For two-point excitation, the input to actuator 1 is given by $V_1 = A_1 \sin(2\pi f t)$, and the input to actuator 2 by $V_2 = A_2 \sin(2\pi f t \pm \phi)$. The combined excitation, which yields a traveling wave, is expressed as

$$\mathrm{TW} = A_1 \sin(2\pi f t) \ \pm \ A_2 \sin(2\pi f t \pm \phi), \tag{2}$$

where A_1 and A_2 are the excitation amplitudes, f is the frequency, t is time, and ϕ is the phase difference, equal to 90° for an ideal traveling wave. In contrast, standing waves occur when excitation is applied at a natural frequency. Under this condition, the actuators respond either in-phase (0°) or out-of-phase (180°), dictated by the symmetry of the corresponding mode shape. To confirm whether the procedure generates a traveling wave, the FRF-based data-driven model is used to construct the ODS of the petri-dish when two of the four stack actuators are excited simultaneously, as described in Equation (2). The ODS is obtained from the real part of the velocity response,

$$\mathbf{v}(t) = \mathrm{Re}\left(\tilde{v}e^{\iota\omega t}\right), \tag{3}$$

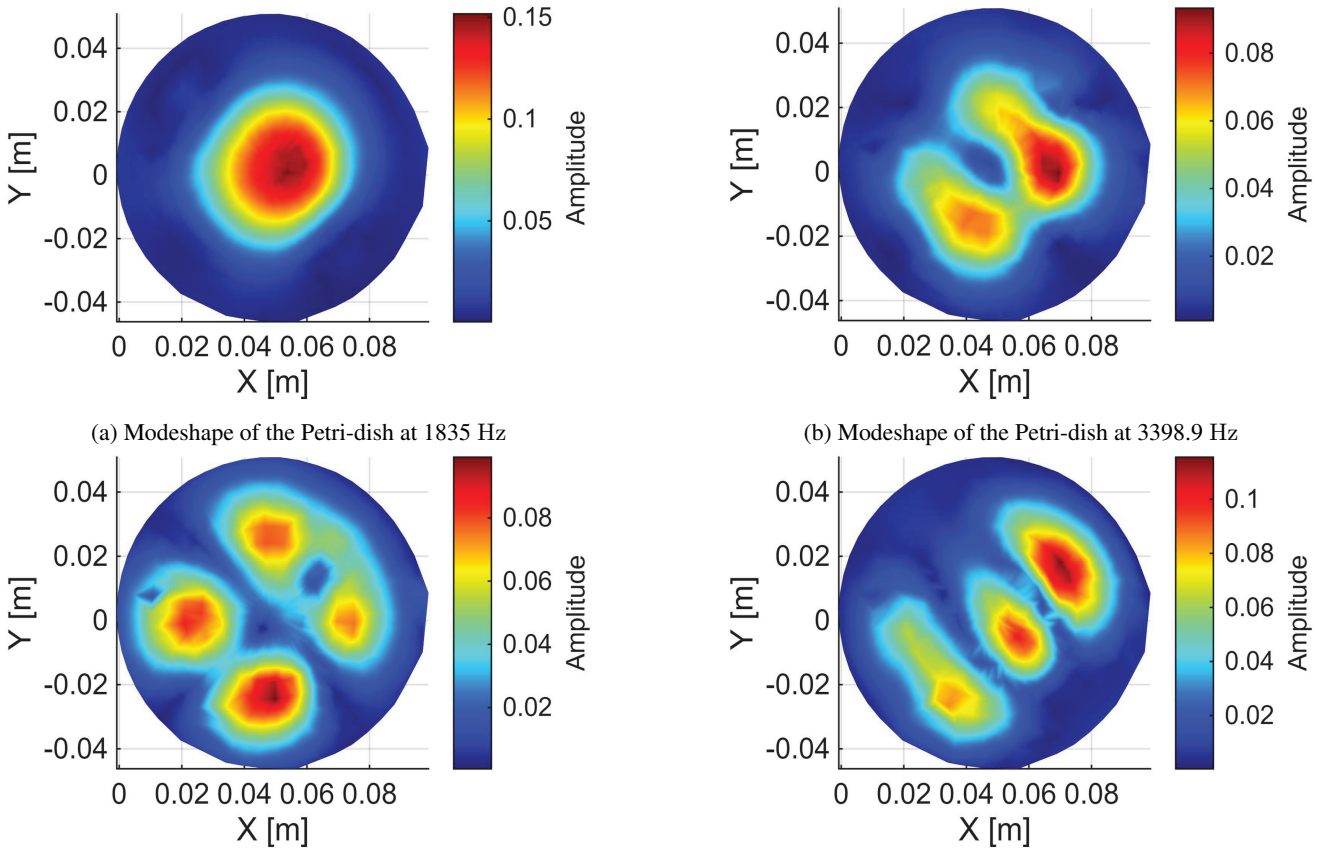

(a) Modeshape of the Petri-dish at 1835 Hz

(b) Modeshape of the Petri-dish at 3398.9 Hz

(c) Modeshape of the Petri-dish at 4025.4 Hz

(d) Modeshape of the Petri-dish at 4640.1 Hz

Fig. 3 Modeshapes of the Petri-dish at selected frequencies

where $\mathbf{v}(t)$ denotes the velocity at a point over time t, and $\tilde{v}$ is the complex velocity response due to two-point excitation. Combining Equation (1) and Equation (2), $\tilde{v}$ can be expressed as

$$\tilde{v}(x_i) = \begin{bmatrix} \mathbf{H_1} & \mathbf{H_2} & \mathbf{H_3} & \mathbf{H_4} \end{bmatrix} \begin{Bmatrix} A_1 e^{\iota\phi_1} \\ A_2 e^{\iota\phi_2} \\ A_3 e^{\iota\phi_3} \\ A_4 e^{\iota\phi_4} \end{Bmatrix}, \tag{4}$$

where A_1, A_2, A_3, A_4 are the excitation amplitudes applied to the actuators, and $\phi_1, \phi_2, \phi_3, \phi_4$ are their respective phase angles. In this study, actuator pairs (1–2), (1–3), and (1–4) are considered, with only two actuators excited at a time. For simplicity, the voltage amplitudes are fixed at unity, while the phases are assigned as 0° and 90° for the respective actuators. The resulting standing and traveling wave patterns are presented in Figure 3 and Table 1, respectively, in the following sections.

Results

The analysis focused on the frequency range of 1400–5000 Hz, within which the Petri dish exhibited four natural frequencies associated with standing waves and three frequencies where traveling waves were observed. These natural frequencies were identified directly from the measured frequency response functions (FRFs), and the corresponding wave types are summarized in Table 2. The operating deflection shapes (ODSs) were then evaluated under three actuator combinations to characterize the vibration patterns across the dish. The measured FRF for standing waves is shown in Figure 2, where resonant peaks indicate the four natural frequencies. The associated mode shapes are presented in Figure 3, which follow the expected behavior of circular plates. The FRF highlighting the frequencies corresponding to traveling waves is given

in Figure 4. In this case, the regions between resonant peaks were used to identify three traveling-wave frequencies. The corresponding ODSs for these traveling modes, measured under three different actuator pairings, are shown in Table 1.

Clear trends emerged across the different actuator combinations. When actuators were positioned along vertical or horizontal axes (Stack Actuator 1-2 and Stack Actuator 1-4), the resulting traveling waves exhibited rotational patterns. In contrast, the diagonal combination (Stack Actuator 1-3) produced transverse traveling waves. Increasing frequency also led to greater spatial complexity: at 4332.5 Hz, the waveforms contained more peaks than at lower frequencies, reflecting the higher-order nature of the response.

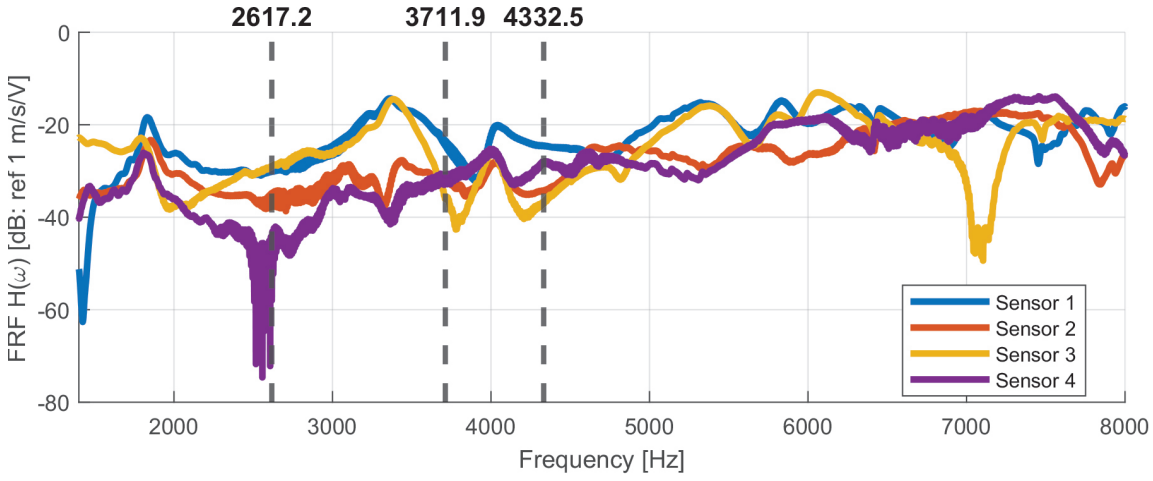

Fig. 4 Frequency response function (FRF) highlighting frequencies corresponding to traveling waves

Table 1 Traveling wave frequencies tested across piezo actuator combinations

TW Frequency	Piezo Combinations		
	Stack Actuator 1–2	Stack Actuator 1–3	Stack Actuator 1–4
2617.2 Hz	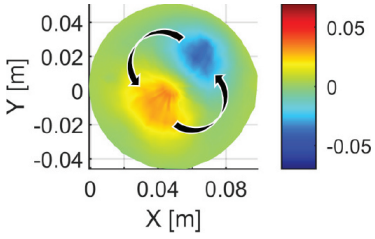	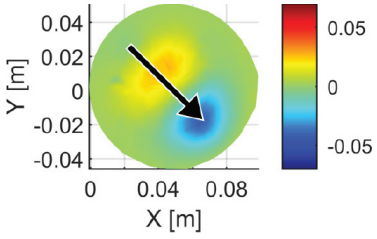	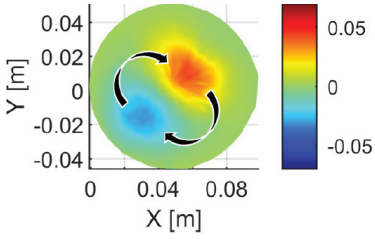
3711.9 Hz	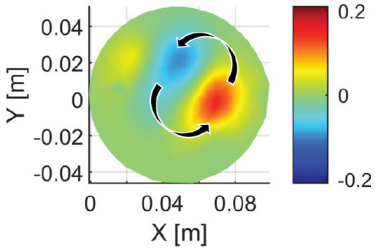	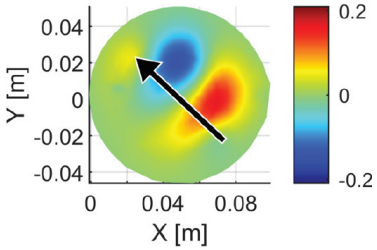	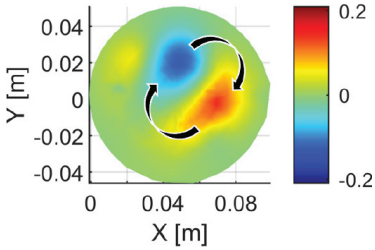
4332.5 Hz	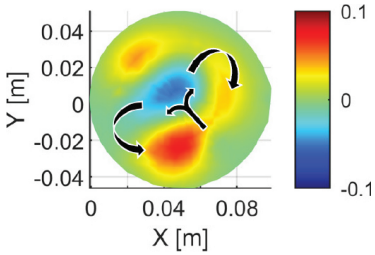	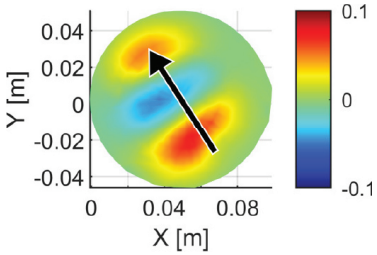	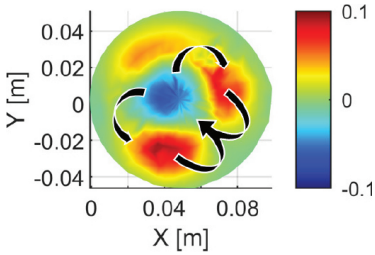

Table 2 Identified frequencies and corresponding modal or traveling-wave responses

Frequency (Hz)	Remarks
1835.0	1st mode shape
2617.2	Traveling wave
3398.9	2nd mode shape
3711.9	Traveling wave
4025.4	3rd mode shape
4332.5	Traveling wave
4640.1	4th mode shape

Conclusion

From the results, it is evident that a traveling wave can be generated on the free–free petri-dish through two-point excitation. An important observation, highlighted in Table 1, is that altering the actuator pair while maintaining the same excitation frequency and phase produces qualitatively different traveling-wave patterns. Specifically, when adjacent actuators are excited, the resulting response resembles a rotational traveling wave, whereas excitation from diagonally opposite actuators leads to a translational traveling wave. These distinctions are not only of theoretical interest but also carry practical implications. The ability to selectively generate rotational or translational traveling waves by simply varying actuator placement demonstrates a tunable actuation strategy for controlling wave characteristics. Such control opens up opportunities for employing spatially biased traveling waves (SBTWs) in future applications, particularly for manipulating particle trajectories on the petri dish. Potential extensions include single-particle transport with high precision as well as coordinated multi-particle manipulation, offering a pathway toward advanced lab-on-chip platforms and microfluidic control systems.

Acknowledgments The author (RC) gratefully acknowledges support from the DoD through the DoD SMART Scholarship. The authors (VVNSM and SG) also acknowledge support from the National Science Foundation under grant CMMI-2301776 for funding the research presented in this paper.

Declaration of generative AI and AI-assisted technologies in the writing process

While preparing this work, the author(s) used ChatGPT to edit the language. After using this tool/service, the author(s) reviewed and edited the content as needed and take(s) full responsibility for the publication's content.

References

1. Brokaw, C. "Non-sinusoidal bending waves of sperm flagella". *J. exp. Biol*, 43(1):155–169 (1965)ifnextchar.gobble.
2. Brokaw, C.J. "Flagellar movement: a sliding filament model: an explanation is suggested for the spontaneous propagation of bending waves by flagella.". *Science*, 178(4060):455–462 (1972)ifnextchar.gobble.
3. Taylor, G.I. "The action of waving cylindrical tails in propelling microscopic organisms". *Proceedings of the Royal Society of London. Series A. Mathematical and Physical Sciences*, 211(1105):225–239 (1952)ifnextchar.gobble.
4. Rikmenspoel, R. "The tail movement of bull spermatozoa: observations and model calculations". *Biophysical journal*, 5(4):365–392 (1965)ifnextchar.gobble.
5. Machin, K. "Wave propagation along flagella". *Journal of Experimental Biology*, 35(4):796–806 (1958)ifnextchar.gobble.
6. Narla, A.V., Cremer, J., and Hwa, T. "A traveling-wave solution for bacterial chemotaxis with growth". *Proceedings of the National Academy of Sciences*, 118(48):e2105138118 (2021)ifnextchar.gobble.
7. Oyarte Galvez, L., Bisot, C., Bourrianne, P., Cargill, R., Klein, M., van Son, M., van Krugten, J., Caldas, V., Clerc, T., Lin, K.K., et al. "A travelling-wave strategy for plant–fungal trade". *Nature*, pages 1–9 (2025)ifnextchar.gobble.
8. Hess, I. and Musgrave, P. "The role of compliance in generating traveling waves on a bio-inspired flexible propulsor". In *Smart Materials, Adaptive Structures and Intelligent Systems*, volume 86274, page V001T06A001. American Society of Mechanical Engineers (2022)ifnextchar.gobble.
9. Sfakiotakis, M., Lane, D.M., and Davies, J.B.C. "Review of fish swimming modes for aquatic locomotion". *IEEE Journal of oceanic engineering*, 24(2):237–252 (2002)ifnextchar.gobble.
10. Liu, F., Lee, K.M., and Yang, C.J. "Hydrodynamics of an undulating fin for a wave-like locomotion system design". *IEEE/ASME Transactions on Mechatronics*, 17(3):554–562 (2011)ifnextchar.gobble.
11. Kancharala, A. and Philen, M. "Enhanced hydrodynamic performance of flexible fins using macro fiber composite actuators". *Smart materials and structures*, 23(11):115012 (2014)ifnextchar.gobble.
12. Soto, K., Hess, I., Schrader, B., He, S., and Musgrave, P. "Improving swimming performance in soft robotic fish with distributed muscles and embedded kinematic sensing". In *2025 IEEE 8th International Conference on Soft Robotics (RoboSoft)*, pages 1–6. IEEE (2025)ifnextchar.gobble.

13. Hess, I. and Musgrave, P. "A continuum soft robotic trout with embedded hasel actuators: Design, fabrication, and swimming kinematics". *Smart materials and structures*, 33(10):105043 (2024)ifnextchar.gobble.
14. Kalani, H., Akbarzadeh, A., and Safehian, J. "Traveling wave locomotion of snake robot along symmetrical and unsymmetrical body shapes". In *ISR 2010 (41st International Symposium on Robotics) and ROBOTIK 2010 (6th German Conference on Robotics)*, pages 1–7. VDE (2010)ifnextchar.gobble.
15. Chen, L., Ma, S., Wang, Y., Li, B., and Duan, D. "Design and modelling of a snake robot in traveling wave locomotion". *Mechanism and Machine Theory*, 42(12):1632–1642 (2007)ifnextchar.gobble.
16. Haomachai, W., Dai, Z., and Manoonpong, P. "Transition gradient from standing to traveling waves for energy-efficient slope climbing of a gecko-inspired robot". *IEEE Robotics and Automation Letters*, 9(3):2423–2430 (2024)ifnextchar.gobble.
17. Salem, L., Gat, A.D., and Or, Y. "Fluid-driven traveling waves in soft robots". *Soft Robotics*, 9(6):1134–1143 (2022)ifnextchar.gobble.
18. Crespi, A. and Ijspeert, A.J. "Online optimization of swimming and crawling in an amphibious snake robot". *IEEE Transactions on robotics*, 24(1):75–87 (2008)ifnextchar.gobble.
19. Crespi, A., Badertscher, A., Guignard, A., and Ijspeert, A.J. "Amphibot i: an amphibious snake-like robot". *Robotics and Autonomous Systems*, 50(4):163–175 (2005)ifnextchar.gobble.
20. Erturk, A. and Delporte, G. "Underwater thrust and power generation using flexible piezoelectric composites: anexperimental investigation toward self-powered swimmer-sensor platforms". *Smart materials and Structures*, 20(12):125013 (2011)ifnextchar.gobble.
21. Lauder, G.V. and Tangorra, J.L. "Fish locomotion: biology and robotics of body and fin-based movements". In *Robot fish: bio-inspired fishlike underwater robots*, pages 25–49. Springer (2015)ifnextchar.gobble.
22. Syuhri, S.N., Pickles, D., Zare-Behtash, H., and Cammarano, A. "Influence of travelling waves on the fluid dynamics of a beam submerged in water". *Journal of Fluids and Structures*, 121:103947 (2023)ifnextchar.gobble.
23. Liao, J.C. "A review of fish swimming mechanics and behaviour in altered flows". *Philosophical transactions of the royal society b: biological sciences*, 362(1487):1973–1993 (2007)ifnextchar.gobble.
24. Davaria, S. and Tarazaga, P.A. "Mems scale artificial hair cell sensors inspired by the cochlear amplifier effect". In *Bioinspiration, Biomimetics, and Bioreplication 2017*, volume 10162, pages 82–91. SPIE (2017)ifnextchar.gobble.
25. Davaria, S., Sriram Malladi, V., and Tarazaga, P.A. "Bio-inspired nonlinear control of artificial hair cells". In *Structural Health Monitoring, Photogrammetry & DIC, Volume 6: Proceedings of the 36th IMAC, A Conference and Exposition on Structural Dynamics 2018*, pages 179–184. Springer (2018)ifnextchar.gobble.
26. Davaria, S., Malladi, V.V.S., Motaharibidgoli, S., and Tarazaga, P.A. "Cochlear amplifier inspired two-channel active artificial hair cells". *Mechanical Systems and Signal Processing*, 129:568–589 (2019)ifnextchar.gobble.
27. Davaria, S. and Tarazaga, P.A. "Self-sensing active artificial hair cells inspired by the cochlear amplifier, part i: Theoretical and numerical realization". *Journal of Intelligent Material Systems and Structures*, 34(2):177–193 (2023)ifnextchar.gobble.
28. Davaria, S., Malladi, V.V.S., and Tarazaga, P.A. "Self-sensing active artificial hair cells inspired by the cochlear amplifier, part ii: Experimental validation". *Journal of Intelligent Material Systems and Structures*, 34(18):2089–2105 (2023)ifnextchar.gobble.
29. Johnstone, B., Patuzzi, R., and Yates, G. "Basilar membrane measurements and the travelling wave". *Hearing research*, 22(1-3):147–153 (1986)ifnextchar.gobble.
30. Musgrave, P.F., Sriram Malladi, V., and Tarazaga, P.A. "Generation of traveling waves in a 2d plate for future drag reduction manipulation". In *Special Topics in Structural Dynamics, Volume 6: Proceedings of the 34th IMAC, A Conference and Exposition on Structural Dynamics 2016*, pages 129–138. Springer (2016)ifnextchar.gobble.
31. Musgrave, P.F. and Tarazaga, P.A. "Skin friction drag reduction in turbulent flow using spanwise traveling surface waves". In *Active and Passive Smart Structures and Integrated Systems 2017*, volume 10164, pages 110–116. SPIE (2017)ifnextchar.gobble.
32. Itoh, M., Tamano, S., Yokota, K., and Taniguchi, S. "Drag reduction in a turbulent boundary layer on a flexible sheet undergoing a spanwise traveling wave motion". *Journal of Turbulence*, (7):N27 (2006)ifnextchar.gobble.
33. Du, Y., Symeonidis, V., and Karniadakis, G. "Drag reduction in wall-bounded turbulence via a transverse travelling wave". *Journal of fluid mechanics*, 457:1–34 (2002)ifnextchar.gobble.
34. Loh, B.G. and Ro, P.I. "An object transport system using flexural ultrasonic progressive waves generated by two-mode excitation". *IEEE transactions on ultrasonics, ferroelectrics, and frequency control*, 47(4):994–999 (2000)ifnextchar.gobble.
35. Fu, L.M., Lee, G.B., Lin, Y.H., and Yang, R.J. "Manipulation of microparticles using new modes of traveling-wave-dielectrophoretic forces: numerical simulation and experiments". *IEEE/ASME Transactions on mechatronics*, 9(2):377–383 (2004)ifnextchar.gobble.
36. Anakok, I. *A study on steady state traveling waves in strings and rods*. PhD thesis, Virginia Tech (2018)ifnextchar.gobble.
37. Anakok, I., Malladi, V.S., and Tarazaga, P.A. "A study on the generation and propagation of traveling waves in strings". In *Topics in Modal Analysis & Testing, Volume 9: Proceedings of the 36th IMAC, A Conference and Exposition on Structural Dynamics 2018*, pages 257–261. Springer (2018)ifnextchar.gobble.
38. Blanchard, A., Gendelman, O.V., McFarland, D.M., Bergman, L.A., and Vakakis, A.F. "Mode complexity in a harmonically forced string with a local spring–damper and transitions from vibrations to waves". *Journal of Sound and Vibration*, 334:282–295 (2015)ifnextchar.gobble.
39. Blanchard, A., McFarland, D., Bergman, L., and Vakakis, A. "Damping-induced interplay between vibrations and waves in a forced non-dispersive elastic continuum with asymmetrically placed local attachments". *Proceedings of the Royal Society A: Mathematical, Physical and Engineering Sciences*, 471(2176):20140402 (2015)ifnextchar.gobble.
40. Anakok, I., Davaria, S., Tarazaga, P.A., and Malladi, V.V.S. "A study on steady-state traveling waves in one-dimensional non-dispersive finite media". *Journal of Sound and Vibration*, 528:116907 (2022)ifnextchar.gobble.
41. Cheng, X., Blanchard, A., Tan, C.A., Lu, H., Bergman, L.A., McFarland, D.M., and Vakakis, A.F. "Separation of traveling and standing waves in a finite dispersive string with partial or continuous viscoelastic foundation". *Journal of Sound and Vibration*, 411:193–209 (2017)ifnextchar.gobble.
42. Krenk, S. "Vibrations of a taut cable with an external damper". *J. Appl. Mech.*, 67(4):772–776 (2000)ifnextchar.gobble.
43. Gabai, R. and Bucher, I. "Excitation and sensing of multiple vibrating traveling waves in one-dimensional structures". *Journal of sound and vibration*, 319(1-2):406–425 (2009)ifnextchar.gobble.
44. Avirovik, D., Malladi, V.S., Priya, S., and Tarazaga, P.A. "Theoretical and experimental correlation of mechanical wave formation on beams". *Journal of Intelligent Material Systems and Structures*, 27(14):1939–1948 (2016)ifnextchar.gobble.

45. Cheng, X., Bergman, L.A., McFarland, D.M., Tan, C.A., Vakakis, A.F., and Lu, H. "Co-existing complexity-induced traveling wave transmission and vibration localization in euler-bernoulli beams". *Journal of Sound and Vibration*, 458:22–43 (2019)ifnextchar.gobble.
46. Malladi, V., Avirovik, D., Priya, S., and Tarazaga, P. "Characterization and representation of mechanical waves generated in piezo-electric augmented beams". *Smart Materials and Structures*, 24(10):105026 (2015)ifnextchar.gobble.
47. Motaharibidgoli, S., Davaria, S., Malladi, V.V.S., and Tarazaga, P.A. "Developing coexisting traveling and standing waves in euler-bernoulli beams using a single-point excitation and a spring-damper system". *Journal of Sound and Vibration*, 556:117728 (2023)ifnextchar.gobble.
48. Malladi, V.S., Avirovik, D., Priya, S., and Tarazaga, P.A. "Travelling wave phenomenon through a piezoelectric actuation on a free-free beam". In *Smart Materials, Adaptive structures and intelligent systems*, volume 46148, page V001T03A017. American Society of Mechanical Engineers (2014)ifnextchar.gobble.
49. Musgrave, P.F., Albakri, M.I., Tenney, C., and Tarazaga, P.A. "Generating and tailoring structure-borne traveling waves on two-dimensional surfaces". *Journal of Sound and Vibration*, 480:115417 (2020)ifnextchar.gobble.
50. Malladi, V.S., Albakri, M., Tarazaga, P.A., and Gugercin, S. "Reduced plate model used for 2d traveling wave propagation". In *Smart Materials, Adaptive Structures and Intelligent Systems*, volume 57298, page V001T03A021. American Society of Mechanical Engineers (2015)ifnextchar.gobble.
51. Malladi, V.V.S., Albakri, M., and Tarazaga, P.A. "An experimental and theoretical study of two-dimensional traveling waves in plates". *Journal of Intelligent Material Systems and Structures*, 28(13):1803–1815 (2017)ifnextchar.gobble.
52. Malladi, V.V.S., Albakri, M.I., Gugercin, S., and Tarazaga, P.A. "Application of projection-based model reduction to finite-element plate models for two-dimensional traveling waves". *Journal of Intelligent Material Systems and Structures*, 28(14):1886–1904 (2017)ifnextchar.gobble.
53. Hariri, H., Bernard, Y., and Razek, A. "2-d traveling wave driven piezoelectric plate robot for planar motion". *IEEE/ASME Transactions on Mechatronics*, 23(1):242–251 (2018)ifnextchar.gobble.
54. Rogers, W.C. and Albakri, M.I. "Estimation, tuning, and evaluation of propagation direction behavior in superimposed orthogonal two-dimensional structure-borne traveling waves". *Smart Materials and Structures*, 33(12):125027 (2024)ifnextchar.gobble.
55. Gabai, R., Ilssar, D., Shaham, R., Cohen, N., and Bucher, I. "A rotational traveling wave based levitation device–modelling, design, and control". *Sensors and Actuators A: Physical*, 255:34–45 (2017)ifnextchar.gobble.
56. Bucher, I. "Estimating the ratio between travelling and standing vibration waves under non-stationary conditions". *Journal of sound and vibration*, 270(1-2):341–359 (2004)ifnextchar.gobble.
57. Xiao, Y., Blanchard, A., Zhang, Y., Lu, H., Michael McFarland, D., Vakakis, A.F., and Bergman, L.A. "Separation of traveling and standing waves in a rigid-walled circular duct containing an intermediate impedance discontinuity". *Journal of Vibration and Acoustics*, 139(6):061001 (2017)ifnextchar.gobble.
58. Xiao, Y., Lu, H., McFarland, D.M., Vakakis, A.F., and Bergman, L.A. "Inducing a nonreflective airborne discontinuity in a circular duct by using a nonresonant side branch to create mode complexity". *The Journal of the Acoustical Society of America*, 143(2):746–755 (2018)ifnextchar.gobble.
59. Qi, M., Dang, D., Yang, X., Wang, J., Zhang, H., and Liang, W. "Surface acoustic wave manipulation of bioparticles". *Soft Matter*, 19(23):4166–4187 (2023)ifnextchar.gobble.
60. Qin, X., Liu, X., Liu, S., Zhang, C., Bai, N., Li, X., Wang, W., Liu, D., Yang, Q., Yang, R., et al. "Movable surface acoustic wave tweezers: a versatile toolbox for micromanipulation". *Microsystems & Nanoengineering*, 10(1):155 (2024)ifnextchar.gobble.
61. Amorim, D., Sousa, P.C., Abreu, C., and Catarino, S.O. "A review of saw-based micro-and nanoparticle manipulation in microfluidics". *Sensors*, 25(5):1577 (2025)ifnextchar.gobble.
62. Mohanty, S., Khalil, I.S., and Misra, S. "Contactless acoustic micro/nano manipulation: a paradigm for next generation applications in life sciences". *Proceedings of the Royal Society A*, 476(2243):20200621 (2020)ifnextchar.gobble.
63. Cao, H.X., Nguyen, V.D., Park, J.O., Choi, E., and Kang, B. "Acoustic actuators for the manipulation of micro/nanorobots: state-of-the-art and future outlooks". *Micromachines*, 15(2):186 (2024)ifnextchar.gobble.
64. Han, W., Zou, H., Yue, H., Zhong, Y., Li, W., Zhang, C., and Zhang, H. "Particle separation using surface acoustic waves based on microfluidic chip". *Chaos, Solitons & Fractals*, 198:116557 (2025)ifnextchar.gobble.
65. Han, J., Hu, H., Lei, Y., Huang, Q., Fu, C., Gai, C., and Ning, J. "Optimization analysis of particle separation parameters for a standing surface acoustic wave acoustofluidic chip". *ACS omega*, 8(1):311–323 (2022)ifnextchar.gobble.
66. Zhang, P., Bachman, H., Ozcelik, A., and Huang, T.J. "Acoustic microfluidics". *Annual Review of Analytical Chemistry*, 13(1):17–43 (2020)ifnextchar.gobble.
67. Ozcelik, A., Rufo, J., Guo, F., Gu, Y., Li, P., Lata, J., and Huang, T.J. "Acoustic tweezers for the life sciences". *Nature methods*, 15(12):1021–1028 (2018)ifnextchar.gobble.
68. Yang, S., Rufo, J., Zhong, R., Rich, J., Wang, Z., Lee, L.P., and Huang, T.J. "Acoustic tweezers for high-throughput single-cell analysis". *Nature protocols*, 18(8):2441–2458 (2023)ifnextchar.gobble.
69. Wu, H., Tang, Z., You, R., Pan, S., Liu, W., Zhang, H., Li, T., Yang, Y., Sun, C., Pang, W., et al. "Manipulations of micro/nanoparticles using gigahertz acoustic streaming tweezers". *Nanotechnology and Precision Engineering*, 5(2) (2022)ifnextchar.gobble.
70. Gadekar, S.S. "An experimental study towards underwater propulsion system using structure borne traveling waves". Master's thesis, Michigan Technological University (2022)ifnextchar.gobble.
71. Gupta, S. and Malladi, V.V.S. "Utilizing steady-state traveling waves in a quiescent water environment for particle propulsion". In *Smart Materials, Adaptive Structures and Intelligent Systems*, volume 88322, page V001T03A008. American Society of Mechanical Engineers (2024)ifnextchar.gobble.

River Rapids

Topics in Modal Analysis & Parameter Identification in Structural Dynamics, Volume 8

Timothy Marinone ■ Jon Furlich ■ Sheyda Davaria

Topics in Modal Analysis & Parameter Identification in Structural Dynamics, Volume 8: Proceedings of the 44th IMAC, A Conference and Exposition on Structural Dynamics, 2026, the eighth volume of ten from the Conference brings together contributions to this important area of research and engineering. The collection presents early findings and case studies on fundamental and applied aspects of Modal Analysis, Modal Testing and Parameter Identification including papers on:

- Analytical Methods
- Modal Applications
- Basics of Modal Analysis
- Operational Modal Analysis
- Novel Techniques
- System Identification
- Modal Parameter Estimation
- BioMechanical Systems
- Aircraft and Aerospace Applications
- Rotating Machinery

ISBN 978-87-438-1447-4

9 788743 814474

River Publishers